UC San Diego
UC San Diego Electronic Theses and Dissertations

Title

Semiconductor Nanostructures for Solar Water Splitting and Hydrogen Production: Design, Growth/Fabrication, Characterization, and Device Performance

Permalink
https://escholarship.org/uc/item/1cg136j9

Author

Kargar, Alireza

Publication Date

2015

Peer reviewed|Thesis/dissertation

eScholarship.org Powered by the California Digital Library
University of California

UNIVERSITY OF CALIFORNIA, SAN DIEGO

Semiconductor Nanostructures for Solar Water Splitting and Hydrogen Production: Design, Growth/Fabrication, Characterization, and Device Performance

A dissertation submitted in partial satisfaction of the requirements for the degree of

Doctor of Philosophy

in

Electrical Engineering (Nanoscale Devices & Systems)

by

Alireza Kargar

Committee in charge:

Professor Sungho Jin, Chair
Professor Prabhakar R. Bandaru, Co-Chair
Professor Shadi A. Dayeh, Co-Chair
Professor Yuan Taur
Professor Joseph Wang
Professor Jie Xiang

2015

Copyright

Alireza Kargar, 2015

All rights reserved.

The dissertation of Alireza Kargar is approved, and it is acceptable in quality and form for publication on microfilm and electronically:

Co-Chair

Co-Chair

Chair

University of California, San Diego

2015

DEDICATION

To my parents

TABLE OF CONTENTS

Signature Page .... **iii**

Dedication .... **iv**

Table of Contents .... **v**

List of Figures .... **viii**

Acknowledgments .... **xiv**

Vita .... **xx**

Abstract of Dissertation .... **xxvi**

1. Introduction **1**

2. Tailoring n-ZnO/p-Si Branched Nanowire Heterostructures for Selective Photoelectrochemical Water Oxidation or Reduction **4**

2.1. Introduction 4

2.2. Experimental Section 6

2.3. Results and Discussion 9

2.4. Conclusions 22

3. 3D Branched Nanowire Photoelectrochemical Electrodes for Efficient Solar Water Splitting **27**

3.1. Introduction 27

3.2. Experimental Section 28

3.3. Results and Discussion 30

3.4. Conclusions 43

4. Three-Dimensional ZnO/Si Broom-Like Nanowire Heterostructures as Photoelectrochemical Anodes for Solar Energy Conversion **47**

4.1. Introduction 47

4.2. Experimental Section 48

4.3. Results and Discussion 52

4.4. Conclusions 64

5. p-Si/SnO_2/Fe_2O_3 Core/Shell/Shell Nanowire Photocathodes for Neutral pH Water Splitting **68**

5.1. Introduction..68
5.2. Experimental Section...70
5.3. Results and Discussion...73
5.4. Conclusions..83
6. Nanowire/Nanotube Array Tandem Cells for Overall Solar Neutral Water Splitting...88
6.1. Introduction..88
6.2. Experimental Section...90
6.3. Results and Discussion...95
6.4. Conclusions..102
7. ZnO/CuO Heterojunction Branched Nanowires for Photoelectrochemical Hydrogen Generation..107
7.1. Introduction..107
7.2. Experimental Section...109
7.3. Results and Discussion...112
7.4. Conclusions..126
8. Solution-Grown 3D Cu_2O Networks for Efficient Solar Water Splitting.........131
8.1. Introduction..131
8.2. Experimental Section...133
8.3. Results and Discussion...136
8.4. Conclusions..148
9. NiO_x-Fe_2O_3-coated p-Si Photocathodes for Enhanced Solar Water Splitting in Neutral pH Water...152
9.1. Introduction..152
9.2. Experimental Section...153
9.3. Results and Discussion...156
9.4. Conclusions..163
10. Solution-Processed $CoFe_2O_4$ Nanoparticles on 3D Carbon Fiber Papers for Durable Oxygen Evolution Reaction..168
10.1. Introduction..168

10.2. Experimental Section 169
10.3. Results and Discussion 173
10.4. Conclusions 181

LIST OF FIGURES

Figure 2.1. SEM images of 3D ZnO/Si branched NW heterostructures. (a-d) b-(10m-ZnO/6m-Si) NWs with the Si NW core diameter of ~200 nm and pitch size of 700 nm. (a) Low-magnification, 45° view image, (b, c) top view images, (d) high-magnification, 45° view image. (e) Cross-sectional view image of b-(10m-ZnO/10m-Si) ………….. ...12

Figure 2.2. Current density versus applied potential of (a) b-(10m-ZnO/12m-p-Si) and (b) b-(10m-ZnO/12m-p^+-Si) NWs, with the Si NW array pitch size of 700 nm. The red and black lines represent the current density under illumination and at dark, respectively. Insets show the current density versus time for the corresponding branched …………14

Figure 2.3. Proposed energy band diagrams of n-ZnO/p-Si branched nanowires at (a) reversed biasing potential (-1.5 V) and (b) forward biasing potential (+1.5 V), and n-ZnO/p^+-Si branched nanowires at (c) reversed biasing potential (-1.5 V) and (d) forward biasing potential (+1.5 V)……………………………………………………………..15

Figure 2.4. (a) 45°-view SEM image of TiO_2-coated b-(5m-ZnO/10m-p-Si) NW array. (b) Current density under illumination versus applied potential of TiO_2-coated (red curve) and TiO_2/Pt coated (blue curve) b-(5m-ZnO/10m-p-Si) NWs. Inset shows the current density under illumination versus time of corresponding TiO_2/Pt coated ………………18

Figure 3.1. Fabrication procedure for 3D ZnO/Si branched NW (b-NW) arrays. After Si etching, the Ni disks at the head of Si NWs were removed by the Ni etchant…………..31

Figure 3.2. SEM images of 3D ZnO/Si b-NWs of 10m-Si NW cores with different ZnO NW growth times. First row, second row, and third row show the top view, cross-sectional view, and 45° view images, respectively. (a)-(c) zero min (bare Si NW array), (d)-(f) 5 mins, and (g)-(i) 10 mins. (j)-(l) are low-magnification images of (g)-(i)……...32

Figure 3.3. SEM images of 3D ZnO/Si b-NWs with 10m-ZnO NW branches on Si NW cores with (a)-(c) 10 mins and (d)-(f) 20 mins RIE etching. First and second columns show the cross-sectional view images, and third column shows the top view images…..33

Figure 3.4. (a) Photocurrent density of 10m-p-Si NW cores with ZnO NW branches grown for different times, (b) transient current density under chopped light illumination of corresponding b-NW samples at -1.5 V, and (c) dark current density of corresponding samples in (a). The inset in (a) shows the dark (black curve) and ………………………34

Figure 3.5. (a) Current density of b(5m-ZnO/10m-p^+-Si) NWs. The red and black lines represent the photo and dark current density, respectively. (b) Photocurrent density of 10m-p^+-Si NW cores with ZnO NW branches grown for various times, and (c) transient current density under chopped light illumination of corresponding b-NWs………..…..36

Figure 3.6. IPCE for the b(5m-ZnO/10m-p-Si) NWs at -1.3 V (orange line), and the 10m-p^+-Si NW cores with various ZnO NW branches at +1.3 V (red: bare Si NW array, blue: 5 mins ZnO, black: 10 mins ZnO). The inset shows the zoom-in spectral IPCE in UV range for the corresponding samples with p^+-Si NW cores. These b-NW ……………...39

Figure 3.7. (a)-(b) SEM images of TiO_2/Pt coated b(5m-ZnO/10m-p-Si) NWs. (c) Current density of b(5m-ZnO/10m-Si) NWs with different coatings (dark cyan and black lines: dark and photo currents of bare b-NWs, respectively, magenta and red lines: dark and photo currents of TiO_2-coated b-NWs, respectively, dark yellow and ………………….41

Figure 4.1. Cross-sectional SEM images of n-Si NW arrays etched for (a) 5min, (b) 10min, (c) 15min, and coated with ZnO seeding layer. The zoomed parts in (c) show the non-uniform coating of ZnO seeding layer on Si NWs………………………………….51

Figure 4.2. SEM images of ZnO/Si nanobroom arrays with different ZnO NW growth times on 15min Si NW backbone array. (a)-(c) and (d)-(f) show the top-view and tilted-view images of samples with 5min, 10min, and 15min ZnO NW growth, respectively. (g) and (h) High- and low-magnification cross-sectional images of ………………………..53

Figure 4.3. (a) Low-magnification bright field TEM image of ZnO/Si nanobroom arrays on Si substrate with 10min Si NW backbones and 10min ZnO NW stalls. Low-magnification dark field STEM image (b) and bright field STEM image (c) of a single ZnO/Si nanobroom. (d, e) High-resolution annular STEM images ……………………..55

Figure 4.4. (a) Low-magnification bright field TEM image of the top of the nanobrooms with 10min Si NW backbones and 10min ZnO NW stalls. (b) Zoom-in TEM image of a single ZnO NW. (c) High-resolution image of labeled part of a ZnO NW tip and the corresponding FFT pattern indicating a ZnO NW growth direction of …………………56

Figure 4.5. (a) Optical image of n-Si NW arrays (etched for 10min) and with ZnO coating or ZnO NWs; A: bare Si NW array, B: with ZnO seeding layer coating, C: with 5min ZnO NW, D: with 10min ZnO NW, E: with 15min ZnO NW. (b) optical image of samples C, D, E with a slightly different view angle. Absorption ………………………56

Figure 4.6. PEC performance and the working principle of the nanobroom photoelectrodes. Current density versus applied potential for the ZnO/Si nanobroom photoelectrodes in neutral solution (pH = 7.25); (a) 10min grown ZnO NWs on n-Si NWs with different lengths (etching times) and (b) ZnO NW stalls with ……………………58

Figure 4.7. Stability performance of bare and TiO_2-coated nanobrooms (5min n-Si NW backbones with 5min ZnO NWs) in neutral solution (pH = 7.25). (a)-(c) Bare nanobroom electrode; (a) SEM images of sample before any PEC and stability tests (as-grown sample), (b) anodic current density under constant light ………………………………..62

Figure 4.8. Current density versus applied potential of TiO_2-coated nanobrooms (5min n-Si NW backbones with 5min ZnO NWs) with and without Ru co-catalyst in neutral solution (pH = 7.25). “Light” and “Dark” indicate the current density under illumination and at dark, respectively. The inset is the zoomed curves …………………………….…64

Figure 5.1. SEM images of $Si/SnO_2/Fe_2O_3$ css-NW arrays. (a-c) Top-view (low magnification), cross-sectional and top-view (high magnification) images of bare 10m-Si NW array. (d-f) Top-view and 45° view images (with two different magnifications) of css(5m-Si/SnO_2/2h-Fe_2O_3) NWs. (g-j) 45° view, top-view ……………………………..74

Figure 5.2. (a) TEM image of a single css(20m-Si/SnO_2/2h-Fe_2O_3) NW broken from the substrate in its length. (b) HRTEM image of labeled area “A” in (a) exhibiting the crystal structure of Si NW core. Inset exhibits the calculated FFT pattern. (c) High-magnification TEM image of labeled area “B” in (a) showing the interfaces among Si ……………….…75

Figure 5.3. (a) Current density under illumination of 10m-Si NW cores with different coatings (black: bare NW, red: Si/SnO_2 cs-NW, blue: $Si/SnO_2/Fe_2O_3$ css-NW). Inset shows the corresponding zoom-in curves with calculated potential shift. (b) Current density under illumination of css(Si/SnO_2/2h-Fe_2O_3) NWs ……………………………77

Figure 5.4. (a) Current density under constant light illumination versus time (stability performance) of css(8.5m-Si(111)/SnO_2/2h-Fe_2O_3) NWs in neutral electrolyte measured at -0.33 V versus RHE. Inset shows the enlarged first part (0-10 min) of the current density. (b) Current density at dark and under illumination of …………………………80

Figure 5.5. SEM images of css(8.5m-Si(111)/SnO_2/2h-Fe_2O_3) NW photoelectrode (a) before PEC and stability tests (as-fabricated sample), and (b) after PEC tests and a long stability test of over 6 hrs……………………………………………………………...81

Figure 6.1. Schematic representation of fabrication procedure for the csh-NWs photocathode (top row) and the cs-NTs photoanode (bottom row). ……………………95

Figure 6.2. (a,b) Top-view (different magnification) and (c,d) cross-sectional view (different magnification) SEM images of p-Si/TiO_2/A-Fe_2O_3 csh-NW array. (e-i) Elemental mapping analysis of p-Si/TiO_2/A-Fe_2O_3 csh-NW array; (e) SEM image of spot used for the elemental mapping, (f) Si map, (g) Ti map, (h) Fe map……………………96

Figure 6.3. Top-view SEM images of (a) bare TiO_2 NTs and (b) TiO_2/TiO_2 cs-NTs. Tilted cross-sectional SEM images of (c) bare TiO_2 NTs and (d) TiO_2/TiO_2 cs-NTs. Note that the tilted angle for (c) and (d) is not the same. (e-g) Elemental mapping analysis of TiO_2/TiO_2 cs-NTs; (e) SEM image of spot used for the elemental ……………………..97

Figure 6.4. Current density under illumination of bare p-Si NW, p-Si/TiO_2/A-Fe_2O_3 csh-NW, and p-Si/TiO_2/N-Fe_2O_3 csh-NW arrays measured in the neutral pH water using (a) a three-electrode and (b) a two-electrode PEC setups. Insets in (a,b) show the dark current of the corresponding samples. (c) Photocathode energy ……………………………..98

Figure 6.5. (a) Current density under illumination of TiO_2/TiO_2 cs-NTs (grown on foil) photoanode along with the current density under illumination of p-Si/TiO_2/N-Fe_2O_3 csh-NWs photocathode measured in the neutral pH water. Note that in this figure, the absolute value of current density for the csh-NWs is plotted ………….………………101

Figure 7.1. SEM images of CuO NW arrays grown at 400°C on Cu foil for different annealing times; (a) 2h, (b) 3h, (c) 4h, and (d) 5h. The insets show the optical images of the corresponding samples. SEM images of CuO NWs grown for 4h on Cu foil at different annealing temperatures; (e) 400°C, (f) 450°C, and (g) 500°C………………..114

Figure 7.2. (a) Low-magnification bright field TEM image of a single 4h-400°C-CuO NW and (b) high-resolution TEM image of left side of corresponding CuO NW. Inset shows the calculated FFT pattern indicating the CuO NW growth direction. (c) Low-magnification high angle annular dark field STEM image of a ………………………..115

Figure 7.3. (a)-(b) SEM images of 4h-400°C-CuO NWs on Cu mesh with ZnO seeding layer. SEM images of ZnO/CuO b-NWs on Cu foil with 3h-400°C-CuO NW cores, and different ZnO NW branches ((c)-(d) 5m-ZnO, (e)-(f) 10m-ZnO, (g)-(h) 15m-ZnO)…..117

Figure 7.4. (a) Low-magnification annular bright field STEM image of a single b(10m-ZnO/4h-400°C-CuO) NW. (b) High angle annular dark field STEM image of labeled single ZnO NW. (c) and (d) High-resolution images of right side of ZnO NW in (b). (e) The corresponding noise-filtered image of (d). (f) ……………………………………118

Figure 7.5. Current density of CuO/ZnO cs-NWs grown at 400°C for different annealing times (black line: 2h, red line: 5h) on Cu foil (a) under light illumination and (b) at dark. (c) Transient current density under chopped illumination of the corresponding samples. Current density of 5m-ZnO NWs on CuO NW cores ………………………………….120

Figure 7.6. Approximate energy band diagram of the ZnO/CuO heterojunction b-NW in contact with the electrolyte at a reversed biasing potential of -0.45 V. The inset shows a STEM image (part of Figure 7.4a) indicating the relative size of the CuO NW radius to the ZnO NW length……………………………………………………………………..122

Figure 7.7. Spectral incident photon-to-current efficiency (IPCE) of b(5m-ZnO/3h-400°C-CuO) NWs at -0.4 V versus Ag/AgCl RE……………………………………124

Figure 7.8. (a)-(b) SEM images of 4h-400°C-CuO NWs on Cu mesh. The inset in (b) shows high-magnification image illustrating the CuO NWs diameter size. SEM images of ZnO/CuO b-NWs grown on Cu mesh with 4h-400°C-CuO NW cores and different ZnO NW branches ((c)-(d) 5m-ZnO and (e)-(f) 10m-ZnO)…………………………………125

Figure 8.1. SEM images of $Cu(OH)_2$ NW array grown for 10 mins on Cu foil; (a) top view, (b) 45° view, and (c) top view (different magnification) images. Top-view SEM images of Cu_2O NWs/NRs/networks synthesized under different annealing temperatures and times; (d) 2h-500°C-Cu_2O, (e) 4h-500°C-Cu_2O…………………………...……138

Figure 8.2. (a) XRD pattern of 2h-700°C-Cu_2O network, showing phase-pure Cu_2O rods. The Cu peaks are from the copper substrate. (b) TEM image of a single 2h-700°C-Cu_2O rod, (c) HRTEM image of the corresponding rod, (d) fast Fourier transform (FFT) analysis, and (e) selected area electron diffraction (SAED) pattern……………………139

Figure 8.3. (a) Current density under illumination of Cu_2O NWs/NRs/networks synthesized under different annealing temperatures and times (black: 2h-500°C-Cu_2O, red: 4h-500°C-Cu_2O, blue: 2h-700°C-Cu_2O). The inset shows dark current of the corresponding samples. Current density under chopped illumination …………………141

Figure 8.4. Transient current density under chopped illumination at 0 V versus RHE for 2h-700°C-Cu_2O networks with different metal oxide coatings; (a) 10-nm-TiO_2 coated sample, (b) ZnO/TiO_2 coated sample, (c) ZnO/TiO_2 coated sample with post annealing, and (d) AZO/TiO_2 coated sample with post annealing……………………………....145

Figure 8.5. SEM images of bare 2h-700°C-Cu_2O network (a) before (as-grown) and (b) after PEC, stability tests, and cyclic voltammetry measurement. SEM images of 2h-700°C-Cu_2O network coated with AZO/TiO_2 followed with the post annealing (c,e) before (as-synthesized) and (d,f) after PEC, stability tests…………………………..…146

Figure 8.6. Spectral incident photon-to-current efficiency (IPCE) of 20-nm-TiO_2 coated 2h-700°C-Cu_2O network at 0 V versus RHE…………………………………………...148

Figure 9.1. Schematic representation of fabrication procedure for the metal-oxide-coated p-Si substrates……………………………………………...154

Figure 9.2. High-magnification (a) cross-sectional and (b) tilted view SEM images of 2h-Fe_2O_3 NRs grown on p-Si substrate using SnO_2 as seeding layer. (c) High- and (d) low-magnification 45° view SEM images of the corresponding sample……………………157

Figure 9.3. (a) Ni 2p and (b) O 1s XPS spectra of NiO_x NPs spin-coated on Si substrate……………………………………………………………………………...158

Figure 9.4. Current density under illumination of different metal-oxide-coated p-Si photocathodes measured in the neutral pH water. Inset shows the dark current of the corresponding samples. (b) Current density under illumination of bare and NiO_x-Fe_2O_3-SnO_2-coated p-Si photocathodes in comparison to Pt-SnO_2-coated…………………....158

Figure 9.5. Current density under illumination versus time (stability test) measured in the neutral pH water at -0.66 V versus RHE of (a) Fe_2O_3-SnO_2-coated p-Si photocathode and

(b) Pt-SnO_2-coated p-Si photocathode. Inset in (a) shows the stability test for the SnO_2-coated p-Si photocathode at -0.86 V versus RHE……………………………………162

Figure 9.6. Cyclic voltammetry (CV) under illumination of (a) Fe_2O_3-SnO_2-coated p-Si photocathode and (b) NiO_x-coated p-Si photocathode for 21 cycles measured in the neutral pH water. (c) Current density under illumination and at dark before and after 21 CV cycles for the NiO_x-coated p-Si photocathode tested in …………………………...162

Figure 10.1. (a-c) SEM images (different magnification) and (d) XRD pattern of $CoFe_2O_4$ NPs on CFP. (e-i) Elemental mapping analysis of $CoFe_2O_4$ NPs on CFP; (e) SEM image of spot used for the elemental mapping, (f) Co map, (g) Fe map, (h) O map, and (i) C map. The scale bar for (f-i) is the same as that in (e)…………………………………...174

Figure 10.2. (a) Cyclic voltammetry (CV) measurement of $CoFe_2O_4$ NPs on CFP and bare CFP recorded at a scan rate of 20 mV/s in 1 M NaOH. Inset shows the zoomed-in current density versus RHE. (b) Tafel plot of corresponding samples in (a). (c) Current density versus time of $CoFe_2O_4$ NPs on CFP measured at a fixed ……………………175

Figure 10.3. Consecutive cyclic voltammetry (CV) scans of (a) $CoFe_2O_4$ NPs on CFP (37 cycles) and (b) bare CFP (27 cycles) collected at a scan rate of 20 mV/s in 1 M NaOH. (c) Long cycling performance of over 1000 cycles, taking over 15 hrs, of $CoFe_2O_4$ NPs on CFP recorded at a scan rate of 20 mV/s in 1 M NaOH……………………………...177

Figure 10.4. Characterization of $CoFe_2O_4$ NPs on CFP after long cycling test of over 15 hrs (shown in Figure 10.3c); (a,b) SEM images with different magnification, (c) XRD pattern along with the XRD of as-synthesized $CoFe_2O_4$ NPs on CFP for comparison, and (d-h) elemental mapping analysis of $CoFe_2O_4$ NPs on CFP……………………………179

Figure 10.5. (a) Linear sweep voltammetry (LSV) measurement of $CoFe_2O_4$ NPs on CFP and bare CFP recorded at a scan rate of 20 mV/s in 1 M NaOH from positive to negative potentials. (b) Corresponding current density versus RHE for the HER performance. The plots are without any iR correction……………………………………………………..180

ACKNOWLEDGEMENTS

First and foremost, I would like to express my sincere appreciation to my advisors Prof. Sungho Jin and Prof. Deli Wang for their vast support, abundant guidance, and continual encouragement over the course of my research in their groups. Both have been excellent mentors to learn from, big supporters for my goals, and perfect role models in conduct of scientific research. Their depth of knowledge with the subject allowed me to work in a really rewarding environment that encouraged collaboration and enforced integrity of scholarship. I would also like to acknowledge their advice, friendship, patience, and fruitful discussions related to my research works and other stuff. It has been a great opportunity to work under their supervision.

I am also highly thankful to the members of my thesis committee, Prof. Prabhakar R. Bandaru, Prof. Shadi A. Dayeh, Prof. Yuan Taur, Prof. Joseph Wang, and Prof. Jie Xiang. Their flexibility and understanding, as well as their valuable inputs and suggestions were of huge value to the completion of this thesis. Due to his depth of knowledge in all aspects of materials and devices, Prof. Dayeh was always extremely exciting and beneficial during numerous discussions that I have had with him. I also deeply appreciate him for accessing his lab and the euipements to use for the research projects. His trust, encouragement, and guidance have been much appreciated. I had interesting and instructive discussions with Prof. Prabhakar R. Bandaru related to electrochemical characterization and nanoparticles synthesis. I also appreciate his support to stay in his lab after the retirement of Prof. Sungho Jin and to continue my research. I am highly appreciative for learning useful leassons related to solid satate physics in the Prof. Yuan Taur's classes. I would also thank Prof. Jie Xiang for the useful discussions related to my research and for the lessons I learnt in his class related to quantum physics. Lastly, I appreciate the opportunity to collaborate with Prof. Joseph Wang and his lab.

I am very fortunate to be able to collaborate with Prof. Xiaoqing Pan from University of Michiganm Ann Arbor and Prof. Gun Young Jung from Gwangju Institute of Science and Technology (GIST), Korea. Prof. Xiaoqing Pan is an extraordinary specialist in the transmission electron microscopy studies and his student, Dr. Sung Joo Kim, performed very factastic TEM characterizations. I am also thankful for the close and fruitful collaboration with Prof. Gun Young Jung and his students Dr. Huisu Jeong and Pak Yousin. I would also like to acknowledge Prof. Ke Xu and Dr. Mu Tong Niu from Suzhou Institute of Nano-Tech & Nano-Bionics, China for their collaboration on the characterization of Cu_2O samples. I am also thankful for the collaboration with Prof. Zhaowei Liu, Prof. Donald J. Sirbuly, and their students Dr. Dylan Lu and Conor Riley for the optical absorption measuremnets. I am also grateful to Prof. Paul K. Yu for access to his lab and using his lab facilities. I am thankful to Dr. Winnie Chen for her training with the XRD chatacterizaiton.

Part of the work presented in this thesis would not have been possible without guidance and collaboration with a number of talented students at UC San Diego. Dr. Ke Sun provided much guidance as I entered the lab for the characterization and fabrication of nanowire devices and their application for solar water splitting. Dr. Yi Jing trained and helped me with the nanowires fabrication and characterization. I would like to thank the rest of Prof. Deli Wang’s lab members; Paniz Allameh, Dr. Namseok Park, Conor Riley, Justin S. Cheung, Seena Partokia, Salomón May, Dr. Siarhei Vishniakou, Brian Lewis, Dr. Sun Young Noh, Dr. Muchuan Yang, Sun Zhelin, Dr. Jen-Chun Chou, Kristian

Madsen, Perry Naughton, Amanda Gao for their friendship, support, and assistance in the experiments and performed studies. I would also like to thank Prof. Jr-Hau He and his student Hsin-Pin Wang for their support and collaboration during their visit at UC San Diego. Prof. Sungho Jin's lab members also have significant contribution in the performed studies. Dr. Chulmin Choi assisted me with the nanoimprinting samples for different studies. Dr. Justin (Taekyung) Kim collaborated with me for the nanoparticles synthesis. Dr. Chin-Hung Liu provided me assistance with the XRD characterization. I would like to greatly appreciate the support and collaboration with Dr. Cihan Kuru from Prof. Sungho Jin's group. I would also like to thank Serdar Yavuz and Dr. Jirapon Khamwannah for their great helps during the experiments. I appreciate the friendship and support of the rest of Prof. Sungho Jin's group memebers.

The research I have carried out here would not have been possible without the world class cleanroom managed by Dr. Bernd Fruhberger and staffed by many outstanding members including Sean Parks, Larry Grissom, Dr. Xuekun Lu, Ryan Anderson, Ivan Harris, Dr. Raffaella Fior, Dr. Maribel Montero, Dr. Ahmet Erten, Matthew Sirriyeh, Steve Schank. I truly appreciate the great and unconditional support of Dr. Bernd Fruhberger and his great assistance for offering me a job to work in the cleanroom during the summer of 2014. All the cleanrrom staff members always gave me their unconditional support in which I deeply appreciate their helps.

I would also like to acknowledge financial support from Department of Energy (DOE), National Science Foundation (NSF), the UCSD ECE department, UCSD Iwama Endowed fund, and the ONR-DURIP support for the ALD acquisition.

I would also like to thank all the staff members in ECE, MAE and Calit2 in which they always supported me and greatly helped me with my orders and research related stuff. I am also thankful to staff members in MAE and ECE during the times that I worked as TA/Reader. I would also like to thank the staff members in ECE for matters related to my graduacte studies and the staff members in UCSD housing for their support and assistance during my stay in on-campus housing.

Lastly, I would like to thank my family and friends within and out of UC San Diego. They have been there for me during my entire graduate studies, sharing with my accomplishments and lifting me from hard times. I would like to thank my mom, sisters, and brothers for their love, support, caring, and advice throughout my life and education.

Chapter 2 was published in *Nano Letters* 2013, A. Kargar, K. Sun, Y. Jing, C. Choi, H. Jeong, Y. Zhou, K. Madsen, P. Naughton, S. Jin, G. Y. Jung and D. Wang, "Tailoring n-ZnO/p-Si branched nanowire heterostructures for selective photoelectrochemical water oxidation or reduction". The dissertation author was the first author of this paper.

Chapter 3 was published in *ACS Nano* 2013, A. Kargar, K. Sun, Y. Jing, C. Choi, H. Jeong, G. Y. Jung, S. Jin and D. Wang, "3D branched nanowire photoelectrochemical electrodes for efficient solar water splitting". The dissertation author was the first author of this paper.

Chapter 4 was published in *Physics Status Solidi A* 2013, A. Kargar, K. Sun, S. J. Kim, D. Lu, Y. Jing, Z. Liu, X. Pan and D. Wang, "Three-dimensional ZnO/Si broom-like nanowire heterostructures as photoelectrochemical anodes for solar energy conversion". The dissertation author was the first author of this paper.

Chapter 5 was published in *Advanced Functional Materials* 2015, A. Kargar, S. J. Kim, P. Allameh, C. Choi, N. Park, H. Jeong, Y. Pak, G. Y. Jung, X. Pan, D. Wang and S. Jin, "p-Si/SnO_2/Fe_2O_3 core/shell/shell nanowire photocathodes for neutral pH water splitting". The dissertation author was the first author of this paper.

Chapter 6 was published in *Nano Energy* 2015, A. Kargar, J. Khamwannah, C.-H. Liu, N. Park, D. Wang, S. A. Dayeh and S. Jin, "Nanowire/nanotube array tandem cells for overall solar neutral water splitting". The dissertation author was the first author of this paper.

Chapter 7 was published in *ACS Nano* 2013, A. Kargar, Y. Jing, S. J. Kim, C. Riley, X. Pan, and D. Wang, "ZnO/CuO heterojunction branched nanowires for photoelectrochemical hydrogen generation". The dissertation author was the first author of this paper.

Chapter 8 was published in *Nanotechnology* 2014, A. Kargar, S. S. Partokia, M. T. Niu, P. Allameh, M. Yang, S. May, J. S. Cheung, K. Sun, X. Ku, and D. Wang, "Solution-grown 3D Cu_2O networks for efficient solar water splitting". The dissertation author was the first author of this paper.

Chapter 9 was published in *Nanoscale* 2015, A. Kargar, J. S. Cheung, C.-H. Liu, T.K. Kim, C. T. Riley, S. Shen, Z. Liu, D. J. Sirbuly, D. Wang and S. Jin, "NiO_x-Fe_2O_3-coated p-Si photocathodes for enhanced solar water splitting in neutral pH water". The dissertation author was the first author of this paper.

Chapter 10 was published in *ACS Applied Materials & Interfaces* 2015, A. Kargar, S. Yavuz, T.K. Kim, C. H. Liu, C. Kuru, C. S. Rustomji, S. Jin and P. Bandaru, “Solution-processed $CoFe_2O_4$ nanoparticles on 3D carbon fiber papers for durable oxygen evolution reaction”. The dissertation author was the first author of this paper.

VITA

2007	B.S., Electrical Engineering, Shiraz University, Shiraz, Iran
2012	M.S., Electrical Engineering, University of California, San Diego
2015	Ph.D., Electrical Engineering, University of California, San Diego

PUBLICATIONS

1. **A. Kargar**, J. Khamwannah, C.-H. Liu, N. Park, D. Wang, S. A. Dayeh, and S. Jin, "Nanowire/Nanotube Array Tandem Cells for Overall Solar Neutral Water Splitting," *Nano Energy*, 2015, in press.

2. C. Kuru, D. Choi, **A. Kargar**, C. H. Liu, S. Yavuz, C. Choi, S. Jin, and P.R. Bandaru, "High-performance flexible hydrogen sensor made of WS_2 nanosheet-Pd nanoparticle composite film," submitted for publication, 2015.

3. S. Yavuz, C. Kuru, D. Choi, **A. Kargar**, S. Jin, and P.R. Bandaru, "Graphene oxide as a p-dopant and anti-reflection coating layer, in graphene/silicon solar cells," submitted for publication, 2015.

4. S. J. Kim, **A. Kargar**, D. Wang, G. W. Graham, and X. Pan, "Lithiation of rutile TiO_2 coated Si NWs observed by in-situ TEM," *Chem. Mater.*, 27, 6929-6933, 2015.

5. **A. Kargar**, S. Yavuz, T.K. Kim, C. H. Liu, C. Kuru, C. S. Rustomji, S. Jin, and P. Bandaru, "Solution-Processed $CoFe_2O_4$ Nanoparticles on 3D Carbon Fiber Papers for Durable Oxygen Evolution Reaction," *ACS Appl. Mater. Interfaces*, 7 , 17851-17856, 2015.

6. **A. Kargar**, S. J. Kim, P. Allameh, C. Choi, N. Park, H. Jeong, Y. Pak, G. Y. Jung, X. Pan, D. Wang, and S. Jin, "p-Si/n-SnO_2/n-Fe_2O_3 Core/Shell/Shell Nanowire Photocathodes for Neutral pH Water Splitting," *Adv. Funct. Mater.,* 25, 2609-2615, 2015.

7. H. P. Wang, K. Sun, S. Y. Noh, **A. Kargar**, M.-L. Tsai, M.-Y. Huang, D. Wang, and J.-H. He, "High-performance a-Si/c-Si heterojunction photoelectrodes for photoelectrochemical oxygen and hydrogen evolution," *Nano Lett.*, 15, 2817-2824, 2015.

8. C. Kuru, C. Choi, **A. Kargar**, D. Choi, and S. Jin, "MoS_2 nanosheet-Pd nanoparticle composite for highly sensitive room temperature detection of hydrogen," *Adv. Sci.,* 2*,* 2015*,* doi: 10.1002/advs.201500004.

9. C. Kuru, S. Yavuz, **A. Kargar**, C. Choi, D. Choi, and S. Jin, "Highly stable graphene/silicon heterojunction solar cells by NiO doping," *J. Nanosci. Nanotechnol.*, 2015, in press.

10. **A. Kargar**, J. S. Cheung, C.-H. Liu, T.K. Kim, C. T. Riley, S. Shen, Z. Liu, D. J. Sirbuly, D. Wang, and S. Jin, "NiO_x-Fe_2O_3-coated p-Si photocathodes for enhanced solar water splitting in neutral pH water," *Nanoscale*, 7, 4900-4905, 2015.

11. M. Shen, A. Han, X. Wang, Y. G. Ro, **A. Kargar**, Y. Lin, H. Guo, P. Du, J. Jiang, J. Zhang, S. A. Dayeh, and B. Xiang, "Atomic Scale Analysis of the Enhanced Electro- and Photo-Catalytic Activity in High-Index Faceted Porous NiO Nanowires," *Scientific Reports*, 5, 8557, 2015.

12. T.K. Kim, B. VanSaders, J. Moon, T. Kim, C-H Liu, J. Khamwannah, D. Chun, D. Choi, **A. Kargar**, R. Chen, Z. Liu, and S. Jin, "Tandem Structured Spectrally Selective Coating Layer of Copper Oxide Nanowires Combined with Cobalt Oxide Nanoparticles," *Nano Energy*, 11, 247-259, 2015.

13. C. Riley, T. Kieu, S. J. Kim, K. Post, **A. Kargar**, D. Basov, X. Pan, D. Wang, and D. Sirbuly, "Plasmonic tuning of aluminum-doped zinc oxide films on silicon nanopillars," *Phys. Status Solidi RRL*, 8, 948-952, 2014.

14. S. J. Kim, S. Y. Noh, **A. Kargar**, D. Wang, G. Graham, and X. Pan, "In-situ TEM observation of the structural transformation of rutile TiO_2 during electrochemical lithiation," *Chem. Commun.*, 50, 9932-9935, 2014.

15. **A. Kargar**, S. S. Partokia, M. T. Niu, P. Allameh, M. Yang, S. May, J. S. Cheung, K. Sun, X. Ku, and D. Wang, "Solution-grown 3D Cu_2O networks for efficient solar water splitting," *Nanotechnology*, 25, 205401, 2014.

16. **A. Kargar**, Y. Jing, S. J. Kim, C. Riley, X. Pan, and D. Wang, "ZnO/CuO heterojunction branched nanowires for photoelectrochemical hydrogen generation," *ACS Nano*, 7, 11112-11120, 2013.

17. **A. Kargar**, K. Sun, Y. Jing, C. Choi, H. Jeong, G. Y. Jung, S. Jin, and D. Wang, "3D branched nanowire photoelectrochemical electrodes for efficient solar water splitting," *ACS Nano*, 7, 9407-9415, 2013.

18. S. Vishniakou, B. W. Lewis, X. Niu, **A. Kargar**, K. Sun, M. Kalajian, N. Park, M. Yang, Y. Jing, P. Brochu, Z. Sun, C. Li, T. Nguyen, Q. Pei and D. Wang, “Tactile feedback display with spatial and temporal resolutions,” *Scientific Reports*, 3, 1–6, 2013.

19. **A. Kargar**, K. Sun, Y. Jing, C. Choi, H. Jeong, Y. Zhou, K. Madsen, P. Naughton, S. Jin, G. Y. Jung and D. Wang, “Tailoring n-ZnO/p-Si branched nanowire heterostructures for selective photoelectrochemical water oxidation or reduction,” *Nano Lett.*, 13, 3017−3022, 2013.

20. **A. Kargar**, K. Sun, S. J. Kim, D. Lu, Y. Jing, Z. Liu, X. Pan, and D. Wang, “Three-dimensional ZnO/Si broom-like nanowire heterostructures as photoelectrochemical anodes for solar energy conversion,” *Phys. Status Solidi A*, 210, 2561-2568, 2013.

21. S. J. Kim, **A. Kargar**, D. Wang, and X. Pan, “In-situ TEM Observation of Electrochemical Cycling a Si/TiO_2 Composite Nanowire,” *Microscopy and Microanalysis*, 20, 454-455, 2014.

22. S. J. Kim, J. R. Jokisaari, **A. Kargar**, D. Wang, and X. Pan, “In-situ TEM study of optical and mechanical effects on electrical properties of CuO nanowires,” *Microscopy and Microanalysis*, 19, 1496-1497, 2013.

23. K. Sun, Y. Jing, C. Li, X. Zhang, R. Aguinaldo, **A. Kargar,** K. Madsen, K. Banu, Y. Zhou, Y. Bando, Z. Liu, and D. Wang “3D branched nanowire heterojunction photoelectrodes for high-efficiency solar water splitting and H_2 generation,” *Nanoscale*, 4, 1515-1521, 2012.

24. K. Sun, **A. Kargar**, N. Park, P. Naughton, K. Madson, T. Bright, Y. Jing, and D. Wang, “Compound semiconductor nanowire solar cells,” *IEEE J. Sel. Top. Quantum Electron.*, 17, 1033-1049, 2011.

CONFERENCE PRESENTATIONS

1. **A. Kargar**, J. Khamwannah, C.-H. Liu, N. Park, D. Wang, S. A. Dayeh, and S. Jin, “Nanowire/Nanotube Heterojunction Tandem Cells for Overall Solar Water Splitting in Neutral pH Water,” will present in *2015 MRS Fall Meeting*, Boston, December 2015.

2. **A. Kargar**, S. Yavuz, T.K. Kim, C. H. Liu, and S. Jin,"$CoFe_2O_4$ nanoparticles grown on carbon fiber papers for efficient and durable oxygen evolution reaction," presented in *2015 MRS Spring Meeting*, San Francisco, April 2015.

3. S. J. Kim, S. Noh, **A. Kargar**, D. Wang, G. Graham, X. Pan, "In-Situ TEM Observation of the Structural Transformation of Rutile TiO_2 during Electrochemical Lithiation," presented in *2015 MRS Spring Meeting*, San Francisco, April 2015.

4. **A. Kargar**, J. Khamwannah, C. Kuru, and S. Jin, "All-Metal-Oxide Nanostructured Tandem Cells for Overall Solar Water Splitting," presented in *2015 MRS Spring Meeting*, San Francisco, April 2015**.**

5. **A. Kargar**, C. Choi, I. Liu, S. J. Kim, X. Pan, D. Wang, and S. Jin, "Si/Metal-Oxide/Metal-Oxide Core/Shell/Shell Nanowires for Efficient Solar Hydrogen Production from Water," presented in *2014 MRS Fall Meeting*, Boston, December 2014.

6. **A. Kargar**, S. Jin, and D. Wang, "3D Metal Oxide Nanowire Heterostructure Mesh Electrodes for Efficient Solar Water Splitting," presented in *2014 MRS Fall Meeting*, Boston, December 2014.

7. H. P. Wang, K. Sun, S. Y. Noh, **A. Kargar**, M. L. Tsai, D. Wang, and J. H. He, "High Photoelectrochemical Oxygen and Hydrogen Evolution Performance by Using a-Si/c-Si Heterojunction Solar Cells as Photoelectrodes," presented in *2014 ECS and SMEQ Joint International Meeting*, Mexico, October 2014.

8. S. J. Kim, **A. Kargar**, D. Wang, and X. Pan, "In-situ TEM Observation of Electrochemical Cycling a Si/TiO_2 Composite Nanowire," presented in *2014 Microscopy & Microanalysis meeting*, Hartford, August 2014.

9. K. Sun, **A. Kargar**, S. Y. Noh, and D. Wang, "3-D Nanowire Heterostructures for High-efficiency Solar Energy Harvesting and Photoelectrochemical Hydrogen Generation," presented in *246th ACS National Meeting & Exhibition 2013*, Indianapolis, Indiana, September 2013.

10. S. J. Kim, J. R. Jokisaari, **A. Kargar**, D. Wang, and X. Pan, "In-situ TEM Study of Optical and Mechanical Effects on Electrical Properties of CuO Nanowires," presented in *2013 Microscopy & Microanalysis meeting*, Indiana, August 2013.

11. **A. Kargar**, S. May, S. S. Partokia, K. Sun, and D. Wang, "Solution-Grown Cu_2O Nanorod Photoelectrodes for Efficient Solar Water Splitting and Hydrogen Generation," presented in *2012 MRS Spring Meeting*, San Francisco, April 2012.

12. **A. Kargar**, K. Sun, Y. Jing, C. Choi, S. Jin, and D. Wang, "3D ZnO/Si Branched Nanowire Photoelectrochemical Solar Cells: Cell Stability and Temperature Effect," presented in *2012 MRS Spring Meeting*, San Francisco, April 2012.

13. **A. Kargar**, S. S. Partokia, C. Choi, K. Sun, Y. Jing, S. Jin and D. Wang "Efficient Photoelectrochemical Solar Cells with 3D Metal-Oxide/Si Branched Nanowire Heterostructures," presented in *UCSD Jacobs School of Engineering 31th Annual Research Expo*, UC San Diego, April 2012.

14. **A. Kargar**, K. Sun, Y. Jing and D. Wang, "Photoelectrochemical Solar Cells with Three-Dimensional CuO/ZnO Nanotree Heterojunctions," presented in *2011 MRS Fall Meeting*, Boston, Dec. 2011.

15. **A. Kargar**, Y. Jing, K. Sun and D. Wang, "CuO Nanowire Mesh Photoelectrodes for High Photoelectrochemical Hydrogen Production," presented in *2011 MRS Fall Meeting*, Boston, Dec. 2011.

16. **A. Kargar**, K. Sun, Y. Jing, C. Choi, H. Jung, G. Y. Jung, S. Jin, D. Wang, "Optimization of 3D ZnO/Si Branched Nanowire Heterostructures for Efficient Photoelectrochemical Solar Water Splitting," presented in *2011 MRS Fall Meeting*, Boston, Dec. 2011.

17. K. Sun, **A. Kargar**, K. Madsen and D. Wang, "Low Cost and High Efficiency Solar Hydrogen Generation Using 3D Branched Nanowire Array based Photoelectrochemical Electrodes," presented in 2nd *NanoToday* conference, Hawaii, USA, Dec. 2011.

18. K. Sun, **A. Kargar**, Y. Zhou, K. Madsen, and D. Wang, "High Photocurrent Photoelectrochemical Cell from Branched Nanowire Heterostructures," Proceedings of *IMAPS*, San Diego, CA, April 2011.

19. **A. Kargar**, K. Sun, and D. Wang, "Performance Optimization of Branched Nanowire Heterostructure-based Photoelectrochemical Cells for Water Splitting," presented in *EMC 2011*, Santa Barbara, CA, USA, June 2011.

20. **A. Kargar**, K. Sun, and D. Wang, "Optimized Photoelectrochemical Cell Based on Branched Nanowire Heterostructure for Efficient Water Solar Splitting," presented in *UCSD Jacobs School of Engineering 30th Annual Research Expo*, UC San Diego, April 2011.

21. K. Sun, K. Madsen, **A. Kargar**, Y. Zhou, and D. Wang, "Hierarchical Nanoheterostructure Photoelectrodes for Efficient Solar Water Splitting," presented in 2011 *MRS Spring Meeting*, San Francisco, CA, USA, April 2011.

22. Y. Jing, H. Jung, S. Vishniakou, M. Yang, **A. Kargar**, G.-Y. Jung, and D. Wang, "Si Nanowire Radial P-N Junction Solar Cells," presented in 2011 *MRS Spring Meeting*, San Francisco, CA, USA, April 2011.

23. K. Sun, K. Madsen, **A. Kargar**, and D. Wang, "High Efficiency Solar Water Splitting," presented in *Innovation Day Expo and Symposia* (*IDEaS*), UCSD, CA, Feb. 2011.

ABSTRACT OF THE DISSERTATION

Semiconductor Nanostructures for Solar Water Splitting and Hydrogen Production: Design, Growth/Fabrication, Characterization, and Device Performance

by

Alireza Kargar

Doctor of Philosophy in Electrical Engineering (Nanoscale Devices & Systems)
University of California, San Diego, 2015

Professor Sungho Jin, Chair
Professor Prabhakar R. Bandaru, Co-Chair
Professor Shadi A. Dayeh, Co-Chair

Solar and seawater are the ultimate energy resources on earth, and together constitute a potential solution to the energy crisis, which at the same time can reduce the carbon emission due to the use of fossil fuels. However, there are challenges in the generation of hydrogen fuel through water splitting using solar energy, such as the cost, and large scale manufacturing of the efficient and durable photoelectrodes. Primary challenge for solar water splitting using photoelectrochemical (PEC) cells is to develop photoelectrodes with sufficient photovoltage to electrolyze water, with maximized photon utilization efficiency, with long lifetime, and with cheap cost. This thesis then focuses on design, characterization and fabrication of novel nanostructured heterojunctions (with focus on nanowire/nanorod array heterostructures) for solar water splitting and hydrogen production. The primary focus of this thesis is to develop such photoelectrodes using low-cost, earth-abundant, non-toxic materials with cheap, facile, scalable fabrication techniques for efficient and durable solar water splitting in neutral solutions. The formation of the nanostructured array heterojunction offers unique combination of desired properties, such as enhanced light absorption, improved charge separation/collection, enlarged reaction surface area, and better electrochemical reaction dynamics. Two different types of nanostructured array heterojunctions present in this thesis including (i) Si/metal-oxides nanowire array heterojunction photoelectrodes (chapters 2-6), and (ii) all-metal-oxides nanowire/nanorod heterostructure photoelectrodes (chapters 7-8). Two different catalysts for hydrogen or oxygen evolution reaction are presented in chapters 9-10. The application of catalyst is to facilitate the gas evolution on the surface of nanostructured heterojunctions to improve the solar hydrogen production efficiency.

1. INTRODUCTION

Hydrogen has more energy capacity than fossil fuels and is clean with zero carbon emission. It is of particular interest and importance to develop fuel cell vehicles that run on hydrogen (H_2) gas rather than gasoline, which has the potential to significantly reduce the transport sector's oil consumption, lowers greenhouse gas emissions, and consequently slows down the global climate change. However, currently the dominant technology for direct production H_2 is by the stem reforming from fossil fuel, which generates CO_2 and causes air pollution (nitrous oxide and smog). In order to be environmentally beneficial and economically competitive, finding a cost-effective and clean method for mass production of H_2 is essential for the future of fuel cell vehicles and further hydrogen economy.

Solar water splitting based on a photoelectrochemical (PEC) cell is very attractive that utilizes solar energy to directly split water and generate H_2 in a clean fashion. A PEC cell uses a semiconductor photoelectrode, which directly interfaces with electrolyte and harvests solar energy to generate a photovoltage in order to break down water electrochemically. To design an efficient PEC cell, the dominate part is the photoelectrodes (photocathode and photoanode). The key photoelectrode design factors are (i) having wide absorption spectrum and effective light absorption, (ii) matching energy band to H_2 or O_2 energy level, (iii) obtaining high photocurrent and H_2 production efficiency, and (iv) achieving long-term stability. And from the practical point of view, there are two other parameters to be considered including (i) using low-cost materials and (ii) applying facile, cost-effective and scalable fabrication methods. Materials that are currently attracting research interests as a photoanode or a photocathode include: Si, metal oxides (TiO_2, ZnO, Fe_2O_3, Cu_2O, CuO, WO_3), as well as III-V materials (GaP, InP, GaAs), and a lot more others. It is well-recognized that there is no single material which can satisfy all the requirements for the efficient and durable solar water splitting.

Using nanoscale heterostructures (multiple materials) is a promising way to achieve efficient and durable solar water splitting, enabling unique integration of different materials at nanometer scale in a low cost and scalable fashion, and has great practical potentials. In fact, using nanoscale heterojunctions, a combination of desired properties can be obtained to result in efficient solar water splitting, such as enhanced light absorption due to different energy band gaps, improved charge separation at the heterojunctions, enhanced charge transport within each nanomaterial layer, and much increased surface area for the water splitting reactions at the electrode surface. Besides achieving a suitable photovoltage coming from the heterojunction, there is need to develop catalysts for hydrogen and oxygen evolution reactions to facilitate the gas evolution on the surface of nanostructured heterojunction photoelectrodes to obtain a high solar hydrogen production.

This thesis focuses on design, fabrication and characterization of novel nanostructured heterojunctions (with focus on nanowire/nanorod array heterostructures) synthesized mainly by facile and scalable fabrication techniques. Chapters 2-6 will discuss Si/metal-oxides nanowire array heterojunctions with different doping types/concentrations and metal oxides structures for both photocathode and photoanode materials, including Si/ZnO core/shell nanowires, Si/ZnO branched nanowires, Si/SnO_2 core/shell nanowires, Si/SnO_2/Fe_2O_3 core/shell/shell nanowires, Si/TiO_2 core/shell nanowires, and Si/TiO_2/Fe_2O_3 core/shell/hierarchical nanowires. Chapters 7-8 will discuss all-metal-oxides nanowire/nanorod heterostructure photoelectrodes including CuO/ZnO core/shell nanowires, CuO/ZnO branched nanowires, Cu_2O nanowires, Cu_2O nanorods, Cu_2O networks, Cu_2O/ZnO nanorods, Cu_2O/AZO nanorods, Cu_2O/TiO_2 nanorods, Cu_2O/ZnO/TiO_2 core/shell/shell nanorods, and Cu_2O/AZO/TiO_2 core/shell/shell nanorods. Last two chapters (9-10) will discuss about the developed catalysts for the hydrogen evolution reaction (which is NiO) and oxygen evolution reaction (which is $CoFe_2O_4$) using solution methods.

2. TAILORING N-ZNO/P-SI BRANCHED NANOWIRE HETEROSTRUCTURES FOR SELECTIVE PHOTOELECTROCHEMICAL WATER OXIDATION OR REDUCTION

2.1 Introduction

Solar splitting of water into hydrogen has been considered as a promising hydrogen production method due to the zero carbon emission nature.[1] Photoelectrochemical (PEC) cells, which utilize sunlight to directly split water at the semiconductor-electrolyte interface, have attracted a lot of interests in academic research[2, 3] and industry[4] because of the potential of cost-effective production of hydrogen[2, 5] with high efficiency[6] for renewable energy. Semiconductor nano/micro wires have been studied in recent years for PEC cells due to their distinctive properties and promises to offer superior PEC performance.[7-12] Vertical nanowire (NW) arrays offer enhanced light absorption, reduced charge recombination and improved carrier collection, and increased surface area and reaction rate compared to planar bulk materials. However, NW arrays synthesized from single materials such as silicon are precluded for practical PEC application due to the limited efficiency[7, 8] and the chemical instability in the electrolyte solution.[13] Having a NW heterostructure allows integration of the properties from different materials. Specifically for PECs, NW heterostructures[10, 14-19] can improve the photocurrent and consequently the hydrogen production efficiency by having enhanced light absorption and improved charge separation, while the formation of heterostructure can simultaneously enhance the chemical stability by choosing a corrosion resistive material to interface with electrolytes.[14]

Three-dimensional (3D) branched NWs have recently been of great interest due to the interesting structure and unique properties. The syntheses of such new materials with different NW backbones (or can be called trunks or cores) and NW branches, such as p-Si/n-Si,[20] GaN/GaN,[20] GaP/GaP,[21] GaP/InP,[21, 22] InP/GaP,[22] ZnS/CdS,[23] CuO/ZnO,[24] ZnSe/CdSe,[25] InAs/GaAs,[26] Si/Ge,[27] Si/III–V,[27] and Si/II–VI,[27] etc. using the chemical vapor deposition, metal-organic chemical deposition, or molecular beam epitaxy, etc. methods were reported and various potential device applications[24, 27] have been demonstrated. 3D ZnO/Si branched NW heterostructures, with ZnO branches on Si NW cores, have shown promising performances for optoelectronic[28, 29] and surface-enhanced Raman spectroscopy[30] applications. Recently, we have reported enhanced photocathodic behavior of randomly positioned 3D ZnO/Si branched NW arrays for PEC solar water splitting, which leads to high-efficiency hydrogen production of ~3%.[31] Generally speaking, the branched NW heterostructures can be very good candidates for solar water splitting (compared to core/shell NW heterostructures) due to increased surface area for surface redox reaction,[31, 32] and improved gas evolution caused by large surface curvature of NW branches.[31] Moreover, the 3D ZnO/Si branched NW arrays can be fabricated in large scales using cost-effective and low-temperature solution based methods.[29, 31] In this paper, we present the fabrication of periodically ordered 3D ZnO/Si branched NW heterostructures and the selective photoelectrochemical reduction or oxidation of water by adjusting the doping concentration in the p-type Si NW core. A working mechanism was proposed to understand the current-voltage (*I-V*) characteristics and incident-photon-conversion-efficiency (IPCE) wavelength dependence study. The photoelectrochemical stability of the TiO_2/Pt coated ZnO/Si branched NW photoelectrodes was also studied.

2.2 Experimental Section

Device fabrication

The boron doped Si(100) wafers with resistivities of 1-20 Ωcm (p-type), and 0.001-0.004 Ωcm (p^+-type) (for Si NW array with 700 nm pitch size) or 0.001-0.005 (for Si NW array with 1 µm pitch size) Ωcm (p^+-type) were patterned using nanoimprint lithography (NIL). The Si wafers were spin-coated with an approximately 300 nm thick layer of poly-methylmethacrylate (PMMA) (Micro Resist Technology, mr-I 35k PMMA 300). A Si nanoimprint mould having a nanopillar array was brought into contact with the sample and they were pressed together under 50 psi pressure using an ANT-2 nano imprinter. When heated up above the glass transition temperature (175°C) of the polymer, the pattern on the mould was pressed into the softened PMMA film. After being cooled down, the Si mould was separated from the sample and the pattern resist is left on the substrate. The substrates were then etched for 1 min using reactive ion etching (RIE) with CF_4 and O_2 gases to remove the residues of PMMA from imprinting. E-beam evaporation was used to deposit 50 nm Ni forming an array of Ni disks as the etch mask. The substrates were then immersed in acetone to do the lift-off process, rinsed with acetone, isopropanol (IPA), and deionized (DI) water consecutively and finally dried with N_2 flow. After that, the substrates were cleaned using 1 min O_2 plasma in a pressure of 200 mT to remove the residues of polymer.

Subsequently, RIE/ICP (Reactive Ion Etching/Inductively Coupled Plasma) dry etching (Oxford Plasmalab P100) was used to create vertical Si NW arrays for different lengths depending on the etching time. The average Si etching rates were ~0.21 µm/min and ~0.24 µm/min for Si NW array with 700 nm and 1 µm pitch sizes, respectively. After the RIE/ICP etching, the Si NW substrates were dipped into Ni etchant for 5 mins to remove the Ni disks at the tip of Si NWs. The Si NW substrates were then cleaned with BOE (10 sec) (for Si NW samples with 700 nm pitch size) or RCA cleaning (for Si NW samples with 1 µm pitch size) to remove the contamination from the RIE/ICP etching. Afterwards, the Si NW samples were immediately transferred to the sputtering machine in order to minimize the oxidation.

To grow the ZnO NW branches, a thin ZnO layer, as seeding layer for ZnO NW growth, was deposited on the Si NW substrates using RF magnetron sputtering with 99.99% ZnO target and argon gas. The sputtering pressure was 2.7 mT during the deposition. The measured thickness of sputtered ZnO on a glass slide were ~60 nm and ~45 nm for Si NW arrays with 700 nm and 1 µm pitch sizes, respectively. Note that the actual thickness of sputtered ZnO on Si NWs is smaller (for example for 10 mins Si NW array with 1 µm pitch size, it was 25-30 nm). Finally, the ZnO NW branches were grown on the Si NWs using hydrothermal growth method. Briefly, 25 mM aqueous solution of zinc acetate dihydrate ($Zn(O_2CCH_3)_2(H_2O)_2$, Sigma-Aldrich) and hexamethylenetetramine (HMTA) ($(CH_2)_6N_4$, Sigma-Aldrich) in DI water (≥ 17.6 MΩ-cm) was prepared. The ZnO-seeded Si NW substrates, fixed on a glass slide with their top side down, were then immersed in the growth solution, which was put in a flask and the flask was positioned in the center of an oil bath. A mild agitation was used during the ZnO growth. After reaching a temperature of 60°C for the growth solution (the temperature was monitored with a thermometer keeping inside the growth solution), the time counting was started for different desired growth times. The as-prepared samples were then rinsed carefully with DI water and dried with N_2 flow. The synthesized branched NW samples were then stored under vacuum for next processes such as morphology study and photoelectrochemical tests. For samples studied for stability test and IPCE measurement (samples with Si NW array of 1 µm pitch size), atomic layer deposition (ALD), using Beneq TFS 200 system, was used to deposit a thin layer of TiO_2 on branched NW substrates at a temperature of 250°C. The measured thickness of deposited TiO_2 was 20 nm based on growth rate of 0.44 Å/cycle on Si(100) film substrate. For Pt co-catalyst deposition, e-beam evaporation was used to deposit 3 nm Pt on TiO_2-coated branched NW substrates.

Structural characterization

The samples morphologies were examined on a Philips XL30 field-emission environmental scanning electron microscope (ESEM) at an accelerating voltage of 10.0 kV.

Photoelectrochemical measurements

To do the PEC tests, the samples were bonded to Cu wire at the back using indium, which provides an ohmic contact. The edges and backside of samples were sealed using epoxy. Photocurrent measurements were performed in a three-electrode photoelectrochemical (PEC) cell using a 400 ml aqueous solution of 0.25 M Na_2SO_4 buffered at pH = 7.25 with Phosphate Buffered Saline (PBS, Sigma) (DI water $\geq$ 17.6 MΩ-cm). The three-electrode configuration consists of branched NW substrate as working electrode (WE), Pt coil/mesh (coil for samples with 700 nm Si NW pitch size, and mesh for samples with 1 µm pitch size) as counter electrode (CE), and Ag/AgCl (1M

KCl) as reference electrode (RE). The photocurrent was measured under illumination from a solar simulator (Newport 67015) using a 150 W Xenon lamp and equipped with a 1.5 AM filter. A light power intensity of 100 mW/cm^2 was measured/tuned at the sample position. The current versus potential/time measurements were collected using a potentiostat (Digi-Ivy Inc). A scan rate of 5 mV/s or 10 mV/s (5 mV/s for samples with 700 nm Si NW pitch size and 10 mV/s for samples with 1 µm pitch size) was used for the linear sweep voltammetry (LSV). Photocurrent stability tests were performed by collecting the electrode light current under constant illumination and a fixed biasing potential. During the PEC tests, a mild agitation was used and the electrolyte was purged with the small flow of N_2 gas.

IPCE measurement

The solar simulator equipped with 1.5 AM filter was used as the light source connected to the monochromator (iHR 550). The monochromatic light spectrum was calibrated by a silicon photodiode (Newport 818-UV). Spectral photoresponse measurements were performed in the same setup as used for the *I-V* and *I-t* measurements; sample as WE, Pt mesh as CE, Ag/AgCl (1M KCl) as RE, and 400 ml aqueous solution of 0.25 M Na_2SO_4 with mild agitation and purging with the small flow of N_2.

2.3 Results and Discussion

Figure 2.1 shows the scanning electron micrograph (SEM) images of 3D ZnO/Si branched NW heterostructures with n-ZnO NW branches grown for 10 mins on Si NW cores etched by reactive ion etching with inductively coupled plasma (RIE-ICP) for different times. Figures 2.1a-1d show branched NW array with Si NWs etched for 6 mins (denoted b-(10m-ZnO/6m-p-Si) for NWs with p-Si core and -p^+- for p^+-Si core) and with pitch size of 700 nm and a diameter of ~200nm, and Figure 2.1e is for branched NWs with Si NWs etched for 10 mins (denoted b-(10m-ZnO/10m-Si)) and with pitch size of 1 μm and a diameter of ~280 nm. Average Si etching rates by RIE-ICP are ~0.21 μm/min and ~0.24 μm/min for Si NW array with 700 nm and 1 μm pitch sizes, respectively. The difference in etching rate is likely due to the diffusion limited gas phase etching reaction. The ZnO NW branches uniformly cover the entire length of Si NWs (Figures 2.1d and 1e). There is also ZnO NW growth in between Si NWs (Figure 2.1e). The ZnO NW branches have uniform lengths along the entire length of Si NWs (Figures 2.1b, 1c and 1e), which are ~150 nm and ~200 nm for Si NW array with 700 nm and 1 μm pitch sizes, respectively, due to diffusion limited growth in solution. The average diameters of ZnO NW branches are ~27 nm and ~35 nm for their growth on Si NW core with 700 nm and 1 μm pitch sizes, respectively, most likely due to the limits from seeding layer due to large surface curvature on the b-(10m-ZnO/6m-Si) NWs. Low-magnification SEM image (Figure 2.1a) also shows the large coverage of 3D branched NW arrays indicating the potential of scaling up to large size of electrodes for practical use.

The current density versus externally applied potential of b-(10m-ZnO/12m-p-Si) NWs (with 700 nm pitch size) is shown in Figure 2.2a, where the red and black lines represent the current density under illumination and at dark, respectively. Under the reversed bias, the n-ZnO/p-Si branched NW array shows a high photocathodic current, while at the forward biasing condition, there is a very small photoanodic current at high forward bias especially at +1.5 V, which is almost negligible compared to the photocathodic current. The photocathodic current of n-ZnO/p-Si branched NW array (Figure 2.2a) is 20 times larger than that of bare p-Si NW array. This improved photocathodic current is due to enhanced light absorption in Si NWs, which can also attribute to the enhanced surface area for redox reaction, enhanced charge separation due to the effective junction between p-Si and n-ZnO NWs, and improved gas evolution (faster gas bulb evolution) caused by large surface curvature of ZnO NWs. Figure 2.2a inset shows the transient current density under chopped illumination of the corresponding branched NW heterostructures at -1.5 V versus Ag/AgCl reference electrode (RE). The sample shows good switching behavior under pulsed illumination. There is a photocathodic current overshoot (spike) in the beginning of switching, which disappears almost instantly and a constant photocurrent is achieved. The current overshoot is possibly due to separation of photo-generated electron/hole (e^-/h^+) pairs resulting in accumulation of electrons at the photocathode surface, and it decays quickly due to the recombination of electrons and holes at the photoelectrode surface. Note that there is no significant current overshoot after switching off illumination. The photocathodic current and photoelectrochemical water reduction efficiency can be further increased by optimizing the Si and ZnO NW dimensions.[33]

Figure 2.2b illustrates the current density versus applied potential for b-(10m-ZnO/12m-p^+-Si) NW electrodes. The red and black lines exhibit the current density under illumination and in the dark, respectively. Interestingly, the n-ZnO/Si branched NW array with p^+-Si NW cores does not show any photocathodic response as there is no specific difference between its light and dark currents under the reversed biasing condition, while

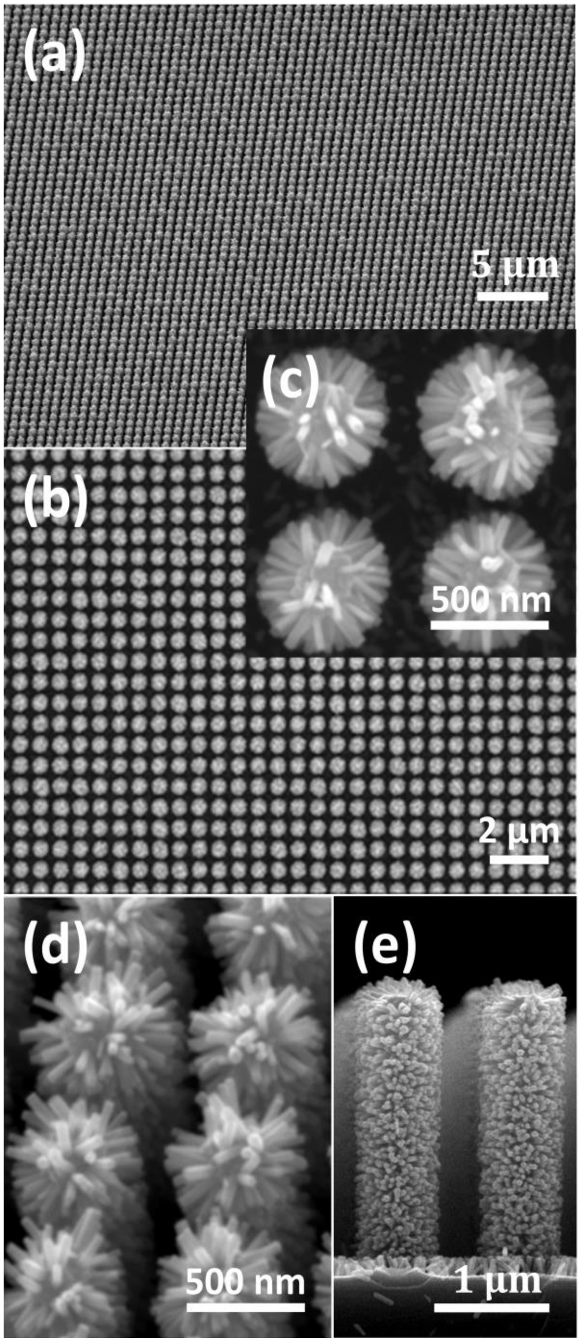

Figure 2.1. SEM images of 3D ZnO/Si branched NW heterostructures. (a-d) b-(10m-ZnO/6m-Si) NWs with the Si NW core diameter of ~200 nm and pitch size of 700 nm. (a) Low-magnification, 45° view image, (b, c) top view images, (d) high-magnification, 45° view image. (e) Cross-sectional view image of b-(10m-ZnO/10m-Si) NWs with the Si NW core diameter of ~280 nm and pitch size of 1 µm.

it only presents photoanodic behavior under forward bias which leads to water oxidation and O_2 gas generation. The current density measurement of p^+-Si NW array without any ZnO NW branches also shows no photocathodic behavior and a negligible photoanodic behavior. The current density versus time under chopped illumination for the corresponding branched NW array at +1 V (versus Ag/AgCl RE) biasing potential is illustrated in the inset of Figure 2.2b. The n-ZnO/p^+-Si branched NW array exhibits switching behavior under chopped illumination at forward biasing potential, while there is no switching behavior under the reversed biasing potential as there is no photocathodic behavior. Compared with the n-ZnO/p-Si branched NW heterostructure (inset of Figure 2.2a), n-ZnO/p^+-Si branched NW array does not show any photocurrent overshoot. This may be explained based on the fact that ZnO NW branches are responsible for the photoanodic behavior and their close proximity to the semiconductor-liquid junction leads to no significant accumulation and consequent recombination.

The observed photocathodic water reduction and photoanodic water oxidation from the 3D branched photoelectrodes can be explained using the energy band diagrams at both reversed and forward biases proposed in Figure 2.3. Figure 2.3a shows the energy band diagram of n-ZnO/Si branched NW heterostructures with lightly-doped Si NW cores at high reversed bias of -1.5 V. For the junction between p-Si and n-ZnO NWs, the depletion region mostly lies in the p-Si NW due to much higher doping concentration of n-ZnO NW, which is in the order of 10^{18} cm^{-3} for the ZnO NW grown by the hydrothermal growth method[34] (the doping of p-Si is in the range of 6.7×10^{14}–1.5×10^{16} cm^{-3} based on its resistivity of 1-20 Ωcm). Under the light illumination, the generated electron-hole pairs in the depletion region increase the number of electrons in the conduction band (CB) of n-ZnO NW as well as the number of holes in valence band (VB)

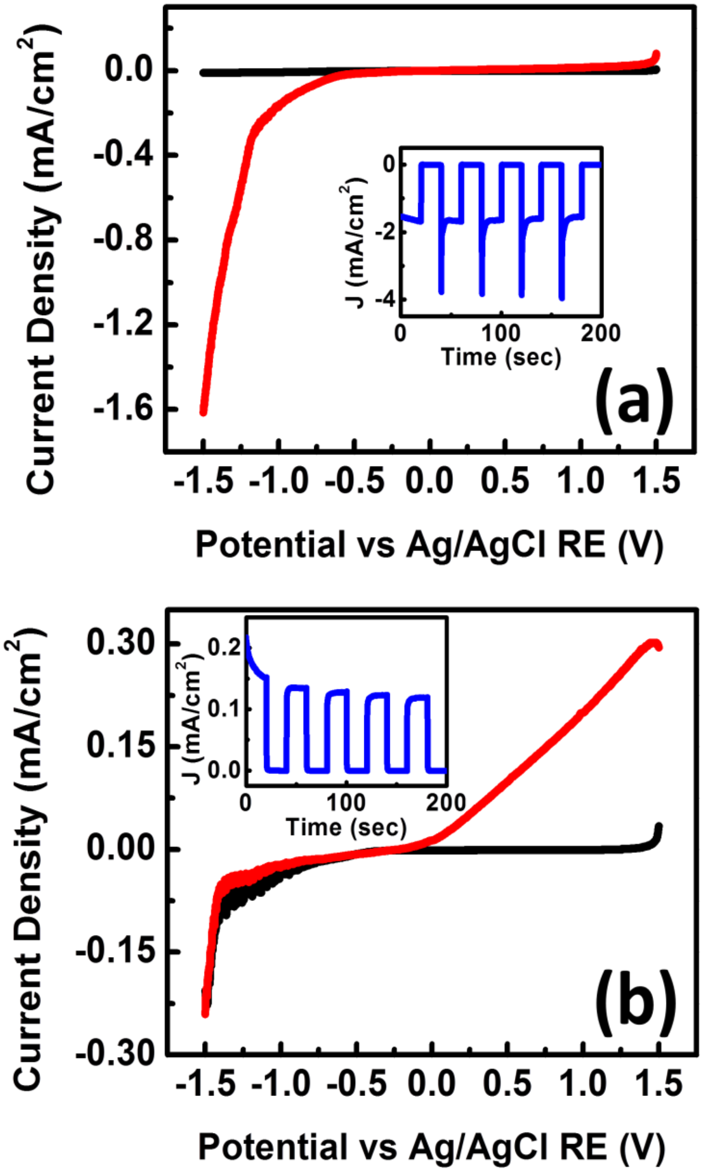

Figure 2.2. Current density versus applied potential of (a) b-(10m-ZnO/12m-p-Si) and (b) b-(10m-ZnO/12m-p$^+$-Si) NWs, with the Si NW array pitch size of 700 nm. The red and black lines represent the current density under illumination and at dark, respectively. Insets show the current density versus time for the corresponding branched NW arrays at (a) -1.5 V versus Ag/AgCl RE and (b) +1 V versus Ag/AgCl RE biasing potentials.

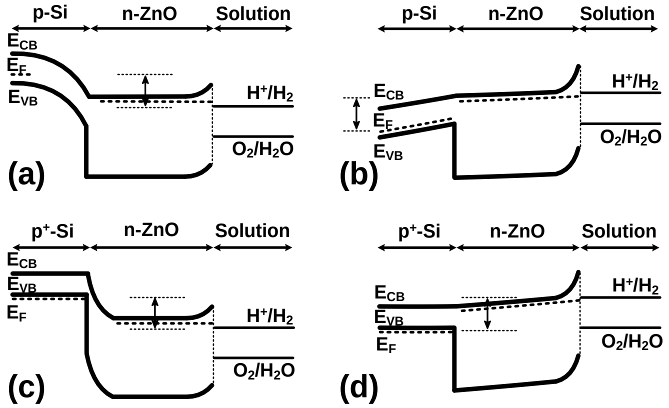
p-Si
n-ZnO
Solution
E_{CB}
E_F
E_{VB}
H^+/H_2
O_2/H_2O
(a)
p-Si
n-ZnO
Solution
E_{CB}
E_F
E_{VB}
H^+/H_2
O_2/H_2O
(b)
p^+-Si
n-ZnO
Solution
E_{CB}
E_{VB}
E_F
H^+/H_2
O_2/H_2O
(c)
p^+-Si
n-ZnO
Solution
E_{CB}
E_{VB}
E_F
H^+/H_2
O_2/H_2O
(d)

Figure 2.3. Proposed energy band diagrams of n-ZnO/p-Si branched nanowires at (a) reversed biasing potential (-1.5 V) and (b) forward biasing potential (+1.5 V), and n-ZnO/p^+-Si branched nanowires at (c) reversed biasing potential (-1.5 V) and (d) forward biasing potential (+1.5 V).

of p-Si NW. The large band bending at the p-Si and n-ZnO NWs junction and reduced barrier between the n-ZnO NW and the electrolyte, caused by the high reverse bias, facilitates the electron transfer into the n-ZnO NW, which consequently travel to the ZnO surface, leading to large photocathodic current, and reduce water into hydrogen. On the other hand, under high forward bias (+1.5 V), as illustrated in Figure 2.3b, the large barrier at the n-ZnO NW and electrolyte junction (compared with that at the Si-ZnO junction) is not favorable for carrier transportation resulting in a very small photocurrent under forward bias. The dark currents are negligible for both reversed and forward biases.

Figures 2.3c and 2.3d show the energy band diagrams of n-ZnO/p^+-Si branched NWs at the reversed biasing potential (-1.5 V) and the forward biasing potential (+1.5 V), respectively. For the p^+-Si and n-ZnO NWs junction, the depletion region mainly lies in the n-ZnO region due to much higher doping concentration of p^+-Si (the doping of p^+-Si is in the range of 2.65×10^{19}–1.2×10^{20} cm^{-3} based on its resistivity of 0.001-0.004 Ωcm).

On the other hand, there is band gap reduction for the heavily doped Si.[35] The position of depletion layer, the band gap reduction and p^+-Si Fermi level position all together lead to having a Zener tunneling at the p^+-Si and n-ZnO NWs junction under the high reversed bias, as shown in Figure 2.3c, similar to the thin film n-ZnO/p^+-Si heterojunctions.[36] The Zener breakdown due to electron tunneling at the p^+-Si and n-ZnO junction leads to large dark current and photocurrent. Moreover, in the branched n-ZnO/p^+-Si NW array, the p^+-Si NW cores do not generate significant amount of carriers due to the small minority carrier diffusion length and short minority carrier lifetime. For example, the measured p^+-Si wafer absorbs light but does not show any spectral photoconductive response under forward or reversed biasing potentials. Due to the lack of photogenerated carriers in p^+-Si and the Zener tunneling, the n-ZnO/p^+-Si branched NW array does not show any photocathodic current under reversed bias (current under light illumination is very similar to the dark current). Because the band bending at the interface mainly is in the n-ZnO region, the external voltage across the Si-ZnO junction accordingly drops onto the depletion region within n-ZnO for the n-ZnO/p^+-Si branched NWs, which leads to easier transport of photogenerated carriers in ZnO, especially for holes, to the electrolyte (Figure 2.3d versus NWs with p-Si cores in Figure 2.3b) and consequently enhanced photoanodic behavior (Figure 2.2b versus Figure 2.2a).

Also note that in Figure 2.3, for the branched NWs with p-Si NW cores, the band bending mostly lies in the p-Si region (Figure 2.3b), while for the branched samples with p^+-Si NWs, the band bending mainly is in the n-ZnO region (Figure 2.3d). In this case, the external voltage across the Si-ZnO junction accordingly drops onto the depletion region within p-Si (Figure 2.3b) and n-ZnO (Figure 2.3d) for the p-Si and p^+-Si NW cores, respectively, which lead to band bending (Figures 2.3b and 2.3d). The band bending and voltage drop (titled conduction band and valance band) on the n-ZnO (Figure 2.3d) for the branched NWs with the p^+-Si NW cores cause that the photogenerated carriers in ZnO are effectively separated and holes are transferred to the ZnO-electrolyte interface and into the electrolyte, compared to the flat CB and VB in the p-Si/n-ZnO case in Figure 2.3b. The enhanced charge separation and transport to surface lead to enhanced photoanodic current of branched NW array with p^+-Si NW cores compared to that with p-Si NW cores, which is, if look closely, about 3 times larger, as shown in Figure 2.2.

The ZnO/Si branched NW array is not stable over a long time, because of the instability of Si and ZnO in the electrolyte under light illumination and biasing condition, which can limit practical application of these promising branched NW photoelectrodes. The Si instability comes from its corrosion in the electrolyte, while ZnO dissolves in the solution under illumination. To solve this corrosion problem and improve the stability, we coated TiO_2 on the top of ZnO branches as a protection layer using atomic layer deposition (ALD). TiO_2 has been widely used as protecting layer for different semiconductor photoelectrodes due to its high resistance to corrosion/decomposition.[14, 37-40] ALD offers several advantages for material deposition including uniform conformal coating with high-quality on nanostructured surfaces, good control over deposition thickness, and low-temperature process.[37, 41] Figure 2.4a shows the SEM image of b-(5m-ZnO/10m-p-Si) NW array coated with 20 nm TiO_2 coating, the pitch size for Si NW array is 1 µm. It is clear that TiO_2-coating completely covers all ZnO NW branches, spaces between ZnO NW branches, and spaces between branched NWs on flat substrate. On the other hand, 20 nm TiO_2 coating did not decrease the photoelectrode activity in a

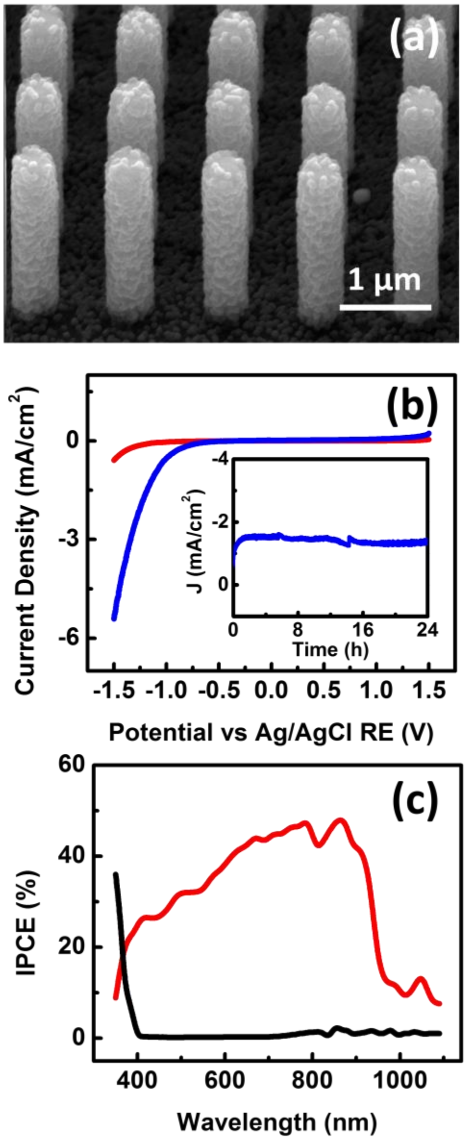

Figure 2.4. (a) 45°-view SEM image of TiO_2-coated b-(5m-ZnO/10m-p-Si) NW array. (b) Current density under illumination versus applied potential of TiO_2-coated (red curve) and TiO_2/Pt coated (blue curve) b-(5m-ZnO/10m-p-Si) NWs. Inset shows the current density under illumination versus time of corresponding TiO_2/Pt coated branched NW array at the applied external potential of -0.33 V versus RHE. (c) IPCE for TiO_2-coated b-(5m-ZnO/10m-p-Si) NWs at -1.3 V versus Ag/AgCl RE (red curve) and b-(5m-ZnO/10m-p^+-Si) at +1.3 V versus Ag/AgCl RE (black curve). The Si NW array pitch size is 1 µm.

significant way. In fact, the photocathodic current is reduced for only a few percents and remained to be the same for certain biasing potentials (from -1.3 V to 0).

Figure 2.4b also shows current densities under illumination versus applied potential of TiO_2-coated (red curve) and TiO_2/Pt-coated (blue curve) b-(5m-ZnO/10m-p-Si) NW photoelectrodes. The TiO_2-coated branched n-ZnO/p-Si NW heterostructure only shows photocathodic behavior, consistent with the observation in Figure 2.2a. Note that the photocathodic current and dark current reduce slightly for branched NW array with thin TiO_2 protection layer compared to the branched NWs without TiO_2 coating due to the low conductivity of TiO_2 layer (also possibly some reduction in light absorption). The surface of most semiconductors such as Si, ZnO and TiO_2 has poor catalytic activity for the hydrogen evolution reaction (HER) due to kinetic limitation.[2] Thus, a catalyst is normally added to enhance the HER kinetics and achieve sufficient hydrogen production efficiency. Pt has been widely used as an efficient HER electrocatalyst.[12, 43] In our study, we deposited 3 nm Pt on the TiO_2-coated n-ZnO/p-Si branched NW array using e-beam evaporation, where Pt, is not a continuous film but in the form of nanoparticles, serves as a co-catalyst working together with TiO_2. Note that 3 nm Pt coating is discontinuous and shall not significantly reduce the light absorption of branched NW heterostructure electrodes.[2, 44] Despite the slightly reduced light absorption due to Pt coating, the use of TiO_2/Pt coating on branched NW photoelectrodes significantly increases the photocathodic current and considerably reduces the photocathodic current turn-on potential, where there is a ~450 mV shift in the turn-on potential compared to that of the TiO_2-coated sample, indicating the very efficient catalytic effect. Similar to the TiO_2-

coated branched n-ZnO/p-Si NWs, TiO_2/Pt coated NW array does not show photoanodic behavior.

Photocurrent stability tests were performed by collecting the photoelectrode current under constant illumination of 100 mW/cm^2 and biasing potential of -0.33 V versus reversible hydrogen electrode (RHE) or -1 V versus Ag/AgCl RE. Inset of Figure 2.4b shows the long-term stability test of b-(5m-ZnO/10m-p-Si) NWs coated with 20 nm TiO_2 layer and 3 nm Pt co-catalyst. The sample shows no degradation of photocurrent for over 24 hrs under constant illumination of 100 mW/cm^2 and external bias of -0.33 V versus RHE, which results in a stationary average light current of -1.45 mA/cm^2. Note that the current density first starts increasing until it reaches its plateau/saturation and after that, it remains constant for the tested period of time. The reason for the observed current increase initially and then reaching a plateau/saturation is not totally clear at this point. However, similar result was also reported for TiO_2-coated silicon photoanodes.[38] SEM examination and energy-dispersive X-ray spectroscopy (EDS) elemental mapping analysis on the samples after the stability test show preserved morphology and composition of the branched NW array electrodes.[35] Note that the measurement was stopped twice (which are after about 6 hrs and 14.3 hrs) and restarted after about 30 mins without switching off the light source or making any change in the PEC setup or on the sample.

Figure 2.4c shows the spectral incident photon to converted electron ratio or incident photon conversion efficiency (IPCE) data for TiO_2-coated b-(5m-ZnO/10m-p-Si) NW array at -1.3 V (red curve) and b-(5m-ZnO/10m-p$^+$-Si) NW array at +1.3 V (black curve). The branched NW array with p-Si NW cores presents a broadband photoresponse from UV to near IR region, which is consistent with the proposed model illustrated by the band structure in Figure 2.3a, where both p-Si NW cores and ZnO NW branches absorb light and contribute to the photocurrent. Note that the IPCE measurement for the TiO_2-coated 5m-ZnO/10m-p-Si branched NW sample was performed after long stability test for this sample. The peak IPCE value here, about 48%, does not represent the best performance of the ZnO/Si branched NW photocathodes, since the photocurrent is slightly reduced due to the poor conductivity of the TiO_2 coating and is also different from the original photoresponse prior to the stability test as shown in the inset of Figure 2.4b. On the other hand, the branched NW array with p^+-Si NW cores only presents photoanodic response in UV region and does not show any photoresponse at the reversed biasing (cathodic) condition. These results are consistent with that shown in Figure 2.2b. The photoresponse is due to the light photogenerated carriers in the ZnO NW branches, as illustrated by the band diagrams in Figures 2.3c and 2.3d. The p^+-Si NW cores do not contribute to photogenerated current due to the extremely small depletion width and small minority diffusion length discussed before. The peak IPCE is about 36% for the ZnO/p^+-Si branched NW photoanode with the current density of less than 0.5 mA/cm^2, which is smaller than the reported branched TiO_2 nanorod photoanodes with a maximum efficiency of 67% for a measured photocurrent density of ~0.7 mA/cm^2,[45] and the TiO_2/Si branched NWs photoanodes with a peak IPCE of ~100% for a measured photocurrent density of ~1.7 mA/cm^2.[46]

2.4 Conclusions

In summary, we fabricated 3D ZnO/Si branched NW heterostructures as PEC photoelectrodes for solar water splitting, which show orders of magnitudes enhancement in photocurrent compared to the bare Si NW photoelectrodes. We showed that by tuning the doping concentration in the p-type Si NW core, selective photoelectrochemical water reduction or oxidation can be accomplished, where the branched NW array with lightly-doped Si NW core shows broadband absorption from UV to near IR region and photocathodic water reduction and the branched NWs with heavily-doped Si NW core exhibits photoanodic water oxidation with only UV photoresponse. The photoelectrode stability was also studied and by coating the branched NWs with a thin layer of ALD-grown TiO_2 and Pt co-catalyst, long-term stability of no change in photocurrent for over 24 hours under constant light illumination and biasing potential of -0.33 V (vs RHE), was obtained. This study reveals the great promise of using the unique 3D branched NW heterostructures for high-efficiency photoelectrochemical solar cells and furthermore, provide insightful understanding enabling rational design of high-efficiency photocathode and photoanode from low-cost and, earth-abundant materials for solar energy harvesting and conversion to clean chemical fuels.

Chapter 2 was published in *Nano Letters* 2013, A. Kargar, K. Sun, Y. Jing, C. Choi, H. Jeong, Y. Zhou, K. Madsen, P. Naughton, S. Jin, G. Y. Jung and D. Wang, “Tailoring n-ZnO/p-Si branched nanowire heterostructures for selective photoelectrochemical water oxidation or reduction”. The dissertation author was the first author of this paper.

References

1. Lewis, N. S.; Nocera, D. G. *Proc. Natl. Acad. Sci. U.S.A.* **2006**, *103*, 15729-15735.

2. Walter, M. G.; Warren, E. L.; McKone, J. R.; Boettcher, S. W.; Mi, Q.; Santori, E. A.; Lewis, N. S. *Chem. Rev.* **2010**, *110*, 6446-6473.

3. Gratzel, M. *Nature* **2001**, *414*, 338-344.

4. Eberle, U.; Mueller, B.; von Helmolt, R. *Energy Environ. Sci.* **2012**, *5*, 8780-8798.

5. Turner, J. A. *Science* **1999**, *285*, 687-689.

6. Khaselev, O. *Science* **1998**, *280*, 425-427.

7. Goodey, A. P.; Eichfeld, S. M.; Lew, K.-K.; Redwing, J. M.; Mallouk, T. E. *J. Am. Chem. Soc.* **2007**, *129*, 12344-12345.

8. Peng, K.; Wang, X.; Lee, S.-T. *Appl. Phys. Lett.* **2008**, *92*, 163103.

9. Sun, J.; Liu, C.; Yang, P. *J. Am. Chem. Soc.* **2011**, *133*, 19306-19309.

10. Chen, Z.; Cummins, D.; Reinecke, B. N.; Clark, E.; Sunkara, M. K.; Jaramillo, T. F. *Nano Lett.* **2011**, *11*, 4168-4175.

11. Boettcher, S. W.; Spurgeon, J. M.; Putnam, M. C.; Warren, E. L.; Turner-Evans, D. B.; Kelzenberg, M. D.; Maiolo, J. R.; Atwater, H. A.; Lewis, N. S. *Science* **2010**, *327*, 185-187.

12. Boettcher, S. W.; Warren, E. L.; Putnam, M. C.; Santori, E. A.; Turner-Evans, D.; Kelzenberg, M. D.; Walter, M. G.; McKone, J. R.; Brunschwig, B. S.; Atwater, H. A.; Lewis, N. S. *J. Am. Chem. Soc.* **2011**, *133*, 1216-1219.

13. Wang, X.; Peng, K.-Q.; Pan, X.-J.; Chen, X.; Yang, Y.; Li, L.; Meng, X.-M.; Zhang, W.-J.; Lee, S.-T. *Angew. Chem., Int. Ed.* **2011**, *50*, 9861-9865.

14. Hwang, Y. J.; Boukai, A.; Yang, P. *Nano Lett.* **2008**, *9*, 410-415.

15. Tak, Y.; Hong, S. J.; Lee, J. S.; Yong, K. *J. Mater. Chem.* **2009**, *19*, 5945-5951.

16. Zhao, X.; Wang, P.; Li, B. *Chem. Commun.* **2010**, *46*, 6768-6770.

17. Wang, X.; Zhu, H.; Xu, Y.; Wang, H.; Tao, Y.; Hark, S.; Xiao, X.; Li, Q. *ACS Nano* **2010**, *4*, 3302-3308.

18. Seol, M.; Kim, H.; Kim, W.; Yong, K. *Electrochem. Commun.* **2010**, *12*, 1416-1418.

19. Myung, Y.; Jang, D. M.; Sung, T. K.; Sohn, Y. J.; Jung, G. B.; Cho, Y. J.; Kim, H. S.; Park, J. *ACS Nano* **2010**, *4*, 3789-3800.

20. Wang, D.; Qian, F.; Yang, C.; Zhong, Z.; Lieber, C. M. *Nano Lett.* **2004**, *4*, 871-874.

21. Dick, K. A.; Deppert, K.; Larsson, M. W.; Martensson, T.; Seifert, W.; Wallenberg, L. R.; Samuelson, L. *Nat. Mater.* **2004**, *3*, 380-384.

22. Dick, K. A.; Kodambaka, S.; Reuter, M. C.; Deppert, K.; Samuelson, L.; Seifert, W.; Wallenberg, L. R.; Ross, F. M. *Nano Lett.* **2007**, *7*, 1817-1822.

23. Jung, Y.; Ko, D.-K.; Agarwal, R. *Nano Lett.* **2006**, *7*, 264-268.

24. Guo, Z.; Chen, X.; Li, J.; Liu, J.-H.; Huang, X.-J. *Langmuir* **2011**, *27*, 6193-6200.

25. Dong, A.; Tang, R.; Buhro, W. E. *J. Am. Chem. Soc.* **2007**, *129*, 12254-12262.

26. Paladugu, M.; Zou, J.; Auchterlonie, G. J.; Guo, Y. N.; Kim, Y.; Joyce, H. J.; Gao, Q.; Tan, H. H.; Jagadish, C. *Appl. Phys. Lett.* **2007**, *91*, 133115.

27. Jiang, X.; Tian, B.; Xiang, J.; Qian, F.; Zheng, G.; Wang, H.; Mai, L.; Lieber, C. M. *Proc. Natl. Acad. Sci. U.S.A.* **2011**, *108*, 12212-12216.

28. Devika, M.; Koteeswara Reddy, N.; Pevzner, A.; Patolsky, F. *ChemPhysChem* **2010**, *11*, 809-814.

29. Sun, K.; Jing, Y.; Park, N.; Li, C.; Bando, Y.; Wang, D. *J. Am. Chem. Soc.* **2010**, *132*, 15465-15467.

30. Cheng, C.; Yan, B.; Wong, S. M.; Li, X.; Zhou, W.; Yu, T.; Shen, Z.; Yu, H.; Fan, H. J. *ACS Appl. Mater. Inter.* **2010**, *2*, 1824-1828.

31. Sun, K.; Jing, Y.; Li, C.; Zhang, X.; Aguinaldo, R.; Kargar, A.; Madsen, K.; Banu, K.; Zhou, Y.; Bando, Y.; Liu, Z.; Wang, D. *Nanoscale* **2012**, *4*, 1515-1521.

32. Song, H. S.; Zhang, W. J.; Cheng, C.; Tang, Y. B.; Luo, L. B.; Chen, X.; Luan, C. Y.; Meng, X. M.; Zapien, J. A.; Wang, N.; Lee, C. S.; Bello, I.; Lee, S. T. *Crys. Growth Des.* **2010**, *11*, 147-153.

33. Kargar, A.; Sun, K.; Jing, Y.; Choi, C.; Jeong, H.; Jung, G. Y.; Jin, S.; Wang, D. *ACS Nano* **2013**, *7*, 9407-9415.

34. Law, M.; Greene, L. E.; Johnson, J. C.; Saykally, R.; Yang, P. *Nat. Mater.* **2005**, *4*, 455-459.

35. Schmid, P. E. *Phys. Rev. B* **1981**, *23*, 5531-5536.

36. Chen, P.; Ma, X.; Yang, D. *J. Appl. Phys.* **2007**, *101*, 053103.

37. Paracchino, A.; Laporte, V.; Sivula, K.; Grätzel, M.; Thimsen, E. *Nat. Mater.* **2011**, *10*, 456-461.

38. Chen, Y. W.; Prange, J. D.; Dühnen, S.; Park, Y.; Gunji, M.; Chidsey, C. E. D.; McIntyre, P. C. *Nat. Mater.* **2011**, *10*, 539-544.

39. Kohl, P. A.; Frank, S. N.; Bard, A. J. *J. Electrochem. Soc.* **1977**, *124*, 225-229.

40. Siripala, W.; Ivanovskaya, A.; Jaramillo, T. F.; Baeck, S.-H.; McFarland, E. W. *Sol. Energy Mater. Sol. Cells* **2003**, 77, 229-237.

41. George, S. M. *Chem. Rev.* **2009**, *110*, 111-131.

42. Chen, Z.; Jaramillo, T. F.; Deutsch, T. G.; Kleiman-Shwarsctein, A.; Forman, A. J.; Gaillard, N.; Garland, R.; Takanabe, K.; Heske, C.; Sunkara, M.; McFarland, E. W.; Domen, K.; Miller, E. L.; Turner, J. A.; Dinh, H. N. *J. Mater. Res.* **2010**, *25*, 3-16.

43. Heller, A.; Aharon-Shalom, E.; Bonner, W. A.; Miller, B. *J. Am. Chem. Soc.* **1982**, *104*, 6942-6948.

44. McKone, J. R.; Warren, E. L.; Bierman, M. J.; Boettcher, S. W.; Brunschwig, B. S.; Lewis, N. S.; Gray, H. B. *Energy Environ. Sci.* **2011**, *4*, 3573-3583.

45. Cho, I. S.; Chen, Z.; Forman, A. J.; Kim, D. R.; Rao, P. M.; Jaramillo, T. F.; Zheng, X. *Nano Lett.* **2011**, *11*, 4978-4984.

46. Shi, J.; Hara, Y.; Sun, C.; Anderson, M. A.; Wang, X. *Nano Lett.* **2011**, *11*, 3413-3419.

3. 3D BRANCHED NANOWIRE PHOTOELECTROCHEMICAL ELECTRODES FOR EFFICIENT SOLAR WATER SPLITTING

3.1 Introduction

Branched nanowires (b-NWs)[1-5] have recently been attracted considerable attention for solar energy conversion[6-20] and energy storage devices[13, 20-23] due to their unique properties such as nanoscale integration of different functional materials, greatly enhanced junction and surface area, etc. b-NWs can be either homojunctions[6, 7, 9, 10, 12, 13, 15, 18, 19, 21] or heterostructures[1, 2, 8, 11, 17, 22] using facile and scalable fabrication methods such as hydrothermal[7, 11, 17-19] or solvothermal growth methods,[6] and VLS-CVD gas phase synthesis methods.[1, 2] Homo b-NWs have been used as anode in lithium-ion batteries (LIBs),[13, 21] photoanode in dye-sensitized solar cells (DSSCs)[6, 9, 12, 15, 16, 18, 19] and photoelectrochemical (PEC) solar cells,[7, 10] etc. Hetero b-NWs made of two different materials have also been shown different device applications such as LIB anode,[22] pseudocapacitive energy storage device,[23] photocatalyst,[8] and PEC cathodes.[11] Larger surface area of b-NWs compared to that of NWs results in higher capacity in LIBs.[21, 22] ZnO[6, 9, 12, 18] or TiO_2[19] b-NWs provide better photovoltaic performance in DSSCs compared to straight ZnO or TiO_2 NWs due to higher dye loading/absorption and increased light absorption. The efficient charge separation in flower-like CuO/ZnO NWs also showed enhanced photocatalytic activity.[8]

For PEC solar hydrogen production, b-NW arrays are also better candidates compared to single composition NWs or core/shell NW (cs-NW) heterostructures, due to improved reaction surface area, increased light absorption,[11, 24] and enhanced gas evolution efficiency.[11] The NW branches normally have much smaller sizes compared to

NW cores, which can also lead to more efficient charge separation and collection due to close proximity between the photo-generated carriers and the semiconductor-electrolyte interface.[7] Moreover, b-NW heterostructures, synthesized with two different materials with small and large band gaps, provide broadband absorption and enhanced charge separation compared to the NWs or homo b-NWs. For example, ZnO/Si b-NW heterostructures show very efficient photocathodic hydrogen production.[11] More interestingly, selective oxidation or reduction of water using b-NW photoelectrodes are demonstrated by simple changing of the NW core doping concentration,[25] which is very interesting feature paving the way for accomplishing solar fuel cells to perform overall solar water splitting without external bias for practical hydrogen production.[26, 27]

In this paper, we present the systematic study of 3D ZnO/Si b-NW electrodes to improve their photo cathodic and anodic performances, and b-NW photoelectrode stability improvement. The PEC performances are optimized in neutral medium based on different dimensions and doping concentrations of NWs as well as the NW array pitch size. The b-NW photoelectrode conversion and incident photon-to-current efficiencies are also studied. Finally, the b-NW electrode stability is investigated in detail with/without protection layer.

3.2 Experimental Section

Fabrication of b-NW electrodes

The device fabrication was carried out identically as reported previously.[25] Briefly, silicon substrates with different doping (p or p^+) were patterned with an array of Ni disks using nanoimprint lithography and e-beam evaporation. RIE-ICP (Reactive Ion

Etching-Inductively Coupled Plasma) dry etching was performed to fabricate vertical Si NW backbone arrays; NW lengths are determined by etching for various times with Ni disks as the etch mask. Followed by Ni removal and RCA cleaning,[28] the Si NW substrates were dried using N_2 and immediately transferred to the sputtering machine for the deposition of a thin ZnO layer, which later serves as seeding layer for ZnO NW growth. The measured thickness of sputtered ZnO on a glass slide was ~45 nm, however its actual thickness on Si NW cores is smaller (for example for 10m-Si NW cores, it was 25-30 nm). Finally, the ZnO NW branches were grown on the Si NW cores using hydrothermal growth method.[17, 31] For the TiO_2-coated samples used for IPCE measurement and stability study, ALD was used to deposit 20 nm TiO_2 at a temperature of 250°C. 3 nm Pt co-catalyst was deposited on the TiO_2-coated b-NW substrates using e-beam evaporation.

Characterization

The samples morphologies were examined on a Philips XL30 field-emission environmental scanning electron microscope (ESEM) at an accelerating voltage of 10.0 kV. Energy dispersive X-ray spectroscopy (EDS) and elemental mapping analyses were used to examine the material composition.

Photoelectrochemical and IPCE measurements

Current density and IPCE measurements were performed in a 400 mL aqueous solution of 0.25 M Na_2SO_4 buffered at pH = 7.25 (neutral solution) with three electrodes configuration, including ZnO/Si b-NWs as working electrode (WE), Pt mesh as counter electrode (CE), and Ag/AgCl (1 M KCl) as reference electrode (RE). Light with a constant power intensity of 100 mW/cm^2 was adjusted at the samples position for the photocurrent measurements. A scan rate of 10 mV/s was used for the linear sweep voltammetry (LSV). During the *J-V* and IPCE measurements, a mild agitation was used and the electrolyte was constantly purged with a small flow of N_2 gas. All the external biasing potentials here are versus Ag/AgCl RE, unless otherwise stated.

3.3 Results and Discussion

The Si NW cores were first fabricated using dry etching and ZnO NW branches were then grown using hydrothermal growth method (see Figure 3.1 for the fabrication procedure). For convenience, ZnO/Si b-NW arrays for different ZnO NW growth and Si NW etching times are denoted as "b(Xm-ZnO/Ym-p-Si) NWs" and "b(Xm-ZnO/Ym-p$^+$-Si) NWs" for NWs with p-Si and p$^+$-Si NW cores, respectively. "X" and "Y" are the ZnO growth and Si etching times in mins (m), respectively (for example, "5m-ZnO" means ZnO NWs grown for 5 mins or "10m-p-Si" means p-Si NWs etched for 10 mins). Figure 3.2 shows the scanning electron microscopy (SEM) images of 3D ZnO/Si b-NWs with 10m-Si NW cores and ZnO NW branches grown for different times (bare Si NW array is considered as zero ZnO growth time (Figures 3.2a-2c)). The average Si etching rate is ~0.24 µm/min, the Si NW array pitch size is ~1 µm, and the Si NW diameters are ~280 nm and ~230 nm for 10 and 20 mins etchings, respectively. Note that we used the same nanoimprinted Si substrates to make all the Si NW samples, however, the Si NW diameters after RIE-ICP etching are smaller than the dot size of nanoimprinting mould (which was 500 nm) and longer etching time results in smaller diameter. In the applied

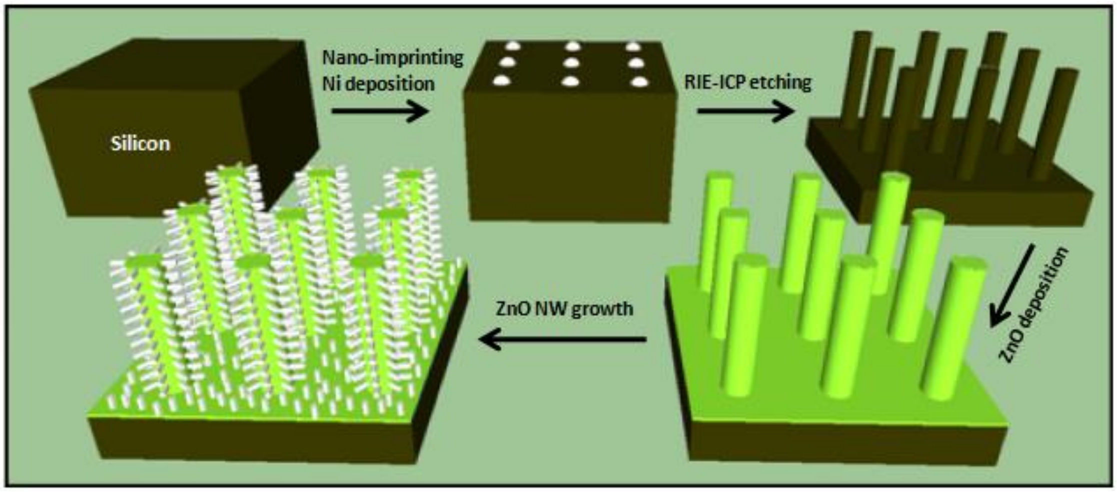

Figure 3.1. Fabrication procedure for 3D ZnO/Si branched NW (b-NW) arrays. After Si etching, the Ni disks at the head of Si NWs were removed by the Ni etchant.

RIE-ICP etching process, the C_4F_8 gas forms a passivation layer on the NW sidewall while the SF_6 etch gas etches this passivation layer and Si.[28] If the C_4F_8 flow is not high enough, the passivation layer is not thick enough to protect the NW sidewall. Therefore, the Si NW becomes thinner with increasing the etching time. Note that we fixed the C_4F_8 flow for all samples with the aim of identical etching conditions. As shown in Figures 3.2d-2i, there is a uniform growth of ZnO NW branches in length on Si NW cores, and ZnO NWs cover the entire length of Si NW trunks as well as on flat surface between Si NWs. Longer ZnO growth time leads to bigger ZnO NW branches (larger diameter and longer length). The average ZnO NW lengths (on 10m-Si NW backbones) are ~90 and ~200 nm for 5 and 10 mins ZnO growth times, respectively. The 10m-ZnO NWs have higher density than 5m-ZnO NWs, which can be due to longer ZnO growth time. Low-magnification SEM images in Figures 3.2j-2l indicate uniform formation of b-NWs over a large area, indicating the scalability of our processing for large area photoelectrodes

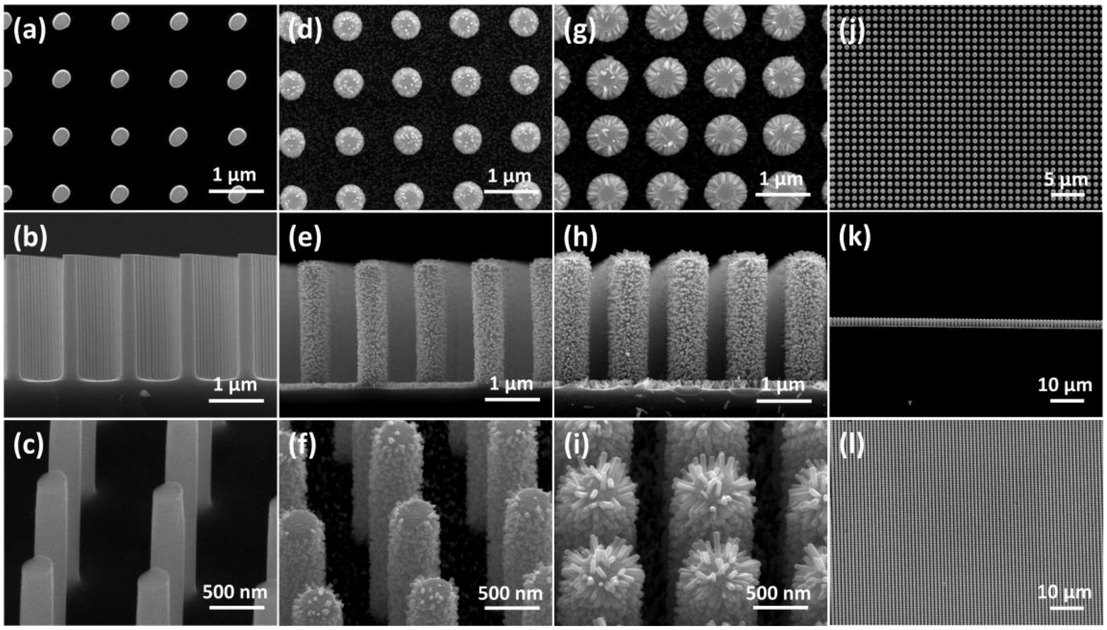

Figure 3.2. SEM images of 3D ZnO/Si b-NWs of 10m-Si NW cores with different ZnO NW growth times. First row, second row, and third row show the top view, cross-sectional view, and 45° view images, respectively. (a)-(c) zero min (bare Si NW array), (d)-(f) 5 mins, and (g)-(i) 10 mins. (j)-(l) are low-magnification images of (g)-(i).

from the low cost materials.

Figure 3.3 exhibits SEM images of 10m-ZnO NW branches on Si NW cores etched for two different times (10 mins – top row and 20 mins – bottom row). Smaller ZnO NWs were found on longer Si NW cores (shorter length and smaller diameter) (Figures 3.3e, 3.3f versus Figures 3.3b, 3.3c) for the same ZnO growth time of 10 mins due to reaction limited ZnO NW growth. The average ZnO NW lengths are ~200 nm and ~140 nm for 10 and 20 mins etching times, respectively. Note that even for long Si NWs (Figure 3.3d), the ZnO NWs also cover the entire length of Si NW backbones and the flat surface between the Si NWs.

The effect of ZnO NW growth time, and consequently NW branch diameters, on

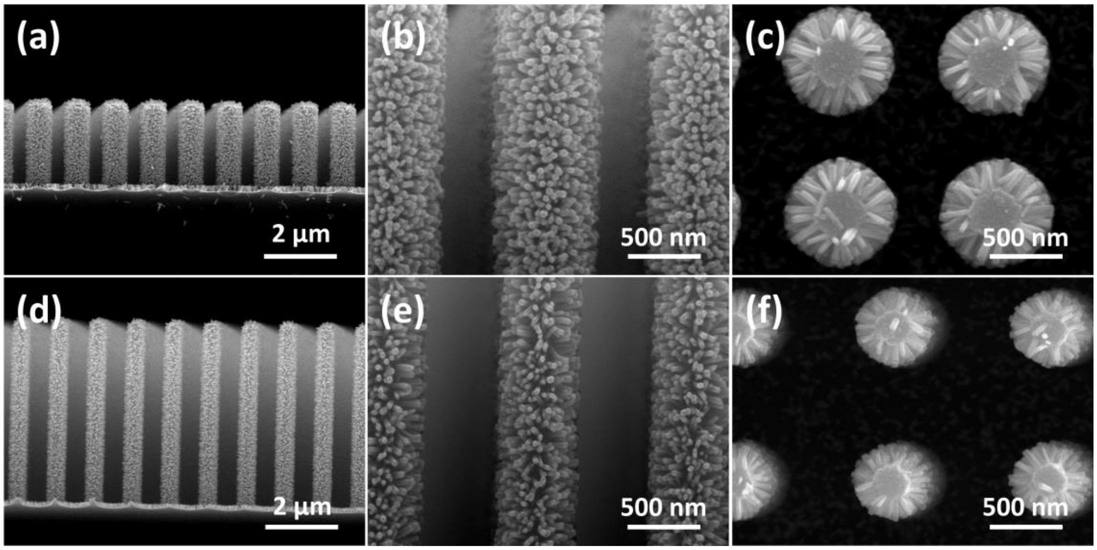

Figure 3.3. SEM images of 3D ZnO/Si b-NWs with 10m-ZnO NW branches on Si NW cores with (a)-(c) 10 mins and (d)-(f) 20 mins RIE etching. First and second columns show the cross-sectional view images, and third column shows the top view images.

the photocurrent of ZnO/p-Si b-NWs is illustrated in Figure 3.4a. Compared to the minimal photocathodic current from the bare Si NW electrodes (inset of Figure 3.4a), the b-NWs provide much enhanced photocathodic current, due to improved charge separation coming from p-Si and n-ZnO NWs junction, increased reaction surface area, enhanced light absorption, and improved gas evolution.[25] Larger ZnO NW branches give higher photocathodic current due to increased surface area. Figure 3.4b illustrates the transient current density under chopped light illumination for corresponding samples at -1.5 V external bias. The dark current densities of corresponding samples are shown in Figure 3.4c. The higher photo and dark currents from b-NW electrodes with larger ZnO NW branches under chopped light illumination (Figure 3.4b) are similar to those in Figures 3.4a and 3.4c. Figures 3.4d and 3.4e show the effect of Si NW length on the photocathodic current under constant and chopped light illumination. Longer Si NW

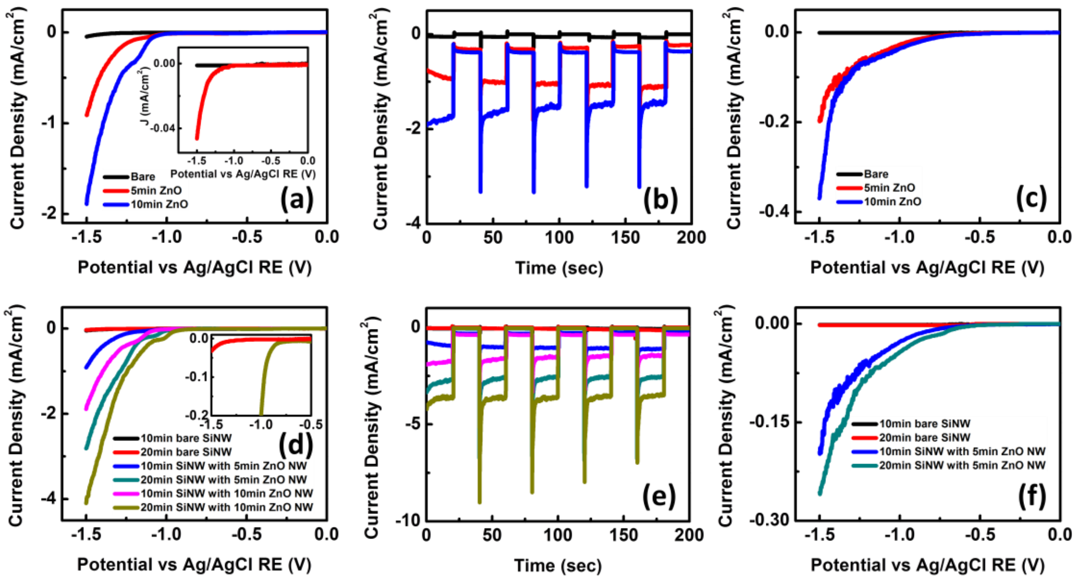

Figure 3.4. (a) Photocurrent density of 10m-p-Si NW cores with ZnO NW branches grown for different times, (b) transient current density under chopped light illumination of corresponding b-NW samples at -1.5 V, and (c) dark current density of corresponding samples in (a). The inset in (a) shows the dark (black curve) and photo (red curve) currents of bare 10m-p-Si NW array. (d) Photocurrent density of p-Si NW trunks etched for different times with ZnO NW branches grown for various times, (e) transient current density of corresponding samples at -1.5 V, and (f) dark current density of various etched p-Si NW cores with different ZnO NW branches (corresponding samples in (d)). The inset in (d) shows the zoom-in photocurrents of bare 20m-Si NW array and b(10m-ZnO/20m-p-Si) NWs.

(20m-p-Si NW) cores lead to higher photocathodic currents mainly due to enhanced light absorption[29] and increased total surface area of b-NWs. Note that 20 mins RIE also leads to smaller diameter and potentially better charge separation and consequently higher photocurrent due to larger band bending at the junction between p-Si and n-ZnO NWs.[25] Also note that even for the same ZnO growth time, the ZnO NW branches are smaller and denser for longer p-Si NW cores (Figure 3.3), leading to more efficient charge separation and collection, as well as further increase in the overall surface area. At forward biasing condition, there is a much smaller photoanodic current, compared to the photocathodic current (data not shown), particularly for b-NWs with longer p-Si NW cores. The increased dark current for b-NWs with longer cores (Figure 3.4f) confirms the enhanced surface area. The photocathodic current overshoot when switching on light (Figure 3.4e) can be from the accumulation of photo-generated electrons at the NWs-electrolyte interface, which subsequently recombine with holes at the interface until a stationary photocurrent is reached.

Very interestingly, the photocurrent turn-on potential reduces (the photocathodic turn-on potential shifts towards more positive potentials) with longer Si NW cores and larger ZnO NW branches. Note that there is a significant shift of ~600 mV towards positive voltages for b(10m-ZnO/20m-p-Si) NWs compared to 20m-p-Si NW array, which was determined with reference to the photocurrent of bare 20m-Si NW array at -1.5 V (inset of Figure 3.4d). The photocathodic turn-on potential of b(10m-ZnO/20m-p-Si) NWs is about -0.3 V versus reversible hydrogen electrode (RHE). The transient current density under chopped illumination and at -1.5 V for corresponding samples is shown in Figure 3.4e confirming the observed trends in Figure 3.4d. The photocathode energy conversion efficiency for hydrogen evolution of the optimized ZnO/p-Si b-NWs is over 2% at the biasing potential of -1 V versus Pt counter electrode (CE) using two-electrode PEC measurement setup and considering no optical losses coming from the PEC setup. The three-electrode measurement setup provides a photocathode efficiency of over 3.5% at -1.26 V versus normal hydrogen electrode (NHE) revealing the efficiency overestimation using three-electrode setup. Longer Si and ZnO NWs than those investigated here can also be further improved the PEC performances.

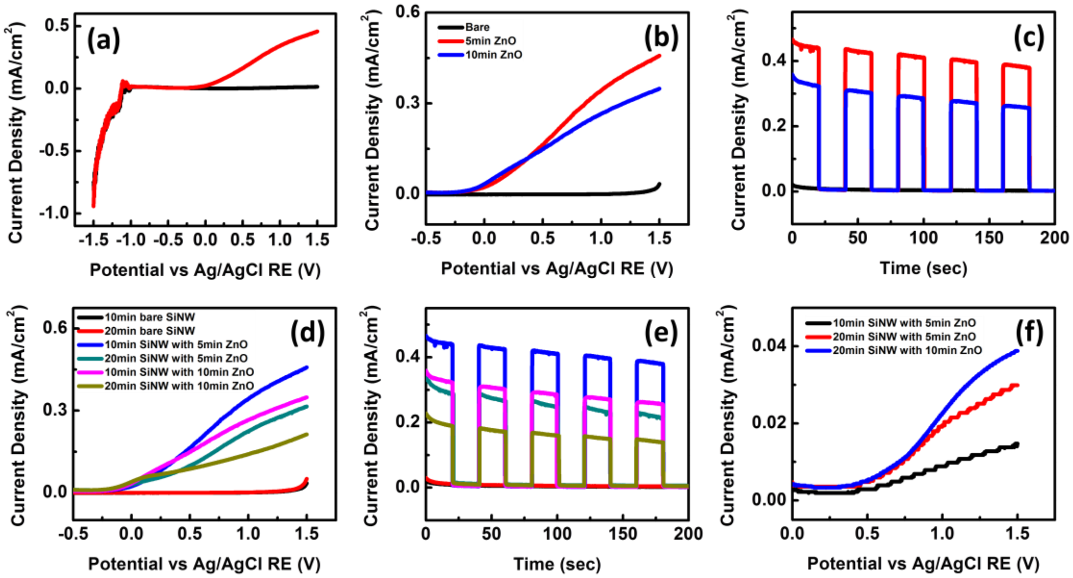

Figure 3.5. (a) Current density of b(5m-ZnO/10m-p$^+$-Si) NWs. The red and black lines represent the photo and dark current density, respectively. (b) Photocurrent density of 10m-p$^+$-Si NW cores with ZnO NW branches grown for various times, and (c) transient current density under chopped light illumination of corresponding b-NWs at +1.5 V. (d) Photocurrent density of p$^+$-Si NW backbones etched for different times with different ZnO NW branches, (e) transient current density of corresponding samples at +1.5 V, and (f) dark current density of various p$^+$-Si NW cores with different ZnO NW branches (corresponding samples in (d)).

The effect of Si NW array pitch size (b-NW center-to-center spacing) on the photocathodic performance of ZnO/p-Si b-NWs is studied and is found to play a significant role in increasing the photocathode conversion efficiency. The smaller pitch size, with smaller core diameter, offers much higher photocathodic current and also shifts the photocathodic turn-on potential towards more positive potentials, which is probably due to enhanced light absorption and increased total surface reaction area of b-NWs.

We have recently demonstrated the photoanodic behavior using ZnO/p$^+$-Si b-NWs, namely tuning of PEC electrode functions by changing the Si NW core doping.[25] In fact, under reversed biasing condition, there is no difference between dark and photo currents meaning that there is no photocathodic behavior (see Figure 3.5a as an example). Note that all the tested b-NW samples with p^+-Si NW cores did not show any photocathodic current, indicating that this behavior is universal, regardless of p^+-Si or ZnO NW dimensions. Note also that our focus in this study is to optimize this photoanodic behavior of ZnO/p^+-Si b-NWs for more efficient water oxidation. Figure 3.5b illustrates the effect of ZnO growth time on the photoanodic behavior. The ZnO/p^+-Si b-NWs exhibit a large photoanodic current compared to the bare NW array, which does not show any photoanodic behavior (Figure 3.5c). The photoanodic current increases with reducing ZnO growth time due to lower recombination for photo-generated carriers. This is easily understandable as, for b-NWs with shorter ZnO NW branches, the photo-generated electrons at the ZnO-electrolyte interface have shorter travel distance to the p^+-Si region, resulting in lower recombination with holes at the interface and consequently larger photoanodic current and more water oxidation.[25] The transient current density under chopped illumination for corresponding b-NWs at +1.5 V (Figure 3.5c) confirms the trend in Figure 3.5b.

The effect of p^+-Si NW core length is shown in Figure 3.5d, in which the photoanodic current decreases with increasing length probably due to longer transport pathway for photo-generated carriers resulting in increased recombination. The dark current, on the other hand, shows opposite trend due to improved surface area (Figure 3.5f). Note that the stepwise shape of the current curves in Figure 3.5f is because dark currents are very low and the sensitivity was selected to be the same for the current scan of all samples. Due to small minority carrier diffusion length and short minority carrier lifetime of p^+-Si NW trunks, they cannot produce considerable amount of carriers,[25] thus higher absorption of longer p^+-Si NW cores is not effective in the improved photocurrent. Note that the photoanodic current of b-NWs with 20m-p^+-Si NWs shows the same trend for different ZnO growth times as that for b-NWs with 10m-p^+-Si NWs, while the dark current increases with increasing ZnO growth time (see Figure 3.5f) due to the increased surface area. The transient current density (Figure 3.5e) confirms the observed trends in Figure 3.5d.

The observed trends for the photoanodic current of ZnO/p^+-Si b-NWs is different from those for the photocathodic current of ZnO/p-Si b-NWs, because the p-Si NW cores contribute to improve the photocathodic current due to the effective junction between p-Si and n-ZnO NWs leading to enhanced charge separation, while the junction between p^+-Si and n-ZnO NWs is not effective for charge separation.[25] The anodic turn-on potential does not significantly change with altering Si NW etching or ZnO growth time (Figure 3.5d), while as observed in Figure 3.4d, there is a shift in cathodic turn-on potential with these changes for the ZnO/p-Si b-NWs. This may be explained with the face that in ZnO/p-Si b-NW heterostructures, the effective Si-ZnO junction delivers photo-generated carriers towards ZnO-liquid junction for surface reactions and higher surface area of longer Si NWs or larger ZnO NWs, providing higher surface reactions, can further shift the turn-on potential. But for the ZnO/p^+-Si b-NWs, as mentioned above, the Si-ZnO junction is not effective and the photo-generated carriers are mainly produced by the ZnO-liquid junction, in which shorter Si NWs or smaller ZnO NWs experience less recombination. Moreover unlike the ZnO/p-Si b-NWs, there is no current overshoot for different p^+-Si NW etching or ZnO growth times in the ZnO/p^+-Si b-NWs.

The PEC performance of the b-NWs is further evaluated using spectral IPCE. The studied samples for the IPCE (except bare Si NW samples) were coated with 20 nm TiO_2 using atomic layer deposition (ALD) to improve the stability of samples and to have stationary current during the IPCE measurement. The spectral IPCE for b(5m-ZnO/10m-p-Si) NWs at -1.3 V (orange line) is shown in Figure 3.6, exhibiting a broadband photoresponse due to combination of p-Si and ZnO NWs. Note that the IPCE for this sample was measured after long stability test, in which there was a constant photocurrent. The small peak at ~1050 nm is due to Si material though the reason for that is not entirely clear at this point. The ZnO/p-Si b-NWs show much higher IPCE than the bare p-Si NW array (data not shown here), which can be due to effective Si-ZnO junction, increased surface area, and probably improved light absorption.[11, 24] The photoanodic behavior of

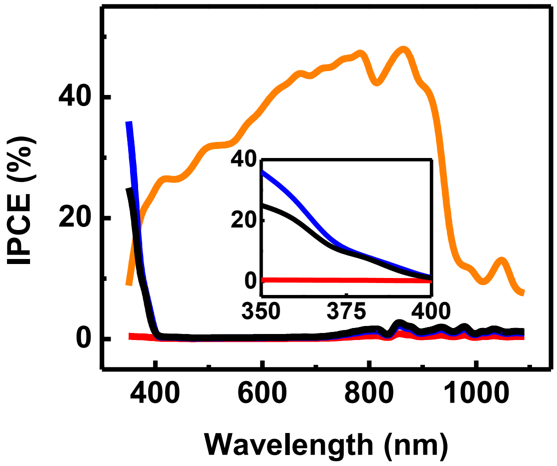

Figure 3.6. IPCE for the b(5m-ZnO/10m-p-Si) NWs at -1.3 V (orange line), and the 10m-p^+-Si NW cores with various ZnO NW branches at +1.3 V (red: bare Si NW array, blue: 5 mins ZnO, black: 10 mins ZnO). The inset shows the zoom-in spectral IPCE in UV range for the corresponding samples with p^+-Si NW cores. These b-NW arrays were coated with 20 nm TiO_2 layer.

the ZnO/p^+-Si b-NWs has been confirmed with their spectral photoresponse which lies below 400 nm due to ZnO band gap.[25] The IPCE for 10m-p^+-Si NW cores with different ZnO NW branches at +1.3 V is illustrated in Figure 3.6, exhibiting the same trend as that for the photoanodic current (Figure 3.5b). Higher IPCE for smaller ZnO NW can be due to the reduced recombination discussed above. The photoresponse lies below 400 nm for different ZnO growth times and there is no photoresponse for the bare p^+-Si NW array. The effect of p-Si and p^+-Si NW core lengths was also investigated (data not shown here) exhibiting the same trends as those in the *J-V* measurements.

Long-term stability, besides hydrogen production cost and efficiency, is another key factor for practical industrial hydrogen production. Due to material instability, ZnO/Si b-NW photoelectrodes cannot offer long-term stability. Using a corrosion-resistant TiO_2 coating layer and with and without Pt co-catalyst, b-NW electrodes' stabilities over a long time were investigated. Figures 3.7a and b show the SEM images of b(5m-ZnO/10m-p-Si) NWs covered with 20 nm TiO_2 layer and 3 nm Pt co-catalyst. The TiO_2 layer covers the surfaces of the NWs and substrate over the entire sample. Also note that the Pt nanoparticles are hard to recognize form the SEM images due to their very small thickness. The current density of b(5m-ZnO/10m-p-Si) NWs with different coatings is shown in Figure 3.7c. The dark and photo currents of TiO_2-coated b-NW electrode reduce compared to that of the bare b-NW one, and the photocurrent reduction is mainly at high reversed biasing potentials (see Figure 3.7c inset). On the other hand, the dark and photo currents of TiO_2/Pt coated b-NW electrode increase compared to that of the bare b-NWs, particularly the photocurrent improves significantly. More importantly, the Pt co-catalyst shifts the photocathodic current turn-on potential towards positive potentials for ~480 mV. Note that we expect similar potential shift for the Pt coated b-NWs (without any TiO_2 coating) due to the negligible photocathodic current reduction of the TiO_2-coated b-NWs at low reversed biasing potentials (Figure 3.7c inset). The turn-on potential shift for the optimized bare b(10m-ZnO/20m-p-Si) NWs is ~260 mV compared to the turn-on potential of bare b(5m-ZnO/10m-p-Si) NWs, which is over half of what is achieved by Pt co-catalyst on the TiO_2-coated b-NWs (~480 mV). This is another interesting feature of these b-NW photoelectrodes showing that significant turn-on potential shift can be obtained even without using costly Pt co-catalyst through optimizing the b-NWs. By further optimization (smaller Si NW pitch size, longer Si NWs, or larger ZnO NWs), it may be possible to achieve similar turn-on potential shift to that of TiO_2/Pt coated sample. The switching behavior of TiO_2/Pt coated b-NWs is investigated using the current density under chopped light illumination (Figure 3.7d), in which the sample exhibits good switching behavior without any current overshoot. The

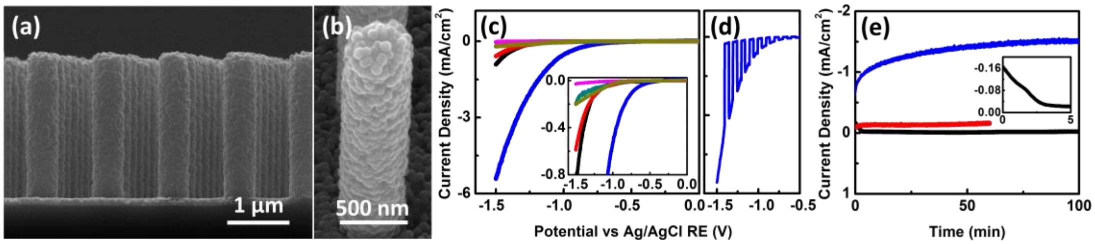

Figure 3.7. (a)-(b) SEM images of TiO_2/Pt coated b(5m-ZnO/10m-p-Si) NWs. (c) Current density of b(5m-ZnO/10m-Si) NWs with different coatings (dark cyan and black lines: dark and photo currents of bare b-NWs, respectively, magenta and red lines: dark and photo currents of TiO_2-coated b-NWs, respectively, dark yellow and blue lines: dark and photo currents of TiO_2/Pt coated b-NWs, respectively). The inset shows the corresponding zoomed-in curves. (d) Current density of TiO_2/Pt coated b-NWs under chopped illumination. (e) Current density under illumination versus time of corresponding samples in (c) (black line: bare, red line: TiO_2-coated, and blue line: TiO_2/Pt coated). The inset exhibits the enlarged first part (0-5 mins) of curve for bare b-NWs. The applied external potential is -1 V for all curves in (e).

transient current density under pulsed illumination also showed the same good switching behavior without current overshoot demonstrating that charge carriers accumulation at the electrode surface is not that significant in these samples like that observed for the bare b-NWs (Figure 3.4).

Photocurrent stability tests for b(5m-ZnO/10m-p-Si) NWs with different coatings were carried out by collecting their currents under a fixed illumination of 100 mW/cm^2 and at a biasing potential of -1 V (Figure 3.7e). The photocurrent for bare b-NW sample decreases significantly after a few minutes (inset of Figure 3.7e) due to dissolution of ZnO NWs in the electrolyte and exposing Si NWs to the electrolyte, which will be discussed in the following. Note that the stability test for this sample was performed after several different PEC tests, thus the current degradation for a fresh bare b-NW sample is less than that observed for this sample. Also, note that for the *J*-*V* measurements of unprotected samples, measurements for several different current scans provided similar photocurrents confirming that lack of long-term stability did not affect the *J*-*V* measurements. Furthermore, the consistent currents between the *J*-*V* and *J*-*t* measurements (Figure 3.4) as well as constant photocurrent during transient current density (Figure 3.4) further confirm that lack of long-term stability did not influence the *J*-*V* measurements. The TiO_2-coated sample shows significant enhancement in the stability revealing that the complete coverage of TiO_2 layer on NWs well protects them. In general, the stability is bias or current dependence in which at higher biasing potentials or photocurrents, the stability reduces. Although the TiO_2/Pt coated sample has much higher photocurrent than the TiO_2-coated sample, it still shows dramatic enhancement in the stability. More importantly, we have shown stability of over 24 hours under constant illumination for such a TiO_2/Pt coated sample.[25] The time that the photocurrent needs to reach its plateau/saturation for TiO_2/Pt coated sample is longer than that for TiO_2-coated sample (Figure 3.7e), which may be due to slow Pt co-catalyst reaction though is not completely clear at this point.

The energy-dispersive X-ray spectroscopy (EDS) elemental mapping analyses for the bare and TiO_2/Pt coated b-NW samples for before and after stability tests are studied. The absence of Zn element in the elemental mapping of bare b-NW sample after stability test shows the dissolution of ZnO NWs (Figure 3.7e), which can also clearly be seen in its SEM image. However for TiO_2/Pt coated sample, all materials within the b-NWs preserve after stability test and ZnO NW branches do not dissolve in the electrolyte confirming that the TiO_2 coating layer well protects the NWs. In fact, shape and morphology of b-NWs remain unchanged after PEC measurements and long-term stability test.

3.4 Conclusions

In summary, we report the systematic studies of 3D ZnO/Si b-NW photoelectrodes for solar water splitting and fuel generation. The PEC performance of the b-NW photoelectrodes with different sizes of NW cores/trunks and branches, different pitch sizes, and different doping concentrations of NW cores were tested in neutral medium. Larger ZnO NW branches, and longer and denser p-Si NW cores gave higher photocathodic current, better efficiency, as well as lower photocurrent turn-on potential, while smaller ZnO NW branches and shorter p^+-Si NW trunks offer higher photoanodic current and better efficiency. The optimized ZnO/p-Si b-NWs exhibited a significant photocathodic turn-on potential shift of ~600 mV compared to the bare p-Si NW array, as well as an energy conversion efficiency of > 2% at -1 V versus Pt CE. Furthermore, by coating a thin TiO_2 protection layer using ALD, the stability of ZnO/Si b-NW photoelectrodes are remarkably improved. These results demonstrate that the b-NWs are effective photoelectrodes that offer enhanced photocurrent and photoresponse, reduced turn-on potential, increased conversion efficiency, improved stability, and most importantly property tunability. These studies also provide useful insights in the design and fabrication of novel 3D b-NW electrodes based on cheap and earth abundant materials for potential high-efficiency and low-cost solar fuel generation.

Chapter 3 was published in *ACS Nano* 2013, A. Kargar, K. Sun, Y. Jing, C. Choi, H. Jeong, G. Y. Jung, S. Jin and D. Wang, “3D branched nanowire photoelectrochemical electrodes for efficient solar water splitting”. The dissertation author was the first author of this paper.

References

1. Wang, D.; Qian, F.; Yang, C.; Zhong, Z.; Lieber, C. M., R. *Nano Lett.* **2004***, 4*, 871−874.

2. Dick, K. A.; Deppert, K.; Larsson, M. W.; Martensson, T.; Seifert, W.; Wallenberg, L. R.; Samuelson, L. *Nat. Mater.* **2004***, 3*, 380−384.

3. Wang, D.; Lieber, C. M. *Nat. Mater.* **2003***, 2*, 355−356.

4. Manna, L.; Milliron, D. J.; Meisel, A.; Scher, E. C.; Alivisatos, A. P. *Nat. Mater.* **2003***, 2*, 382−385.

5. Jiang, X.; Tian, B.; Xiang, J.; Qian, F.; Zheng, G.; Wang, H.; Mai, L.; Lieber, C. M. *Proc. Natl. Acad. Sci. U.S.A.* **2011**, *108*, 12212−12216.

6. Cheng, H.-M.; Chiu, W.-H.; Lee, C.-H.; Tsai, S.-Y.; Hsieh, W.-F. *J. Phys. Chem. C* **2008**, *112*, 16359−16364.

7. Cho, I. S.; Chen, Z.; Forman, A. J.; Kim, D. R.; Rao, P. M.; Jaramillo, T. F.; Zheng, X. *Nano Lett.* **2011**, *11*, 4978−4984.

8. Jung, S.; Yong, K. *Chem. Commun.* **2011**, *47*, 2643−2645.

9. McCune, M.; Zhang, W.; Deng, Y. *Nano Lett.* **2012**, *12*, 3656−3662.

10. Qiu, Y.; Yan, K.; Deng, H.; Yang, S. *Nano Lett.* **2011**, *12*, 407−413.

11. Sun, K.; Jing, Y.; Li, C.; Zhang, X.; Aguinaldo, R.; Kargar, A.; Madsen, K.; Banu, K.; Zhou, Y.; Bando, Y. *et al.* *Nanoscale* **2012**, *4*, 1515−1521.

12. Xu, F.; Dai, M.; Lu, Y.; Sun, L. *J. Phys. Chem. C* **2010**, *114*, 2776−2782.

13. Ahmad, M.; Yingying, S.; Nisar, A.; Sun, H.; Shen, W.; Wei, M.; Zhu, J. *J. Mater. Chem.* **2011**, *21*, 7723−7729.

14. Bierman, M. J.; Jin, S. *Energy Environ. Sci.* **2009**, *2*, 1050−1059.

15. Herman, I.; Yeo, J.; Hong, S.; Lee, D.; Nam, K. H.; Choi, J.-h.; Hong, W.-h.; Lee, D.; Grigoropoulos, C. P.; Ko, S. H. *Nanotechnology* **2012**, *23*, 194005.

16. Chen, W.; Qiu, Y.; Yang, S. *Phys. Chem. Chem. Phys.* **2012**, *14*, 10872−10881.

17. Sun, K.; Jing, Y.; Park, N.; Li, C.; Bando, Y.; Wang, D. *J. Am. Chem. Soc.* **2010**, *132*, 15465−15467.

18. Ko, S. H.; Lee, D.; Kang, H. W.; Nam, K. H.; Yeo, J. Y.; Hong, S. J.; Grigoropoulos, C. P.; Sung, H. J. *Nano Lett.* **2011**, *11*, 666−671.

19. Shao, F.; Sun, J.; Gao, L.; Yang, S.; Luo, J. *J. Mater. Chem.* **2012**, *22*, 6824−6830.

20. Cheng, C.; Fan, H. J. *Nano Today* **2012**, *7*, 327−343.

21. Li, C. C.; Yin, X. M.; Chen, L. B.; Li, Q. H.; Wang, T. H. *Appl. Phys. Lett.* **2010**, *97*, 043501.

22. Zhou, W.; Cheng, C.; Liu, J.; Tay, Y. Y.; Jiang, J.; Jia, X.; Zhang, J.; Gong, H.; Hng, H. H.; Yu, T. *et al. Adv. Funct. Mater.* **2011**, *21*, 2439−2445.

23. Liu, J.; Cheng, C.; Zhou, W.; Li, H.; Fan, H. J. *Chem. Commun.* **2011**, *47*, 3436−3438.

24. Song, H. S.; Zhang, W. J.; Cheng, C.; Tang, Y. B.; Luo, L. B.; Chen, X.; Luan, C. Y.; Meng, X. M.; Zapien, J. A.; Wang, N. *et al. Cryst. Growth Des.* **2010**, *11*, 147−153.

25. Kargar, A.; Sun, K.; Jing, Y.; Choi, C.; Jeong, H.; Zhou, Y.; Madsen, K.; Naughton, P.; Jin, S.; Jung, G. Y. *et al. Nano Lett.* **2013**, *13*, 3017−3022.

26. Gray, H. B. *Nat. Chem.* **2009**, *1*, 7−7.

27. Hou, Y.; Abrams, B. L.; Vesborg, P. C. K.; Björketun, M. E.; Herbst, K.; Bech, L.; Setti, A. M.; Damsgaard, C. D.; Pedersen, T.; Hansen, O. *et al. Nat. Mater.* **2011**, *10*, 434−438.

28. Henry, M. D. Ph.D. thesis, California Institute of Technology, **2010**.

29. Garnett, E.; Yang, P. *Nano Lett.* **2010**, *10*, 1082−1087.

30. Kern, W. *J. Electrochem. Soc.* **1990**, *137*, 1887−1892.

31. Law, M.; Greene, L. E.; Johnson, J. C.; Saykally, R.; Yang, P. Nanowire Dye-Sensitized Solar Cells. *Nat. Mater.* **2005**, *4*, 455−459.

4. THREE-DIMENSIONAL ZNO/SI BROOM-LIKE NANOWIRE HETEROSTRUCTURES AS PHOTOELECTROCHEMICAL ANODES FOR SOLAR ENERGY CONVERSION

4.1 Introduction

Direct solar water splitting to generate hydrogen using photoelectrochemical (PEC) cells, as a cost-effective and carbon-emission-free hydrogen production method, has attracted considerable attention.[1, 2] Solar water splitting has great potential for practical clean hydrogen production.[3, 4] Efficient photocathodes and photoanodes are required to couple to each other to perform overall solar water splitting without any external bias.[2] Semiconductor photoelectrodes are the key components to determine the PEC performance and solar energy harvesting/conversion efficiency. Among the semiconductor materials studied, nanowire (NW) heterostructures have been of great interest due to the potential of superior efficiency coming from the unique geometry and properties, unlimited combination and effective integration at nanoscale to implement design, and material integrity.[5, 6] Particularly core/shell[5-7] and branched NW heterostructures[8] have been reported to offer higher efficiency compared to pure semiconductor NWs or bulk materials because of the enhanced absorption in broad solar spectra, improved charge separation and reduced recombination of photo-generated carriers, and increased charge transportation. Moreover, branched NW heterostructures can provide better PEC performance and higher solar-to-fuel production efficiency than the core/shell NW heterojunctions due to much increased surface reaction area and improved gas evolution coming from the large surface curvature of NW branches.[8, 9] We have recently demonstrated efficient, stable, and cost-effective three-dimensional

(3D) n-ZnO/p-Si branched NW photocathodes with low photocathodic turn-on potential for water reduction and hydrogen gas production.[9, 10] This paper reports the low-cost fabrication and systematic characterization of 3D n-ZnO/n-Si broom-like NW (nanobroom) heterostructures, with n-ZnO NWs only covering the tip of n-Si NWs, and their application as photoanodes for water oxidation and oxygen gas generation. The optical absorption and photocurrent, as well as the electrode stability, of the nanobroom photoelectrodes are studied and the PEC performances are optimized based on different Si and ZnO NWs dimensions. The effect of the catalyst on the PEC performance of nanobrooms is also investigated.

4.2 Experimental Section

Device fabrication

Firstly, wafer-scale vertically ordered Si NW arrays on Si wafer were obtained using an aqueous Ag-assisted electroless etching method.[11, 12] N-type phosphorus-doped silicon (100) wafers with resistivity of 1-20 Ωcm were first cleaned with solvent, rinsed with deionized (DI) water, and dried with N_2 flow. The cleaned Si wafer was then fixed on a homemade etching setup, and after that the setup with the attached wafer was submerged in a mixture solution of HF and $AgNO_3$ solution. The etching solution container was then put in a water bath at a temperature 50 °C. The wafers were then etched for different times to achieve different lengths of Si NWs. The etched wafer was then taken out of etching solution and rinsed with DI water. Finally, it was submerged in a 1:10 diluted HNO_3 solution for 2 hrs to remove the Ag dendrite film formed during the etching. The samples were denoted by the etching time (for example, “10min Si NWs” means the Si NW backbones that were etched for 10min).

Secondly, the etched Si NW samples were then dipped in buffered oxide etching (BOE) solution for 10 sec to remove the native oxide layer, cleaned with DI water, dried with N_2 gun, and instantly transferred to a sputter machine in order to minimize oxidation. A thin ZnO seeding layer was deposited on the Si NW substrates using RF magnetron sputtering with ZnO target (purity; 99.99%) in argon carrier gas. The sputtering pressure was 1.9 mTorr during the deposition.

Finally, the ZnO NW stalls were grown on the Si NWs using hydrothermal growth method reported before.[10, 12-14] Briefly, 25 mM aqueous solutions of zinc acetate dihydrate ($Zn(O_2CCH_3)_2(H_2O)_2$, Sigma-Aldrich) and hexamethylene-tetramine (HMTA) ($(CH_2)_6N_4$, Sigma-Aldrich) in DI water ($\geq$ 17.5 MΩ-cm) were prepared (growth solution). The ZnO-seeded Si NW substrates, fixed on a supporting glass slide using double-sided tape with their top facing down, were then immersed in the growth solution which was pour in a flask. Then, the flask was positioned in the center of an oil bath and a mild agitation was used at the bottom of the flask. After reaching a temperature of 60°C for the growth solution (the temperature was monitored with a thermometer kept inside the growth solution), the time counting was started for different desired growth times (5min, 10min, 15min here). The as-synthesized samples were then rinsed carefully with DI water and dried with N_2 gun. The samples were denoted by the growth time (for example, “10min ZnO NWs” means the nanobrooms with ZnO NW stalls grown for 10min).

For the TiO_2-coated samples, atomic layer deposition (ALD), using Beneq TFS 200 system, was used to deposit a thin layer of TiO_2 on the nanobroom substrates at a temperature of 250°C. The measured thickness of deposited TiO_2 was 10 nm based on growth rate of 0.44 Å/cycle on Si(100) film substrate. For Ru catalyst/co-catalyst deposition, sputtering was used to deposit ~5 nm Ru on the samples at a sputtering pressure of 10 mTorr.

Characterization

The nanobroom morphology was examined using field-emission environmental scanning electron microscope (SEM, Phillips XL30) and ultra high-resolution scanning electron microscope (UHR SEM, FEI XL30-SFEG), both at an accelerating voltage of 10.0 kV. The atomic-scale structural analyses were performed using high-resolution transmission electron microscopy (HRTEM, JEOL JEM3100F) operated at 300 kV. Spherical aberration-corrected scanning transmission electron microscopy (Cs-corr. STEM, JEOL JEM2100F) operated at 200 kV was employed to identify the actual atomic structure of NWs. The reflectance spectra were taken by an optical spectrometer. White light (Xenon lamp 75 W) was focused through a microscope objective of 50x with a numerical aperture (NA) of 0.8 onto the samples. The absorption spectra (A) were achieved by reflectance spectra (R) using $A(\%) = 100 - R(\%)$.

Photoelectrochemical measurements

For the PEC tests, Cu wire was bonded to the samples at the back using indium, which provides an ohmic contact. The edges and backside of samples were sealed using epoxy to protect from contact to the electrolyte. Photocurrent measurements were carried out in a 400 mL aqueous solution of 0.25 M Na_2SO_4 buffered with Phosphate Buffered

Saline (PBS, Sigma) (pH = 7.25) with three electrode configuration, including ZnO/Si nanobroom array as a working photoelectrode (WE), Pt coil/mesh as a counter electrode (CE), and Ag/AgCl (1 M KCl) as a reference electrode (RE). The samples were illuminated with a constant light power intensity of ~109 mW/cm^2, from a solar simulator (Newport 67015) equipped with a 150 W Xenon lamp and a 1.5 AM filter. Note that the light power intensity was tuned to 100 mW/cm^2 for the samples tested for the stability tests and catalyst effect (Figures 3.7 and 3.8). The current versus potential/time measurements were collected using a potentiostat (DY2300, Digi-Ivy). A scan rate of 5 mV/s was used for the current versus potential measurements. The time for each current density versus potential test was 10min because the scan rate was 5 mV/sec and the electrodes were scanned from -1.5 V to 1.5 V versus Ag/AgCl RE. The electrolyte was purged with N_2 gas before start of each test for at least 5min and a mild agitation was used during the PEC tests. Photocurrent stability tests were performed by collecting the electrode light current under constant light illumination and at a fixed biasing potential.

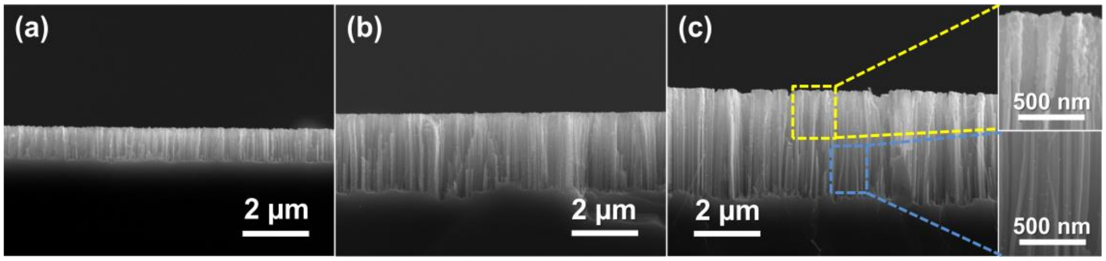

Figure 4.1. Cross-sectional SEM images of n-Si NW arrays etched for (a) 5min, (b) 10min, (c) 15min, and coated with ZnO seeding layer. The zoomed parts in (c) show the non-uniform coating of ZnO seeding layer on Si NWs.

The potentials versus normal hydrogen electrode (NHE) were calculated using E_{bias}(vs NHE) = E_{bias} (vs Ag/AgCl) + 0.236 V, where 0.236 V is the potential difference of Ag/AgCl RE (1 M KCl) to the NHE at 25°C (Digi-Ivy, Inc., Austin, TX).

4.3 Results and Discussion

Figure 4.1 shows cross-sectional SEM images of n-Si NW arrays with different wet etching times and coated with a ZnO seeding layer. The average Si NW lengths are ~900 nm, ~2.35 µm, and ~3.21 µm for 5min, 10min, and 15min etching times, respectively, resulting in an average etching rate of ~200 nm/min, which is consistent with that reported elsewhere.[5]. The ZnO seeding layer does not uniformly cover the entire length of Si NWs, with larger thickness at the tips of Si NWs than other parts of NWs (see the zoomed SEM images in Figure 4.1c for the top and bottom parts of Si NWs). In fact, at the bottom region of Si NWs, only ZnO nanoparticles or not a continuous film was observed (see the zoomed SEM image for the bottom part of NWs in Figure 4.1c). The growth of ZnO NW stalls on the Si NW backbones for different growth times is illustrated in Figure 4.2. Longer ZnO NW growth time results in bigger ZnO NWs (larger diameter and longer length), which can clearly be seen by comparison between Figures 4.2d, 4.2e and 4.2f. Note that the ZnO NW growth is only found at the tips of Si NWs and there is no growth on the sidewalls especially at the top parts of Si NWs, despite that the ZnO seeding layer covers uniformly the top portions of Si NWs (see Figures4.2d-2f and 4.2g). The reason is not totally clear. It can be due to either a critical seeding layer thickness on the Si NW tips for ZnO NW nucleation or a higher local pH due to initial

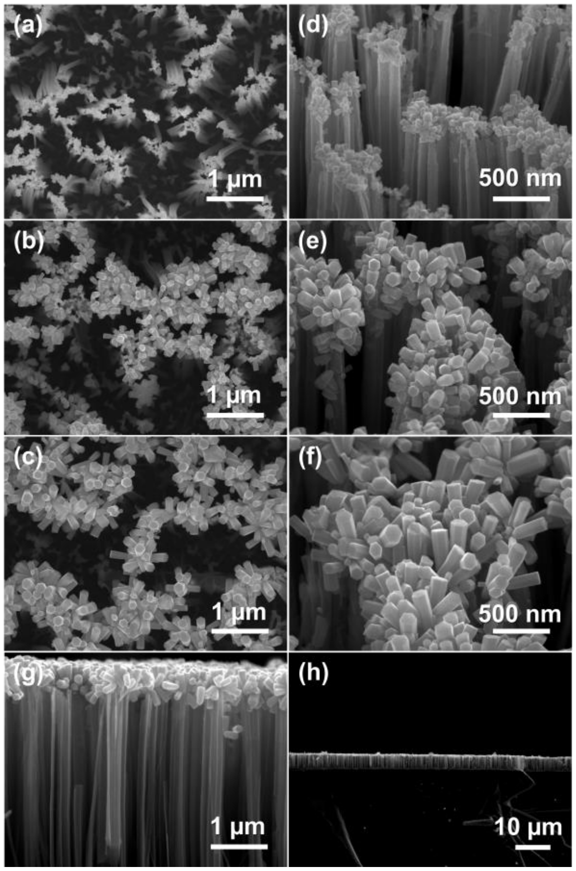

Figure 4.2. SEM images of ZnO/Si nanobroom arrays with different ZnO NW growth times on 15min Si NW backbone array. (a)-(c) and (d)-(f) show the top-view and tilted-view images of samples with 5min, 10min, and 15min ZnO NW growth, respectively. (g) and (h) High- and low-magnification cross-sectional images of nanobrooms with 15min ZnO NW stalls grown on the Si NW backbone array with 15min etching.

growth reaction.[15, 16] Low-magnification image in Fig. 2h shows the large coverage of 3D ZnO/Si nanobrooms. Note that different parts on samples were investigated and the formation of nanobrooms was throughout the entire area of samples.

Figure 4.3a shows low-magnification bright field transmission electron microscopy (BF-TEM) image of 3D ZnO/Si nanobrooms on Si substrate with 10min Si NW backbones and 10min ZnO NW stalls. Low-magnification dark field (DF) and bright field (BF) scanning transmission electron microscopy (STEM) images of a single ZnO/Si nanobroom are shown in Figures 4.3b and 4.3c. The average diameter of Si NW backbone in this nanobroom is ~100 nm. Note that for the wet-etched Si NWs, the NWs are random in diameter (see Figure 4.3a as an example) due to the nature of Ag-assisted electroless etching method. High-resolution high angle annular dark field (HAADF) STEM image (Figure 4.3d) for the highlighted position in Figure 4.3b demonstrates defect-free and single-crystalline Si NW, which can also be seen in annular bright field (ABF) STEM image (Figure 4.3e). The inset shows a lattice spacing of 0.13 nm down a 110 plane for the wet-etched Si NW. The red circle in the inset shows the diamond structure of Si. The diffraction patterns for various positions along the Si NW backbone clearly show the single-crystalline nature along the entire length of the Si NW. Low-magnification BF TEM image of ZnO NWs at the tip of Si NWs is shown in Figure 4.4a. Figure 4.4b exhibits high-resolution TEM (HRTEM) image of a single ZnO NW marked in Figure 4.4a. The darker contrast shown in ZnO NW is due to the overlap with another ZnO NW, also as seen in Figure 4.4a. The HRTEM image in Figure 4.4c demonstrates defect-free and single-crystalline wurtzite structure for the ZnO NW, which also shows very smooth surfaces. The calculated fast Fourier transform (FFT) pattern of this image, shown in the inset, illustrates the ZnO NW growth direction of (002). The calculated lattice spacing is 0.52 nm, shown in Figure 4.4d, achieved from the modified image from noise-filtering of Figure 4.4c.

Figure 4.5a shows the optical image of wet-etched n-Si NW arrays and arrays with ZnO NWs grown for various times. The as-etched Si NW samples are uniformly black in color over a large area indicating the uniform etching of the Si wafer. Sputtering a thin ZnO layer on the Si NW array changes its color to dark brown. There is a gradual color change towards more whiter/lighter with growth of larger ZnO NWs, in which sample with 15min ZnO NWs looks grey (see "E" in Figure 4.5a). The color change of nanobroom samples can be seen more clearly in Figure 4.5b. Note that the optical images were taken in an angle less than 90 degree compared to the surface of samples so that the

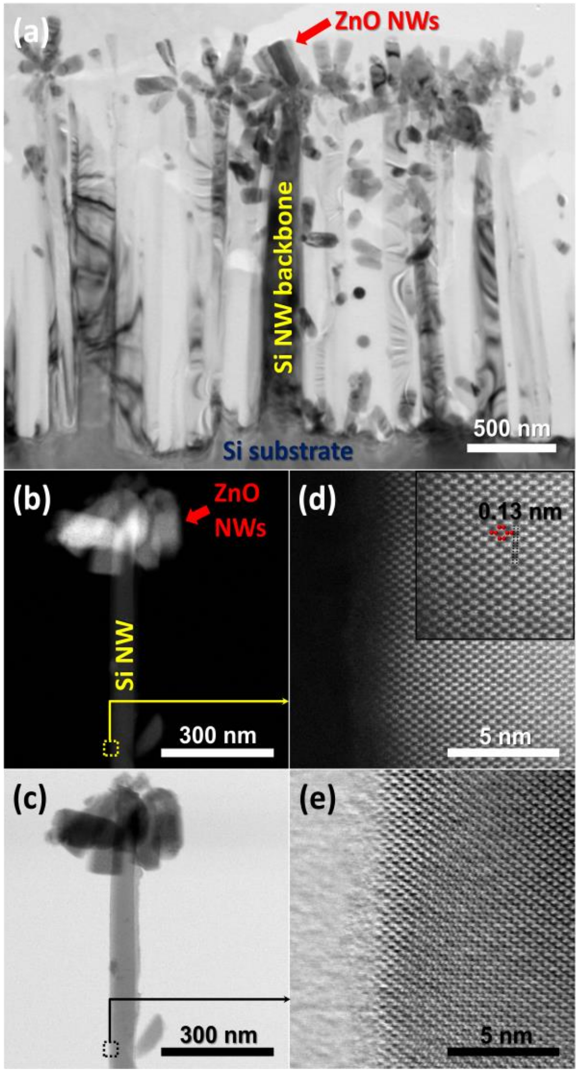

Figure 4.3. (a) Low-magnification bright field TEM image of ZnO/Si nanobroom arrays on Si substrate with 10min Si NW backbones and 10min ZnO NW stalls. Low-magnification dark field STEM image (b) and bright field STEM image (c) of a single ZnO/Si nanobroom. (d, e) High-resolution annular STEM images of labeled parts in (b) and (c), respectively. (d) Inset shows the magnified STEM image with lattice spacing of corresponding Si NW, where red circle shows the diamond structure of Si.

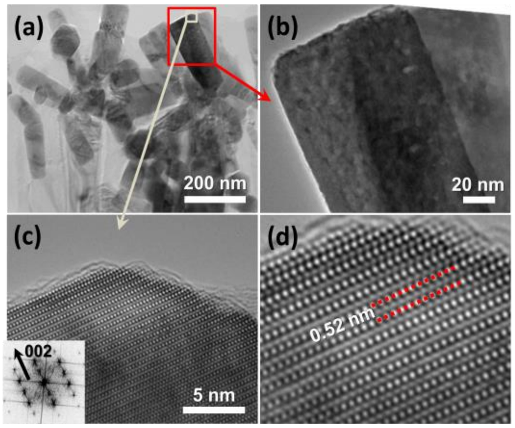

Figure 4.4. (a) Low-magnification bright field TEM image of the top of the nanobrooms with 10min Si NW backbones and 10min ZnO NW stalls. (b) Zoom-in TEM image of a single ZnO NW. (c) High-resolution image of labeled part of a ZnO NW tip and the corresponding FFT pattern indicating a ZnO NW growth direction of 002 orientation. (d) Corresponding noise-filtered TEM image of (c) with higher magnification showing the ZnO lattice spacing.

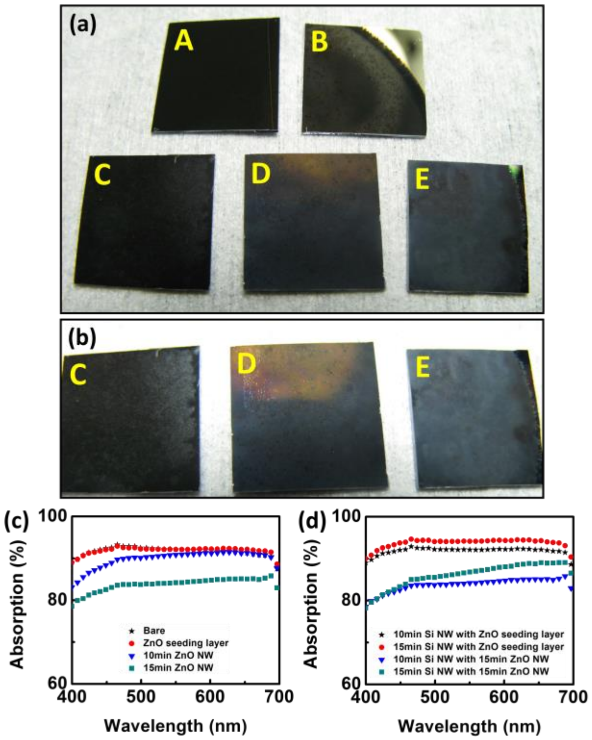

Figure 4.5. (a) Optical image of n-Si NW arrays (etched for 10min) and with ZnO coating or ZnO NWs; A: bare Si NW array, B: with ZnO seeding layer coating, C: with 5min ZnO NW, D: with 10min ZnO NW, E: with 15min ZnO NW. (b) optical image of samples C, D, E with a slightly different view angle. Absorption spectra of (c) Si NW backbones (etched for 10min) and coated with ZnO seeding layer or NW stalls and (d) ZnO-seeding-layer coated n-Si NWs and nanobrooms with different Si NW etching times.

difference in samples color can be seen (the view angle of Fig. 5a and b is slightlydifferent). Obviously, this color change is due to the alteration of optical absorption, as shown in Figure 4.5c. The Si NW array shows the highest absorption (though there is only a very small difference from that of the ZnO-seeding-layer coated Si NW array) and the absorption decreases with bigger ZnO NWs. The enhanced absorption of the vertical Si NW array is due to its excellent antireflection and light trapping effect properties.[17-19] Longer Si NWs lead to greater absorption due to improved light trapping,[20] as shown in Figure 4.5d. The reduced absorption for samples with ZnO NW stalls can be due to increased scattering from ZnO NWs at the tip of Si NWs and the change in the refractive index gradient along the Si NWs due to ZnO coating.

The PEC performance of the nanobroom photoanodes in neutral solution (pH = 7.25 at room temperature) are shown in Figure 4.6. The current density versus the externally applied potential for different Si NW etching times is presented in Figure 4.6a. The photoanodic current increases with increasing Si NW length due to enhanced surface area for redox reaction and improved light absorption (see Figure 4.5). The photoanodic current is comparable with that of TiO_2-coated n-Si NW arrays considering the same length for n-Si NW arrays.[5] The effect of ZnO NW growth time on current is illustrated in Figure 4.6b. Smaller ZnO NWs result in higher photoanodic current, which is probably due to better light absorption (see Figure 4.5). Also, the smaller ZnO NWs in nanobrooms may lead to more efficient charge separation and collection due to close proximity between photo-generated holes in ZnO and the ZnO-electrolyte interface.[21] The n-Si NW array coated with ZnO seeding layer (i.e., zero ZnO NW growth time) shows a lower photoanodic current compared to ZnO/Si nanobroom heterostructures, agrees well with reported 3D branched NW photoelectrodes in which bare or ZnO-coated

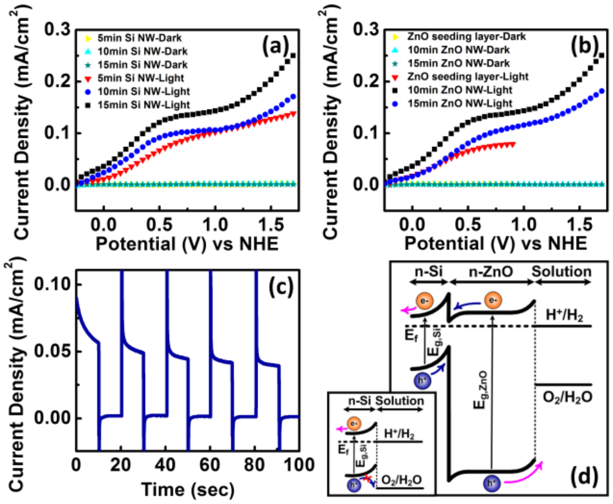

Figure 4.6. PEC performance and the working principle of the nanobroom photoelectrodes. Current density versus applied potential for the ZnO/Si nanobroom photoelectrodes in neutral solution (pH = 7.25); (a) 10min grown ZnO NWs on n-Si NWs with different lengths (etching times) and (b) ZnO NW stalls with different growth times on 15min etched n-Si NW backbones. “Light” and “Dark” indicate the current density under illumination and at dark, respectively. Scan rates were 5 mV/s and the scans direction was from reversed to forward biases (from -0.25 V to 1.72 V versus NHE). (c) Transient current density under chopped illumination for the nanobrooms with 15min n-Si NW backbones and 15min ZnO NWs at biasing potential of 1.236 V versus NHE. (d) Proposed (approximate) energy band diagram of n-ZnO/n-Si NW heterojunction in contact with electrolyte under thermal equilibrium and illuminated with solar light having both UV and visible lights. The inset in (d) shows the approximate band diagram of n-Si NW in contact with solution at equilibrium and under the solar illumination.

Si NW arrays show lower photocurrent than the branched NWs.[8-10] This can be due mainly to the increased surface area of ZnO/Si nanobrooms than that of the ZnO-seeding-layer coated Si NWs. Note that the dark currents are very small for all the tested samples. The transient current density under chopped illumination for the nanobrooms with 15min Si NW backbones and 15min ZnO NW stalls at biasing potential of 1.236 V versus NHE is shown in Figure 4.6c. As shown, there is a good switching behavior under switching on/off the light source. There are current overshoots (spikes) in the beginning of switching on/off, which can be attributed to accumulation of photo-generated carriers at the interface between NWs and the electrolyte, and the following recombination until reaching a stationary current. Note also that the photoanodic current gradually decreases over time, which will be discussed in detail in the next discussion.

Figure 4.6d shows the band diagram of the ZnO/Si nanobroom heterostructure at the tips. The photo-generated electrons in the conduction band of ZnO recombine with the photo-generated holes in the valence band of n-Si at the n-Si/n-ZnO NW heterojunction, while the photo-generated holes in the ZnO travel to the ZnO NW surface, oxidize water and generate oxygen. Therefore, the band alignment and bending result in improved photoanodic behavior. Similar band alignment and explanation have been reported for the n-Si/n-TiO_2 core/shell nanowire heterostructure photoanodes.[5] Another key issue is the effect of the ZnO NW coverage on the Si NWs. Although the ZnO NWs do not cover the entire Si NW backbones, there is still an effective junction between Si and ZnO NWs at the tip of Si NWs (discussed above), and thus effective charge separation and enhanced photoactivity, similar to the reported flower-like CuO/ZnO NW heterostructures where CuO NWs grown only at the tip of ZnO NWs.[22] The photocurrent of n-ZnO/n-Si nanobrooms is higher than the bare n-Si NW arrays due to the increased surface area and effective Si-ZnO junction discussed above. In fact, the bare n-Si NW photoanode cannot provide much photocurrent due to the barrier for photo-generated holes to transfer to the electrolyte for water oxidation (inset of Figure 4.6d). By applying a positive bias and increasing it, this barrier gradually reduces resulting in a small saturating photocurrent at high biases. If the ZnO/Si nanobroom array is exposed to only visible light, the photo-generated carriers in Si NWs cannot lead to a significant current because the holes face a big barrier to transfer to the ZnO valence band and they eventually recombine with the photo-generated electrons. When the ZnO/Si nanobrooms are illuminated with solar light having both UV and visible lights (see Figure 4.6d), there are photo-generated carriers in both Si and ZnO. Note that, in this case, Si can absorb both UV and visible lights. The effective Si-ZnO junction (discussed above) assists that generated carriers in both Si and ZnO can more contribute to the current resulting in an improved photoanodic current than the bare n-Si NWs. In fact, in this case, ZnO assists that photo-generated carriers in silicon can more contribute to the current (compared to the case with the bare n-Si NWs) revealing the significance of ZnO NWs in the improved PEC performance. Also comparing with the case with only visible light illumination, in this case ZnO NWs assist that photo-generated carriers in silicon contribute to current while they cannot contribute to a significant current under only visible light.

The ZnO/Si nanobrooms are not stable over a long time and their photoanodic current decreases after a short time of a couple of minutes due to Si and ZnO instability in the electrolyte under light illumination and biasing condition. Therefore, the surface of nanobrooms is required to coat with a dissolution/corrosion-resistant layer in order to achieve long-term stability. TiO_2 has been extensively applied as protection layer for the surface of different semiconductor photoelectrodes due to its high resistance to corrosion/dissolution.[23, 24] Thus, to completely cover the surface of nanobrooms here, a thin TiO_2 layer (10 nm) was deposited on them by atomic layer deposition (ALD). The ALD is a gas phase deposition method and can deposit very conformal and ultrathin layers on complicated nanostructures such as nanobrooms here. The 10 nm TiO_2

protection layer covers all surfaces of nanobrooms even the bottom of Si NW backbones. Figures 4.7a-7c show the stability performance of bare nanobrooms in neutral solution (pH = 7.25). The nanobrooms in Figure 4.7 are from 5min n-Si NW backbones with 5min ZnO NWs. As shown, the current under light illumination (light current) significantly decreases after a very short time (the light current of 0.14 mA/cm^2 drops quickly), which is mainly due to the ZnO dissolution. The comparison between SEM images for before and after PEC and stability tests clearly demonstrates the ZnO decomposition as there is not any ZnO NW and we can only see the Si NWs. The low-magnification cross-sectional SEM image in the inset of Figure 4.7c shows that the Si NWs did not fall off and even their length is the same as that for before PEC and stability tests. The surface of the Si NWs may also face some small changes such as very little oxidation or corrosion, which was hard to realize by the SEM imaging investigation. The stability test on the bare n-Si NW array also showed that the shape and morphology of n-Si NWs remained unchanged after the PEC and stability tests though there was photocurrent degradation overtime. Note that the current density versus potential measurements of nanobrooms cannot significantly affect by this lack of long-term stability because for the long-term stability test, the electrode faces intense fixed conditions (high biasing potential and current), while for the current density measurements, the biasing potential and current gradually change from low to high. Therefore, it is reasonable that the current density versus potential does not affect considerably. We have shown this for the n-ZnO/p-Si branched NW photocathodes, in which different current scans provide similar currents while the photocurrent under fixed high bias reduce after a short time of a couple of

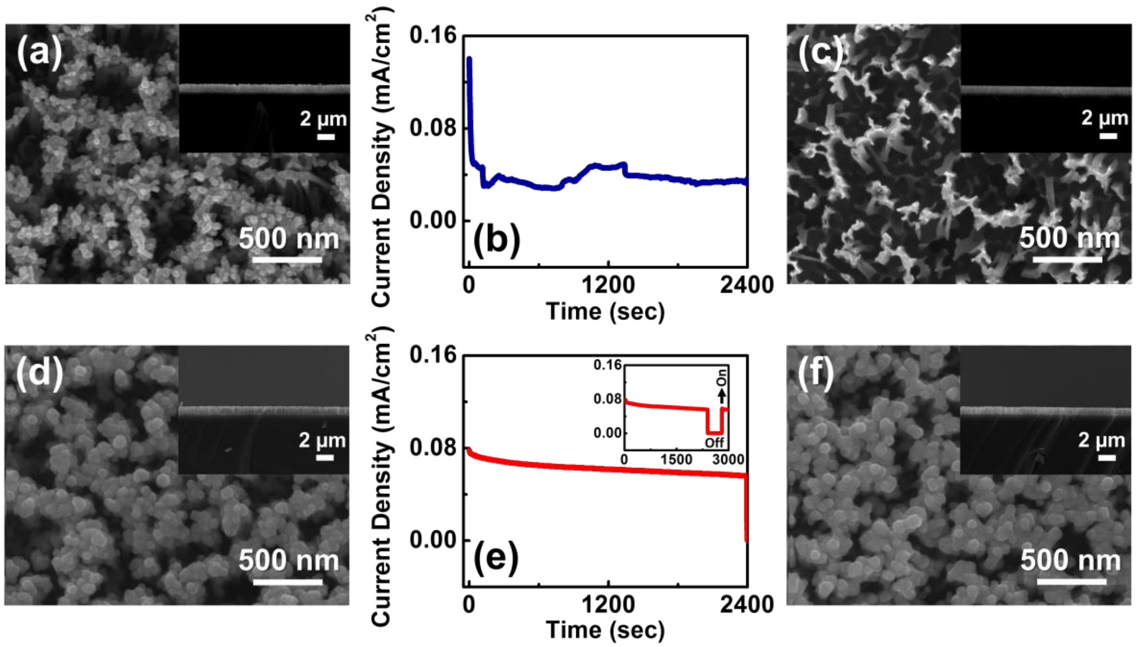

Figure 4.7. Stability performance of bare and TiO_2-coated nanobrooms (5min n-Si NW backbones with 5min ZnO NWs) in neutral solution (pH = 7.25). (a)-(c) Bare nanobroom electrode; (a) SEM images of sample before any PEC and stability tests (as-grown sample), (b) anodic current density under constant light illumination versus time, (c) SEM images of sample after PEC tests and long-term stability test shown in (b). (d)-(f) TiO_2-coated nanobroom sample; (d) SEM images of as-grown sample, (e) current density under fixed light illumination, (f) SEM images after PEC tests and long-term stability test in (e). The inset in (e) shows the stability test for longer time with one switching off/on the light illumination. The thickness of TiO_2 was 10 nm. The insets in SEM images show the low-magnification cross-sectional images of corresponding samples in (a), (c), (d) and (f). The biasing potential was 1.236 V versus NHE for (b) and (e).

minutes.[9] The stability performance of the TiO_2-coated nanobrooms in neutral solution is shown in Figures 4.7d-7f. The light current of ~0.08 mA/cm^2 does not significantly change after long time. The current density at dark is constant over time as can be seen during the light off in the inset of Figure 4.7e. Thus, there is a little reduction in photoanodic current (light current – dark current) over long time, which may be due to the charges trap in the TiO_2 layer or at the interface.[25] After switching off/on the light illumination during the stability test and after a long time (see the inset of Figure 4.7e), the light current comes back to its original level before switching off, revealing the photoactivity of the nanobroom electrode after a long time stability test. Note that this was not the case for the bare nanobrooms as they lost their photoactivity after a short time. Interestingly, the shape and morphology of nanobrooms remain unchanged after the PEC and long stability tests revealing that the TiO_2 coating layer well protects the surface of Si and ZnO NWs in which there is not any NW dissolution.

To enhance the oxygen evolution reaction (OER) at the surface of TiO_2-coated ZnO/Si nanobrooms, a metal catalyst can be used because there is OER kinetic limitation on the surface of bare semiconductors, especially TiO_2.[2] There are different metal OER catalysts such as Ru, Ir, and Pt. One of the most efficient catalysts is Ru.[24, 26] The effect of Ru (~5 nm) OER catalyst on the PEC performance of TiO_2-coated ZnO/Si nanobrooms (5min n-Si NW backbones with 5min ZnO NWs) in neutral solution is shown in Figure 4.8. The Ru catalyst greatly increases the photoanodic current and also significantly reduces the anodic turn-on potential. The photoanodic current density (light current density – dark current density) of Ru/TiO_2-coated nanobroom array is 6.27 mA/cm^2 at biasing potential of 1.236 V versus NHE, while it is only 0.08 mA/cm^2 for the TiO_2-coated nanobroom demonstrating the significance of using OER catalyst for efficient solar water splitting. The Ru catalyst also significantly improved the photocurrent of bare n-Si NWs but with smaller photocurrent improvement than nanobrooms. Note that the thickness of TiO_2 for the Ru/TiO_2-coated nanobroom sample was a little less than 10 nm, however this thinner TiO_2 layer did not significantly increase

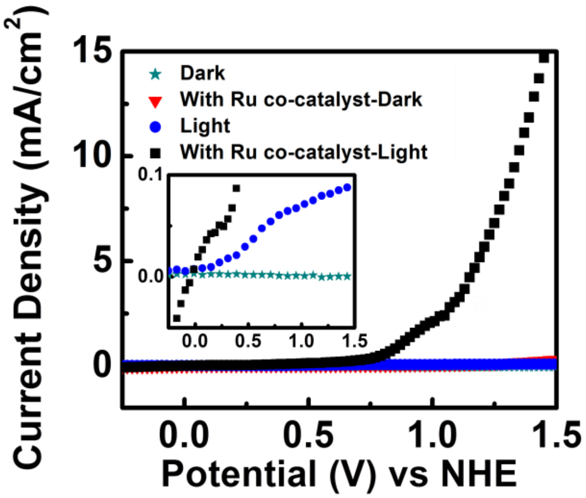

Figure 4.8. Current density versus applied potential of TiO_2-coated nanobrooms (5min n-Si NW backbones with 5min ZnO NWs) with and without Ru co-catalyst in neutral solution (pH = 7.25). "Light" and "Dark" indicate the current density under illumination and at dark, respectively. The inset is the zoomed curves to show the level of current densities for the TiO_2-coated nanobroom array in comparison to the light current of TiO_2-coated nanobrooms with Ru co-catalyst. Scan rates were 5 mV/s and the scans direction was from reversed to forward biases (from -0.25 V to 1.5 V versus NHE).

the sample photocurrent before Ru co-catalyst deposition in comparison with the photocurrent of the TiO_2-coated nanobrooms with 10 nm TiO_2 (blue curve in the inset of Figure 4.8) (in fact, the photocurrent increase was almost negligible). An efficient and cheap metal oxide OER catalyst such as NiO[27] can be used instead of metal OER catalyst in order to reduce the cost of photoelectrode.

4.4 Conclusions

In summary, we reported the fabrication of 3D ZnO/Si nanobroom heterostructures using low-cost solution processing method and their application as PEC photoanodes for solar energy harvesting and solar fuel conversion. The morphology and atomic structure of the nanobrooms were characterized using high resolution SEM, TEM, and STEM. The nanobrooms consist of defect-free and single-crystalline Si nanowire backbones and ZnO nanowire stalls with smooth surfaces. The PEC performance of the nanobroom photoelectrodes with different Si and ZnO nanowire dimensions were studied and longer Si NW backbones and smaller ZnO NW stalls led to better light absorption and larger photoanodic current. The ZnO/Si nanobroom electrodes showed much higher photoanodic current than the bare Si NW arrays. Long-term electrode stability was achieved using a thin TiO_2 passivation layer protecting the NWs against decomposition. Large improvement in the photoanodic current and considerable reduction in the anodic turn-on potential were obtained by using Ru OER catalyst. These results show the promise of the use of 3D NW photoelectrodes from earth abundant materials by low-cost and simple fabrication methods for clean solar energy harvesting and conversion.

Chapter 4 was published in *Physics Status Solidi A* 2013, A. Kargar, K. Sun, S. J. Kim, D. Lu, Y. Jing, Z. Liu, X. Pan and D. Wang, "Three-dimensional ZnO/Si broom-like nanowire heterostructures as photoelectrochemical anodes for solar energy conversion". The dissertation author was the first author of this paper.

References

1. Gratzel, M. *Nature* **2001**, *414*, 338-344.

2. Walter, M. G.; Warren, E. L.; McKone, J. R.; Boettcher, S. W.; Mi, Q.; Santori, E. A.; Lewis, N. S. *Chemical Reviews* **2010**, *110*, 6446-6473.

3. Lewis, N. S.; Nocera, D. G. *Proceedings of the National Academy of Sciences* **2006**, *103*, 15729-15735.

4. Gray, H. B. *Nat Chem* **2009**, *1*, 7-7.

5. Hwang, Y. J.; Boukai, A.; Yang, P. *Nano Letters* **2009**, *9*, 410-415.

6. Tak, Y.; Hong, S. J.; Lee, J. S.; Yong, K. *Journal of Materials Chemistry* **2009**, *19*, 5945-5951.

7. Su, J.; Guo, L.; Bao, N.; Grimes, C. A. *Nano Letters* **2011**, *11*, 1928-1933.

8. Sun, K.; Jing, Y.; Li, C.; Zhang, X.; Aguinaldo, R.; Kargar, A.; Madsen, K.; Banu, K.; Zhou, Y.; Bando, Y.; Liu, Z.; Wang, D. *Nanoscale* **2012**, *4*, 1515-1521.

9. Kargar, A.; Sun, K.; Jing, Y.; Choi, C.; Jeong, H.; Jung, G. Y.; Jin, S.; Wang, D. *ACS Nano* **2013**, *7*, 9407-9415.

10. Kargar, A.; Sun, K.; Jing, Y.; Choi, C.; Jeong, H.; Zhou, Y.; Madsen, K.; Naughton, P.; Jin, S.; Jung, G. Y.; Wang, D. *Nano Lett.* **2013**, *13*, 3017-3022.

11. Peng, K. Q.; Yan, Y. J.; Gao, S. P.; Zhu, J. *Advanced Materials* **2002**, *14*, 1164-1167.

12. Sun, K.; Jing, Y.; Park, N.; Li, C.; Bando, Y.; Wang, D. *Journal of the American Chemical Society* **2010**, *132*, 15465-15467.

13. Law, M.; Greene, L. E.; Johnson, J. C.; Saykally, R.; Yang, P. *Nat Mater* **2005**, *4*, 455-459.

14. Greene, L. E.; Law, M.; Goldberger, J.; Kim, F.; Johnson, J. C.; Zhang, Y.; Saykally, R. J.; Yang, P. *Angewandte Chemie International Edition* **2003**, *42*, 3031-3034.

15. Zainelabdin, A.; Amin, G.; Zaman, S.; Nur, O.; Lu, J.; Hultman, L.; Willander, M. *J. Mater. Chem.* **2012**, *22*, 11583.

16. Jung, S. K.; Jeon, S.; Yong, K. *Nanotechnology* **2011**, *22*, 015606.

17. Sun, K.; Kargar, A.; Park, N.; Madsen, K. N.; Naughton, P. W.; Bright, T.; Jing, Y.; Wang, D. *Selected Topics in Quantum Electronics, IEEE Journal of* **2011**, 1-17.

18. Zhang, A.; You, S.; Soci, C.; Liu, Y.; Wang, D.; Lo, Y.-H. *Applied Physics Letters* **2008**, *93*, 121110.

19. Soci, C.; Zhang, A.; Bao, X.-Y.; Kim, H.; Lo, Y.; Wang, D. *Journal of Nanoscience and Nanotechnology* **2010**, *10*, 1430-1449.

20. Garnett, E.; Yang, P. *Nano Letters* **2010**, *10*, 1082-1087.

21. Cho, I. S.; Chen, Z.; Forman, A. J.; Kim, D. R.; Rao, P. M.; Jaramillo, T. F.; Zheng, X. *Nano Letters* **2011**, *11*, 4978-4984.

22. Jung, S.; Yong, K. *Chemical Communications* **2011**, *47*, 2643-2645.

23. Paracchino, A.; Laporte, V.; Sivula, K.; Grätzel, M.; Thimsen, E. *Nat Mater* **2011**, *10*, 456-461.

24. Chen, Y. W.; Prange, J. D.; Dühnen, S.; Park, Y.; Gunji, M.; Chidsey, C. E. D.; McIntyre, P. C. *Nature materials* **2011**, *10*, 539-544.

25. Paracchino, A.; Mathews, N.; Hisatomi, T.; Stefik, M.; Tilley, S. D.; Gratzel, M. *Energy & Environmental Science* **2012**, *5*, 8673-8681.

26. Reier, T.; Oezaslan, M.; Strasser, P. *ACS Catalysis* **2012**, *2*, 1765-1772.

27. Sun, K.; Park, N.; Sun, Z.; Zhou, J.; Wang, J.; Pang, X.; Shen, S.; Noh, S. Y.; Jing, Y.; Jin, S.; Yu, P. K. L.; Wang, D. *Energy & Environmental Science* **2012**, *5*, 7872-7877

5. P-SI/SNO$_2$/FE$_2$O$_3$ CORE/SHELL/SHELL NANOWIRE PHOTOCATHODES FOR NEUTRAL PH WATER SPLITTING

5.1 Introduction

Silicon is the most widely used semiconductor for solar cells[1-4] and has also shown promising performances in photoelectrochemical (PEC) cells for hydrogen production.[5-10] Silicon photoelectrodes with nano/micro structures such as nano/micro wire array[9, 11] and black silicon[7] have exhibited improved PEC performances. Silicon nanowire (NW) arrays, in particular, are of considerable interest due to their distinctive properties, facile and scalable techniques for their fabrication, etc.[11-19] On the other hand, there are two key factors limiting the application of silicon photoelectrodes for practical solar hydrogen generation including their large external biasing potential (high overpotential) required to drive hydrogen or oxygen evolution reaction (HER or OER) and their instability in the electrolyte. Tremendous efforts have been expended to overcome these limiting factors such as using metal catalysts (noble[20, 21] or non-noble[22-24]) to reduce the turn-on (or onset) potential and by coating the electrodes surface with a corrosion-resistant layer such as TiO_2[25-27] for stability improvement. A thin TiO_2 coating layer can significantly enhance the stability,[27] however due to its poor conductivity, a metal co-catalyst needs to be deposited on its surface to boost the HER or OER.[25, 26]

Therefore, a more functional metal oxide coating layer, which can simultaneously enhance the PEC performance and HER/OER kinetics, and electrode stability, is desirable. Recent studies have demonstrated that chemical-vapor and atomic-layer deposited Fe_2O_3,[17, 28] atomic layer-deposited MnO,[29] and sputtered $NiRuO_x$,[30] thin layers can considerably improve the photoanodic performance and OER kinetics of n-Si photoanodes, while also enhancing the n-Si stability. On the other hand, less attention has been paid to the application of a functional metal oxide layer on the p-Si photocathodes to concurrently enhance the photocathodic performance and HER kinetics, and p-Si stability. There are reports for coating of p-Si photocathodes with different metal oxides such as SnO_2,[31] TiO_2,[32] ITO,[33] WO_3,[34] FeO_x,[35] etc, however none of them are efficient in both enhanced performance and stability. The metal oxide coating layer can also be in the form of a nanostructure increasing the reaction surface area. We have recently shown that growing ZnO NWs on the p-Si NW cores enhances the photocathodic performance, however they cannot stabilize the p-Si NWs for a long time.[36] Moreover, to facilitate the overall spontaneous solar water splitting, a low photocathodic onset potential is required.

Fe_2O_3 (α phase: hematite), an n-type semiconductor with a band gap of ~2.1 eV absorbing the visible light, is chemically stable in an aqueous medium, is made from abundant and low-cost elements, and environmentally friendly.[37-39] Moreover, the hematite nanostructures can be synthesized in large scales using facile and cost-effective methods such as hydrothermal growth technique.[40-42] These properties make hematite of particular interest to couple with the p-Si NW photocathodes. On the other hand, hematite suffers from several drawbacks[37, 43] including short hole diffusion length (2-4 nm),[44] short light penetration length,[45] short excited-state carrier lifetime,[46] poor gas evolution reaction kinetics,[37] low carrier mobility[47, 48] (both electron and hole mobilities are low but electron mobility is higher than hole mobility[49]), and surface trapping states.[50] Consequently, the PEC performance of hematite is morphology dependent.[37, 51]

Herein, to improve the photocathodic performance and HER kinetics of p-Si NWs and simultaneously to enhance the p-Si stability, we grew dense Fe_2O_3 nanocrystals (NCs) (forming a shell) on the patterned and dry-etched 3D p-Si NW arrays pre-coated with a thin SnO_2 seeding layer (this structure is called "p-Si/n-SnO_2/n-Fe_2O_3 core/shell/shell nanowires (css-NWs)") using an easily scalable hydrothermal synthesis method. The morphology and atomic structure of the css-NWs are studied in detail. The css-NWs' PEC performances including photocurrent and PEC stability are investigated and presented. Moreover, the effects of Si NW length and electrolyte pH on the PEC performance are evaluated.

5.2 Experimental Section

Fabrication of Si/SnO_2/Fe_2O_3 css-NW electrodes

The boron doped Si(100) and Si(111) substrates with resistivities of 1-20 Ωcm (p-type) were patterned into 3D configurations with an array of Ni disk masks prepared using nanoimprint lithography and e-beam evaporation.[26] The Reactive Ion Etching-Inductively Coupled Plasma (RIE-ICP) dry etching was used to make vertical Si NW arrays for different diameters and lengths by etching for various times with Ni disks serving as the etch mask. The average Si(100) etching rate was ~0.24 μm/min. Note that for p-Si(111) samples, the newly used mold for nanoimprinting had a little larger diameter so the etching rate was ~0.27 μm/min for these samples. The pitch size (center-to-center spacing) of Si NW array was 1 μm for both Si(100) and Si(111) samples. After the RIE-ICP etching, the Si NW substrates were dipped into Ni etchant for 5 mins to etch/remove the Ni disks at the head of Si NWs. The Si NW substrates were then cleaned with RCA cleaning to remove the contamination from the RIE-ICP etching. Afterwards, the Si NW samples were immediately transferred to the sputtering machine to deposit a thin SnO_2 layer, as seeding layer for the Fe_2O_3 NCs shell growth, using RF magnetron sputtering with 99.99% SnO_2 target and argon gas at room temperature. The RF power was 400 W during the sputtering deposition. SnO_2 is physisorbed on the Si surface in the Si NW samples by mechanisms of hydroxyl group bonding and van der Waals force. Hydroxyl comes from the RCA cleaning and even humidity or water. The SnO_2 layer uniformly covered the Si NWs due to substrate rotation during the sputtering deposition. The uniform SnO_2 deposition is evident with uniform growth of the Fe_2O_3 NCs on the Si NWs as well as on the flat surface between the Si NWs due to the fact that without the SnO_2 seeding layer, there is no Fe_2O_3 growth, which we tested it. The actual thickness of sputtered SnO_2 seeding layer on the 10m-Si NWs was ~28 nm according to the high-magnification SEM images. Finally, the Fe_2O_3 NCs were grown on the SnO_2-coated Si NW cores using hydrothermal growth method.[40, 42] First, akaganeite (β-FeOOH) NCs were grown on the SnO_2-coated Si NW trunks as follows. The SnO_2-coated Si NW substrate was put in a 45 mL sealed Teflon autoclave containing a 30 mL aqueous solution consisting of 0.15 M $FeCl_3.6H_2O$ (Iron(III) chloride hexahydrate) (Sigma-Aldrich, ≥99%) and 1 M $NaNO_3$ (Sodium nitrate) (Sigma-Aldrich, ≥99.0%). The deionized (DI) water resistivity and pH of growth solution were 17.6-17.7 MΩ-cm and ~1.44, respectively. The hydrothermal reaction was performed at a temperature of ~107°C, putting the autoclave in a regular oven, for the desirable growth time. The as-prepared sample was then rinsed carefully with DI water to remove the residues and dried with N_2 flow. After the FeOOH NC growth, the color of Si NW substrate turned into yellowish indicating the FeOOH growth. Finally, the as-grown Si/SnO_2/FeOOH css-NW substrates were annealed at 450°C under air (in an open furnace) for 2 hrs to have phase transition from the β-FeOOH to α-Fe_2O_3. The yellowish color of substrate turned into reddish color showing the transformation of β-FeOOH into α-Fe_2O_3.

Structural characterization

A Philips XL30 field-emission environmental scanning electron microscope (ESEM) working at an accelerating voltage of 10.0 kV was used for examining the samples morphologies. A high resolution transmission electron microscopy (HRTEM, JEOL JEM3100F) operated at 300 kV was used for the atomic-scale structural analyses. Spherical aberration-corrected scanning transmission electron microscopy (Cs-corr. STEM, JEOL JEM2100F) operated at 200 kV was also employed for further studies and to identify the actual atomic configuration of NWs. High resolution energy dispersive X-ray spectroscopy (EDS, EDAX) was performed to obtain the elemental information on individual layers within the css-NW.

Photoelectrochemical (PEC) measurements

To perform the PEC tests, the samples were bonded to Cu wire at the back using indium, which provides an ohmic contact. The edges and backside of samples were sealed using epoxy. Current density (*J*-*V* and *J*-*t*) measurements were carried out in a 400 mL aqueous solution of 0.25 M Na_2SO_4 buffered at pH = 7.25 with Phosphate Buffered Saline (PBS, Sigma) (DI water resistivity, 17.6-17.7 MΩ-cm) (neutral solution) with a three-electrode configuration, including sample as working electrode (WE), Pt mesh as counter electrode (CE), and Ag/AgCl (1 M KCl) as reference electrode (RE). For the J-V measurements in an electrolyte with a pH of 13.5, a 400 mL aqueous solution of 1 M NaOH was used. A light power intensity of 100 mW/cm^2 was adjusted at the samples position provided by a solar simulator (Newport 67015) using a 150 W Xenon lamp and equipped with a 1.5 AM filter. The current density measurements were collected using a potentiostat (Digi-Ivy Inc). A scan rate of 10 mV/s was employed for the linear sweep voltammetry (LSV) (J-V measurements). Photocurrent stability tests were carried out by collecting the electrodes current under a fixed illumination of 100 mW/cm^2 and at a biasing potential of -0.33 V versus reversible hydrogen electrode (RHE). During the current density measurements, a mild agitation was employed and the electrolyte was constantly purged with a small flow of N_2 gas. The biasing potentials versus Ag/AgCl RE ($E_{\mathrm{Ag/AgCl}}$) were converted to the potentials versus reversible hydrogen electrode (RHE), E_{RHE}, using the Nernst equation;

$$E_{\mathrm{RHE}} = E_{\mathrm{Ag/AgCl}} + 0.059\ \mathrm{pH} + E^{0}_{\mathrm{Ag/AgCl}} \quad (\mathrm{V}) \tag{1}$$

where pH is the electrolyte pH (7.25 or 13.5 here) and $E^{0}_{\mathrm{Ag/AgCl}}$= 0.236 V for the Ag/AgCl RE in 1 M KCl and at 25°C. The current densities here are calculated using geometric areas.

5.3 Results and Discussion

Figure 5.1a-1c show the top-view and cross-sectional scanning electron microscopy (SEM) images of bare p-Si NW array etched for 10 mins (denoted 10m-Si NW). The center-to-center spacing (pitch size) is 1 μm, the average Si etching rate is

~0.24 µm/min, and the diameters are ~330 nm and ~280 nm (see Figure 5.1c) for 5 mins and 10 mins etching times, respectively. Note that the p-Si NWs were made from the same nanoimprinting mold; thus, the difference in diameter after different etching times is due to the RIE-ICP etching process.[36] The p-Si NWs in this study were made from p-Si(100) and p-Si(111) wafers denoting with p-Si(100) and p-Si(111) NWs, respectively (see the Experimental Section for details). Note that unless otherwise stated, the p-Si orientation is (100). For convenience, p-Si/SnO_2/Fe_2O_3 css-NWs for Fe_2O_3 NCs grown for 2 hrs and different p-Si NW core etching times are denoted as "css(Xm-Si/SnO_2/2h-Fe_2O_3) NWs", in which "X" is the p-Si NW etching time in mins (m). The SEM images of css(5m-Si/SnO_2/2h-Fe_2O_3) NWs are shown in Figure 5.1d-1f. Formation of the Si/SnO_2/Fe_2O_3 css-NWs is within the whole area of samples (this was investigated for different parts on the samples), which can be realized and seen by the low-magnification

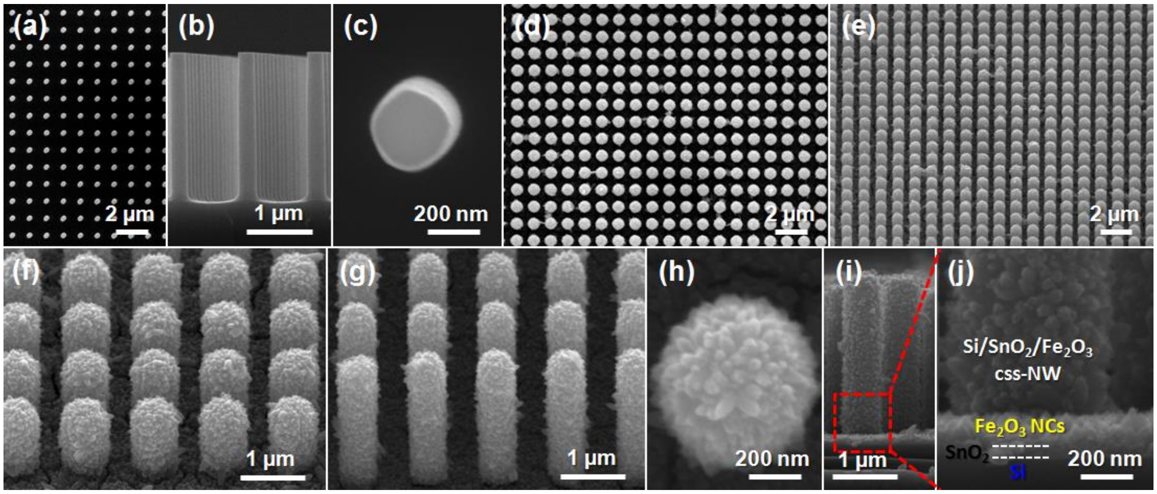

Figure 5.1. SEM images of Si/SnO_2/Fe_2O_3 css-NW arrays. (a-c) Top-view (low magnification), cross-sectional and top-view (high magnification) images of bare 10m-Si NW array. (d-f) Top-view and 45° view images (with two different magnifications) of css(5m-Si/SnO_2/2h-Fe_2O_3) NWs. (g-j) 45° view, top-view and cross-sectional images of css(10m-Si/SnO_2/2h-Fe_2O_3) NWs.

SEM images (Figure 5.1d and 5.1e). The Fe_2O_3 NCs cover the whole length of Si NW core surface as well as the spaces between Si NWs on the flat surface (see Figure 5.1f) due to uniform coverage of SnO_2 seeding layer (see Experimental Section for uniform coating). Figure 5.1g-1j exhibit the SEM images of the css(10m-Si/SnO_2/2h-Fe_2O_3) NWs revealing the similar observation of uniform growth of the Fe_2O_3 NCs on the entire length of Si NWs. The average diameter and length of Fe_2O_3 NCs on 10m-Si NW cores are ~37 nm and ~136 nm, respectively (see Figure 5.1h and 5.1j). Using the Fe_2O_3 NCs compared to the Fe_2O_3 NWs can assist to minimize/overcome some of the Fe_2O_3 limiting factors especially the short diffusion length issue, leading to increased photogenerated carrier

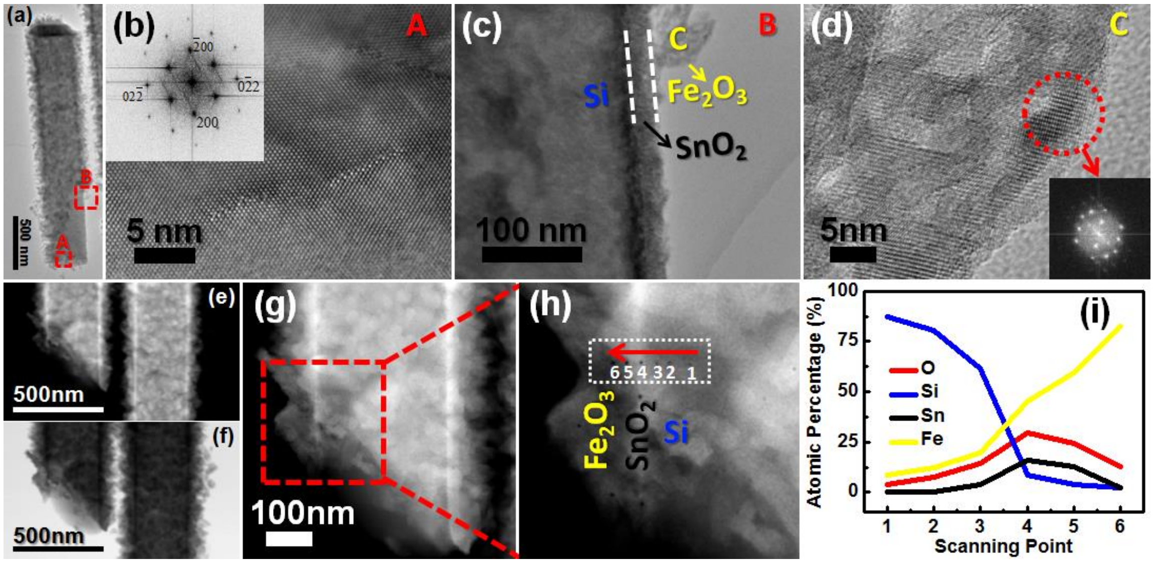
(a)
500 nm
A
B
(b)
A
200
022
022
200
5 nm
(c)
B
Si
C
Fe2O3
SnO2
100 nm
(d)
C
5nm
(e)
500nm
(f)
500nm
(g)
100nm
(h)
6 5 4 3 2 1
Fe2O3
SnO2
Si
(i)
Atomic Percentage (%)
100
75
50
25
0
O
Si
Sn
Fe
1
2
3
4
5
6
Scanning Point

Figure 5.2. (a) TEM image of a single css(20m-Si/SnO_2/2h-Fe_2O_3) NW broken from the substrate in its length. (b) HRTEM image of labeled area “A” in (a) exhibiting the crystal structure of Si NW core. Inset exhibits the calculated FFT pattern. (c) High-magnification TEM image of labeled area “B” in (a) showing the interfaces among Si, SnO_2, and Fe_2O_3. (d) HRTEM image of labeled Fe_2O_3 NC (“C”) in (c). Inset shows the calculated FFT pattern of selected area. Low-magnification annular (e) dark and (f) bright field STEM images of two broken single css(20m-Si/SnO_2/2h-Fe_2O_3) NWs. (g) High angle annular dark field STEM image of the left css-NW in (e). (h) Higher magnification high angle annular dark field STEM image of labeled area in (g). (i) EDS point scan taken along the interfaces of Si, SnO_2, and Fe_2O_3 (points indicated in (h)).

transport. The cross-sectional SEM images, shown in Figure 5.1i and 5.1j, exhibit different regions including Si substrate, thin SnO_2 seeding layer (thickness of ~28 nm), and Fe_2O_3 NCs (average length of ~136 nm). These interfaces on the surface of Si NW backbone will be further shown in the transmission electron microscopy (TEM) images.

TEM image of a single css(20m-Si/SnO_2/2h-Fe_2O_3) NW is shown in Figure 5.2a. Note that the single css-NW was broken from about the middle of its length as 20m-Si NW has a length of ~5 μm. The single crystalline Si NW core with growth along [200] orientation is demonstrated from the high-resolution TEM (HRTEM) image in Figure 5.2b with its calculated fast Fourier transform (FFT) pattern, in the inset, further confirms it. High-magnification TEM image (Figure 5.2c) clearly exhibits the interfaces among Si NW core, SnO_2 seeding layer, and Fe_2O_3 NC, which are sharp (also see Figure 5.2e-2h) without an amorphous layer revealing the clean interfaces. The HRTEM image shown in Figure 5.2d exhibits a polycrystalline nature for the Fe_2O_3 NC. The FFT pattern of the labelled part of HRTEM image shows the crystal structure of a single grain of Fe_2O_3 NC. The high angle annular dark field (HAADF) scanning transmission electron microscopy (STEM) image of a broken part of the single css(20m-Si/SnO_2/2h-Fe_2O_3) NW (Figure 5.2g) clearly shows the existence of thin SnO_2 layer, which is within the total length of Si NW core (see Figure 5.2e and 5.2f). Energy dispersive X-ray spectroscopy (EDS) point scan (Figure 5.2i) taken along the interfaces of Si, SnO_2, and Fe_2O_3 (points indicated in Figure 5.2h) further exhibits the sharp interfaces between Si, SnO_2, and Fe_2O_3. Note that the atomic percentage of oxygen is expected to be low because a light element like oxygen is hard to detect in a single NW of which the scanning volume is small. Also, it is difficult to scan through the cross section of a css-NW with individual layer-by-layer;

there is a scanning overlap between Fe_2O_3 NC and SnO_2 layer, resulting in higher atomic percentage of oxygen than that from a pure Fe_2O_3 region.

Figure 5.3a shows the current density under illumination in a neutral solution of 10m-Si NW cores with different coatings including bare Si NWs, SnO_2-seeding-layer-coated Si NWs (Si/SnO_2 cs-NWs), and Si/SnO_2/Fe_2O_3 css-NWs, in which all the samples show photocathodic behavior. The Si/SnO_2/Fe_2O_3 css-NWs present much higher photocathodic current and significant photocathodic turn-on potential shift toward more positive potentials than the bare Si NWs or Si/SnO_2 cs-NWs. The potential shift is ~719 mV compared to the bare Si NW array (Figure 5.3a inset). This is an interesting feature showing that we can significantly reduce the photocathodic turn-on potential of p-Si NW photocathodes in a neutral solution using Si/metal-oxides heterojunctions without using a metal nanoparticle catalyst coating on the p-Si NWs. The improved photocathodic performance is due to the increased reaction surface area (which comes from the

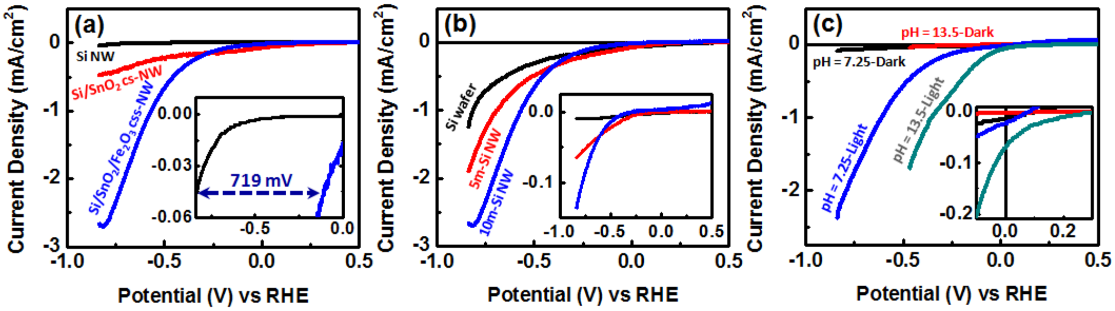

Figure 5.3. (a) Current density under illumination of 10m-Si NW cores with different coatings (black: bare NW, red: Si/SnO_2 cs-NW, blue: Si/SnO_2/Fe_2O_3 css-NW). Inset shows the corresponding zoom-in curves with calculated potential shift. (b) Current density under illumination of css(Si/SnO_2/2h-Fe_2O_3) NWs with different Si etching times. Inset shows the dark current of corresponding samples. (c) Current density at dark and under illumination of css(10m-Si/SnO_2/2h-Fe_2O_3) NWs measured in two different electrolytes with different pHs (0.25 M Na_2SO_4, pH = 7.25 and 1 M NaOH, pH = 13.5). Inset shows the zoom-in curves around 0 V versus RHE.

nanotextured shell), effective energy band alignment among p-Si, n-SnO_2 and n-Fe_2O_3, enhanced optical absorption due to combination of materials with different band gaps,[17, 52] and improved gas evolution coming from the Fe_2O_3 NCs. The effective band alignment at an electrolyte pH of 7.25 provides multiple junctions enhancing the charge separation within the css-NW. There may also be a catalyst effect from the Fe_2O_3 NCs shell contributing to the enhanced photocathodic current.[28] The Si/SnO_2 cs-NWs exhibit higher photocathodic current than the bare Si NWs due to the enhanced optical absorption and junction between p-Si and n-SnO_2 improving the charge separation.

The effect of Si NW etching time (Si NW length) on the photocathodic current of Si/SnO_2/Fe_2O_3 css-NWs is shown in Figure 5.3b (Si wafer is considered for zero etching time). Longer Si NW core in the NW samples results in higher photocathodic current mainly due to increased reaction surface area. The smaller diameter for longer NW backbone in the NW samples can also be an effective factor leading to lower recombination and consequently contributing to the improved photocathodic current. Note that for comparison of the NW samples with the bare Si wafer, the enhanced surface area may not be the dominant factor due to the pitch size of 1 μm. In fact, other factors coming from the advantages of vertical NW arrays (including enhanced light absorption, reduced charge recombination, improved carrier collection, and increased reaction rate) can contribute in the enhanced photocathodic performance. The dark current of corresponding samples is shown in the inset exhibiting the same trend as the photocathodic current. The Si NW array pitch size is another key factor, which can further increase the photocurrent and shift the photocathodic turn-on potential toward more positive potentials.[36] Using Si NWs with higher density and longer length, we can get higher photocurrent and a positive photocathodic turn-on (onset) potential, which we are working on that, to build a tandem PEC cell for overall solar water splitting in neutral pH water.

Another parameter affecting the PEC performance of the Si/SnO_2/Fe_2O_3 css-NWs is the type of measurement electrolyte and its pH (Figure 5.3c). The dark current in both neutral and basic electrolytes with pH = 7.25 and pH = 13.5, respectively, is almost the same and negligible, while the current under illumination at the basic electrolyte is much higher than that in the neutral solution. Furthermore, the basic electrolyte shifts the photocathodic turn-on potential compared to the performance in the neutral solution. However, note that for practical solar hydrogen production, a neutral medium can be more desirable as the natural water resources such as seawater are usually in a neutral condition and using a neutral solution prevents the use of strong acids and bases which can result in environmental and handling issues. As shown in Figure 5.3c inset, the Si/SnO_2/Fe_2O_3 css-NWs are photoactive at 0 V versus RHE in both neutral and basic electrolytes, which was confirmed by the current densities under chopped illumination. The photocurrent at 0 V versus RHE can be further enhanced by using Si NW cores with longer length and smaller pitch size as discussed above. The current densities under chopped illumination of css(5m-Si/SnO_2/2h-Fe_2O_3) and css(10m-Si/SnO_2/2h-Fe_2O_3) NWs in both neutral and basic electrolytes exhibit the same currents as that shown in Figure 5.3b and 5.3c, revealing that the high photoactivity of the css-NWs preserve under different scans. Measured incident photon-to-current efficiency (IPCE) of the css-NWs (data not shown here) exhibited a broadband absorption spectrum due to coupling of Si and Fe_2O_3 with ~1.11 eV and ~2.1 eV band gaps, respectively.

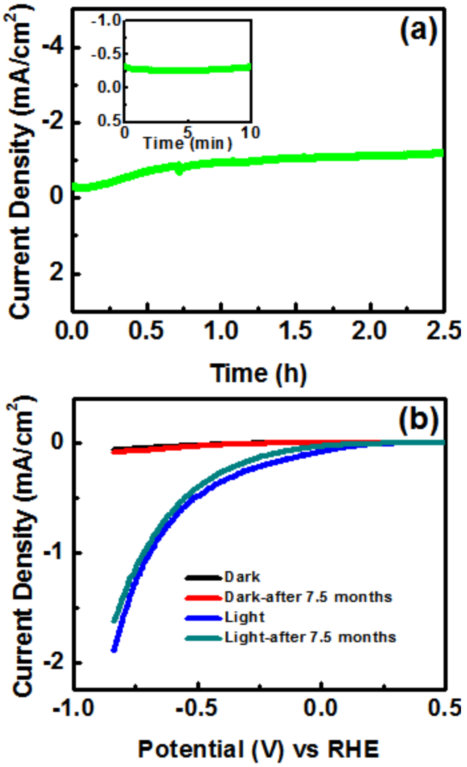

Figure 5.4. (a) Current density under constant light illumination versus time (stability performance) of css(8.5m-Si(111)/SnO_2/2h-Fe_2O_3) NWs in neutral electrolyte measured at -0.33 V versus RHE. Inset shows the enlarged first part (0-10 min) of the current density. (b) Current density at dark and under illumination of css(5m-Si/SnO_2/2h-Fe_2O_3) NWs measured in two different times (the sample was kept in vacuum and retested after 7.5 months).

Photocurrent stability tests were performed by collecting the samples current under a fixed illumination of 100 mW/cm^2 and at a biasing potential of -0.33 V versus RHE. Figure 5.4a shows the stability test of css(8.5m-Si(111)/SnO_2/2h-Fe_2O_3) NWs in the neutral electrolyte exhibiting a constant photocurrent. Note that the Si(111) NW cores were made from slightly larger diameter nanoimprinting substrates resulting in different etching rate compared to that of the Si(100) NWs (see the Experimental Section for more details), in which the 8.5m-Si(111) NWs have similar length to that of the 10m-Si(100)

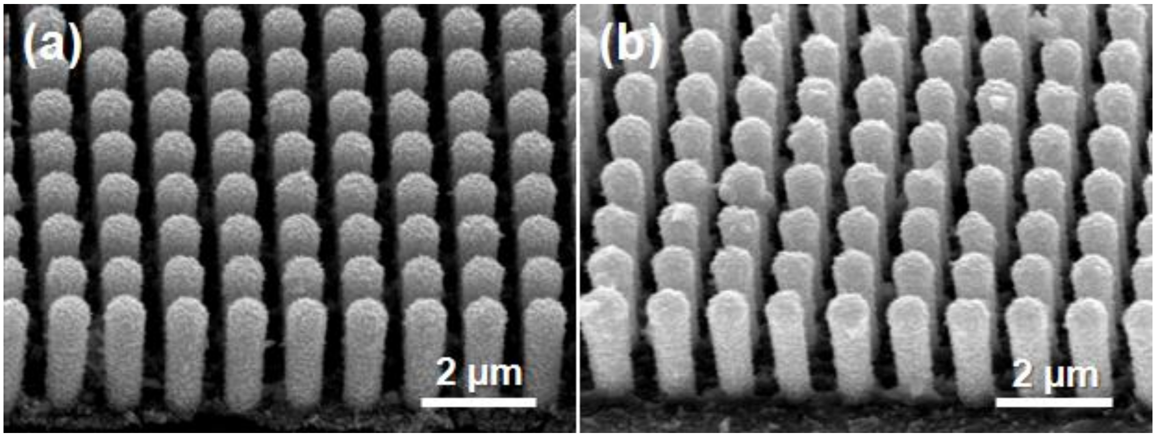

Figure 5.5. SEM images of css(8.5m-Si(111)/SnO_2/2h-Fe_2O_3) NW photoelectrode (a) before PEC and stability tests (as-fabricated sample), and (b) after PEC tests and a long stability test of over 6 hrs.

NWs (the pitch size is also the same). Note that the photocurrent first starts increasing until it reaches its plateau/saturation and after that, it remains constant, similar to that reported for the TiO_2/Ir-coated n-Si photoanodes[25] or TiO_2/Pt-coated ZnO/Si branched NW photocathodes.[26] The reason for the observed current increase initially and then reaching a plateau/saturation is not totally clear at this point and is under investigation. Note also that the beginning of stability test also exhibits a constant current as shown in Figure 5.4a inset. The comparison between SEM images of electrode before any PEC test (as-synthesized sample), and after PEC tests and a long photocurrent stability test of over 6 hrs (Figure 5.5) show that there is no significant morphological changes with preservation of all materials within the css-NWs. The photoelectrochemical stability test of the Si/SnO_2/Fe_2O_3 css-NWs with Si(100) NW shows that there is no saturation behavior and constant current like that shown in Figure 5.4a for the css-NWs with Si(111) NWs. In fact, the photocurrent continuously increases with a small slope indicating the gradual and slow decomposition of Fe_2O_3 NCs. These observations reveal that the stability performance of the Si/SnO_2/Fe_2O_3 css-NWs is dependent on the p-Si surface orientation in which the css-NWs with p-Si(111) present higher stability because the p-Si(111) surface is more stable than p-Si(100) surface in aqueous solutions.[53, 54] The investigation of Fe_2O_3 NCs grown on the SnO_2-coated p-Si wafers also showed that the photocathode samples with Si(111) exhibit a long-term stability without any significant Fe_2O_3 NCs morphology change or dissolution, which was not the case for the electrodes with p-Si(100). Note that despite not providing a constant photocurrent over long time, the starting of photocurrent stability test (0-20 min) for the Si(100)/SnO_2/Fe_2O_3 css-NWs exhibits a constant current further confirming the high PEC activity shown in the *J-V* measurements and disproofing the fact that dissolution of Fe_2O_3 may contribute to the *J-V* measurements. Moreover, the Si(100)/SnO_2/Fe_2O_3 css-NWs preserve their high photoactivity after several months by keeping them in vacuum (see Figure 5.4b). The cyclic voltammetry measurement on the Si(100)/SnO_2/Fe_2O_3 css-NWs (data not shown here) also showed that there is no corrosive peak.

To further evaluate the photocathodic performance of the Si/SnO_2/Fe_2O_3 css-NWs, their photocurrent and stability were compared to our previously reported ZnO/Si branched NWs and TiO_2/Pt-coated ZnO/Si branched NWs[36] that have almost similar core and shell dimensions. The Si/SnO_2/Fe_2O_3 css-NWs show higher photocathodic current and lower photocathodic turn-on potential than the ZnO/Si branched NWs. Moreover, they provide comparable long-term stability to that of the TiO_2/Pt-coated ZnO/Si branched NWs, while the ZnO/Si branched NWs cannot provide a long-term stability. Therefore, we emphasize that our achieved results for the Si/SnO_2/Fe_2O_3 css-NW photocathodes are promising considering several factors; (i) performance was evaluated in a neutral electrolyte with a low morality of 0.25, (ii) there is no any metal catalyst coating on the samples, and (iii) the css-NWs provide long-term stability without any need for the atomic-layer-deposition (ALD) passivation which is a costly technique.

5.4 Conclusions

In summary, we showed the fabrication of p-Si/n-SnO_2/n-Fe_2O_3 css-NW photocathodes using facile synthesis methods and their use for improved and durable solar water splitting in a neutral medium. The p-Si/SnO_2/Fe_2O_3 css-NW photocathodes exhibited considerably increased photocathodic photocurrent, lowered turn-on potential, and improved conversion efficiency, compared to that of the bare p-Si NW or p-Si/n-SnO_2 cs-NW photocathodes. The photoactivity at 0 V versus RHE and low onset potential for the css-NW photocathodes revealed the promising potential of overcoming the HER kinetics limitation at the surface of the p-Si photocathodes using metal oxides. More notably, the css-NW electrodes showed significant PEC stability of hours without any considerable morphological change. These results can pave the way to achieve overall solar water splitting in a full PEC system.

Chapter 5 was published in *Advanced Functional Materials* 2015, A. Kargar, S. J. Kim, P. Allameh, C. Choi, N. Park, H. Jeong, Y. Pak, G. Y. Jung, X. Pan, D. Wang and S. Jin, "p-Si/SnO_2/Fe_2O_3 core/shell/shell nanowire photocathodes for neutral pH water splitting". The dissertation author was the first author of this paper.

References

1. Hochbaum, A. I.; P. Yang, *Chem. Rev.* **2009**, *110*, 527.

2. Oh, J.; Yuan, H.-C.; Branz, H. M. *Nat. Nanotechnol.* **2012**, *7*, 743.

3. Wang, H.-P.; Lin, T.-Y.; Hsu, C.-W.; Tsai, M.-L.; Huang, C.-H.; Wei, W.-R.; Huang, M.-Y.; Chien, Y.-J.; Yang, P.-C.; Liu, C.-W.; Chou, L.-J.; He, J.-H. *ACS Nano* **2013**,*7,* 9325.

4. Zhu, J.; Hsu, C.-M.; Yu, Z.; Fan, S.; Cui, Y. *Nano Lett.* **2009**, *10*, 1979.

5. Maiolo, J. R.; Kayes, B. M.; Filler, M. A.; Putnam, M. C.; Kelzenberg, M. D.; Atwater, H. A.; Lewis, N. S. *J. Am. Chem. Soc.* **2007**, *129*, 12346.

6. Walter, M. G.; Warren, E. L.; McKone, J. R.; Boettcher, S. W.; Mi, Q.; Santori, E. A.; Lewis, N. S. *Chem. Rev.* **2010**, *110*, 6446.

7. Oh, J.; Deutsch, T. G.; Yuan, H.-C.; Branz, H. M. *Energy Environ. Sci.* **2011**, *4*, 1690.

8. Cho, S. K.; Fan, F.-R. F.; Bard, A. J. *Angew. Chem. Int. Ed.* **2012**, *51*, 12740.

9. Boettcher, S. W.; Spurgeon, J. M.; Putnam, M. C.; Warren, E. L.; Turner-Evans, D. B.; Kelzenberg, M. D.; Maiolo, J. R.; Atwater, H. A.; Lewis, N. S. *Science* **2010**, *327*, 185.

10. Lin, Y.; Battaglia, C.; Boccard, M.; Hettick, M.; Yu, Z.; Ballif, C.; Ager, J. W.; Javey, A. *Nano Lett.* **2013**, *13*, 5615.

11. Peng, K.; Wang, X.; Lee, S.-T. *Appl. Phys. Lett.* **2008**, *92*, 163103.

12. Kargar, A.; Sun, K.; Kim, S. J.; Lu, D.; Jing, Y.; Liu, Z.; Pan, X.; Wang, D. *Phys. Status Solidi A* **2013**, *210*, 2561.

13. Oh, I.; Kye, J.; Hwang, S. *Nano Lett.* **2011**, *12*, 298.

14 Sun, K.; Jing, Y.; Li, C.; Zhang, X.; Aguinaldo, R.; Kargar, A.; Madsen, K.; Banu, K.; Zhou, Y.; Bando, Y.; Liu, Z.; Wang, D. *Nanoscale* **2012**, *4*, 1515.

15. Wang, X.; Peng, K.-Q.; Pan, X.-J.; Chen, X.; Yang, Y.; Li, L.; Meng, X.-M.; Zhang, W.-J.; Lee, S.-T. *Angew. Chem. Int. Ed.* **2011**, *50*, 9861.

16. Hwang, Y. J.; Wu, C. H.; Hahn, C.; Jeong, H. E.; Yang, P. *Nano Lett.* **2012**, *12*, 1678.

17. Mayer, M. T.; Du, C.; Wang, D. *J. Am. Chem. Soc.* **2012**, *134*, 12406.

18. Cheng, C.; Fan, H. J. *Nano Today* **2012**, *7*, 327.

19. Bierman, M. J.; Jin, S. *Energy Environ. Sci.* **2009**, *2*, 1050.

20. Dominey, R. N.; Lewis, N. S.; Bruce, J. A.; Bookbinder, D. C.; Wrighton, M. S. *J. Am. Chem. Soc.* **1982**, *104*, 467.

21. Boettcher, S. W.; Warren, E. L.; Putnam, M. C.; Santori, E. A.; Turner-Evans, D.; Kelzenberg, M. D.; Walter, M. G.; McKone, J. R.; Brunschwig, B. S.; Atwater, H. A.; Lewis, N. S. *J. Am. Chem. Soc.* **2011**, *133*, 1216.

22. Warren, E. L.; McKone, J. R.; Atwater, H. A.; Gray, H. B.; Lewis, N. S. *Energy Environ. Sci.* **2012**, *5*, 9653.

23. McKone, J. R.; Warren, E. L.; Bierman, M. J.; Boettcher, S. W.; Brunschwig, B. S.; Lewis, N. S.; Gray, H. B. *Energy Environ. Sci.* **2011**, *4*, 3573.

24. Reece, S. Y.; Hamel, J. A.; Sung, K.; Jarvi, T. D.; Esswein, A. J.; Pijpers, J. J. H.; Nocera, D. G. *Science* **2011**, *334*, 645.

25. Chen, Y. W.; Prange, J. D.; Dühnen, S.; Park, Y.; Gunji, M.; Chidsey, C. E. D.; McIntyre, P. C. *Nat. Mater.* **2011**, *10*, 539.

26. Kargar, A.; Sun, K.; Jing, Y.; Choi, C.; Jeong, H.; Zhou, Y.; Madsen, K.; Naughton, P.; Jin, S.; Jung, G. Y.; Wang, D. *Nano Lett.* **2013**, *13*, 3017.

27. Hwang, Y. J.; Boukai, A.; Yang, P. *Nano Lett.* **2009**, *9*, 410.

28. Jun, K.; Lee, Y. S.; Buonassisi, T.; Jacobson, J. M. *Angew. Chem. Int. Ed.* **2012**, *51*, 423.

29. Strandwitz, N. C.; Comstock, D. J.; Grimm, R. L.; Nichols-Nielander, A. C., Elam, J.; Lewis, N. S. *J. Phys. Chem. C* **2013**, *117*, 4931.

30. Sun, K.; Pang, X.; Shen, S.; Qian, X.; Cheung, J. S.; Wang, D. *Nano Lett.* **2013**, *13*, 2064.

31. Maruska, H. P.; Ghosh, A. K. *Sol. Energy Mater.* **1979**, *1*, 411.

32. Kohl, P. A.; Frank, S. N.; Bard, A. J. *J. Electrochem. Soc.* **1977**, *124*, 225.

33. Hodes, G.; Thompson, L.; DuBow, J.; Rajeshwar, K. *J. Am. Chem. Soc.* **1983**, *105*, 324.

34. Yoon, K. H.; Seo, D. K.; Cho, Y. S.; Kang, D. H. *J. Appl. Phys.* **1998**, *84*, 3954.

35. Lu, X.; Minegishi, T.; Kubota, J.; Domen, K. *Jpn. J. Appl. Phys.* **2011**, *50*, 085702.

36. Kargar, A.; Sun, K.; Jing, Y.; Choi, C.; Jeong, H.; Jung, G. Y.; Jin, S.; Wang, D. *ACS Nano* **2013**, *7*, 9407.

37. Sivula, K.; Formal, F. Le; Grätzel, M. *ChemSusChem.* **2011**, *4*, 432.

38. Warren, S. C.; Thimsen, E. *Energy Environ. Sci.* **2012**, *5*, 5133.

39. Warren, S. C.; Voïtchovsky, K.; Dotan, H.; Leroy, C. M.; Cornuz, M.; Stellacci, F.; Hébert, C.; Rothschild, A.; Grätzel, M. *Nat. Mater.* **2013**, *12*, 842.

40. Vayssieres, L.; Beermann, N.; Lindquist, S.-E.; Hagfeldt, A. *Chem. Mater.* **2001**, *13*, 233.

41. Ling, Y.; Wang, G.; Reddy, J.; Wang, C.; Zhang, J. Z.; Li, Y. *Angew. Chem. Int. Ed.* **2012**, *51*, 4074.

42. Zhou, W.; Cheng, C.; Liu, J.; Tay, Y. Y.; Jiang, J.; Jia, X.; Zhang, J.; Gong, H.; Hng, H. H.; Yu, T.; Fan, H. J. *Adv. Funct. Mater.* **2011**, *21*, 2439.

43. Dare-Edwards, M. P.; Goodenough, J. B.; Hamnett, A.; Trevellick, P. R. *J. Chem. Soc., Faraday Trans. 1* **1983**, *79*, 2027.

44. Kennedy, J. H.; Frese, K. W. *J. Electrochem. Soc.* **1978**, *125*, 709.

45. Itoh, K.; Bockris, J. O. M. *J. Electrochem. Soc.* **1984**, *131*, 1266.

46. Cherepy, N. J.; Liston, D. B.; Lovejoy, J. A.; Deng, H.; Zhang, J. Z. *J. Phys. Chem. B* **1998**, *102*, 770.

47. Bosman, A. J.; Daal, H. J. van *Adv. Phys.* **1970**, *19*, 1.

48. Sanchez, C.; Sieber, K. D.; Somorjai, G. A. *J. Electroanal. Chem.* **1988**, *252*, 269.

49. Iordanova, N.; Dupuis, M.; Rosso, K. M. *J. Chem. Phys.* **2005**, *122*, 144305

50. Formal, F. Le; Tetreault, N.; Cornuz, M.; Moehl, T.; Gratzel, M.; Sivula, K. *Chem. Sci.* **2011**, *2*, 737.

51. Townsend, T. K.; Sabio, E. M.; Browning, N. D.; Osterloh, F. E. *Energy Environ. Sci.* **2011**, *4*, 4270.

52. Kargar, A.; Cheung, J. S.; Liu, C.-H.; Kim, T. K.; Riley, C. T.; Shen, S.; Liu, Z.; Sirbuly, D. J.; Wang, D.; Jin, S. *Nanoscale* **2015**, *7*, 4900.

53. Sakaino, K.; Adachi, S. *J. Electrochem. Soc.* **2002**, *149*, G543.

54. Bressers, P. M. M. C.; Kelly, J. J.; Gardeniers, J. G. E.; Elwenspoek, M. *J. Electrochem. Soc.* **1996**, *143*, 1744.

6. NANOWIRE/NANOTUBE ARRAY TANDEM CELLS FOR OVERALL SOLAR NEUTRAL WATER SPLITTING

6.1 Introduction

Photoelectrochemical (PEC) hydrogen production through solar water splitting is considered as a promising approach for clean hydrogen fuel generation,[1-7] which has potential for high solar-to-hydrogen (STH) efficiencies of up to 31.1%.[8] Obtaining a PEC tandem cell (full PEC device/system) in a Z-scheme configuration to handle efficient and durable overall spontaneous solar water splitting is a challenge, in which its key difficulties remain in design and engineering efficient and stable photoelectrodes (photocathode and photoanode) using earth-abundant materials with cost-effective and scalable fabrication processes. To run overall solar water splitting in a full PEC device, both individual photocathode and photoanode should provide a low onset potential in one specific electrolyte in a way that their photocurrents cross each other.[1] There has been tremendous progress on individual photoelectrodes with high cathodic or anodic performances,[2, 7, 9-19] however, coupling of most of such photoelectrodes to build a PEC tandem cell has been difficult due to some limitations such as operation of photoelectrodes in different electrolytes, high onset potentials that prevent the crossing of photocurrents, etc.

Si/metal-oxide heterojunction electrodes have shown promising PEC performances for both cathodic and anodic conditions exhibiting potential to reduce their onset potential to the desirable values.[16, 20-24] For example for the Si/Fe_2O_3 electrodes, Mayer *et al.* have shown the reduction of photoanodic turn-on potential through the dualabsorber nature of the n-Si/n-Fe_2O_3 junction,[16] while Jun *et al.* have reported the photoanodic onset potential decrease due to the catalytic effect of n-Fe_2O_3 on n-Si.[25] Building full PEC systems based on nanowire (NW) heterojunction photoelectrodes is a promising approach for solar fuel production due to unique characteristics of NWs, facile NW fabrication methods, ability to form different NW heterostructures, etc. Liu *et al.* have reported an integrated system of catalyst-loaded Si and TiO_2 NWs for direct solar water splitting achieving a 0.12% solar-to-fuel efficiency in 0.5 M H_2SO_4 solution.[4] On the other hand, having a PEC tandem cell working in neutral pH water is highly desirable as the natural water resources such as seawater are usually in a neutral condition, and are abundant and easily disposable. Employing a neutral electrolyte for solar water splitting also prevents the undesirable use of strong acids or bases, which can lead to environmental and handling issues.

In this paper, we demonstrate a novel PEC tandem cell, consisting of p-Si/TiO_2/Fe_2O_3 core/shell/hierarchical nanowire (csh-NW) array photocathode and TiO_2/TiO_2 core/shell nanotube (cs-NT) array photoanode, for overall solar water splitting in a neutral pH water. The csh-NWs, made mainly by solution-processed methods, provide significantly enhanced performance in the neutral pH water with a very low onset potential and photoactivity at zero bias. Nitrogen modification obtained by thermal annealing under N_2 is applied to further improve the csh-NWs performance. A photocathode energy conversion efficiency of ~0.3% at zero bias in a two-electrode setup is obtained for the csh-NWs with the nitrogen modification. The cs-NTs also offer improved performance. The mechanism of performance improvement for the photoelectrodes is studied. The PEC tandem cell is able to handle overall solar neutral water splitting with a STH efficiency of ~0.18%.

6.2 Experimental Section

Fabrication of p-Si/TiO_2/Fe_2O_3 csh-NWs photocathodes

Wafer-scale vertically ordered Si NW arrays on p-type boron-doped Si(100) wafers with resistivity of 1–20 Ωcm were achieved using an aqueous Ag-assisted electroless etching technique.[36] The etching time was 20 mins resulting in a NW length of ~6.5 μm. The etched Si NW samples were then dipped into buffered oxide etch (BOE) solution for 10 sec to remove the native oxide layer, rinsed with deionized (DI) water, dried with N_2 gas, and transferred to ALD chamber (Beneq TFS 200). A thin TiO_2 shell, working as a seeding layer for the Fe_2O_3 NRs growth, was then deposited on the Si NW substrates using ALD deposition in thermal mode (thermal ALD) at a temperature of 250°C. The number of cycles was 568 giving a thickness of ~25 nm on flat Si substrate based on a growth rate of 0.44 Å/cycle on Si(100) film substrate. The Fe_2O_3 NRs were finally grown on the TiO_2-coated Si NW trunks using a hydrothermal growth technique.[26, 37] Briefly, akaganeite (β-FeOOH) NRs were first grown on the TiO_2-coated Si NW cores by immersing the sample in a 45 mL sealed Teflon autoclave containing a 30 mL aqueous solution consisting of 0.15 M $FeCl_3 \cdot 6H_2O$ (Iron(III) chloride hexahydrate) (Sigma-Aldrich, ≥99%) and 1 M $NaNO_3$ (sodium nitrate) (Sigma-Aldrich, ≥99.0%). The DI water resistivity and solution pH were 17.6-17.7 MΩ-cm and ~1.44, respectively. The hydrothermal reaction was carried out at a temperature of ~106°C for 3 hrs. The sample was then rinsed cautiously with DI water to remove the residues and dried with N_2 gas. Lastly, the Si/TiO_2/FeOOH core/shell/hierarchical nanowires (csh-NWs) substrates were annealed at 450°C in air (denoted as Si/TiO_2/A-Fe_2O_3 csh-NWs) or under N_2 atmosphere (denoted as Si/TiO_2/N-Fe_2O_3 csh-NWs) for 1 hr. The N_2 flow during the annealing was 1000 scc/min. The growth of A-Fe_2O_3 and N-Fe_2O_3 NRs on FTO substrates was also performed in the same way as that mentioned for the csh-NWs samples. Before the growth, the FTO substrate was cleaned consecutively by sonication in acetone, isopropanol, and DI water for 5 mins each and finally rinsed with DI water and dried with N_2 flow.

Fabrication of p-Si/TiO_2 core/shell NWs (cs-NWs) samples

The cleaned Si NW samples (discussed above) were transferred to the ALD machine to deposit a thin TiO_2 shell using the thermal ALD at a temperature of 300°C. The number of cycles was 682 giving a thickness of ~30 nm on the Si film substrate. Similar deposition condition was used for the TiO_2-coated glass slides. Note that the ALD growth rate is a little larger (not significant) at higher temperature of 300°C, but we considered the same rate to calculate the thickness. For the N_2 annealed cs-NW samples, they were annealed at a temperature of 450°C for 1 hr under a N_2 flow of 1000 scc/min, similar condition to that mentioned for the Si/TiO_2/N-Fe_2O_3 csh-NWs.

Fabrication of TiO_2/TiO_2 cs-NTs photoanodes

Highly ordered TiO_2 NT arrays were prepared by an anodization process in a two-electrode electrochemical bath. Ti foil (99.5% purity, 0.25 mm thick, Alfa Aesar) and Ti mesh (80 mesh woven from 0.13 mm dia wire, Alfa Aesar) (working electrode (WE)) were cleaned in a mild detergent, rinsed with DI water and ultra-sonicated in acetone and ethanol for 5 mins in each solvent. Then, the Ti foil/Ti mesh was immersed in 1:18:81 HF:HNO_3:H_2O (volume ratio) for 2 mins, rinsed generously with DI water and ultra-sonicated in DI water for another 5 mins. They were then dried by N_2 gas flow. A Pt foil was used as the counter electrode (CE). The voltage was applied by a DC power supply (Agilent, E3612A). A thin TiO_2 NT array layer was produced by anodizing the Ti foil/Ti mesh in a solution of ethylene glycol (99.8%, JT Baker), containing 0.30% ammonium fluoride (NH_4F, 96%, Alfa Aesar) and 5% H_2O, for 3.5 hrs at 60 V. A thin TiO_2 shell was finally deposited on the TiO_2 NTs using the thermal ALD at a temperature of 300°C for 454 cycle numbers providing a thickness of ~20 nm on the flat Si substrate.

Characterization

The samples morphology was examined on a Philips XL30 field-emission environmental scanning electron microscope (ESEM) at an accelerating voltage of 10.0 kV. Energy-dispersive X-ray spectroscopy (EDS) and elemental mapping analyses were used to examine the materials composition. Crystal structures of samples were characterized using X-ray diffraction (XRD) by a Bruker D2 Phaser X-ray diffractometer with Cu Kα ($\lambda = 0.154$ nm) as the radiation source.

Photoelectrochemical (PEC) and IPCE measurements

To evaluate the samples performance, they were bonded to coated Cu wire at the back using indium. For the Ti substrates, indium was also used to provide ohmic contact to Ti. The edges and backside of samples were sealed using Hysol 1C epoxy. For the mesh samples, only the contact area and edges were covered with epoxy. Current density measurements were performed in an aqueous solution of 0.25 M Na_2SO_4 buffered at pH = 7.25 or 7.1 with Phosphate Buffered Saline (PBS, Sigma) (DI water resistivity was 17.6-17.7 or 18.2 MΩ-cm for pH = 7.25 or 7.1, respectively) (neutral pH water) with a three- or two-electrode setup. The three-electrode setup includes sample as working electrode (WE), Pt mesh/foil as counter electrode (CE), and Ag/AgCl (1 M KCl) as reference electrode (RE). The two-electrode setup consists of sample as WE and Pt mesh/foil as CE. An aqueous solution of 1 M NaOH was used for the current density measurements in an electrolyte with a pH of 13.97. A light power intensity of 100 mW/cm^2 was tuned at the samples position using a Newport solar simulator with a xenon lamp equipped with a 1.5 AM filter. The current density measurements were collected using a Digi-Ivy potentiostat. A scan rate of 10 mV/s was used for the current density measurements (linear sweep voltammetry (LSV)). During the current density measurements, a mild agitation was employed and the electrolyte was constantly purged with a small flow of N_2 gas. The applied potentials versus Ag/AgCl RE were converted to the potentials versus reversible hydrogen electrode (RHE) or normal hydrogen electrode (NHE) using the Nernst equation. The current densities here are calculated using the geometric areas. To test the full PEC system, consisting of the csh-NWs photocathode (set as WE) and the cs-NTs photoanode (set as CE) in a two-electrode setup, samples were put next to each other in a way that solar simulator can shine both samples. A monochromator (iHR 550) equipped with the solar simulator with the 1.5 AM filter as the light source was used to carry out the spectral photoresponse and incident photon-to-current efficiency (IPCE) measurements. The monochromatic light spectrum was calibrated by a silicon photodiode (Newport 818-UV). Spectral photoresponse and IPCE measurements were performed in the same three-electrode setup and electrolyte (0.25 M Na_2SO_4 buffered at pH = 7.25) as used for the current density measurements with N_2 purging but without using agitation during the tests.

Efficiency calculation

The photocathode energy conversion efficiency for hydrogen evolution is calculated using;[38]

$$\eta(\%) = \frac{100J_{ph}(E_{bias} - E(H^+/H_2))}{P_{in}} \tag{1}$$

where J_{ph} is the net photocurrent density $(J_{light} - J_{dark})$ (mA/cm^2) at each biasing potential versus Pt CE, E_{bias} is the biasing potential versus Pt CE (V), $E(H^+/H_2)$ is the Nernstian (thermodynamic) potential for hydrogen evolution (water reduction) relative to normal hydrogen electrode (NHE) (V), and P_{in} is the incident light power density (mW/cm^2) (which is 100 mW/cm^2 here). J_{light} and J_{dark} are the current density under illumination and at dark, respectively. Note that we ignored any light attenuation, which may come from the PEC setup, resulting in not having exact 100 mW/cm^2 on the sample surface. $E(H^+/H_2)$ was calculated using the Nernst equation;

$$E(H^+/H_2) = -0.059 \times \mathrm{pH} \quad (\mathrm{V\ vs\ NHE}) \tag{2}$$

where pH is the electrolyte pH. The solar-to-hydrogen (STH) efficiency is calculated using below equation considering 100% faradaic efficiency;[1, 39]

$$\eta_{\mathrm{STH}}(\%) = \frac{100J_{op}(1.23\ \mathrm{V})}{P_{in}} \tag{3}$$

where J_{op} is the photocurrent density of crossing point between photocurrents of photocathode and photoanode. For the PEC tandem cell (full PEC system), J_{op} is the photocurrent density at zero bias (short-circuit photocurrent density).

6.3 Results and Discussion

Figure 6.1 shows a schematic representation of fabrication procedure for the photoelectrodes. Wafer-scale vertically ordered p-Si NW arrays/cores using p-Si(100) wafer were first fabricated using an aqueous Ag-assisted electroless etching method, followed by coating of a thin atomic-layer-deposited (ALD) TiO_2 layer served as a seeding layer for the β-FeOOH nanorods (NRs) growth, and finally β-FeOOH NRs were grown on the TiO_2-coated Si NW backbones using hydrothermal growth method. The β-FeOOH NRs were subsequently converted into the α-Fe_2O_3 NRs by annealing the samples at 450°C in air (denoted as A-Fe_2O_3) or under N_2 atmosphere (denoted as N-Fe_2O_3) for 1 hr. The fabricated 3D array structure is denoted as p-Si/TiO_2/A-Fe_2O_3 and

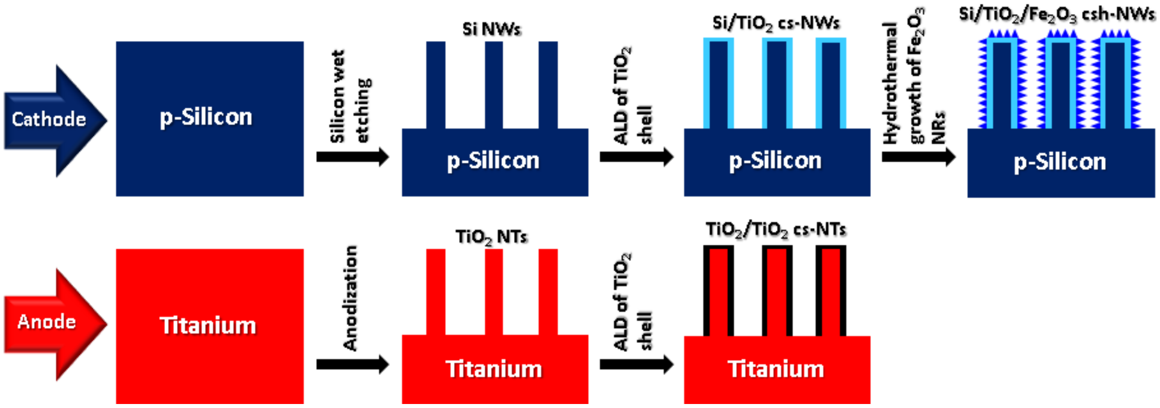
Cathode
p-Silicon
Silicon wet etching
Si NWs
p-Silicon
ALD of TiO2 shell
Si/TiO2 cs-NWs
p-Silicon
Hydrothermal growth of Fe2O3 NRs
Si/TiO2/Fe2O3 csh-NWs
p-Silicon
Anode
Titanium
Anodization
TiO2 NTs
Titanium
ALD of TiO2 shell
TiO2/TiO2 cs-NTs
Titanium

Figure 6.1. Schematic representation of fabrication procedure for the csh-NWs photocathode (top row) and the cs-NTs photoanode (bottom row).

p-Si/TiO_2/N-Fe_2O_3 csh-NWs for annealing in air and under N_2 environment, respectively. Highly ordered TiO_2 NT arrays on Ti foil/mesh were prepared by an anodization process and subsequently, the TiO_2 NTs were coated with a thin ALD TiO_2 layer to form TiO_2/TiO_2 cs-NTs (see Figure 6.1).

Figure 6.2a-d show scanning electron microscopy (SEM) images of p-Si/TiO_2/A-Fe_2O_3 csh-NWs. The Fe_2O_3 NRs are polycrystalline (Figure 6.2a). Figure 6.2b shows that there are spaces between the csh-NWs, coming from good spaces between the etched Si NW cores, in which water molecules can easily penetrate for water splitting reaction on the surface of csh-NWs. As shown in Figure 6.2c, the growth of Fe_2O_3 NRs is uniform through the entire length of tall Si NW backbones with ~6.5 µm length due to uniform coverage of ALD TiO_2 layer. The csh-NWs growth is also uniform within the whole area of samples (which can be evident by the low-magnification image in Figure 6.2d) revealing the potential of scaling up the electrodes. Note that we did not observe any significant morphological difference in the csh-NWs with A-Fe_2O_3 and N-Fe_2O_3 NRs

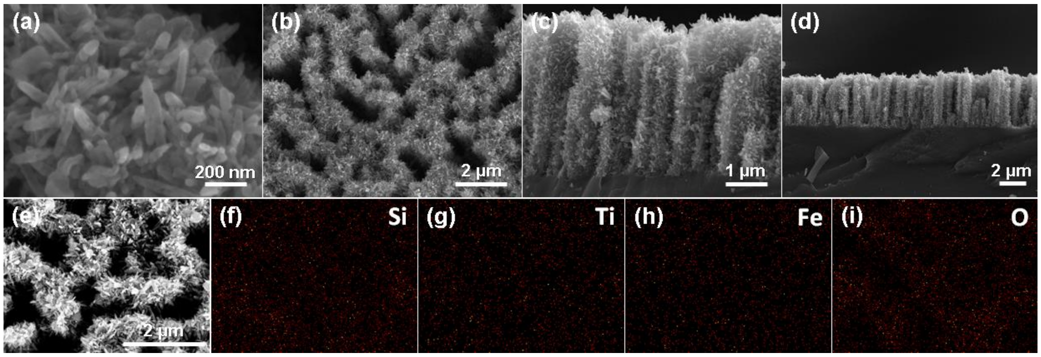

Figure 6.2. (a,b) Top-view (different magnification) and (c,d) cross-sectional view (different magnification) SEM images of p-Si/TiO_2/A-Fe_2O_3 csh-NW array. (e-i) Elemental mapping analysis of p-Si/TiO_2/A-Fe_2O_3 csh-NW array; (e) SEM image of spot used for the elemental mapping, (f) Si map, (g) Ti map, (h) Fe map, and (i) O map. The scale bar for (f-i) is the same as that in (e).

suggesting that the N_2 atmosphere did not significantly change the csh-NWs morphology. Also p-Si/TiO_2/A-Fe_2O_3 and p-Si/TiO_2/N-Fe_2O_3 csh-NWs showed similar X-ray diffraction (XRD) pattern indicating that there is no difference in their crystal structure. The A-Fe_2O_3 and N-Fe_2O_3 NRs grown directly on fluorine-doped tin oxide (FTO) substrate exhibit similar red color, evident of successful transformation of β-FeOOH to α-Fe_2O_3 for both cases, and this was also confirmed with the same XRD pattern for both samples. Elemental mapping analysis shown in Figure 6.2e-i confirms the materials composition of the csh-NWs.

Figure 6.3a-d exhibit the SEM images of bare TiO_2 NTs and TiO_2/TiO_2 cs-NTs with an average top inner diameter of 97 nm and 57 nm, respectively. The TiO_2 shell can cover the entire length of long TiO_2 NTs (see Figure 6.3c and d) due to gas phase nature of ALD deposition. However, from the SEM images, it was hard to realize uniform coating of ALD TiO_2 for both inner and outer sidewalls of NTs along the whole NTs

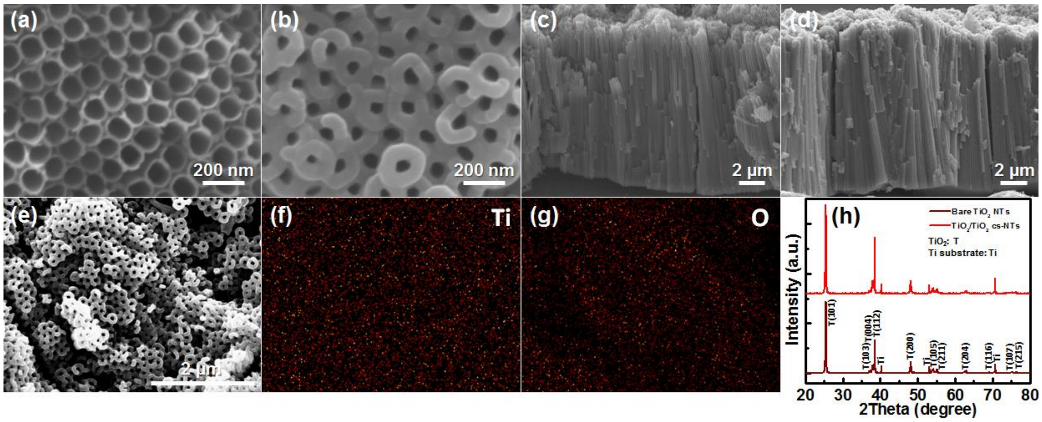
(a)
200 nm
(b)
200 nm
(c)
2 μm
(d)
2 μm
(e)
2 μm
(f)
Ti
(g)
O
(h)
Bare TiO2 NTs
TiO2/TiO2 cs-NTs
TiO2: T
Ti substrate: Ti
Intensity (a.u.)
T(101)
T(103)
T(004)
T(112)
Ti
T(200)
Ti
T(105)
T(211)
T(204)
T(116)
Ti
T(107)
T(215)
20
30
40
50
60
70
80
2Theta (degree)

Figure 6.3. Top-view SEM images of (a) bare TiO_2 NTs and (b) TiO_2/TiO_2 cs-NTs. Tilted cross-sectional SEM images of (c) bare TiO_2 NTs and (d) TiO_2/TiO_2 cs-NTs. Note that the tilted angle for (c) and (d) is not the same. (e-g) Elemental mapping analysis of TiO_2/TiO_2 cs-NTs; (e) SEM image of spot used for the elemental mapping, (f) Ti map, and (g) O map. The scale bar for (f,g) is the same as that in (e). (h) XRD patterns of bare TiO_2 NTs and TiO_2/TiO_2 cs-NTs. All TiO_2 NTs here are from those grown on Ti foil.

length. The materials composition was confirmed with the elemental mapping analysis shown in Figure 6.3e-g. The XRD analyses show similar patterns for both bare TiO_2 NTs and TiO_2/TiO_2 cs-NTs (Figure 6.3h) revealing that both core and shell exhibit similar phase of anatase.

Current density measurements were performed in an aqueous solution of 0.25 M Na_2SO_4 buffered at pH = 7.25 or 7.1 (neutral pH water) with both three-electrode and two-electrode PEC setups. A light power intensity of 100 mW/cm^2 was used for the PEC measurements. A scan rate of 10 mV/s was employed for the linear sweep voltammetry (LSV) (*J-V* measurements). Figure 6.4a shows the current density of bare p-Si NWs, p-Si/TiO_2/A-Fe_2O_3 csh-NWs, and p-Si/TiO_2/N-Fe_2O_3 csh-NWs using a three-electrode setup in which all the samples show photocathodic behavior and there is no significant photoanodic current even at high biasing potentials of over +1.5 V versus reversible hydrogen electrode (RHE). The p-Si/TiO_2/A-Fe_2O_3 csh-NWs offer much higher photocathodic current and significant onset potential shift toward positive potentials

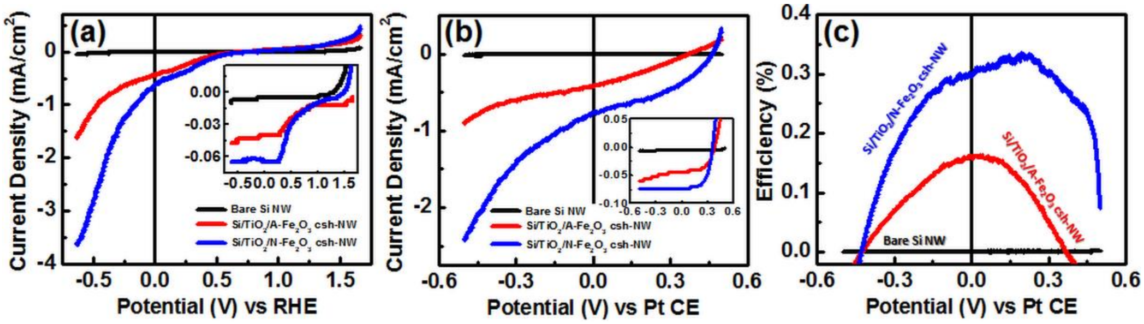

Figure 6.4. Current density under illumination of bare p-Si NW, p-Si/TiO_2/A-Fe_2O_3 csh-NW, and p-Si/TiO_2/N-Fe_2O_3 csh-NW arrays measured in the neutral pH water using (a) a three-electrode and (b) a two-electrode PEC setups. Insets in (a,b) show the dark current of the corresponding samples. (c) Photocathode energy conversion efficiency of the corresponding samples calculated by the two-electrode measurements in (b).

compared to the bare p-Si NWs, leading to an onset potential of about +0.38 V versus RHE, a photocurrent of about -0.4 mA/cm^2 at 0 V versus RHE (see Figure 6.4a), and a photocurrent of about -0.43 mA/cm^2 at the water reduction potential. Note that the onset potential is calculated when the net photocurrent (light current – dark current) reaches a value of -0.1 mA/cm^2. The significantly enhanced photocathodic performance is attributed to the increased reaction surface area which is evident from the SEM images, effective energy band alignment among p-Si, n-TiO_2 and n-Fe_2O_3 enhancing the charge separation, improved optical absorption,[16, 26] and increased gas evolution coming from the Fe_2O_3 NRs. The csh-NWs dark current is also larger confirming the photocurrent trend and contribution of enhanced surface area in the increased photocurrent. The morphology and PEC performance of p-Si/TiO_2 core/shell NWs (cs-NWs) are studied revealing the uniform coating of ALD TiO_2 shell and its contribution in the enhanced performance. Stability of the Fe_2O_3-coated p-Si photocathodes has been investigated to rule out effect from Fe_2O_3 dissolution which may contribute to the *J-V* measurements.[27] The csh-NWs performance further improves by N_2 annealing (using N-Fe_2O_3 instead of A-Fe_2O_3) resulting in an onset potential of about +0.46 V versus RHE, a photocurrent of about -0.55 mA/cm^2 at 0 V versus RHE (see Figure 6.4a), and a photocurrent of about -0.61 mA/cm^2 at the water reduction potential. The performance improvement can be mainly due to superior conductivity of Fe_2O_3 NRs[28, 29] resulting in an enhanced collection efficiency of photoexcited electrons. Annealing under N_2 atmosphere can also enhance the conductivity of TiO_2 seeding layer assisting the performance enhancement. However, annealing at 450°C under the applied N_2 atmosphere condition may not change appreciably the band gap of Fe_2O_3 or TiO_2. Furthermore, the dark current also increases confirming the increased conductivity. The N-Fe_2O_3 NRs grown on the FTO substrate also showed improved photoanodic performance than A-Fe_2O_3 NRs (data not shown here) further confirming the improved conductivity which is consistent with the reported observation elsewhere.[28]

The current density measurements of the corresponding samples using a two-electrode PEC setup in Figure 6.4b exhibit similar trends for both dark and photo currents as those observed with a three-electrode setup in Figure 6.4a. The photocathode energy conversion efficiency for hydrogen evolution is calculated using the two-electrode measurement in Figure 6.4b and shown in Figure 6.4c exhibiting efficiencies of ~0.16% and ~0.3% at zero bias for the p-Si/TiO_2/A-Fe_2O_3 and p-Si/TiO_2/N-Fe_2O_3 csh-NWs, respectively. The bare p-Si NW array does not show any significant efficiency at zero bias or other biasing potentials. As expected from the photocurrent measurements, the efficiency of the p-Si/TiO_2/N-Fe_2O_3 csh-NWs is larger than that of the p-Si/TiO_2/A-Fe_2O_3 NWs within the entire scanned potential range. The p-Si/TiO_2/N-Fe_2O_3 csh-NWs also exhibit high incident photon-to-current efficiencies (IPCEs) in a wide range.

The achieved performance facilitates to obtain a full PEC device for overall spontaneous solar water splitting in the neutral pH water. To make the PEC tandem cell for overall solar water splitting, we used TiO_2 NT array as a model for the photoanode since it can provide a low onset potential. However, the bare TiO_2 NT sample cannot provide a high photoanodic current due to TiO_2 poor properties,[30, 31] and its onset potential needs to be further reduced. The TiO_2 NTs were then coated with a thin ALD TiO_2 layer forming TiO_2/TiO_2 cs-NTs to achieve a higher photoanodic current. The enhanced photoanodic current can be due to passivation of surface states[32, 33] and improved reaction surface area. The surface of ALD TiO_2 coating is not smooth meaning that the shell coating provides more junction area. As mentioned above, both TiO_2 core and shell are anatase phase, thus there is no junction barrier between core and shell to block the charge transfer. The photoanodic current of the TiO_2/TiO_2 cs-NTs grown on Ti foil in the neutral pH water is shown in Figure 6.5a along with the photocathodic current of p-Si/TiO_2/N-Fe_2O_3 csh-NWs to determine the crossing point between the *J*-*V* curves. The photocurrents intersection is at ~0.42 V versus RHE with a photocurrent density of ~0.17 mA/cm^2, resulting in a STH efficiency of ~0.21%. Using TiO_2/TiO_2 cs-NTs grown on Ti mesh instead of Ti foil, the photoanodic performance improves (Figure 6.5a inset) in which the photocurrents cross each other at ~0.3 V versus RHE with a photocurrent density of ~0.3 mA/cm^2 leading to a STH efficiency of ~0.37%, due to enhanced reaction surface area coming from the mesh substrate. To illuminate both sides of the mesh

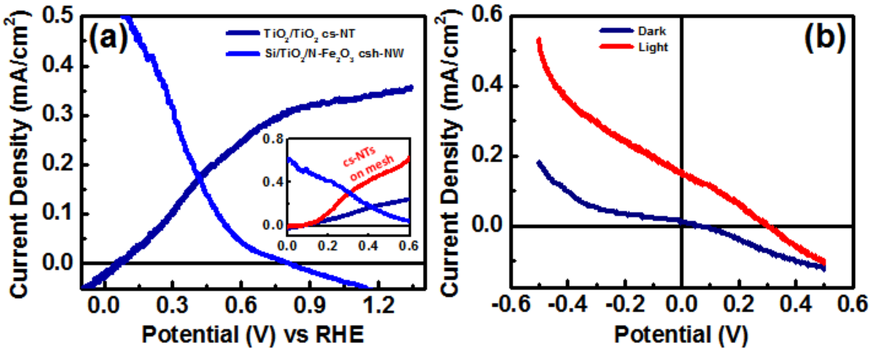

Figure 6.5. (a) Current density under illumination of TiO_2/TiO_2 cs-NTs (grown on foil) photoanode along with the current density under illumination of p-Si/TiO_2/N-Fe_2O_3 csh-NWs photocathode measured in the neutral pH water. Note that in this figure, the absolute value of current density for the csh-NWs is plotted. Inset shows the zoomed-in currents of the corresponding samples along with the current density under illumination of TiO_2/TiO_2 cs-NTs grown on mesh. (b) Current density at dark and under illumination of full PEC system, consisting of csh-NWs photocathode and TiO_2/TiO_2 cs-NTs (grown on foil) photoanode, tested in the neutral pH water.

sample during the current density measurement, the glass PEC cell was covered with a piece of aluminium foil.

The achieved performances reveal the fact that the developed photoelectrodes can run overall solar water splitting. To figure out this feasibility, a full PEC system made of these two photoelectrodes were tested in a way that the csh-NWs photocathode was set as working electrode (WE) and the cs-NTs (grown on Ti foil) photoanode was set as counter electrode (CE) in a two-electrode setup. The current density of full system is shown in Figure 6.5b exhibiting the operation of full system in the neutral pH water with a non-zero photocurrent density of ~0.15 mA/cm^2 at zero bias, which leads to a STH efficiency of ~0.18%. Note that the photocurrent density of full system at zero bias (~0.15 mA/cm^2) is a little smaller than the photocurrent density at the crossing point (~0.17 mA/cm^2) which results in a slightly lower efficiency. The obtained performance is promising considering several factors; (i) performance was assessed in a neutral solution with a low morality of 0.25, (ii) all photoelectrodes were fabricated using earth-abundant materials with cheap fabrication processes except for ALD which may be replaced with another fabrication technique, and (iii) there is no catalyst loaded on the electrodes. To obtain a high STH efficiency in such a full system, a catalyst (preferably bifunctional) working in neutral or near-neutral pH water toward basic solution such as NiO[26, 34, 35] can be added to both photoelectrodes.

6.4 Conclusions

In summary, we demonstrated the fabrication and characterization of a novel PEC tandem cell, consisting of p-Si/TiO_2/Fe_2O_3 csh-NW array photocathode and TiO_2/TiO_2

cs-NT array photoanode, for overall solar water splitting in the neutral pH water. The csh-NWs, made mostly from solution growth methods, exhibited considerably improved photocathodic performance in the neutral pH water with onset potentials of about +0.38 V and +0.46 V versus RHE, and photocurrents of about -0.4 mA/cm^2 and -0.55 mA/cm^2 at 0 V versus RHE for the unmodified and N-modified Fe_2O_3 NRs, respectively. The csh-NWs with the N-modified Fe_2O_3 NRs offered a photocathode energy conversion efficiency of ~0.3% at zero bias in a two-electrode configuration. The cs-NTs grown on Ti foil/mesh also provided enhanced performance. The PEC tandem cell was finally shown to handle overall solar neutral water splitting with a STH efficiency of ~0.18%. The obtained results reveal promising potential of making PEC tandem cells using earth-abundant materials for solar hydrogen fuel production.

Chapter 6 was published in *Nano Energy* 2015, A. Kargar, J. Khamwannah, C.-H. Liu, N. Park, D. Wang, S. A. Dayeh and S. Jin, “Nanowire/nanotube array tandem cells for overall solar neutral water splitting”. The dissertation author was the first author of this paper.

References

1. Walter, M. G.; Warren, E. L.; McKone, J. R.; Boettcher, S. W.; Mi, Q.; Santori, E. A.; Lewis, N. S. *Chem. Rev.* **2010**, *110*, 6446-6473.

2. Kenney, M. J.; Gong, M.; Li, Y.; Wu, J. Z.; Feng, J.; Lanza, M.; Dai, H. *Science* **2013**, *342*, 836-840.

3. Reece, S. Y.; Hamel, J. A.; Sung, K.; Jarvi, T. D.; Esswein, A. J.; Pijpers, J. J. H.; Nocera, D. G. *Science* **2011**, *334*, 645-648.

4. Liu, C.; Tang, J.; Chen, H. M.; Liu, B.; Yang, P. *Nano Lett.* **2013**, *13*, 2989-2992.

5. Khaselev, O.; Turner, J. A. *Science* **1998**, *280*, 425-427.

6. Luo, J.; Im, J.-H.; Mayer, M. T.; Schreier, M.; Nazeeruddin, M. K.; Park, N.-G.; Tilley, S. D.; Fan, H. J.; Grätzel, M. *Science* **2014**, *345*, 1593-1596.

7. Wang, G.; Wang, H.; Ling, Y.; Tang, Y.; Yang, X.; Fitzmorris, R. C.; Wang, C.; Zhang, J. Z.; Li, Y. *Nano Lett.* **2011**, *11*, 3026-3033.

8. Hu, S.; Xiang, C.; Haussener, S.; Berger, A. D.; Lewis, N. S. *Energy Environ. Sci.* **2013**, *6*, 2984-2993.

9. Hu, S.; Shaner, M. R.; Beardslee, J. A.; Lichterman, M.; Brunschwig, B. S.; Lewis, N. S. *Science* **2014**, *344*, 1005-1009.

10. Chen, Y. W.; Prange, J. D.; Dühnen, S.; Park, Y.; Gunji, M.; Chidsey, C. E. D.; McIntyre, P. C. *Nat. Mater.* **2011**, *10*, 539-544.

11. Paracchino, A.; Laporte, V.; Sivula, K.; Grätzel, M.; Thimsen, E. *Nat. Mater.* **2011**, *10*, 456-461.

12. Lee, M. H.; Takei, K.; Zhang, J.; Kapadia, R.; Zheng, M.; Chen, Y.-Z.; Nah, J.; Matthews, T. S.; Chueh, Y.-L.; Ager, J. W.; Javey, *Angew. Chem. Int. Ed.* **2012**, *124*, 10918-10922.

13. Warren, S. C.; Voïtchovsky, K.; Dotan, H.; Leroy, C. M.; Cornuz, M.; Stellacci, F.; Hébert, C.; Rothschild, A.; Grätzel, M. *Nat. Mater.* **2013**, *12*, 842-849.

14. Wang, H.-P.; Sun, K.; Noh, S. Y.; Kargar, A.; Tsai, M.-L.; Huang, M.-Y.; Wang, D.; He, J.-H. *Nano Lett.* **2015**, *15*, 2817-2824.

15. Boettcher, S. W.; Spurgeon, J. M.; Putnam, M. C.; Warren, E. L.; Turner-Evans, D. B.; Kelzenberg, M. D.; Maiolo, J. R.; Atwater, H. A.; Lewis, N. S. *Science* **2010**, *327*, 185-187.

16. Mayer, M. T.; Du, C.; Wang, D. *J. Am. Chem. Soc.* **2012**, *134*, 12406-12409.

17. Dasgupta, N. P.; Liu, C.; Andrews, S.; Prinz, F. B.; Yang, P. *J. Am. Chem. Soc.* **2013**, *135*, 12932-12935.

18. Benck, J. D.; Lee, S. C.; Fong, K. D.; Kibsgaard, J.; Sinclair, R.; Jaramillo, T. F. *Adv. Energy Mater.* **2014**, *4*, 1400739.

19. Ding, Q.; Meng, F.; English, C. R.; Cabán-Acevedo, M.; Shearer, M. J.; Liang, D.; Daniel, A. S.; Hamers, R. J.; Jin, S. *J. Am. Chem. Soc.* **2014**, *136*, 8504-8507.

20. Hwang, Y. J.; Boukai, A.; Yang, P. *Nano Lett.* **2008**, *9*, 410-415.

21. Shaner, M. R.; Fountaine, K. T.; Ardo, S.; Coridan, R. H.; Atwater, H. A.; Lewis, N. S. *Energy Environ. Sci.* **2014**, *7*, 779-790.

22. Yang, J.; Walczak, K.; Anzenberg, E.; Toma, F. M.; Yuan, G.; Beeman, J.; Schwartzberg, A.; Lin, Y.; Hettick, M.; Javey, A.; Ager, J. W.; Yano, J.; Frei, H.; Sharp, I. D. *J. Am. Chem. Soc.* **2014**, *136*, 6191-6194.

23. Shi, J.; Hara, Y.; Sun, C.; Anderson, M. A.; Wang, X. *Nano Lett.* **2011**, *11*, 3413-3419.

24. Kargar, A.; Sun, K.; Jing, Y.; Choi, C.; Jeong, H.; Zhou, Y.; Madsen, K.; Naughton, P.; Jin, S.; Jung, G. Y.; Wang, D. *Nano Lett.* **2013**, *13*, 3017-3022.

25. Jun, K.; Lee, Y. S.; Buonassisi, T.; Jacobson, J. M. *Angew. Chem. Int. Ed.* **2012**, *51*, 423-427.

26. Kargar, A.; Cheung, J. S.; Liu, C.-H.; Kim, T. K.; Riley, C. T.; Shen, S.; Liu, Z.; Sirbuly, D. J.; Wang, D.; Jin, S. *Nanoscale* **2015**, *7*, 4900-4905.

27. Kargar, A.; Kim, S. J.; Allameh, P.; Choi, C.; Park, N.; Jeong, H.; Pak, Y.; Jung, G. Y.; Pan, X.; Wang, D.; Jin, S. *Adv. Funct. Mater.* **2015**, *25*, 2609-2615.

28. Ling, Y.; Wang, G.; Reddy, J.; Wang, C.; Zhang, J. Z.; Li, Y. *Angew. Chem. Int. Ed.* **2012**, *51*, 4074-4079.

29. Lu, X.; Zeng, Y.; Yu, M.; Zhai, T.; Liang, C.; Xie, S.; Balogun, M.-S.; Tong, Y. *Adv. Mater.* **2014**, *26*, 3148-3155.

30. Linsebigler, A. L.; Lu, G.; Yates, J. T. *Chem. Rev.* **1995**, *95*, 735-758.

31. Hendry, E.; Koeberg, M.; O'Regan, B.; Bonn, M. *Nano Lett.* **2006**, *6*, 755-759.

32. Le Formal, F.; Tetreault, N.; Cornuz, M.; Moehl, T.; Gratzel, M.; Sivula, K. *Chem. Sci.* **2011**, *2*, 737-743.

33. Hwang, Y. J.; Hahn, C.; Liu, B.; Yang, P. *ACS Nano* **2012**, *6*, 5060-5069.

34. Gong, M.; Zhou, W.; Tsai, M.-C.; Zhou, J.; Guan, M.; Lin, M.-C.; Zhang, B.; Hu, Y.; Wang, D.-Y.; Yang, J.; Pennycook, S. J.; Hwang, B.-J.; Dai, H. *Nat. Commun.* **2014**, *5*, 4695.

35. Trotochaud, L.; Ranney, J. K.; Williams, K. N.; Boettcher, S. W. *J. Am. Chem. Soc.* **2012**, *134*, 17253-17261.

36. Kargar, A.; Sun, K.; Kim, S. J.; Lu, D.; Jing, Y.; Liu, Z.; Pan, X.; Wang, D. *Phys. Status Solidi A* **2013**, *210*, 2561-2568.

37. Vayssieres, L.; Beermann, N.; Lindquist, S.-E.; Hagfeldt, A. *Chem. Mater.* **2001**, *13*, 233-235.

38. Kargar, A.; Sun, K.; Jing, Y.; Choi, C.; Jeong, H.; Jung, G. Y.; Jin, S.; Wang, D. *ACS Nano* **2013**, *7*, 9407-9415.

39. Chen, Z.; Jaramillo, T. F.; Deutsch, T. G.; Kleiman-Shwarsctein, A.; Forman, A. J.; Gaillard, N.; Garland, R.; Takanabe, K.; Heske, C.; Sunkara, M.; McFarland, E. W.; Domen, K.; Miller, E. L.; Turner, J. A.; Dinh, H. N. *J. Mater. Res.* **2010**, *25*, 3-16.

7. ZNO/CUO HETEROJUNCTION BRANCHED NANOWIRES FOR PHOTOELECTROCHEMICAL HYDROGEN GENERATION

7.1 Introduction

The photoelectrochemical (PEC) water splitting for clean and practical hydrogen production requires cheap, efficient, and stable semiconductor photoelectrodes to split water and consequently generate hydrogen at large scales. Among the vast majority of studied materials so far, semiconductor metal oxides (Fe_2O_3, TiO_2, WO_3, ZnO, Cu_2O, and CuO) have shown promising potentials,[1-13] which are abundant, cheap, non-toxic, and can be fabricated using facile, cost-effective, and scalable fabrication techniques, such as hydro/solvothermal growth method[4, 5, 9, 10] and electrodeposition.[1, 7] Despite their potential for high solar-to-hydrogen (STH) conversion efficiencies,[1, 5, 14] there are several limiting factors, such as short diffusion length,[5, 15-17] low conductivity,[9, 18, 19] and poor surface evolution kinetics,[20, 21] that cause the STH efficiencies to be considerably lower than the predicated theoretical values.[2, 4, 5, 9, 10]

The formation of nano-structured metal oxides reduces the carrier diffusion length and increases the reaction surface area as well as improves the surface evolution kinetics.[22] Specifically, vertical metal oxide NWs have shown promising performances for the PEC solar water splitting because they provide enhanced light absorption, increased surface area, reduced carrier recombination, and improved charge collection efficiency.[4, 6, 9-11, 19, 23, 24] Intrinsically n-type metal oxide NWs (Fe_2O_3,[2, 9, 19] TiO_2,[3, 10] WO_3,[4, 5, 25] and ZnO[6, 23]) have mostly been studied for the oxygen generating photoanode materials.[4, 9, 10, 19, 23] Copper oxides (CuO and Cu_2O) are the most studied metal oxides for the photocathodic hydrogen production as they are naturally p-type with proper band gaps for light absorption (E_g (CuO) ≅ 1.4 eV,[26] E_g (Cu_2O) ≅ 2 eV).[1, 7, 11, 12, 27, 28] The formation of NW heterostructures can enhance the PEC performance of copper oxide photocathodes resulting in an improvement of their STH efficiency due to increased charge separation and enlarged reaction surface area/sites. Furthermore, stable materials such as TiO_2 that are coupled with the copper oxides in the heterostructure, can improve the stability of copper oxide photocathodes because they can protect the surface of copper oxide electrodes against decomposition/corrosion in the electrolyte.[29]

Compared to core/shell NW (cs-NW) heterostructures, branched NWs are very promising for PEC solar hydrogen production[30-32] due to enhanced surface area, improved light absorption,[22, 33] and increased gas evolution.[22] In addition, the smaller size of the NW branches (compared to the size of NW cores) can also result in more efficient charge separation and collection due to the close proximity between the photogenerated carriers and the semiconductor-electrolyte interface.[24] We have recently demonstrated the ZnO/Si b-NW heterostructures for efficient solar water splitting and photocathodic hydrogen production,[22, 31] which also provide tunable PEC performance resulting in selective water oxidation or reduction.[32] There are several reports for all-metal-oxide NW heterostructures for photoanode materials, however, to the best of our knowledge, there is no report employing all-metal-oxide NW heterostructures for photocathode materials for hydrogen production.[34, 35] Having a b-NW heterostructure based on CuO and ZnO metal oxides can be a promising candidate for the photocathodic hydrogen production because it uses advantages of both CuO and ZnO[23, 36] metal oxides for the solar water splitting as well as the aforementioned beneficial characteristics of the heterojunction b-NWs.

Furthermore, such a b-NW structure is easily synthesized using facile, cost-effective and scalable fabrication methods such as thermal oxidation and hydrothermal growth.[37] The b-NWs based on all-metal-oxide NWs can also be used for other device applications such as lithium-ion batteries (LIBs),[38] and optoelectronic devices.[39]

In this paper, we present the facile and large-scale fabrication of 3D ZnO/CuO b-NW heterojunction photocathodes for PEC solar hydrogen production. The ZnO/CuO b-NWs are synthesized on different copper substrates, including copper foils and meshes, for different ZnO and CuO NWs sizes and densities. High-resolution scanning and transmission electron microscopies are employed to characterize the b-NWs in detail. The ZnO/CuO b-NWs are used as photocathodes and the correlation between the electrode currents and different NWs sizes and densities are studied. The spectral incident photon-to-current efficiency (IPCE) of the ZnO/CuO b-NW photoelectrodes is also investigated. An energy band diagram of the ZnO/CuO heterojunction b-NW is also proposed to help illustrating the working mechanism of the ZnO/CuO b-NWs.

7.2 Experimental Section

ZnO/CuO b-NWs synthesis

The CuO NW arrays were grown on different copper substrates (copper foils and meshes) using thermal oxidation growth method.[40] The number of meshes in the Cu mesh substrates was 200 (TWP Inc). First, small pieces (~1 cm^2) of Cu foils and meshes were cut and cleaned by sonication in Acetone, Isopropanol (IPA), and deionized (DI) water for 5 mins each case, consecutively and finally rinsed with DI water and dried with N_2 flow. Then, they were immediately transferred into an open furnace (without using any gas flow) and annealed under air at different temperatures and for various times. The annealing procedure was performed as the following: the furnace temperature was raised to the desirable temperature (400°C, 450°C or 500°C) for 10 mins and at each annealing temperature, samples were kept at this temperature for the desirable time (2h, 3h, 4h or 5h), respectively, finally the furnace was gradually cooled down without opening the furnace, and the samples were taken out. Note that for both foil and mesh samples, CuO NWs grew on both sides of the Cu substrates due to exposure to oxygen during annealing. The CuO NW substrates were then transferred into the sputtering machine to deposit a thin ZnO seeding layer for the ZnO NW growth using RF magnetron sputtering using a 99.99% ZnO target and in argon gas. The sputtering pressure was 2.5 mT during the deposition. The measured thickness of sputtered ZnO on a glass slide was ~69 nm. Note that the actual thickness of sputtered ZnO on CuO NWs is smaller than this thickness (see text). For the mesh samples, both sides of the mesh substrates were coated with the ZnO seeding layer. Finally, the ZnO NW branches were grown on the CuO NW cores using identical hydrothermal growth method as reported previously.[32] Note that for the mesh samples, ZnO NWs uniformly grew on all surfaces of Cu wires in the mesh since ZnO seeding layer covered all surfaces on both sides of the mesh. The synthesized b-NW samples were then stored under vacuum for the next processes such as morphology study and PEC tests.

Structural characterization

A Philips XL30 field-emission environmental scanning electron microscope (ESEM), working at an accelerating voltage of 10.0 kV, was used to obtain the SEM images to study the samples morphologies. The atomic-scale structural analyses were performed using high resolution transmission electron microscopy (HRTEM, JEOL JEM3100F) operated at 300 kV. For further study, spherical aberration-corrected scanning transmission electron microscopy (Cs-corr. STEM, JEOL JEM2100F) operated at 200 kV was employed to identify the actual atomic configuration of NWs. For the TEM sample preparation, the copper foil containing CuO NWs was held with a tweezer and scraped it onto a holey carbon grid to pull out NWs to be attached onto a grid.

Photoelectrochemical and IPCE measurements

To perform the PEC tests, first the back side of foil samples were completely scratched to have Cu surface because there was CuO NW growth on both sides of the Cu foil, while for mesh samples, only one edge was cleaned. The foil samples were then bonded to Cu wire at the back using indium, which provides an ohmic contact. The edges and backside of foil samples were sealed using epoxy. For mesh samples, the cleaned edge was only connected to the Cu wire and sealed by epoxy. A three-electrode PEC cell using a 400 mL aqueous solution of 0.25 M Na_2SO_4 buffered at pH = 7.25 (neutral solution) with Phosphate Buffered Saline (PBS, Sigma) (DI water; 17.6-17.9 MΩ-cm) was used to carry out the current density measurements. The cs-NW or b-NW substrate as working electrode (WE), Pt coil as counter electrode (CE), and Ag/AgCl (1 M KCl) as reference electrode (RE) were the three electrodes in the PEC cell. Illumination was provided by a solar simulator (Newport 67015) using a 150 W Xenon lamp and equipped with 1.5 AM filter. Light power intensity was ~109 mW/cm^2 at the samples position. A potentiostat (Digi-Ivy Inc) was used to collect the current density measurements. A scan rate of 5 mV/s was used for the linear sweep voltammetry (LSV) (*J-V* measurement). A mild agitation was used during the PEC tests and the electrolyte was purged with N_2 gas for at least 5 mins before start of each PEC test. For spectral photoresponse and IPCE measurements, a monochromator (iHR 550) with the solar simulator (equipped with 1.5 AM filter) as the light source was used. A silicon photodiode (Newport 818-UV) was used to calibrate the monochromatic light spectrum. Spectral photoresponse and IPCE measurements were performed in the same setup and electrolyte as used for the current density measurements. All the external biasing potentials here are *versus* Ag/AgCl RE, unless otherwise stated.

7.3 Results and Discussion

CuO NW arrays were synthesized on copper foil and mesh using the thermal oxidation growth method for different growth annealing times and temperatures. After the CuO NW growth, a thin ZnO layer as seeding layer for the ZnO NW growth was deposited on the as-grown CuO NW substrates by RF magnetron sputtering. The ZnO NW branches were finally grown on the CuO NW cores using the hydrothermal growth method. A three electrodes configuration (sample as working electrode (WE), Pt coil as counter electrode (CE), and Ag/AgCl (1 M KCl) as reference electrode (RE)) placed in 400 mL of a neutral aqueous electrolyte (0.25 M Na_2SO_4 buffered at pH = 7.25) was used to perform the current density measurements. A constant light power intensity of ~109 mW/cm^2 was tuned on the samples. The spectral photoresponse and incident photon-to-current efficiency (IPCE) measurements were carried out using the same setup and electrolyte as described for the current density measurements. For convenience, ZnO/CuO b-NW arrays for different ZnO NW growth times, and different CuO NW growth annealing times and temperatures are denoted as “b(Xm-ZnO/Yh-Z°C-CuO) NWs”. “X”, “Y”, and “Z” are the ZnO growth time in mins (m), growth annealing time in hours (h), and growth annealing temperature, respectively (for example, “5m-ZnO” means ZnO NWs grown for 5 mins or “3h-400°C-CuO” means CuO NWs grown for 3 hours at 400°C.

Figure 7.1 exhibits the scanning electron microscopy (SEM) images of the CuO NW arrays grown on Cu foil for different annealing times (2h, 3h, 4h or 5h) and temperatures (400°C, 450°C or 500°C). Longer annealing time results in larger average diameter and length (Figures 7.1a-1d), higher density, and darker sample color (see optical images in the insets of Figures 7.1a-1d). The growth of CuO NWs is uniform through the whole area of samples as can be seen by the optical images in the insets of Figures 7.1a-1d. The CuO NW growth mechanism involves two steps;[40]

$$4\mathrm{Cu} + \mathrm{O_2} \rightarrow 2\mathrm{Cu_2O} \qquad (1)$$

$$2\mathrm{Cu_2O} + \mathrm{O_2} \rightarrow 4\mathrm{CuO} \qquad (2)$$

In the first step (equation 1), a Cu_2O layer forms on the surface of copper substrate which serves as the precursor for the CuO growth in the second step (equation 2). The CuO NWs are then formed through rapid and short-circuit diffusion of Cu ions across grain

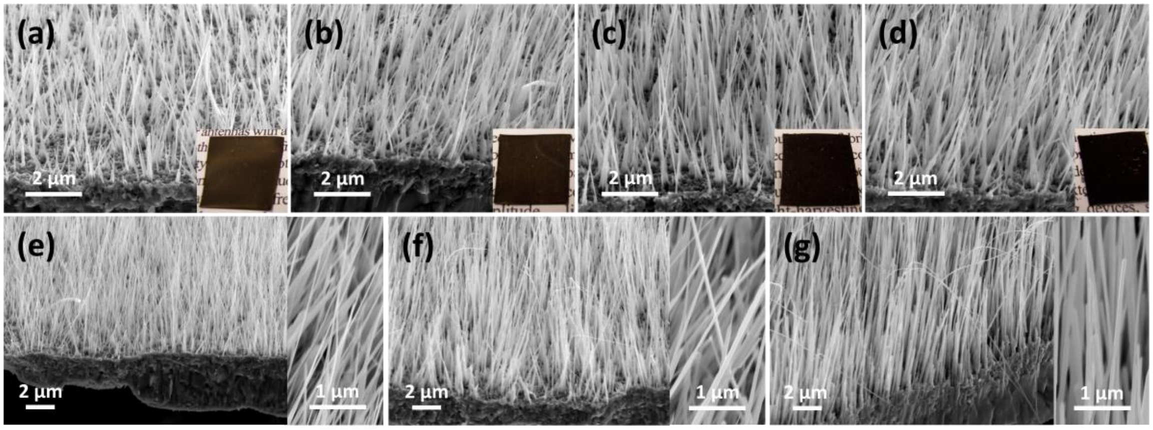

Figure 7.1. SEM images of CuO NW arrays grown at 400°C on Cu foil for different annealing times; (a) 2h, (b) 3h, (c) 4h, and (d) 5h. The insets show the optical images of the corresponding samples. SEM images of CuO NWs grown for 4h on Cu foil at different annealing temperatures; (e) 400°C, (f) 450°C, and (g) 500°C. The insets show the high-magnification images of the corresponding samples.

boundaries and/or defects in the Cu_2O layer.[41] This is evident by the observation of three different parallel copper oxide layers on the copper substrate, including Cu_2O film, CuO layer, and CuO NW array. The order of copper oxide layers on the Cu substrate can also be explained by the diffusion theory in which Cu_2O with higher Cu concentration than CuO is the closest layer to the Cu substrate.[26] The thickness of CuO film underneath the CuO NW layer increases with increasing the annealing time, consistent with longer CuO NWs for longer annealing time. Higher temperature results in larger average length and diameter (insets of Figures 7.1e-1g), and lower NW density. In addition, at higher temperature, bending is observed due to the high aspect ratio of the NWs.

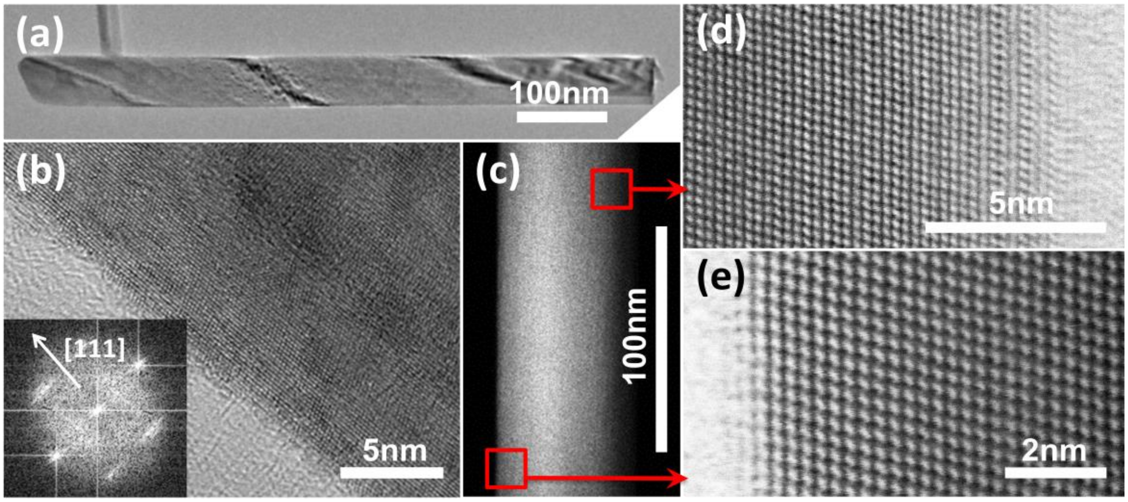

Figure 7.2. (a) Low-magnification bright field TEM image of a single 4h-400°C-CuO NW and (b) high-resolution TEM image of left side of corresponding CuO NW. Inset shows the calculated FFT pattern indicating the CuO NW growth direction. (c) Low-magnification high angle annular dark field STEM image of a similar-sized CuO NW. (d) and (e) High-resolution annular bright field STEM images of NW sides.

Low-magnification bright field (BF) transmission electron microscopy (TEM) image of a single 4h-400°C-CuO NW is shown in Figure 7.2a, exhibiting a diameter of ~55 nm. The CuO NWs show different diameters and lengths for one specific growth temperature and time as realized by the TEM imaging and SEM images (Figure 7.1). By examining different CuO NWs, we can conclude that they are rather defect free. A partly-magnified TEM image of the CuO NW along its length further reveals the quite defect-free structure. The high-resolution TEM (HRTEM) image (Figure 7.2b) exhibits the single-crystalline nature of CuO NW. The calculated lattice spacing is ~0.27 nm corresponding to (110) plane of monoclinic CuO, which is consistent with that reported elsewhere for the CuO NWs synthesized with the same method.[11, 26] The fast Fourier transform (FFT) pattern of the HRTEM image shows CuO single crystallinity oriented along the (111) direction indicating a growth direction of [111]. In addition, the NW surface is smooth without any amorphous layer. The partly-magnified TEM image also shows that the CuO NW has smooth surfaces along its entire length though there is an amorphous layer in some parts which can be due to either long exposure of NWs in air or contamination from the microscope. Low-magnification high angle annular dark field (HAADF) scanning transmission electron microscopy (STEM) image of a similar-sized CuO NW is shown in Figure 7.2c. High-resolution annular bright field (ABF) STEM images of left and right sides of NW clearly reveal the CuO NW single crystallinity.

Figures 7.3a and 7.3b show 4h-400°C-CuO NWs grown on Cu mesh with ZnO seeding layer coating. After the ZnO seeding layer deposition, longer CuO NWs bend. The ZnO/CuO b-NW arrays on Cu foil with 3h-400°C-CuO NW cores, and different ZnO NW branches are shown in Figures 7.3c-7.3h. For different ZnO growth times, ZnO NWs grow through the entire length of CuO NW cores due to the conformal coating of ZnO seeding layer. There is ZnO NW growth in spaces between CuO NWs on flat surface since the ZnO seeding layer covers all surfaces on the substrate. Longer ZnO growth time results in longer ZnO NW branches. Besides the growth time, the size of ZnO NW branches can be tuned by altering the precursor concentrations for ZnO growth.[39] After the ZnO NW growth, longer CuO NW cores bend and bending increases with longer ZnO growth time (Figure 7.3). The growth of ZnO/CuO b-NWs is through the entire area of samples and it is not limited to the small parts.

Figure 7.4a shows low-magnification ABF STEM image of a single ZnO/CuO b-NW clearly exhibiting three different regions including CuO NW core, ZnO seeding

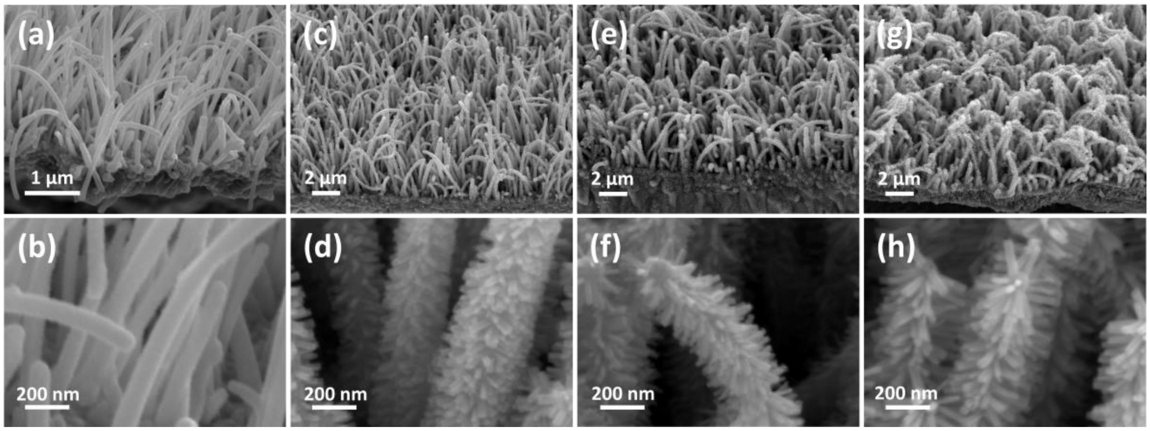

Figure 7.3. (a)-(b) SEM images of 4h-400°C-CuO NWs on Cu mesh with ZnO seeding layer. SEM images of ZnO/CuO b-NWs on Cu foil with 3h-400°C-CuO NW cores, and different ZnO NW branches ((c)-(d) 5m-ZnO, (e)-(f) 10m-ZnO, (g)-(h) 15m-ZnO).

layer, and ZnO NW branches. There is formation of an amorphous layer in interface between CuO NW and ZnO seeding layer. The formation of such an amorphous layer is throughout the entire length of the CuO NW. HAADF STEM image of a single ZnO NW with ~25 nm diameter, selected from Figure 7.4a, is shown in Figure 7.4b. The brighter portion is due to overlap from another ZnO NW sitting on the back of this ZnO NW. High-resolution HAADF STEM images (Figures 7.4c and 7.4d) indicate that the ZnO NW is comprised of the single crystal wurtzite structure, and defect free with smooth and clean surfaces. The modified image of high-resolution HAADF STEM image *via* noise filtering (Figure 7.4e) exhibits a lattice spacing of ~0.26 nm along (0002) plane, which is consistent with that reported elsewhere for the ZnO NWs grown with the same method.[42] The ZnO growth direction for this selected ZnO NW is along [0001] (c-direction). Figure 7.4f shows a high-resolution HAADF STEM image of interface between ZnO NW and ZnO seeding layer. Note that it is hard to clearly see the crystal structure of the ZnO

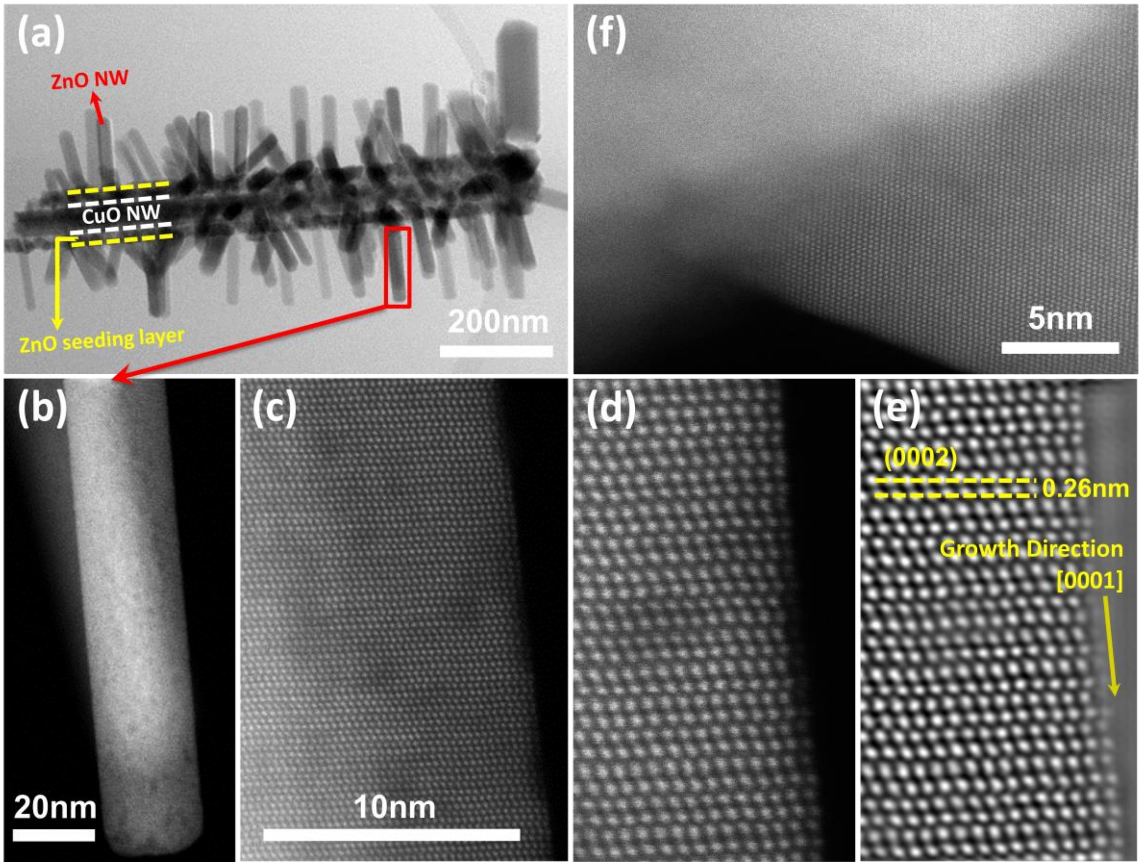
(a)
ZnO NW
CuO NW
ZnO seeding layer
200nm
(f)
5nm
(b)
20nm
(c)
10nm
(d)
(e)
(0002)
0.26nm
Growth Direction
[0001]

Figure 7.4. (a) Low-magnification annular bright field STEM image of a single b(10m-ZnO/4h-400°C-CuO) NW. (b) High angle annular dark field STEM image of labeled single ZnO NW. (c) and (d) High-resolution images of right side of ZnO NW in (b). (e) The corresponding noise-filtered image of (d). (f) High-resolution high angle annular dark field STEM image of interface between a ZnO NW and ZnO seeding layer from a b-NW.

seeding layer due to the overlap of many NWs with the seeding layer. The actual thickness of the ZnO seeding layer on the CuO NW is ~30 nm, which is less than half of predicted deposition thickness due to the high surface area of CuO NWs. Besides the ZnO NWs with crystallographic orientation of [0001] shown in Figures 7.4d and 7.4e, we have also observed ZnO NWs with [110] growth orientation, identified with the <0001> zone axis.

The current density measurements in a neutral solution of ZnO/CuO b-NWs on Cu foil for different CuO growth annealing and ZnO growth times are shown in Figure 7.5. Figures 7.5a and 7.5b exhibit the *J-V* measurements for the ZnO-seeding-layer-coated CuO NWs (CuO/ZnO core/shell NWs (cs-NWs)) grown at 400°C for different annealing times, showing a photocathodic behavior due to the p-type nature of the CuO NWs. The dark and light currents increase with longer annealing time due to the increased reaction surface area. In addition, the CuO NWs grown with longer annealing time provide higher absorption (see optical images in the insets of Figures 7.1a-7.1d), allowing higher photocathodic current. Figure 7.5c illustrates the transient current density under chopped illumination for the corresponding cs-NWs at -0.5 V exhibiting good switching behavior.

The effect of CuO growth annealing time on the light and dark currents of ZnO/CuO b-NWs are exhibited in Figures 7.5d and 7.5e. The ZnO/CuO heterojunction b-NWs also show photocathodic behavior. Longer annealing time results in higher dark and light currents due to the enhanced surface area and probably increased optical absorption which can come from the improved light trapping of longer NWs.[43] The trends for different annealing times in the transient current density (Figure 7.5f) confirm the trends in Figures 7.5d and 7.5e. Figures 7.5g and 7.5h show the effect of ZnO NW growth time on the light and dark currents of b-NWs. The ZnO/CuO b-NWs show higher light and dark currents than the CuO/ZnO cs-NWs resulting in improved photocathodic current which can be due to the increased reaction surface area and enhanced gas evolution as a result of the large curvature of ZnO NWs.[22, 32] The ZnO/CuO b-NWs with 10m-ZnO NWs exhibit the highest dark and light currents between the investigated b-NWs. Despite

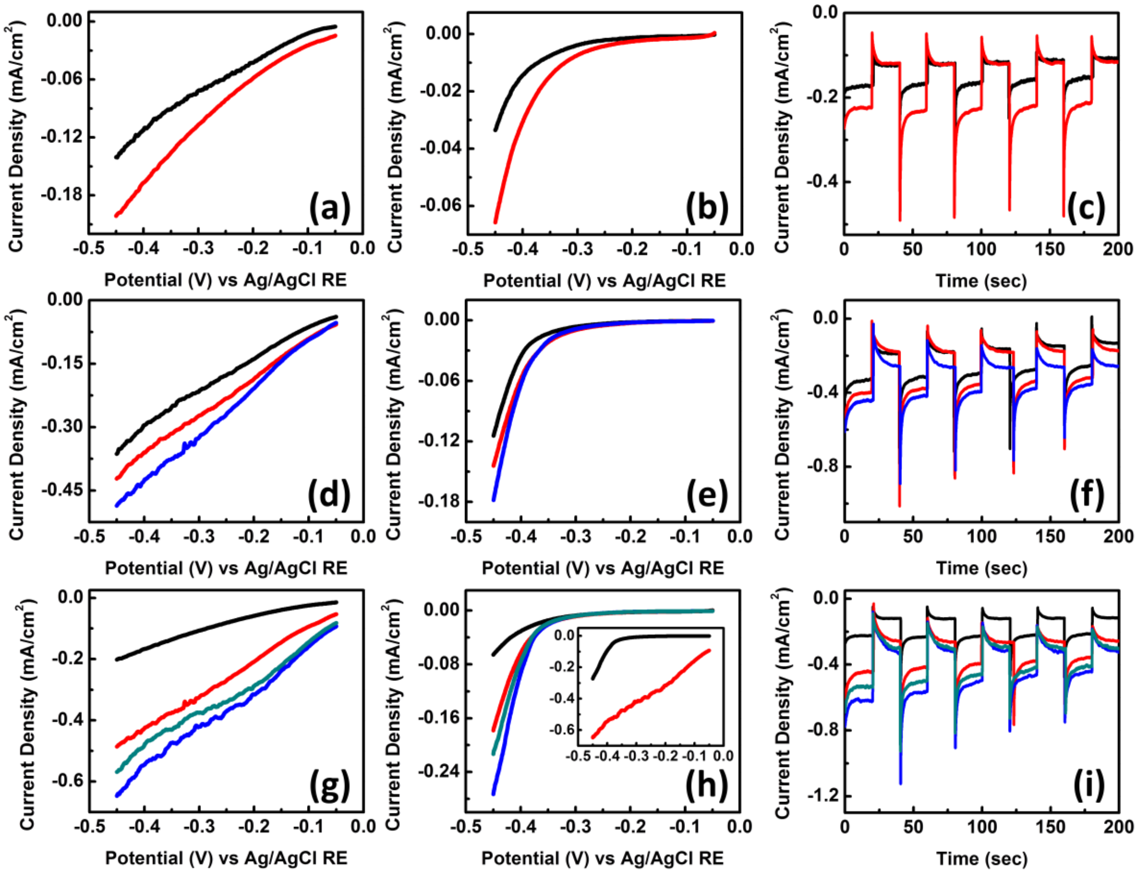

Figure 7.5. Current density of CuO/ZnO cs-NWs grown at 400°C for different annealing times (black line: 2h, red line: 5h) on Cu foil (a) under light illumination and (b) at dark. (c) Transient current density under chopped illumination of the corresponding samples. Current density of 5m-ZnO NWs on CuO NW cores grown at 400°C for different annealing times (black line: 2h, red line: 4h, blue line: 5h) on Cu foil (d) under light illumination and (e) at dark. (f) Transient current density under chopped illumination of the corresponding samples. Current density of 5h-400°C-CuO NW cores on Cu foil with different ZnO NW branches (black line: ZnO seeding layer, red line: 5m-ZnO, blue line: 10m-ZnO, dark cyan line: 15m-ZnO) (g) under light illumination and (h) at dark. The inset in (h) shows the dark (black line) and light (red light) currents for 10m-ZnO NWs on 5h-400°C-CuO NW cores. (i) Transient current density of the corresponding samples. The applied external bias for all the transient current densities in (c),(f),(i) is -0.5 V versus Ag/AgCl RE.

the higher surface area of b-NWs with 15m-ZnO NWs, they show lower dark and light currents than the b-NWs with 10m-ZnO NWs. This may be due to the increased bending of b-NWs with 15m-ZnO NWs (Figure 7.3), which may reduce the effective area for surface reactions leading to lower dark and light currents. The trends for different ZnO growth times in the transient current density (Figure 7.5i) confirm the observed trends in Figures 7.5g and 7.5h. As shown in Figures 7.5f and 7.5i, the b-NWs show good switching behavior for different CuO growth annealing and ZnO growth times. The photocathodic current overshoots in the beginning of switching light on in Figures 7.5c, 7.5f and 7.5i can be due to the accumulation of photogenerated carriers at the interface between NWs and electrolyte, and consequent recombination until reaching a stationary photocurrent. Note that there are also current overshoots under switching off though their magnitude is much smaller. Note that the shapes of dark and light currents in the *J-V* plots for the cs-NWs and b-NWs (Figure 7.5) are similar to that reported for the CuO film photocathodes.[13]

The approximate energy band diagram of the ZnO/CuO heterojunction b-NW in contact with the electrolyte at a reversed biasing potential of -0.45 V is shown in Figure 7.6. For the junction between p-CuO and n-ZnO NWs, the depletion region mostly lies in the p-CuO NW due to much higher doping concentration of n-ZnO NW, which is in the order of 10^{18} cm^{-3} for the ZnO NW grown by the hydrothermal growth method.[44] The calculated doping concentration for the p-CuO NW is about 9×10^{16} cm^{-3}, which is in the range of that reported elsewhere.[41] Furthermore, in general, the radius of CuO NW core is smaller than the length of ZnO NW branch (see Figure 7.6 inset and Figures 7.3 and 7.4). These two factors cause that there is a large band bending in the CuO NW core. The considered band gaps for CuO and ZnO NWs are 1.4 eV[26] and 3.4 eV, respectively. The energy levels of bottom of the conduction band (CB) for the CuO and ZnO are estimated

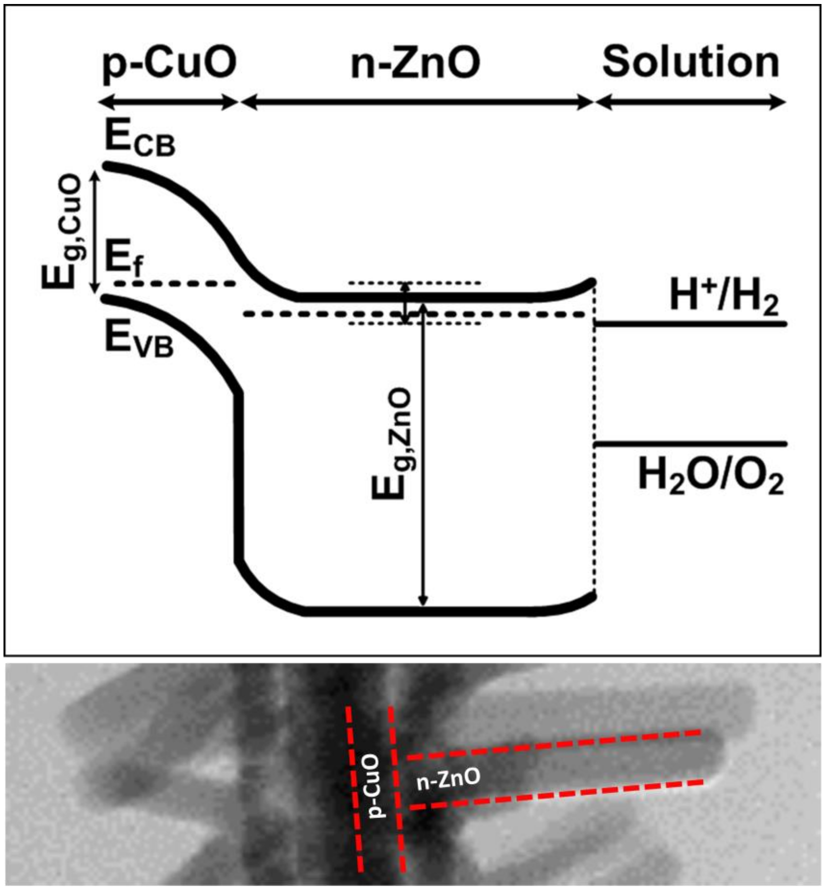

Figure 7.6. Approximate energy band diagram of the ZnO/CuO heterojunction b-NW in contact with the electrolyte at a reversed biasing potential of -0.45 V. The inset shows a STEM image (part of Figure 7.4a) indicating the relative size of the CuO NW radius to the ZnO NW length.

to be 4.07 eV and 4.35 eV,[45, 46] respectively, resulting in the estimated values of 0.28 eV and 1.72 eV for the ΔE_{CB} and ΔE_{VB}, respectively, under the thermal equilibrium condition. Under light illumination, there is a small photocurrent at around zero biasing potential (see Figure 7.5h inset for a photocurrent of 0.09 mA/cm^2 at -0.05 V) due to photogenerated carriers coming from the CuO-ZnO and ZnO-electrolyte junctions. By increasing the reversed biasing potential, the energy levels of ZnO move downward resulting in more band bending at the CuO-ZnO junction (the junction becomes more favorable and effective for charge separation and transport) and reduced barrier at the ZnO-electrolyte junction (see Figure 7.6). These increased band bending and decreased barrier lead to the enhanced light current.

To further evaluate the performance of ZnO/CuO b-NWs, the spectral IPCE of b(5m-ZnO/3h-400°C-CuO) NWs at -0.4 V is presented in Figure 7.7. From 450 nm to 500 nm, there are IPCEs larger than 8% with a maximum efficiency of 10%. The ZnO/CuO b-NWs show broadband photoresponse from UV to near IR region due to coupling of low band gap CuO with high band gap ZnO. The 4h-450°C-CuO NW shows a field effect mobility of 0.0052 $cm^2/(V\text{-}s)$, which is much higher than reported before.[41] Although mobility of the CuO NWs grown by the applied thermal oxidation method is very low which affects the PEC performance shown in Figure 7.5, the PEC performance can significantly be enhanced by increasing the effective surface area. The CuO NWs on Cu mesh provide much higher surface area than that on Cu foil, in which the surface area enhancement has been estimated to be 135%.[47] Note that this estimated value can vary for different meshes with different diameter and density for Cu wires. Figures 7.8a and 7.8b show the SEM images of 4h-400°C-CuO NWs on Cu mesh, in which there is uniform growth on all surfaces of Cu wires in the Cu mesh, and NWs are approximately vertical to the surface. Like on Cu foil, three different parallel copper oxide layers form on the Cu mesh. SEM images of ZnO/CuO b-NWs on Cu mesh with 4h-400°C-CuO NW cores and for two different ZnO growth times ((c)-(d) 5m and (e)-(f) 10m) are exhibited in Figures 7.8c-7.8f, in which ZnO/CuO b-NWs on mesh show the same characteristics as that described earlier for Cu foil.

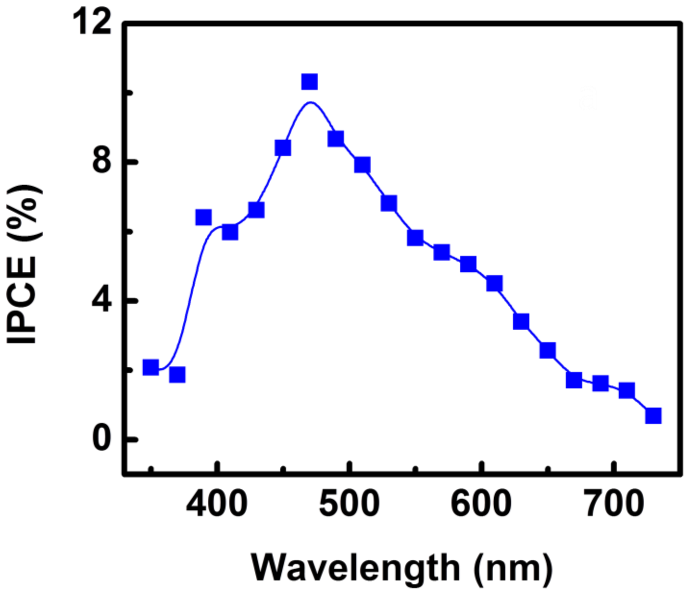

Figure 7.7. Spectral incident photon-to-current efficiency (IPCE) of b(5m-ZnO/3h-400°C-CuO) NWs at -0.4 V versus Ag/AgCl RE.

The current densities of b(10m-ZnO/3h-400°C-CuO) NWs grown on different Cu substrates (foil and mesh) are shown in Figure 7.8g. Due to the increased surface area caused by the mesh substrate, the dark and light currents of b-NWs on Cu mesh are higher than that on Cu foil. To use both sides of mesh, an aluminum reflector (which was angled a little during the *J*-*V* measurement) was used to reflect the incident light and illuminate the back of mesh (see Figure 7.8g inset). As shown, the light current of b-NWs on mesh significantly increases after using the reflector. Photocathode energy conversion efficiency[31] of b-NWs on mesh with the reflector is much higher than that on foil due to much enhanced photocurrent (light current – dark current). Connecting two mesh samples together and illuminating both sides of the connected sample can further increase the photocathode conversion efficiency.

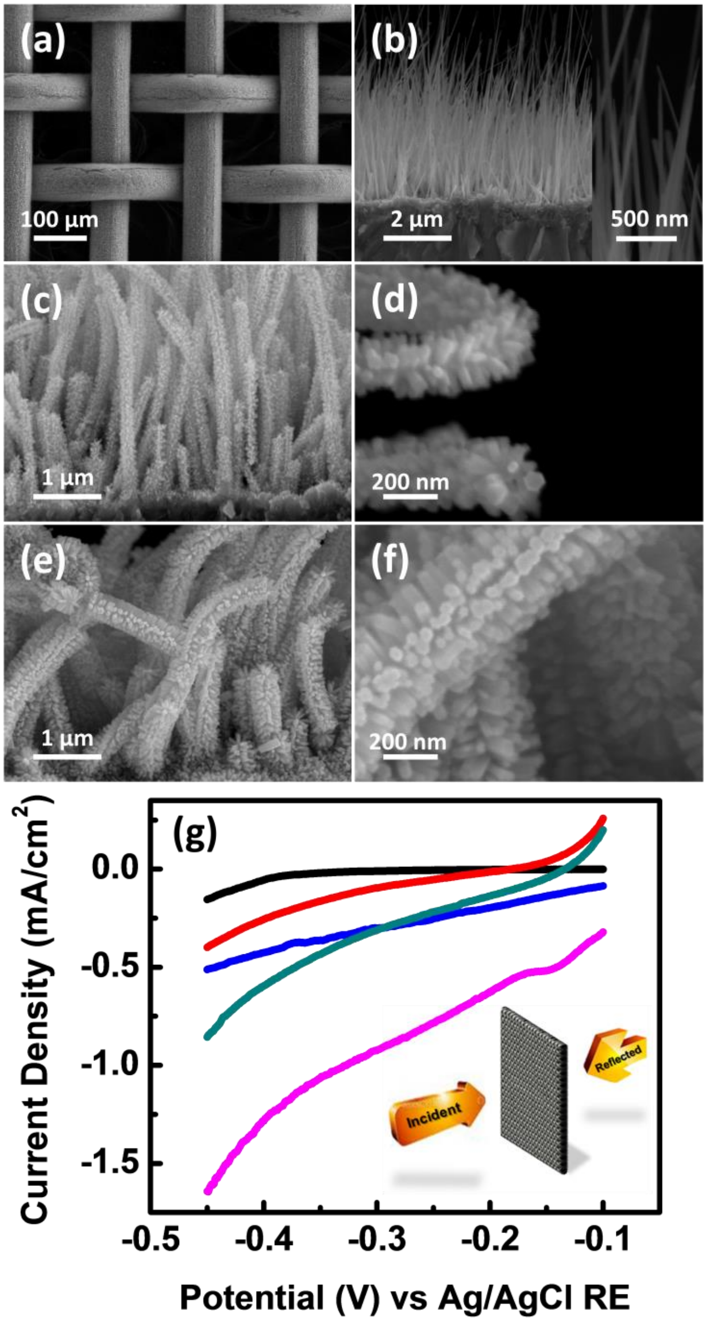

Figure 7.8. (a)-(b) SEM images of 4h-400°C-CuO NWs on Cu mesh. The inset in (b) shows high-magnification image illustrating the CuO NWs diameter size. SEM images of ZnO/CuO b-NWs grown on Cu mesh with 4h-400°C-CuO NW cores and different ZnO NW branches ((c)-(d) 5m-ZnO and (e)-(f) 10m-ZnO). (g) Current density of b(10m-ZnO/3h-400°C-CuO) NWs on Cu foil (black line: dark current, blue line: light current) and on Cu mesh (red line: dark current, dark cyan line: light current, magenta line: light current with the reflector). Inset shows a schematic of mesh sample with incident and reflected light illuminating both sides of the mesh.

Although our reported ZnO/Si b-NWs show high hydrogen production efficiency, they require high biasing potential to drive water splitting.[22, 31] In this regard, the ZnO/CuO b-NWs can be more promising because they are photoactive at low biasing potentials. The main challenge to use the ZnO/CuO b-NWs for efficient/practical hydrogen production is long-term stability since both CuO and ZnO NWs are not stable over long time resulting in photocurrent degradation for b-NWs over time (Figures 7.5f and 7.5i). To improve the stability of ZnO/CuO b-NW photoelectrodes and obtain long-term stability, a decomposition/dissolution-resistant coating layer such as TiO_2 can be used to protect the b-NWs.[31] Using such a coating strategy, we have shown stability of over one day under constant light illumination for the TiO_2/Pt coated ZnO/Si b-NWs.[32]

7.4 Conclusions

In summary, we showed the facile and large-scale fabrication of 3D ZnO/CuO b-NW photocathodes for solar hydrogen production in a neutral electrolyte. The ZnO/CuO b-NWs were grown on different copper substrates for different ZnO and CuO NWs sizes and densities applying simple, cost-effective thermal oxidation and hydrothermal growth methods. The b-NWs were characterized in detail using high-resolution scanning and transmission electron microscopies showing single-crystalline defect-free b-NWs with smooth and clean surfaces. The b-NWs with longer and denser CuO NW cores exhibited higher photocathodic current due to increased surface area. The ZnO/CuO b-NWs presented higher photocurrent than the CuO/ZnO cs-NWs because of increased surface area and improved gas evolution. The ZnO/CuO b-NWs showed a broadband photoresponse from UV to near IR region. The ZnO/CuO b-NWs grown on the copper mesh exhibited a significantly improved photocathodic current than that grown on the copper film due to improved surface area caused by the mesh substrate. These results provide useful insights in the design and fabrication of unique 3D b-NWs mesh electrodes based on low-cost and earth abundant materials for potential cost-effective and high-efficiency solar fuel production.

Chapter 7 was published in *ACS Nano* 2013, A. Kargar, Y. Jing, S. J. Kim, C. Riley, X. Pan, and D. Wang, "ZnO/CuO heterojunction branched nanowires for photoelectrochemical hydrogen generation". The dissertation author was the first author of this paper.

References

1. Paracchino, A.; Laporte, V.; Sivula, K.; Grätzel, M.; Thimsen, E. *Nat. Mater.* **2011**, *10*, 456–461.
2. Kay, A.; Cesar, I.; Grätzel, M. *J. Am. Chem. Soc.* **2006**, *128*, 15714–15721.
3. Chen, X.; Liu, L.; Yu, P. Y.; Mao, S. S. *Science* **2011**, *331*, 746–750.
4. Su, J.; Feng, X.; Sloppy, J. D.; Guo, L.; Grimes, C. A. *Nano Lett.* **2010**, *11*, 203–208.
5. Wang, G.; Ling, Y.; Wang, H.; Yang, X.; Wang, C.; Zhang, J. Z.; Li, Y. *Energy Environ. Sci.* **2012**, *5*, 6180–6187.
6. Qiu, Y.; Yan, K.; Deng, H.; Yang, S. *Nano Lett.* **2011**, *12*, 407–413.
7. Paracchino, A.; Mathews, N.; Hisatomi, T.; Stefik, M.; Tilley, S. D.; Gratzel, M. *Energy Environ. Sci.* **2012**, *5*, 8673–8681.

8. Warren, S. C.; Thimsen, E. *Energy Environ. Sci.* **2012***, 5,* 5133–5146.

9. Ling, Y.; Wang, G.; Reddy, J.; Wang, C.; Zhang, J. Z.; Li, Y. *Angew. Chem., Int. Ed.* **2012**, *51*, 4074–4079.

10. Wang, G.; Wang, H.; Ling, Y.; Tang, Y.; Yang, X.; Fitzmorris, R. C.; Wang, C.; Zhang, J. Z.; Li, Y. *Nano Lett.* **2011**, *11*, 3026–3033.

11. Zhao, X.; Wang, P.; Li, B. *Chem. Commun.* **2010**, *46*, 6768–6770.

12. Jin, W.-M.; Kang, J.-H.; Moon, J. H. *ACS Appl. Mater. Interfaces* **2010**, *2*, 2982–2986.

13. Chiang, C.-Y.; Epstein, J.; Brown, A.; Munday, J. N.; Culver, J. N.; Ehrman, S. *Nano Lett.* **2012**, *12*, 6005–6011.

14. Tilley, S. D.; Cornuz, M.; Sivula, K.; Grätzel, M. *Angew. Chem., Int. Ed.* **2010**, *49*, 6405–6408.

15. Salvador, P. *J. Appl. Phys.* **1984**, *55*, 2977–2985.

16. Sivula, K.; Zboril, R.; Le Formal, F.; Robert, R.; Weidenkaff, A.; Tucek, J.; Frydrych, J.; Grätzel, M. *J. Am. Chem. Soc.* **2010**, *132*, 7436–7444.

17. de Jongh, P. E.; Vanmaekelbergh, D.; Kelly, J. J. *Chem. Mater.* **1999**, *11*, 3512–3517.

18. Hendry, E.; Koeberg, M.; O'Regan, B.; Bonn, M. *Nano Lett.* **2006**, *6*, 755–759.

19. Ling, Y.; Wang, G.; Wheeler, D. A.; Zhang, J. Z.; Li, Y. *Nano Lett.* **2011**, *11*, 2119–2125.

20. Seabold, J. A.; Choi, K.-S. *Chem. Mater.* **2011**, *23*, 1105–1112.

21. Dare-Edwards, M. P.; Goodenough, J. B.; Hamnett, A.; Trevellick, P. R. *J. Chem. Soc., Faraday Trans. 1* **1983**, *79*, 2027–2041.

22. Sun, K.; Jing, Y.; Li, C.; Zhang, X.; Aguinaldo, R.; Kargar, A.; Madsen, K.; Banu, K.; Zhou, Y.; Bando, Y.; *et al. Nanoscale* **2012**, *4*, 1515–1521.

23. Yang, X.; Wolcott, A.; Wang, G.; Sobo, A.; Fitzmorris, R. C.; Qian, F.; Zhang, J. Z.; Li, Y. *Nano Lett.* **2009**, *9*, 2331–2336.

24. Cho, I. S.; Chen, Z.; Forman, A. J.; Kim, D. R.; Rao, P. M.; Jaramillo, T. F.; Zheng, X. *Nano Lett.* **2011**, *11*, 4978–4984.

25. Su, J.; Guo, L.; Bao, N.; Grimes, C. A. *Nano Lett.* **2011**, *11*, 1928–1933.

26. Hansen, B. J.; Kouklin, N.; Lu, G.; Lin, I. K.; Chen, J.; Zhang, X. *J. Phys. Chem. C* **2010**, *114*, 2440–2447.

27. Zhang, Z.; Wang, P. *J. Mater. Chem.* **2012**, *22*, 2456–2464.

28. Kargar, A.; Partokia, S. S.; Allameh, P.; May, S.; Niu, M.; Sun, K.; Yang, M.; Wang, D. *Nanotechnology* **2014**, *25*, 205401.

29. Siripala, W.; Ivanovskaya, A.; Jaramillo, T. F.; Baeck, S.-H.; McFarland, E. W. *Sol. Energy Mater. Sol. Cells* **2003**, *77*, 229–237.

30. Cheng, C.; Fan, H. J. *Nano Today* **2012**, *7*, 327–343.

31. Kargar, A.; Sun, K.; Jing, Y.; Choi, C.; Jeong, H.; Jung, G. Y.; Jin, S.; Wang, D. *ACS Nano* **2013**, *7*, 9407–9415.

32. Kargar, A.; Sun, K.; Jing, Y.; Choi, C.; Jeong, H.; Zhou, Y.; Madsen, K.; Naughton, P.; Jin, S.; Jung, G. Y.; *et al. Nano Lett.* **2013**, *13*, 3017–3022.

33. Song, H. S.; Zhang, W. J.; Cheng, C.; Tang, Y. B.; Luo, L. B.; Chen, X.; Luan, C. Y.; Meng, X. M.; Zapien, J. A.; Wang, N.; *et al. Cryst. Growth Des.* **2010**, *11*, 147–153.

34. Kronawitter, C. X.; Vayssieres, L.; Shen, S.; Guo, L.; Wheeler, D. A.; Zhang, J. Z.; Antoun, B. R.; Mao, S. S. *Energy Environ. Sci.,* **2011**,*4,* 3889–3899.

35. Yin, Z.; Wang, Z.; Du, Y.; Qi, X.; Huang, Y.; Xue, C.; Zhang, H. *Adv. Mater.* **2012**, *24*, 5374–5378.

36. Lu, X.; Wang, G.; Xie, S.; Shi, J.; Li, W.; Tong, Y.; Li, Y. *Chem. Commun.* **2012**, *48*, 7717–7719.

37. Guo, Z.; Chen, X.; Li, J.; Liu, J.-H.; Huang, X.-J. *Langmuir* **2011**, *27*, 6193–6200.

38. Zhou, W.; Cheng, C.; Liu, J.; Tay, Y. Y.; Jiang, J.; Jia, X.; Zhang, J.; Gong, H.; Hng, H. H.; Yu, T.; *et al. Adv. Funct. Mater.* **2011**, *21*, 2439–2445.

39. Cheng, C.; Liu, B.; Yang, H.; Zhou, W.; Sun, L.; Chen, R.; Yu, S. F.; Zhang, J.; Gong, H.; Sun, H.; *et al. ACS Nano* **2009**, *3*, 3069–3076.

40. Jiang, X.; Herricks, T.; Xia, Y. *Nano Lett.* **2002**, *2*, 1333–1338.

41. Goncalves, A. M. B.; Campos, L. C.; Ferlauto, A. S.; Lacerda, R. G. *J. Appl. Phys.* **2009**, *106*, 034303.

42. Sun, K.; Jing, Y.; Park, N.; Li, C.; Bando, Y.; Wang, D. *J. Am. Chem. Soc.* **2010**, *132*, 15465–15467.

43. Garnett, E.; Yang, P. *Nano Lett.* **2010**, *10*, 1082–1087.

44. Law, M.; Greene, L. E.; Johnson, J. C.; Saykally, R.; Yang, P. *Nat. Mater.* **2005**, *4*, 455–459.

45. Zainelabdin, A.; Zaman, S.; Amin, G.; Nur, O.; Willander, M. *Appl. Phys. A* **2012**, *108*, 921–928.

46. Wang, P.; Zhao, X.; Li, B. *Opt. Express* **2011**, *19*, 11271–11279.

47. Jung, S.; Yong, K. *Chem. Commun.* **2011**, *47*, 2643–2645.

8. SOLUTION-GROWN 3D CU_2O NETWORKS FOR EFFICIENT SOLAR WATER SPLITTING

8.1 Introduction

Solar energy is believed to be the ultimate energy source to meet the global energy demand due to dramatic growth of world population. Photoelectrochemical (PEC) solar cells harvest solar energy and convert it into hydrogen fuel through water splitting, a very promising sustainable clean energy solution that combines the energy harvesting and storage processes.[1] Hydrogen fuel has higher energy density and zero carbon emission compared to hydrocarbons.

Semiconductor metal oxides have attracted extensive attention as photoelectrode materials.[2-9] Among different metal oxides, cuprous oxide (Cu_2O), a p-type semiconductor, is of particular interest for the PEC solar water splitting and hydrogen production,[8-15] due to its distinctive characteristics such as a direct bandgap of 2 eV for the visible light absorption, favorable band positions for the PEC water splitting, and good carrier mobility.[16] A theoretical photocurrent of -14.7 mA/cm^2 with corresponding efficiency of 18% for the light-to-hydrogen conversion has been predicted.[8] Cu_2O is also earth abundant, environmentally benign, and can be made using facile, cost-effective, and scalable fabrication techniques.

Cu_2O nanowire/nanorod (NW/NR) arrays have distinct advantages over Cu_2O bulk/film materials for solar water splitting such as enhanced light absorption, increased surface area for redox reactions, enhanced carrier separation and collection. Cu_2O

NW/NR arrays can be fabricated by a numbers of techniques, such as electrochemical deposition,[10] electrodeposition,[11] anodization,[17] wet chemical growth,[13] oxidation/reduction growth,[18] and atmospheric plasma/wet chemical oxidation methods.[15] Among which, solution growth is very promising for the large-scale fabrication of Cu_2O NW/NR photoelectrodes.

The challenge of Cu_2O photoelectrodes is the instability in the electrolyte under illumination, which limits their practical application for solar hydrogen production. Different coating strategies have been reported to stabilize the Cu_2O photoelectrodes. A thin layer of TiO_2 on the Cu_2O film can protect the Cu_2O photocathode against photocorrosion.[14] CuO coating in the Cu_2O/CuO composite photocathodes minimizes the Cu_2O photocorrosion and improves the electrode stability.[19] A thin layer of NiO_x co-catalyst coating can also enhance the stability of Cu_2O photocathodes.[20] Recently, the Grätzel's group has demonstrated a multi-metal-oxide-layers protection for the Cu_2O films against photocathodic decomposition providing chemical stability for the Cu_2O photoelectrodes.[8] On the other hand, the Cu_2O stability depends on morphology, in which quick removal of photogenerated carriers from the photocathode surface enhances the Cu_2O electrode stability.[21] In this regard, the Cu_2O NW/NR arrays can be better candidates compared to the Cu_2O films because they can show better surface kinetics and hydrogen bubbles can leave the electrode surface faster improving the electrode stability.

In this paper, we report a facile and scalable solution fabrication of 3D Cu_2O NW/NR and network photocathodes for efficient solar water splitting. The growth mechanism and structural characterization of Cu_2O network electrodes are investigated. The effects of Cu_2O growth parameters on the photocathodic current, the photoelectrochemical stability Cu_2O network with/without protection layers, and the Cu_2O network spectal photoresponse and IPCE are all studied in a neutral solution.

8.2 Experimental Section

Device fabrication

To fabricate the Cu_2O NW/NR/network photoelectrodes, first $Cu(OH)_2$ NW arrays were grown directly on Cu foils using a solution growth method.[22] Small pieces of Cu foils (area of 1 cm^2) were cut and cleaned by sonication in Acetone, Isopropanol (IPA), and deionized (DI) water (17.6 MΩ-cm) for 5 mins each case, consecutively and finally rinsed with DI water and dried with N_2 gas. The growth solution was prepared by mixing 13.5 mL of 1 M NaOH (Beads, Fisher Scientific) aqueous solution, 6.5 mL of 0.1 M $(NH_4)_2S_2O_8$ (≥98%, Sigma Aldrich) aqueous solution, and 30 mL DI water (17.6 MΩ-cm) in a glass beaker. The cleaned Cu substrate was then immersed into the growth solution and held for 10 mins (or another desirable time) in which its surface gradually turned into light blue. The as-grown substrate was finally washed with DI water and dried with N_2 flow.

The $Cu(OH)_2$ NW arrays were then converted into the Cu_2O NWs/NRs/networks by annealing under N_2 gas.[23] The furnace temperature was first raised to 120°C for 6 mins, maintained at 120°C for 1 hr, raised to 180°C for 1 hr, kept at 180°C for 1 hr, raised to 500°C or 700°C or another desirable temperature for 1 hr, and kept at this specific temperature for 2 hrs or 4 hrs depending on the desirable growth annealing time. The blue-colored $Cu(OH)_2$ NW substrate converted into a uniform red-colored substrate indicating the transformation of $Cu(OH)_2$ NW array to Cu_2O network. Note that the sample color after annealing at other temperatures was different from that for the sample annealed at 700°C (for example, it was yellowish after annealing at 500°C). The different color for the Cu_2O substrates is an indication of different Cu_2O morphologies or sizes, which can be clearly realized from Figure 8.1. For convenience, the Cu_2O samples are denoted as "Xh-Y°C-Cu_2O", in which "X" and "Y" are the growth annealing time in hours (h) and temperature of last step of annealing process mentioned above (for example, "2h-700°C-Cu_2O" means the Cu_2O is converted at 700°C for 2 hours.

For conversion of $Cu(OH)_2$ NWs to CuO NWs, the annealing procedure was slightly different in which the annealing was carried out at lower temperatures.[24] The temperature was first raised to 120°C or 180°C (depending on the desirable temperature) for 10 mins and kept at this temperature for 3 hrs. The blue-colored $Cu(OH)_2$ NW substrate turned into a uniform black-colored substrate exhibiting the transformation of $Cu(OH)_2$ NWs to CuO NWs.

For electrode stability studies, the 2h-700°C-Cu_2O samples were coated with different metal oxide layers using multi-layer metal oxide protection approach.[8] First, a thin ZnO or Al:ZnO (2%) (AZO) layer was deposited on samples using RF magnetron sputtering (Denton Discovery 18 Sputter System) with 99.9% ZnO or AZO target and argon gas. The sputtering pressure during the deposition was 2.7 mT and the measured thickness of sputtered ZnO or AZO on a glass slide was 25 nm. The ZnO or AZO layer uniformly covered the NRs in the 3D Cu_2O networks due to the substrate rotation during the sputtering deposition. A thin layer of TiO_2 was then deposited on the metal-oxide-coated Cu_2O network substrates using atomic layer deposition (ALD) (Beneq TFS 200

System) at a temperature of 120°C. The measured thickness of deposited TiO_2 was 10 nm based on growth rate of 0.44 Å/cycle on Si(100) film substrate. For the 20 nm-TiO_2 coated network samples, the TiO_2 coating layer was deposited at 250°C with 20 nm thickness. For a post annealing process, the metal-oxides-coated samples were then annealed at 200°C in air for 45 mins. The studied samples for the IPCE were coated with a thin ALD-grown TiO_2 layer, which was deposited at 250°C with 20 nm thickness (the same samples as the 20 nm-TiO_2 coated network samples).

Structural characterization

The samples morphologies were examined on a Philips XL30 field-emission environmental scanning electron microscope (ESEM) at an accelerating voltage of 10.0 kV. X-ray diffraction (XRD) spectrum was collected using a Bruker D8 Discover XRD system. Transmission electron microscopy (TEM) measurements were conducted with a FEI Tecnai G^2 F20 S-TWIN transmission electron microscope, operating at an accelerating voltage of 200 kV. The Cu_2O rods on Cu foil were transferred to the TEM gird by dispersing the Cu_2O network substrate in IPA, dispensing the solution on the TEM grid, and drying it in air for a few mins.

Photoelectrochemical and incident photon-to-current efficiency (IPCE) measurements

Current density measurements were performed in a three-electrode PEC setup (Cu_2O substrate as working electrode (WE), Pt mesh as counter electrode (CE), and

Ag/AgCl (1 M KCl) as reference electrode (RE)) with a 400 mL aqueous solution of 0.25 M Na_2SO_4 (using DI water with 17.6 MΩ-cm) buffered at pH = 7.25 with Phosphate Buffered Saline (PBS). To buffer the 400 mL aqueous solution of 0.25 M Na_2SO_4, two tablets of PBS (Sigma, tablet) were added to the solution resulting in a neutral electrolyte with a pH of 7.25. The sample photocurrent was measured under fixed or manually-chopped illumination from a solar simulator (Newport 67015) using a 150 W Xenon lamp and equipped with 1.5 AM filter. A light power intensity of 100 mW/cm^2 was measured at the sample position. The current density measurements were collected using a potentiostat (Digi-Ivy, Inc). A scan rate of 10 mV/s was used for the linear sweep voltammetry (*J-V* measurement). Note that the scan rate for curves in Figure 8.3a was 5 mV/s instead of 10 mV/s. Photocurrent stability tests were performed by collecting the electrode current under chopped illumination at a constant external biasing potential. During all PEC tests, a mild agitation was used and the electrolyte was constantly purged with a small flow of N_2 gas. The solar simulator equipped with 1.5 AM filter was used as the light source entering the monochromator (iHR 550) for spectral photoresponse measurements. The monochromator light spectrum was calibrated by a silicon photodiode (Newport 818-UV). The spectral photoresponse measurements were performed in the same three-electrode setup as used for the current density measurement with the same mild agitation and small flow of N_2.

8.3 Results and Discussion

The transformation of $Cu(OH)_2$ NWs to Cu_2O NWs/NRs or networks includes two steps as;[23]

$$\mathrm{Cu(OH)_2 \rightarrow CuO + H_2O} \tag{1}$$

$$\mathrm{4CuO \rightarrow 2Cu_2O + O_2} \tag{2}$$

The first product is CuO NWs (equation 1), achieving after annealing the $Cu(OH)_2$ NWs at a low temperature such as 120°C, in which the $Cu(OH)_2$ NWs lose H_2O. This transformation is evident from the sample black color after annealing. In the second step (equation 2), by releasing O_2 at higher temperatures (≥ 400°C), the CuO NWs turned into the Cu_2O NWs/NRs/networks. Note that all the presented Cu_2O NWs/NRs/ networks here were synthesized from the $Cu(OH)_2$ NW arrays grown for 10 mins. Longer time for the $Cu(OH)_2$ growth (30 mins) resulted in having $Cu(OH)_2$ nanotubes (NTs) instead of NWs, consistent with that has been reported.[22] Transformation into Cu_2O NTs by thermal annealing led to cracks and delamination from substrate due to probably the stress from high-temperature reactions leading to the release of H_2O and O_2.

Figure 8.1 shows the scanning electron microscopy (SEM) images of $Cu(OH)_2$ NW array and Cu_2O NWs/NRs/networks synthesized under different conditions. The $Cu(OH)_2$ NW growth is uniform throughout the whole area of sample (Figure 8.1a), which can also be realized by the uniform blue color of the sample. The $Cu(OH)_2$ NWs are not totally vertical to the Cu substrate (Figures 8.1b and 8.1c). Annealing the $Cu(OH)_2$ NW substrates at temperatures of < 500°C, does not much change the sample morphology (Figures 8.1d and 8.1e) in which still there is NW/NR morphology, while annealing at a high temperature of 700°C alters the morphology resulting in conversion of NW array into a 3D porous network-like configuration (Figure 8.1f). The Cu_2O NWs/NRs compose of many small pieces of Cu_2O resulting in having a polycrystalline structure (see Figure 8.1e). The Cu_2O rods in the 3D porous network also have a polycrystalline structure but with higher crystalline degree since mostly each Cu_2O rod consists of a few

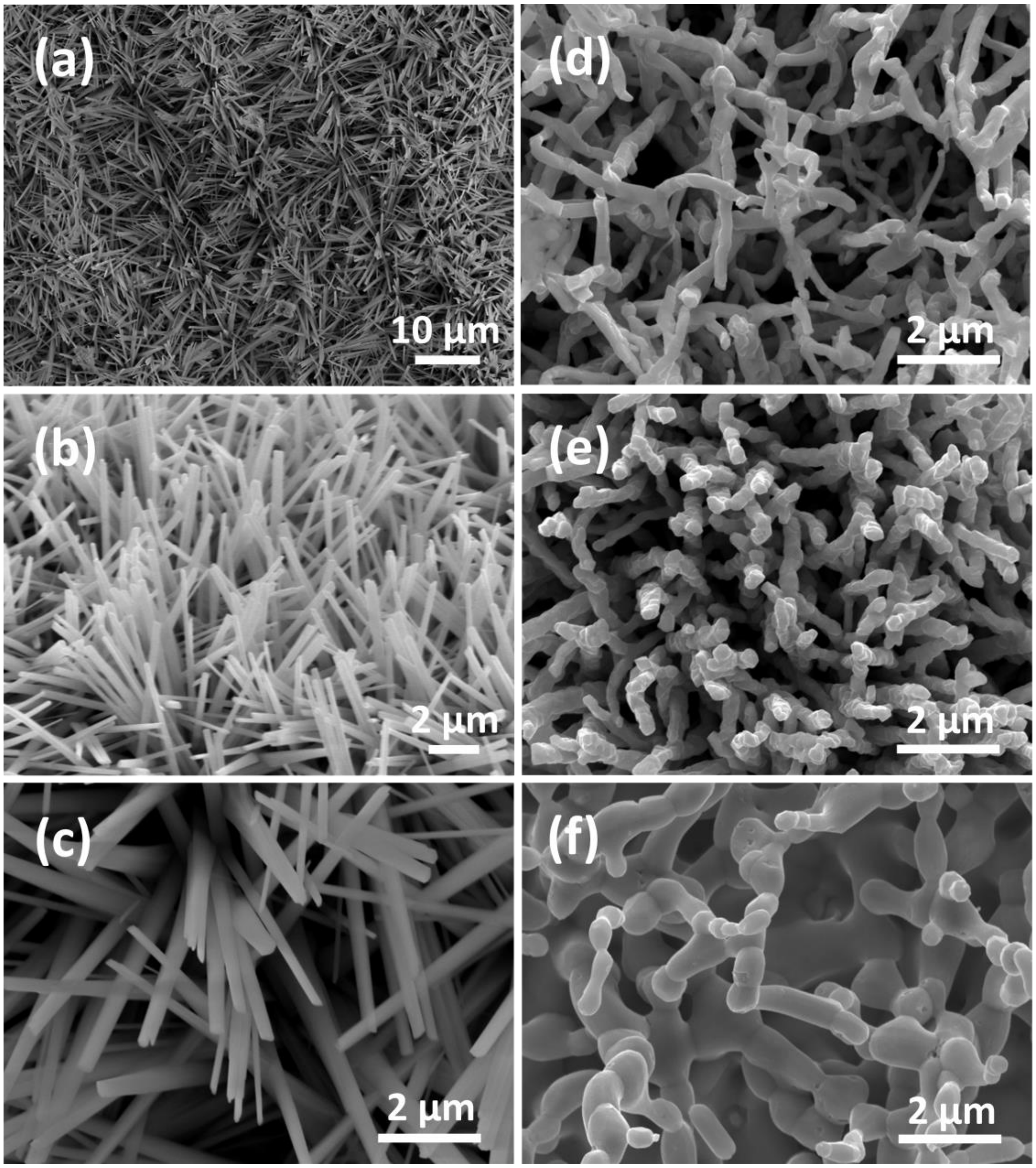

Figure 8.1. SEM images of $Cu(OH)_2$ NW array grown for 10 mins on Cu foil; (a) top view, (b) 45° view, and (c) top view (different magnification) images. Top-view SEM images of Cu_2O NWs/NRs/networks synthesized under different annealing temperatures and times; (d) 2h-500°C-Cu_2O, (e) 4h-500°C-Cu_2O, and (f) 2h-700°C-Cu_2O (porous network).

segments/parts in which each segment/part is single crystalline (see Figures 8.1f and 8.2). As shown in Figure 8.1, increasing the growth temperature and annealing time reduces the surface area.

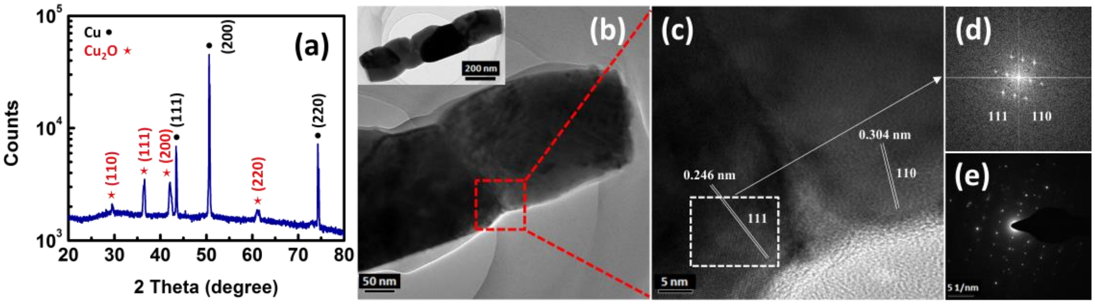

Figure 8.2. (a) XRD pattern of 2h-700°C-Cu_2O network, showing phase-pure Cu_2O rods. The Cu peaks are from the copper substrate. (b) TEM image of a single 2h-700°C-Cu_2O rod, (c) HRTEM image of the corresponding rod, (d) fast Fourier transform (FFT) analysis, and (e) selected area electron diffraction (SAED) pattern. The inset in (b) shows low-magnification TEM image of the corresponding rod in (b).

The X-ray diffraction (XRD) pattern of the 2h-700°C-Cu_2O network sample is shown in Figure 8.2a. The Cu_2O reflection peaks in the XRD pattern are all indexed to the Cu_2O cubic structure. The absence of CuO peaks in the XRD pattern exhibits that the sample is phase-pure Cu_2O revealing the complete transformation of $Cu(OH)_2$ to Cu_2O. The Cu peaks, indexed to the (111), (200) and (220) crystal planes of metallic copper, are from the Cu substrate. The (111) and (200) orientations are the main reflection peaks for the 3D porous Cu_2O network. A preferred orientation of (111) can be seen though both (111) and (200) orientations have almost similar intensities. The Cu_2O photocathodes with different crystallographic orientations give different PEC performances as different orientations show different conductivity properties.[9, 19, 25] It has been reported that (111) orientation has higher carrier mobility,[9, 26] and PEC performance than other orientations.[9, 25]

A transmission electron microscopy (TEM) image of a single 2h-700°C-Cu_2O rod is exhibited in Figure 8.2b with its low-magnification image in the inset. The Cu_2O rod consists of a few segments/parts which can also be realized from the SEM image in Figure 8.1f. The high-resolution TEM (HRTEM) image of the corresponding rod in the border of two segments/parts (Figure 8.2c) shows interplanar spacings of 0.246 nm and 0.304 nm consistent with the (111) and (110) lattice planes of cubic-phase cuprous oxide, respectively. The lattice planes in the HRTEM image are well matched with those in the XRD pattern. The twist in the growth direction makes the structure polycrystalline. Fast Fourier transform (FFT) analysis and selected area electron diffraction (SAED) pattern are shown in Figures 8.2d and 8.2e, respectively. The SAED pattern also exhibits that the whole rod is polycrystalline.

The CuO NWs, synthesized from annealing of $Cu(OH)_2$ NWs at low temperatures of 120°C or 180°C, do not show a significant photocurrent, while the Cu_2O NWs/NRs/networks exhibit considerably enhanced photocurrent (Figure 8.3a). There are some cracks and missing parts in the CuO NWs, possibly due to the stress from releasing H_2O, which may explain their very low photoactivity. Better crystalline structure, coming from annealing at higher temperatures, and higher Cu_2O carrier mobility[18] may also explain the improved photocathodic activity of Cu_2O NWs/NRs/networks compared to the CuO NWs. The effects of growth annealing time and temperature on the current density of Cu_2O electrodes are shown in Figure 8.3a. The Cu_2O NWs/NRs/networks made under different growth annealing times and temperatures show photocathodic behavior because of p-type nature of Cu_2O. The dark current for different annealing times and temperatures is very small (<0.075 mA/cm^2 at the scanned potential range of 0.26-0.5 V versus reversible hydrogen electrode (RHE)) (see Figure 8.3a inset), while there are large light currents showing high photoactivity for these Cu_2O NWs/NRs/networks. The

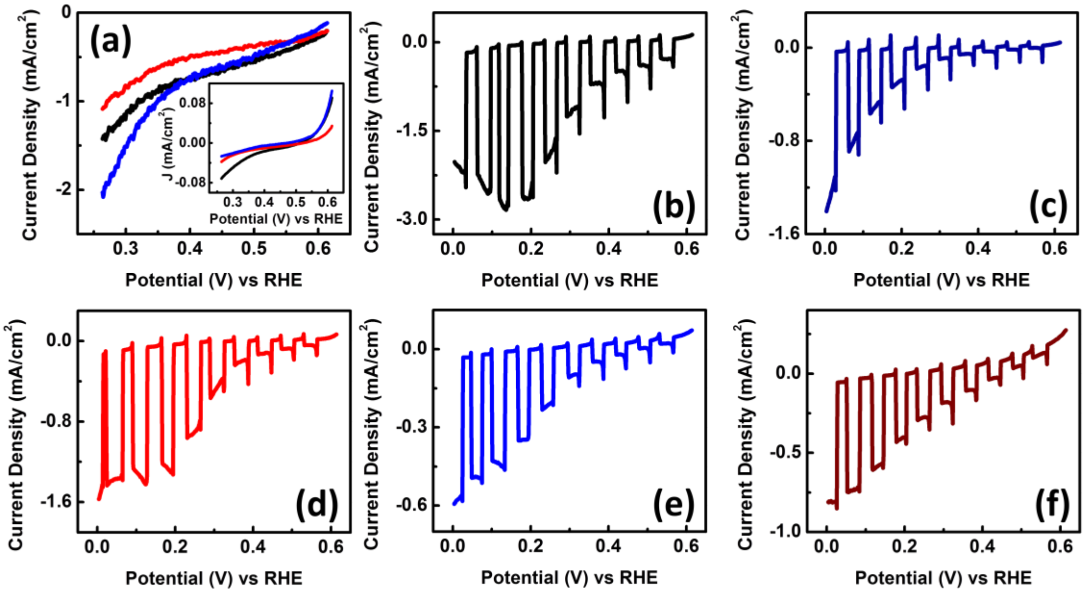

Figure 8.3. (a) Current density under illumination of Cu_2O NWs/NRs/networks synthesized under different annealing temperatures and times (black: 2h-500°C-Cu_2O, red: 4h-500°C-Cu_2O, blue: 2h-700°C-Cu_2O). The inset shows dark current of the corresponding samples. Current density under chopped illumination of 2h-700°C-Cu_2O networks with different metal oxide coatings; (b) bare sample, (c) 20-nm-TiO_2 coated sample, (d) ZnO/TiO_2 coated sample, (e) ZnO/TiO_2 coated sample with post annealing, and (f) AZO/TiO_2 coated sample with post annealing. The thickness of TiO_2 in (d)-(f) is 10 nm.

dark and light currents reduce with increasing the annealing time because of decreased reaction surface area shown in Figure 8.1. Increasing the annealing temperature from 500°C to 700°C also decreases the dark current based on the reduced surface area, while it increases the light current. As a result, the 3D porous Cu_2O network presents the lowest dark and highest light currents resulting in the highest photocathodic current between the investigated structures here (light current – dark current = –2.05 mA/cm^2 at +0.265 V versus RHE). The enhanced photocathodic current of the porous Cu_2O network than the Cu_2O NWs/NRs may be due to better crystallinity, coming from annealing at higher temperature. As mentioned earlier, some Cu_2O crystal orientations can provide higher conductivity and PEC performance than others,[9, 25, 26] therefore different crystalline structure or arrangement of the Cu_2O network may also explain their improved photocathodic behavior. Moreover, the 3D porous network structure may be effective in the enhanced photocathodic activity since it can improve the light trapping due to higher internal light scattering. The 3D Cu_2O network may also be considered as a textured micro-sized Cu_2O substrate. Higher light trapping in the textured substrates results in improved short circuit current increasing the solar cell efficiency.[27, 28]

It is difficult to directly compare the photocathodic performance of the 3D porous Cu_2O network with that of the reported Cu_2O photocathodes in literature because the PEC measurement conditions are slightly different. However, the photocathodic current of 2h-700°C-Cu_2O network is much higher than the reported photocathodic currents for the Cu_2O NWs,[10, 13, 15, 20] or the Cu_2O films.[9, 12, 15, 19] Furthermore, it is comparable to the performance of best reported Cu_2O film photocathode in literature to the best of our knowledge, which was synthesized by ectrodeposition.[8, 25] The PEC performance of Cu_2O photocathodes is strongly pH-dependent,[14, 29] thus photocurrent of the 3D Cu_2O network may further be increased by performing the PEC tests in an electrolyte with a lower pH compared to the pH = 7.25 used here.

Despite the high photocathodic current of the Cu_2O network photoelectrodes, they are not stable based on the Cu_2O instability in electrolyte resulting in reductive decomposition and Cu formation at the sample surface according to;

$$Cu_2O + 2H^+ + 2e^- \rightarrow 2Cu + H_2 \qquad (3)$$

To be useful for practical hydrogen production, these promising 3D Cu_2O network photoelectrodes need to be stabilized for a long time. Among various Cu_2O stabilization strategies mentioned earlier, the multi-metal-oxide-layers protection strategy[8] can be a promising approach because it provides long-term stability for unstable Cu_2O photoelectrodes.[29] Moreover, this strategy is a general approach and can be applied on different Cu_2O photocathodes with various structures and morphologies. This strategy also enables the Cu_2O photocathodes can work in different environments/electrolytes with different pHs giving the flexibility to these electrodes to be matched with different environments.[14]

Figures 8.3b-8.3f exhibit the current density under chopped illumination of the Cu_2O networks with various metal oxide coatings. Note that the curve in Figure 8.3b for the bare Cu_2O network is from a similar-fabricated sample as the sample in Figure 8.3a, which was scanned up to 0 V versus RHE for the current density measurement. The cathodic light current of bare Cu_2O network increases with reducing biasing potential (versus RHE) until it reaches a peak and after that, it starts to reduce, consistent with the reported observation elsewhere.[25] The maximum photocathodic current (light current – dark current) of the 3D porous Cu_2O network is -2.78 mA/cm^2 at 0.135 V versus RHE. The 20 nm-TiO_2-coated Cu_2O network shows lower dark and light currents than the bare network, resulting in lower photocathodic current (Figure 8.3c) due to low conductivity of TiO_2. However the current density at 0 V versus RHE is not much lower than that of bare Cu_2O network since the light current is increasing with reducing the biasing voltage (versus RHE) throughout the whole potential range in which there is no peak. The Cu_2O network coated with ZnO and 10 nm-TiO_2 layers have lower photocathodic current (Figure 8.3d) than the bare Cu_2O network because of low conductivity of both ZnO and TiO_2. As mentioned earlier, the ZnO coating layer was deposited by sputtering, while the TiO_2 layer was deposited by ALD. The ALD deposition provides higher quality film than the sputtering and this may affect the level of photocurrent compared to the case that both ZnO and TiO_2 layers are deposited by ALD. Annealing the ZnO/TiO_2-coated Cu_2O network at 200°C further reduces the photocathodic current (Figure 8.3e), which can be because of the increased resistivity for the sputtered ZnO layer.[30] Replacing the ZnO coating layer with a AZO layer in the post-annealed sample improves the photocurrent (Figure 8.3f), which can be explained by the increased carrier concentration in the AZO layer.[8] The multi-metal-oxides coated samples do not show any peak in their photocathodic current (Figures 8.3c-8.3f), while the bare Cu_2O sample exhibits a peak as discussed earlier (Figure 8.3b).

The light current of bare Cu_2O network significantly reduces after a very short time due to the Cu_2O decomposition mentioned above (see Figure 8.5b for this decomposition). The red color of sample also changed to black after the PEC measurement probably indicating this reductive decomposition.[8] The cyclic voltammetry measurement (not shown here) also exhibited corrosive peaks further showing instability of bare Cu_2O network. The 10 nm TiO_2 coating layer improves the stability but not

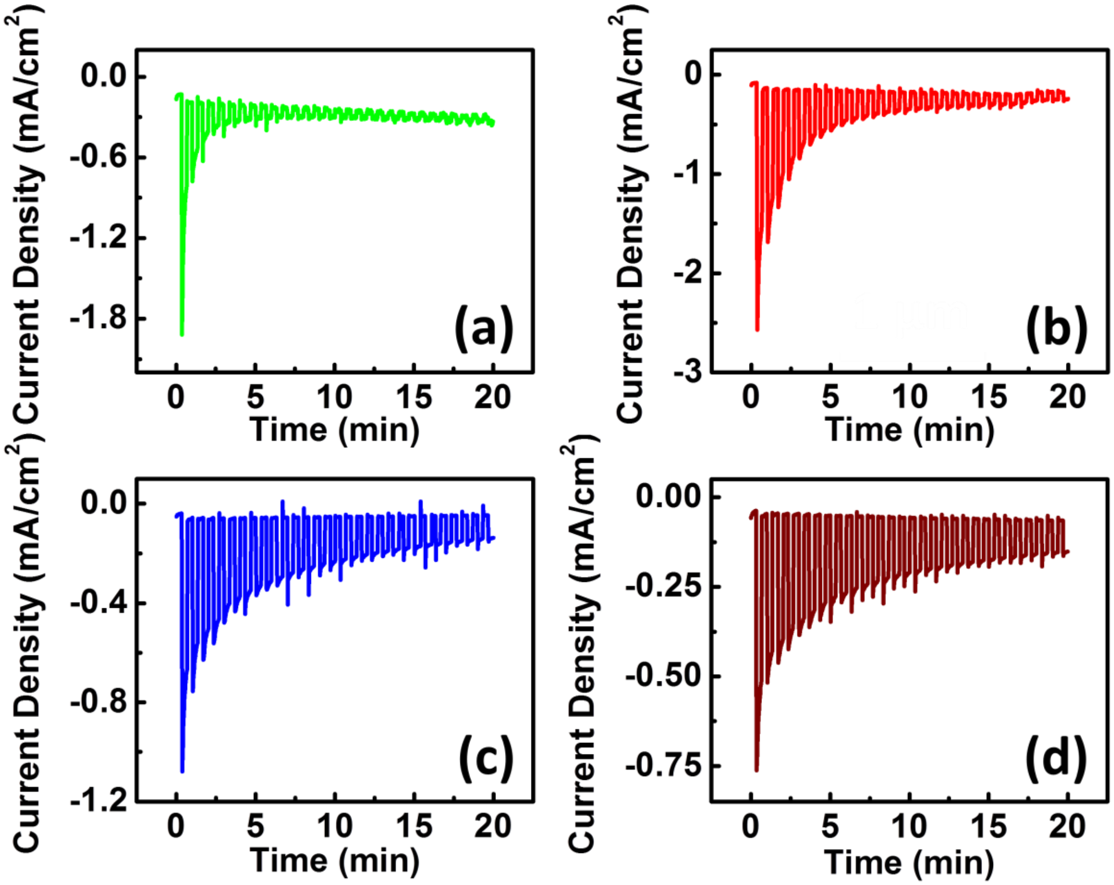

Figure 8.4. Transient current density under chopped illumination at 0 V versus RHE for 2h-700°C-Cu_2O networks with different metal oxide coatings; (a) 10-nm-TiO_2 coated sample, (b) ZnO/TiO_2 coated sample, (c) ZnO/TiO_2 coated sample with post annealing, and (d) AZO/TiO_2 coated sample with post annealing.

considerably (Figure 8.4a). This is because the TiO_2 growth is not uniform and there are parts on the Cu_2O rods in which the TiO_2 coverage is not complete. The non-uniformity of TiO_2 coating layer on the Cu_2O rods may be due to formation of HCl by reaction of $TiCl_4$ and H_2O precursors in the ALD chamber as HCl can etch Cu_2O. Note that the presented stability here for the TiO_2-coated Cu_2O network is better compared to that reported for the TiO_2-coated Cu_2O films,[8] which can be due to better gas evolution of Cu_2O rods. The stability test for the Cu_2O network covered with the ZnO stability

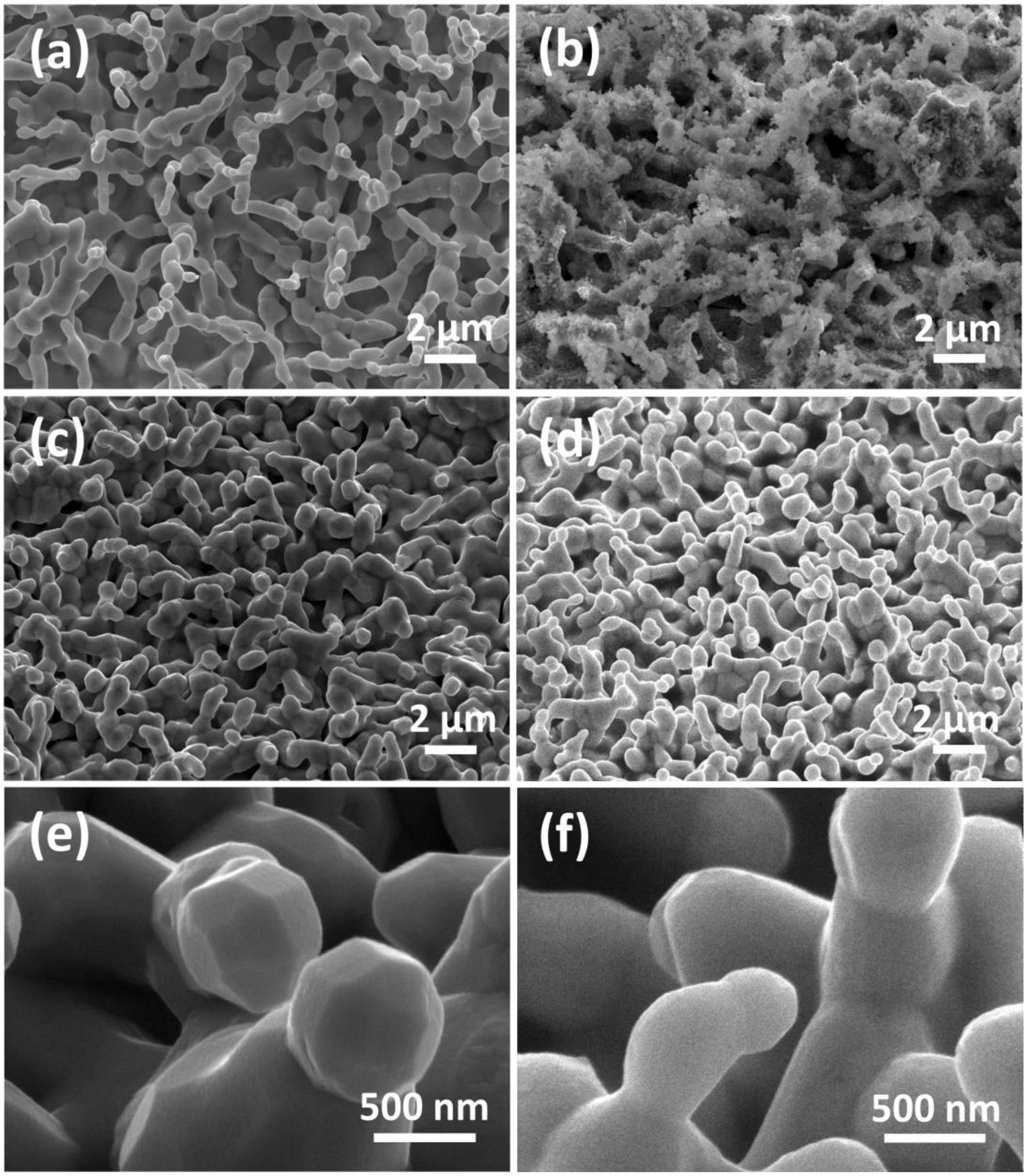

Figure 8.5. SEM images of bare 2h-700°C-Cu_2O network (a) before (as-grown) and (b) after PEC, stability tests, and cyclic voltammetry measurement. SEM images of 2h-700°C-Cu_2O network coated with AZO/TiO_2 followed with the post annealing (c,e) before (as-synthesized) and (d,f) after PEC, stability tests, and cyclic voltammetry measurement.

because of assistance of ZnO layer for uniform growth of TiO_2 on the Cu_2O rods in which there are no uncovered Cu_2O parts (see Figures 8.5c and 8.5e for the AZO/TiO_2-

coated sample as an example). Annealing (in the post-annealing step) the ZnO/TiO_2-coated Cu_2O network improves the sample stability as shown in Figure 8.4c, which can be due to higher crystallinity for the TiO_2 coating layer.[29] Replacing the ZnO layer by an AZO layer in the post-annealed ZnO/TiO_2-coated Cu_2O network further increases the electrode stability (Figure 8.4d), which can be explained by higher stability of the AZO layer than the ZnO layer.[8] The SEM images of the post-annealed AZO/TiO_2-coated Cu_2O network after PEC and stability tests (Figures 8.5d and 8.5f) reveal that there is no damage or decomposition for the Cu_2O rods in the 3D porous network indicating their chemical stability. This shows that the applied stability approach well protects the Cu_2O network against the photocathodic decomposition. The cyclic voltammetry measurement after the stability test also showed that there are no significant corrosive peaks as observed for the bare Cu_2O network. However, the photocurrent still reduces over time which is due to the formation of Ti^{3+} electron traps in the TiO_2 protection layer and the amorphous state of the TiO_2 coating layer.[8, 29] The Ti^{3+} electron traps issue can be solved by depositing the ALD-grown TiO_2 coating layer at higher temperature to provide favorable band alignment for flow of photogenerated electrons to electrolyte.[29] Improving the crystallinity of TiO_2 coating layer to improve its chemical stability can be achieved by annealing at a specific temperature that assists the crystallization of anatase phase.[29]

To further evaluate the performance of Cu_2O network photoelectrode, the spectral incident photon-to-current efficiency (IPCE) for the 20 nm-TiO_2-coated porous Cu_2O network at 0 V versus RHE is calculated and presented in Figure 8.6. The shape of spectral IPCE is consistent with that reported for the Cu_2O film photocathodes.[8, 9] The spectral IPCE becomes almost zero at 630 nm confirming the Cu_2O bandgap which is

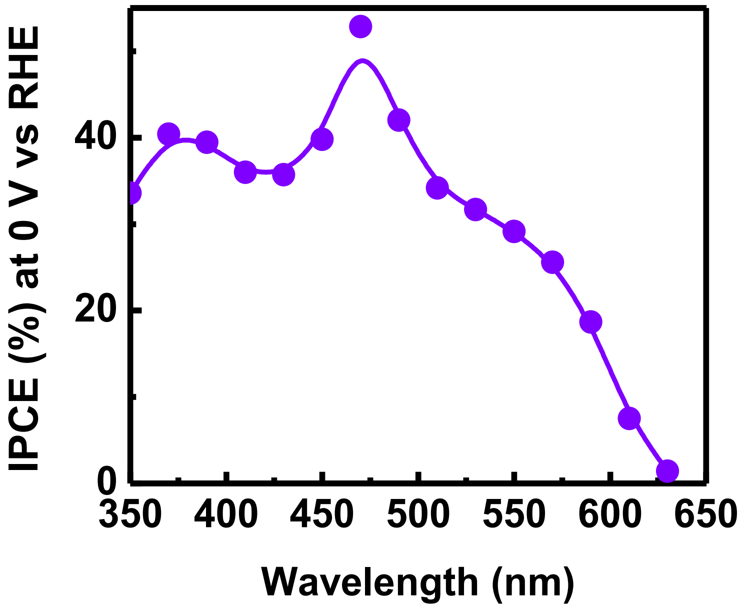

Figure 8.6. Spectral incident photon-to-current efficiency (IPCE) of 20-nm-TiO_2 coated 2h-700°C-Cu_2O network at 0 V versus RHE.

around 2 eV. From 350 nm to 510 nm, there are high IPCEs with an average of 39%. As discussed earlier, the 3D porous network structure may be effective for enhanced light trapping, which can assist to obtain the high IPCEs observed in Figure 8.6.

8.4 Conclusions

In summary, we report the facile and scalable solution fabrication of low-cost Cu_2O nanowires/nanorods and 3D Cu_2O networks for efficient solar water splitting and hydrogen generation. Compared to the Cu_2O nanowire/nanorod photocathodes, the 3D porous Cu_2O network electrodes, composed of phase-pure Cu_2O rods, offered high photocathodic current and IPCE in the pH neutral electrolyte. Using a robust metal oxide, such as TiO_2, protection layer, significantly enhanced electrode stability was demonstrated, promising a practical solution for using cost-effective Cu_2O photoelectrodes for solar fuel generation.

Chapter 8 was published in *Nanotechnology* 2014, A. Kargar, S. S. Partokia, M. T. Niu, P. Allameh, M. Yang, S. May, J. S. Cheung, K. Sun, X. Ku, and D. Wang, “Solution-grown 3D Cu_2O networks for efficient solar water splitting”. The dissertation author was the first author of this paper.

References

1. Lewis, N. S.; Nocera, D. G. *Proc. Natl. Acad. Sci USA* **2006**, *103*, 15729-35.

2. Wang, G.; Wang, H.; Ling, Y.; Tang, Y.; Yang, X.; Fitzmorris. R. C.; Wang, C.; Zhang, J. Z.; Li. Y. *Nano Lett.* **2011**, *11*, 3026-33.

3. Kay, A.; Cesar, I.; Grätzel, M. *J. Am. Chem. Soc.* **2006**, *128,* 15714-21.

4. Thimsen, E.; Le Formal, F.; Grätzel, M.; Warren, S. C. *Nano Lett.* **2010,** *11*, 35-43.

5. Qiu, Y.; Yan, K.; Deng, H.;Yang, S. *Nano Lett.* **2011**, *12*, 407-13.

6. Wang, G.; Ling, Y.; Wang, H.; Yang, X.; Wang, C.; Zhang, J. Z.; Li, Y. *Energy Environ. Sci.* **2012**, *5,* 6180-7.

7. Zhao, X.; Wang, P.; Li, B. *Chem. Commun.* **2010**,*46*, 6768-70.

8. Paracchino, A.; Laporte, V.; Sivula, K.; Grätzel, M.; Thimsen, E. *Nat. Mater.* **2011,***10***,** 456-61.

9. Nian, J-N.; Hu, C-C.; Teng, H.; *Int. J. Hydrogen Energy* **2008**, 33, 2897-903.

10. Chen, L.; Shet, S.; Tang, H.; Wang, H.; Deutsch, T.; Yan, Y.; Turner, J.; Al-Jassim, M.; *J. Mater. Chem.* **2010,** 20**,** 6962-7.

11. Inguanta, R.; Sunseri, C.; Piazza, S. *Electrochemical and Solid-State Lett.* **2007,**10, K63-K6.

12. Ma, L.; Lin. Y.; Wang, Y.; Li. J.; Wang. E.; Qiu. M.; Yu, Y. *J. Phys. Chem. C* **2008**, *112*, 18916-22.

13. Qian, F.; Wang, G.; Li, Y. *Nano Lett.* **2010,**10, 4686-91.

14. Siripala, W.; Ivanovskaya, A.; Jaramillo, T. F.; Baeck, S-H.; McFarland, E. W. *Sol. Energy Mater. Sol. Cells* **2003 ,**77, 229-37.

15. Sunkara, S.; Vendra, V. K.; Kim, J. H.; Druffel, T.; Sunkara, M. K. *Catal. Today* **2013,**199, 27-35.

16. Mittiga, A.; Salza, E.; Sarto, F.; Tucci, M.; Vasanthi, R. *Appl. Phys. Lett.* **2006,** *88* 163502.

17. Deo, M.; Mujawar, S.; Game, O.; Yengantiwar, A.; Banpurkar, A.; Kulkarni, S.; Jog, J.; Ogale, S. *Nanoscale* 2011, **3,** 4706-12.

18. Liao, L.; Yan, B.; Hao, Y. F.; Xing, G. Z.; Liu, J. P.; Zhao, B. C.; Shen, Z. X.; Wu, T. Wang, L.; Thong, J. T. L.; Li, C. M., Huang, W.; Yu, T. *Appl. Phys. Lett.* **2009**, *94*, 113106.

19. Zhang, Z.; Wang, P. *Journal J. Mater. Chem.* **2012**, *22* ,2456-64.

20. Lin, C-Y.; Lai, Y-H.; Mersch, D.; Reisner, E.; *Chem. Sci.* **2012**, *3*,3482-7.

21. Mor, G. K.; Varghese, O. K.; Wilke, R. H. T.; Sharma, S.; Shankar, K.; Latempa, T. J.; Choi, K-S.; Grimes, C. A. *Nano Lett.* **2008**, *8*, 1906-11.

22. Zhang, W.; Wen. X.; Yang, S.; Berta, Y.; Wang, Z. L. *Adv. Mater.* **2003,** *15*, 822-5.

23. Wen, X.; Xie, Y.; Choi, C. L.; Wan, K. C.; Li, X-Y.; Yang, S. *Langmuir* **2005**, *21*, 4729-37.

24. Wen, X.; Zhang, W.; Yang, S.; *Langmuir*, **2003**, *19*, 5898-903.

25. Paracchino, A.; Brauer, J. C.; Moser, J. E.; Thimsen, E.; Grätzel, M.; *J. Phys. Chem. C* **2012,***116,* 7341-50.

26. Kuo, C-H.; Yang, Y-C.; Gwo, S.; Huang, M. H. *J. Am. Chem. Soc.* **2010**, *133* 1052-7.

27. Liu, Y.; Das, A.; Xu, S.; Lin. Z.; Xu, C.; Wang, Z. L.; Rohatgi, A.; Wong, C. P. *Adv. Energy Mater* **2012**, *2*, 47-51.

28. Ko, S. H.; Lee, D.; Kang, H. W.; Nam, K. H.; Yeo, J. Y.; Hong, S. J.; Grigoropoulos, C. P. Sung, H. J. *Nano Lett.* **2011**, *11*, 666-71.

29. Paracchino, A.; Mathews, N.; Hisatomi, T.; Stefik, M.; Tilley, S. D.; Gratzel, M.; *Energy Environ. Sci.* **2012**, *5*, 8673-81.

30. Chu, S-Y.; Water, W.; Liaw, J-T. *J. Euro. Ceram. Soc*. **2003**, *23*, 1593-8.

9. NIO$_X$-FE$_2$O$_3$-COATED P-SI PHOTOCATHODES FOR ENHANCED SOLAR WATER SPLITTING IN NEUTRAL PH WATER

9.1 Introduction

Photoelectrochemical (PEC) hydrogen production through solar water splitting is one of the promising clean routes to renewable energy sources to minimize the dependency on polluting energy sources,[1-9] which can lead to high solar-to-hydrogen (STH) efficiencies of up to 31.1%.[10] To obtain such high efficiencies for long-time PEC operation, however, major challenges remain in design and engineering of cost-effective stable photoelectrodes which can offer bias-free photoactivity for efficient full PEC systems/devices. Furthermore, offering such a performance in neutral pH water is highly desirable as the natural water resources such as seawater are usually in a neutral condition, and are abundant and easily disposable. Employing a neutral electrolyte for solar water splitting also prevents the undesirable use of strong acids or bases, which can lead to environmental and handling issues.

Silicon is one of the promising materials for the PEC cells considering its unique properties as well as mature fabrication industry.[8, 11-23] However from the electrochemical point of view, the surface of Si photoelectrodes has poor catalytic activity (kinetic limitation) for hydrogen evolution reaction (HER) or oxygen evolution reaction (OER). To accelerate the HER or OER for achieving sufficient hydrogen production, it is essential that a catalyst is added to the electrode surface. Metal oxides have shown promising potential to catalyze the Si surface,[15, 24-26] in which they can also simultaneously stabilize the Si surface against corrosion/oxidation.[15, 24, 26] We have demonstrated that ZnO nanowires (NWs)[12, 27] can catalyze the surface of p-Si NWs for the enhanced HER revealing promise to investigate other proper metal oxides for more efficient HER on the surface of p-Si photocathodes. NiO, a wide band gap metal oxide, can be used as an OER catalyst,[25, 28-30] or a HER catalyst/cocatalyst.[29, 31-36]

In this article, we report facile solution growth of novel nanocomposite films consisting of Fe_2O_3 nanorods (NRs) and NiO_x nanoparticles (NPs), which are used to improve the HER on the inactive surface of p-Si film photocathodes in neutral pH water. Very interestingly, the new NiO_x-Fe_2O_3-coated p-Si photocathodes show photoactivity at 0 V versus reversible hydrogen electrode (RHE) with a cathodic onset potential of 0.25 V versus RHE the in neutral pH water. The achieved performance at zero bias in neutral solution shows promising application of the newly developed photoelectrodes.

9.2 Experimental Section

Device fabrication

Boron doped (p-type) Si(100) wafers with resistivity of 1-20 Ω-cm were cleaned with buffered oxide etching (BOE) solution for 10 sec, rinsed with deionized (DI) water, and dried with N_2 flow. Then, they were immediately transferred to the sputtering machine to deposit a thin SnO_2 layer as seeding layer for the α-Fe_2O_3 NR film growth using RF magnetron sputtering with 99.99% SnO_2 target and argon gas at room temperature. The sputtering pressure was ~10 mTorr during the deposition. The α-Fe_2O_3 NR film was finally grown on the substrate using hydrothermal growth method reported elsewhere with slight modification.[37] Akaganeite (β-FeOOH) NRs were first grown on the SnO_2-coated Si substrate by immersing them in a 45 mL sealed Teflon autoclave

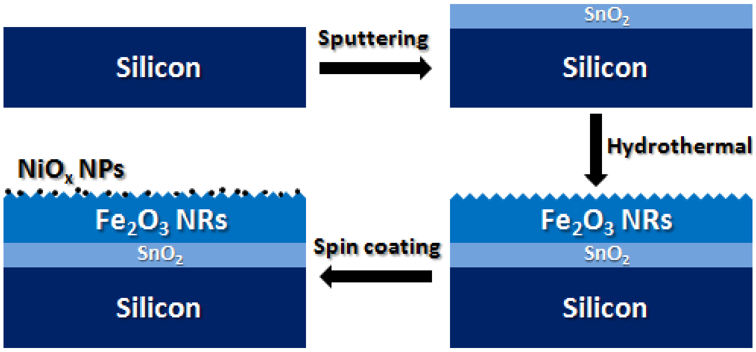

Figure 9.1. Schematic representation of fabrication procedure for the metal-oxide-coated p-Si substrates.

containing a 30 mL aqueous solution consisting of 0.15 M $FeCl_3.6H_2O$ (Iron(III) chloride hexahydrate) (Sigma-Aldrich, ≥99%) and 1 M $NaNO_3$ (Sodium nitrate) (Sigma-Aldrich, ≥99.0%). The deionized (DI) water resistivity and pH of growth solution were 17.6-17.7 MΩ-cm and ~1.44, respectively. The hydrothermal reaction was performed at a temperature of ~110°C, placing the autoclave in a regular oven for 2 hrs. The as-prepared sample was then rinsed carefully with DI water to remove the residues and dried with N_2 flow. After the FeOOH NR growth, the color of Si substrate turned yellowish indicating the FeOOH growth. Finally, the as-grown FeOOH-SnO_2-coated Si substrate was annealed at 450°C in air for 2 hrs to have phase transition from β-FeOOH to α-Fe_2O_3, which was evident with the yellowish color changing to a reddish color. For convenience, Fe_2O_3 NRs synthesized from 2 hrs FeOOH NRs with subsequent 2 hrs annealing in air are denoted as 2h-Fe_2O_3 NRs. The NiO_x solution was prepared by 0.12 M monoethanolamine (MEA, C_2H_7NO) (Sigma-Aldrich) and 0.05 M nickel acetate tetrahydrate ($Ni(OCOCH_3)_2 \cdot 4H_2O$) (Sigma-Aldrich) in 10 mL ethanol. Then, the as-prepared solution was spin-coated on the p-Si or Fe_2O_3-SnO_2-coated p-Si substrates with a subsequent annealing at 300°C for 30 sec on a hot plate. Figure 9.1 exhibits the fabrication procedure for the metal-oxide-coated p-Si substrates. For Pt catalyst deposition, electron beam (e-beam) evaporation was used to deposit 2 nm Pt at a base pressure of 6×10^{-7} Torr and a deposition rate of 0.2 Å/sec on the SnO_2-coated p-Si substrates. To minimize the incident light loss, such a thin thickness for Pt was selected to provide a non-continuous film in the form of nanoparticles.

Characterization

The sample morphology was examined using a Philips XL30 field-emission environmental scanning electron microscope (ESEM) working at an accelerating voltage of 10.0 kV. X-ray photoelectron spectroscopy (XPS) spectra were obtained using a Kratos spectrometer (AXIS Ultra DLD) with a monochromatic Al K_α radiation ($h\upsilon$ = 1486.69 eV) and a concentric hemispherical analyzer. Optical absorption measurements were obtained using a 150 mm integrating sphere connected to a LAMBDA 1050 UV/Vis/NIR spectrophotometer.

Measurements

To evaluate the samples performances, they were bonded to Cu wire at the back using indium, which provides an ohmic contact to the used p-type Si substrate. The edges and backside of samples were sealed using epoxy (Hysol 1C). Current density measurements were performed in a 200 mL aqueous solution of 0.25 M Na_2SO_4 buffered at pH = 7.1 with Phosphate Buffered Saline (PBS, Sigma) (DI water resistivity, 18.2 MΩ-cm) (neutral pH water) with a three-electrode setup, including the sample as working electrode (WE), Pt foil as counter electrode (CE), and Ag/AgCl (1 M KCl) as reference electrode (RE). A light power intensity of 100 mW/cm^2 was tuned at the sample position using a solar simulator (Newport 66905) with a Xenon lamp equipped with 1.5 AM filter. The current density measurements were collected using a potentiostat (Digi-Ivy, DY2300). A scan rate of 10 mV/s was employed for the linear sweep voltammetry (LSV) and cyclic voltammetry (CV) measurements, unless otherwise stated. During the current density measurements, a mild agitation was used and the electrolyte was constantly purged with a small flow of N_2 gas. The applied potentials versus Ag/AgCl RE ($E_{\mathrm{Ag/AgCl}}$) were converted to the potentials versus reversible hydrogen electrode (RHE), E_{RHE}, using the Nernst equation as;

$$E_{\mathrm{RHE}} = E_{\mathrm{Ag/AgCl}} + 0.059\ \mathrm{pH} + E^{0}_{\mathrm{Ag/AgCl}}\ \ (\mathrm{V}) \qquad (1)$$

where pH is the electrolyte pH (7.1 here) and $E^{0}_{\mathrm{Ag/AgCl}} = 0.222$ V for the Ag/AgCl RE in 1 M KCl and at 25°C (Digi-Ivy, Inc.).

9.3 Results and Discussion

Figure 9.2 exhibits scanning electron microscopy (SEM) images of 2h-Fe_2O_3 NRs, which form a nearly continuous but individually separated NRs film, grown on p-Si substrate coated with SnO_2 seeding layer (this structure is referred to as “Fe_2O_3-SnO_2-coated p-Si” hereafter). The thicknesses of the Fe_2O_3 NR film and the SnO_2 seeding layer are ~141 nm and ~82 nm, respectively. The NRs form a vertically elongated textured film

(Figure 9.2b and 9.2c), increasing optical absorption and electrochemical reaction surface area. The Fe_2O_3 NR growth is uniform over the large area (Figure 9.2d) indicating the potential of scaling up the fabricated electrodes. Due to the small size of NiO_x NPs, we were not able to observe them under the SEM imaging. The X-ray diffraction (XRD) analysis of 2h-Fe_2O_3 NRs grown on fluorine-doped tin oxide (FTO) substrate (data not shown here) exhibited the characteristic peaks of α-Fe_2O_3 (hematite). The XPS spectra of Ni 2p and O 1s of NiO_x NPs spin- coated on the Si substrate are exhibited in Figure 9.3a and 9.3b revealing the chemical composition of NiO_x. The nickel XPS spectrum (Figure 9.3a) shows four peaks including a dominant 2p3/2 peak at binding energy of 856.2 eV, a 2p1/2 peak at 873.5 eV (these two are Ni peaks), and two small satellite peaks at 861.2 eV and 880.6 eV. The satellite peaks are because of the X-ray source emitting X-rays of higher photon energy leading to nickel ionization. The oxygen XPS spectrum (Figure 9.3b) exhibits only an O 1s peak corresponding to binding energy of 532.1 eV. Therefore,

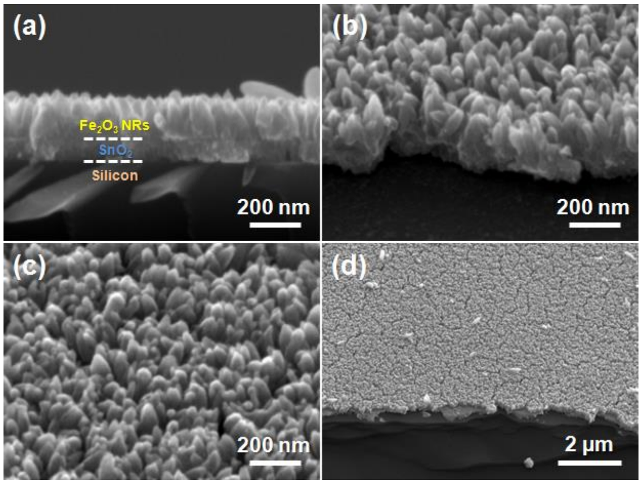

Figure 9.2. High-magnification (a) cross-sectional and (b) tilted view SEM images of 2h-Fe_2O_3 NRs grown on p-Si substrate using SnO_2 as seeding layer. (c) High- and (d) low-magnification 45° view SEM images of the corresponding sample.

there is a good NiO_x formation with the dominant Ni 2p3/2 peak at 856.2 eV and O 1s.

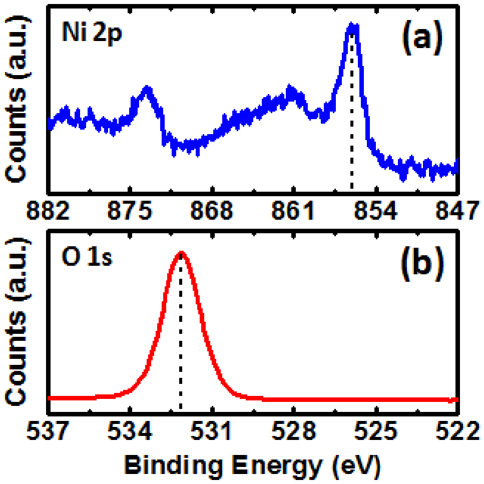

Figure 9.3. (a) Ni 2p and (b) O 1s XPS spectra of NiO_x NPs spin-coated on Si substrate.

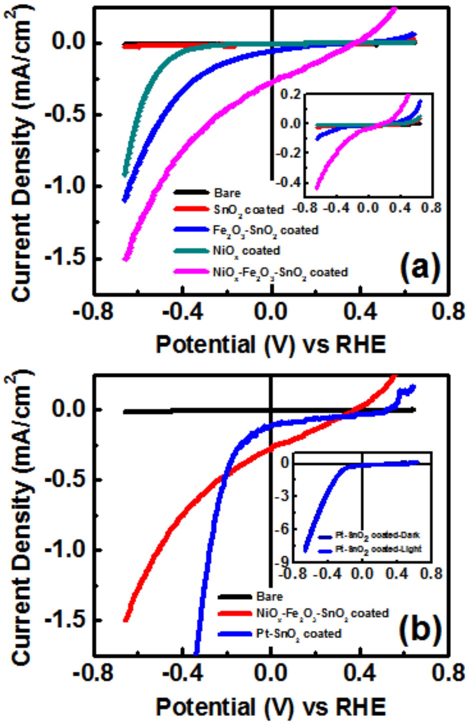

Figure 9.4. Current density under illumination of different metal-oxide-coated p-Si photocathodes measured in the neutral pH water. Inset shows the dark current of the corresponding samples. (b) Current density under illumination of bare and NiO_x-Fe_2O_3-SnO_2-coated p-Si photocathodes in comparison to Pt-SnO_2-coated p-Si photocathode measured in the neutral pH water. Inset exhibits the current density of Pt-SnO_2-coated p-Si photocathode at dark and under illumination. Scan rate was 10 mV/sec.

The PEC performance of p-Si substrates with different metal oxide coatings is shown in Figure 9.4, in which all the samples exhibit photocathodic behavior in the scanned potential range. The Fe_2O_3-SnO_2-coated p-Si sample provides much higher photocurrent than the bare or SnO_2-coated p-Si substrates due to enhanced optical absorption originating from the textured surface and coupling of materials with different band gaps, improved charge separation coming from the junctions between p-Si, n-SnO_2 and n-Fe_2O_3, and increased reaction surface area coming from the NRs as shown in SEM images. As the optical absorption of Fe_2O_3-SnO_2-coated p-Si sample significantly increases than bare p-Si substrate, we believe that the absorption enhancement and after that improved charge separation play key roles in the performance enhancement. Due to coupling of Si and Fe_2O_3 with ~1.11 eV and ~2.1 eV band gaps, respectively, the Fe_2O_3-SnO_2-coated p-Si substrate can provide broadband spectral photoresponse and incident photon-to-current efficiency (IPCE).[38] The NiO_x NP coating also improves the photocurrent of p-Si substrate which can be because of catalytic effect of NiO_x NPs. The NiO_x NPs do not change the optical absorption of p-Si substrate in a significant way probably due to very thin and discontinuous NiO_x coating layer in the form of very small NPs and NiO_x large band gap. Note that the Fe_2O_3-SnO_2 coating layer is more effective in enhancing photocathodic performance than the NiO_x NP coating layer especially for photoactivity at 0 V versus RHE (as shown in Figure 9.4a) due to the aforementioned Fe_2O_3-SnO_2 layer properties. Using NiO_x NPs on the Fe_2O_3-SnO_2-coated p-Si substrate (this structure is called "NiO_x-Fe_2O_3-SnO_2-coated p-Si" hereafter), the photocurrent significantly increases resulting in a net photocathodic current (light current – dark current) of 0.25 mA/cm^2 at 0 V versus RHE and a cathodic onset potential of 0.25 V versus RHE. Note that the onset potential is calculated when the photocurrent reaches a value of -0.1 mA/cm^2. The onset potential shift of the NiO_x-Fe_2O_3-SnO_2-coated p-Si photocathode is 0.7 V and 0.38 V compared to the onset potential of NiO_x-coated (which is -0.45 V versus RHE) and Fe_2O_3-SnO_2-coated (that is -0.13 V versus RHE) p-Si photocathodes, respectively. The photocurrent at zero bias and onset potential can be further improved (shifting onset potential towards more positive potentials) using nanotextured Si substrates. These obtained results are really promising paving the way to achieve overall spontaneous solar water splitting in a full PEC system/device working in the neutral pH water.

The photocathodic performance of the NiO_x-Fe_2O_3-SnO_2-coated p-Si substrate is compared to that of the Pt-SnO_2-coated p-Si photocathode (Figure 9.4b) to see the effect of NiO_x-Fe_2O_3 NR film compared to Pt NPs for the improved HER performance. The Pt-SnO_2-coated p-Si photocathode provides lower current around 0 V versus RHE than the NiO_x-Fe_2O_3-SnO_2-coated p-Si photocathode with an onset potential of about 0 V versus RHE in the tested neutral solution. However, the Pt-SnO_2-coated p-Si photocathode offers much higher current than the NiO_x-Fe_2O_3-SnO_2-coated p-Si substrate at higher reversed biasing potentials. The achieved cathodic onset potential for the Pt-SnO_2-coated p-Si substrate is consistent with that reported for a nominally ~1 nm thick Pt coating using e-beam evaporation on the p-Si substrate at an electrolyte with a pH of 4.5[39] and the 5 nm thick Pt coating using e-beam evaporation on the sputtered-ZnO-coated p-Si substrate at a solution with a pH of 7.2.[40] In fact, the Pt-SnO_2-coated p-Si substrate does not provide significant photoactivity in which its current density at dark and under illumination is almost the same (Figure 9.4b inset). Note that the sputtered thin SnO_2

coating does not significantly improve the photocurrent of p-Si (see Figure 9.4a). Direct Pt coating on p-Si substrate also showed the same behavior of not having significant photoactivity, which is consistent with that reported before.[40] This is because e-beam evaporated Pt coating provides ohmic contact to p-Si substrate leading to high catalytic activity but without enabling a photovoltage at the interface.[39] Type of Pt deposition technique affects the HER performance in which an electroless deposition for Pt coating on p-Si substrate can provide high photocurrent at 0 V versus RHE and positive cathodic onset potential due to the fact that the electroless deposition provides an interfacial oxide barrier enabling an photovoltage at the interface.[11, 39] A buried n^+p junction can be used to get a photovoltage leading to obtain high photocurrent at 0 V versus RHE and positive onset potential for the e-beam-evaporated Pt coating on p-Si photocathodes.[11] Furthermore, the type of electrolyte significantly affects the performance of Pt-coated p-Si photocathodes in which acidic electrolytes provide much better performance than neutral solutions mainly due to higher activity of Pt in acidic electrolytes.

The stability performance of the Fe_2O_3-SnO_2- and Pt-SnO_2-coated p-Si photocathodes is shown in Figure 9.5. The Fe_2O_3-SnO_2 coating layer can stabilize the inherently unstable p-Si substrate. The orientation and morphology of p-Si substrate can affect the stability performance of Fe_2O_3-SnO_2-coated p-Si photocathodes in which p-Si nanowires made with Si(111) wafer provide much longer stability without any significant morphological changes after long-term stability and with preservation of all materials.[38] There is a gradual performance degradation for the Pt-SnO_2-coated p-Si electrode in which its current density decreases over time which can be possibly due to detachment of Pt NPs from the substrate. Note that the SnO_2-coated p-Si photocathode is not stable and

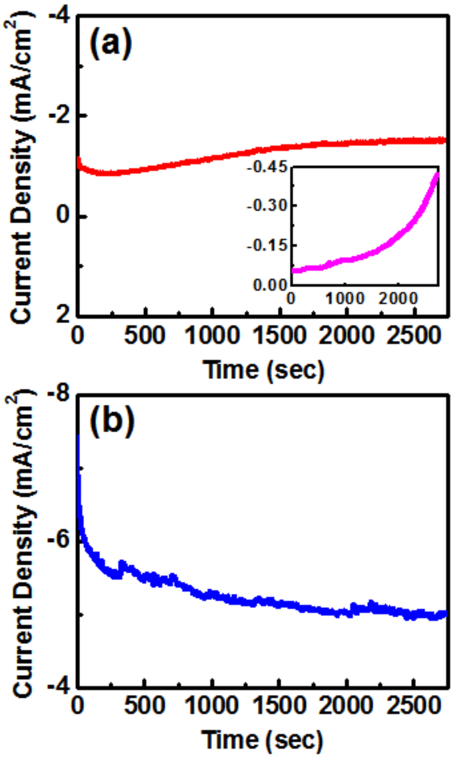

Figure 9.5. Current density under illumination versus time (stability test) measured in the neutral pH water at -0.66 V versus RHE of (a) Fe_2O_3-SnO_2-coated p-Si photocathode and (b) Pt-SnO_2-coated p-Si photocathode. Inset in (a) shows the stability test for the SnO_2-coated p-Si photocathode at -0.86 V versus RHE.

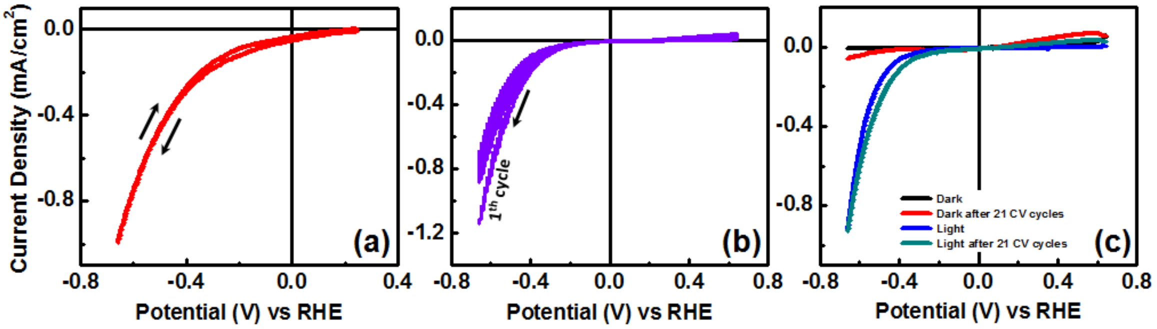

Figure 9.6. Cyclic voltammetry (CV) under illumination of (a) Fe_2O_3-SnO_2-coated p-Si photocathode and (b) NiO_x-coated p-Si photocathode for 21 cycles measured in the neutral pH water. (c) Current density under illumination and at dark before and after 21 CV cycles for the NiO_x-coated p-Si photocathode tested in the neutral pH water. Scan rate for (b) was 50 mV/sec, and for (a) and (c) was 10 mV/sec.

its photocurrent continuously increases possibly due to SnO_2 dissolution in the electrolyte (Figure 9.5a inset).

To further evaluate the stability performance of metal-oxide-coated p-Si substrates, we performed CV measurements as shown in Figure 9.6. The Fe_2O_3-SnO_2-coated p-Si photocathode does not show any corrosive peak indicating preservation of all materials within this heterostructure, which was also investigated by the SEM imaging after the PEC tests. The NiO_x-coated p-Si electrode was investigated under subsequent CV measurements (Figure 9.6b) in which its photocurrent decreases a little then reaches a stationary current level. There is no any corrosive peak in all CV scans as can be seen from Figure 9.6b. Although we did not observe any significant peak in the CV measurements indicating any NiO_x transformation in the performed neutral electrolyte, the NiO_x NPs may be converted to $Ni(OH)_2$ or Ni NPs under the HER condition.[32, 33] The current density (LSV measurement) of the NiO_x-coated p-Si photocathode does not change significantly after the long CV measurement shown in Figure 9.6b, indicating that a stable state is reached for the NiO_x catalyst on the p-Si substrate during the tested period. The NiO_x-Fe_2O_3-SnO_2-coated p-Si electrode also did not show any corrosive peak.

9.4 Conclusions

In summary, we showed facile and scalable solution growth of uniform NiO_x-Fe_2O_3 NR films, consisting of vertically aligned Fe_2O_3 NRs and coated NiO_x NPs. This new structure exhibited an improved solar water reduction characteristic in neutral solution on the surface of p-Si film photocathodes leading to photoactivity at 0 V versus

RHE and a cathodic onset potential of 0.25 V versus RHE. This study reveals the promising potential to design and engineer cost-effective Si/metal-oxide photoelectrodes for efficient solar water splitting in neutral and zero-bias conditions.

Chapter 9 was published in *Nanoscale* 2015, A. Kargar, J. S. Cheung, C.-H. Liu, T.K. Kim, C. T. Riley, S. Shen, Z. Liu, D. J. Sirbuly, D. Wang and S. Jin, "NiO_x-Fe_2O_3-coated p-Si photocathodes for enhanced solar water splitting in neutral pH water". The dissertation author was the first author of this paper.

References

1. McKone, J. R.; Lewis, N. S.; Gray, H. B. *Chem. Mater.*, **2013**, *26*, 407-414.

2. Wang, G.; Ling, Y.; Li, Y. *Nanoscale*, **2012**, *4*, 6682-6691.

3. Faber M. S.; Jin S. *Energy Environ. Sci.*, **2014**, *7*, 3519-3542.

4. Pinaud B. A.; Benck, J. D.; Seitz, L. C.; Forman, A. J.; Chen, Z.; Deutsch, T. G.; James, B. D.; Baum, K. N.; Baum, G. N.; Ardo, S.; Wang, H.; Miller, E.; Jaramillo T. F. *Energy Environ. Sci.*, **2013**, *6*, 1983-2002.

5. Walter, M. G.; Warren, E. L.; McKone J. R.; Boettcher, S. W.; Mi, Q.; Santori, E. A.; Lewis, N. S. *Chem. Rev.*, **2010**, *110*, 6446-6473.

6. Kibsgaard, J.; Chen, Z.; Reinecke, B. N.; Jaramillo, T. F. *Nat. Mater.*, **2012**, *11*, 963-969.

7. Lu, Z.; Wang, H.; Kong, D.; Yan, K.; Hsu, P.-C.; Zheng, G.; Yao, H.; Liang, Z.; Sun, X.; Cui, Y. *Nat. Commun.*, **2014**, *5*, doi:10.1038/ncomms5345.

8. Reece, S. Y.; Hamel, J. A.; Sung, K.; Jarvi, T. D.; Esswein, A. J.; Pijpers, J. J. H.; Nocera, D. G. *Science*, **2011**, *334*, 645-648.

9. Liu, C.; Dasgupta, N. P.; Yang, P. *Chem. Mater.*, **2013**, *26*, 415-422.

10. Hu, S.; Xiang, C.; Haussener S.; Berger, A. D.; Lewis, N. S. *Energy Environ. Sci.*, **2013**, *6*, 2984-2993.

11. Boettcher, S. W.; Warren, E. L.; Putnam, M. C.; Santori. E. A.; Turner-Evans, D.; Kelzenberg, M. D.; Walter, M. G.; McKone, J. R.; Brunschwig. B. S.; Atwater, H. A.; Lewis, N. S. *J. Am. Chem. Soc.*, **2011**, *133*, 1216-1219.

12. Sun, K.; Jing, Y.; Li, C.; Zhang, X.; Aguinaldo, R.; Kargar, A.; Madsen, K.; Banu, K.; Zhou, Y.; Bando, Y.; Liu, Z.; Wang, D. *Nanoscale*, **2012**, *4*, 1515-1521.

13. Mayer, M. T.; Du, C.; Wang, D. *J. Am. Chem. Soc.*, **2012**, *134*, 12406-12409.

14. Hu, S., Shaner, M. R.; Beardslee, J. A.; Lichterman, M.; Brunschwig, B. S.; Lewis, N. S. *Science*, **2014**, *344*, 1005-1009.

15. Yang, J.; Walczak, K.; Anzenberg, E.; Toma, F. M.; Yuan, G.; Beeman, J., Schwartzberg, A.; Lin, Y.; Hettick, M.; Javey, A.; Ager, J. W.; Yano Frei, H.; Sharp I. D. *J. Am. Chem. Soc.*, **2014**, *136*, 6191-6194. J.

16. Kenney, M. J.; Gong, M.; Li, Y.; Wu, J. Z.; Feng, J.; Lanza, M.; Dai, H. *Science*, **2013**, *342*, 836-840.

17. Oh, J.; Deutsch, T. G.; Yuan, H.-C.; Branz, H. M. *Energy Environ. Sci.*, **2011**, *4*, 1690-1694.

18. Cho, S. K.; Fan, F.-R. F.; Bard, A. J. *Angew. Chem. Int. Ed.*, **2012**, *51*, 12740-12744.

19. Boettcher, S. W.; Spurgeon, J. M.; Putnam, M. C.; Warren. E. L.; Turner-Evans, D. B.; Kelzenberg, M. D.; Maiolo, J. R.; Atwater, H. A.; Lewis, N. S. *Science*, **2010**, *327*, 185-187.

20. Chen, Y. W.; Prange, J. D.; Dühnen, S.; Park, Y.; Gunji, M.; Chidsey, C. E. D.; McIntyre, P. C. *Nat. Mater.*, **2011**, *10*, 539-544.

21. Liu, C.; Tang. J.; Chen, H. M.; Liu, B.; Yang, P. *Nano Lett.*, **2013**, *13*, 2989-2992.

22. Kargar, A.; Sun, K.; Jing, Y.; Choi, C.; Jeong, H.; Zhou, Y.; Madsen, K.; Naughton, P.; Jin, S.; Jung, G. Y.;Wang, D. *Nano Lett.*, **2013**, 13, 3017-3022.

23. Shi, J.; Hara, Y.; Sun, C.; Anderson, M. A.;Wang, X. *Nano Lett.*, **2011**, *11*, 3413-3419.

24. Jun, K.; Lee, Y. S.; Buonassisi, T.; Jacobson, J. M. *Angew. Chem. Int. Ed.*, **2012**, *51*, 423-427.

25. Sun, K.; Park, N.; Sun Z.; Zhou, J.; Wang, J.; Pang, X.; Shen, S.; Noh, S. Y.; Jing, Y.; Jin, S.; Yu, P. K. L.; Wang, D. *Energy Environ. Sci.*, **2012**, *5*, 7872-7877.

26. Strandwitz, N. C.; Comstock, D. J.; Grimm, R. L.; Nichols-Nielander, A. C.; Elam J.; Lewis, N. S. *J. Phys. Chem. C*, 2013, **117**, 4931-4936.

27. Kargar, A.; Sun, K.; Jing, Y.; Choi, C.; Jeong, H.; Jung, G. Y.; Jin, S.; Wang, D. *ACS Nano*, **2013**, *7*, 9407-9415.

28. Trotochaud, L.; Ranney, J. K.; Williams, K. N.; Boettcher, S. W. *J. Am. Chem. Soc.*, **2012**, *134*, 17253-17261.

29. Townsend, T. K.; Browning, N. D.; Osterloh, F. E. *Energy Environ. Sci.*, **2012**, *5*, 9543-9550.

30. McCrory, C. C. L.; Jung, S.; Peters, J. C.; Jaramillo, T. F. *J. Am. Chem. Soc.*, **2013**, *135*, 16977-16987.

31. Gong, M.; Zhou, W.; Tsai, M.-C.; Zhou, J.; Guan, M.; Lin, M.-C.; Zhang, B.; Hu Y.; Wang, D.-Y.; Yang, J.; Pennycook, S. J.; Hwang, B.-J.; Dai, H. *Nat. Commun.*, **2014**, *5*, doi:10.1038/ncomms5695.

32. Lin, C.-Y.; Lai, Y.-H.; Mersch, D.; Reisner, E. *Chem. Sci.*, **2012**, *3*, 3482-3487.

33. Koffyberg, F. P.; Benko, F. A. *J. Electrochem. Soc.*, **1981**, 128, 2476-2479.

34. Kato, H.; Asakura, K.; Kudo, A. *J. Am. Chem. Soc.*, **2003**, *125*, 3082-3089.

35. Osterloh, F. E. *Chem. Mater.*, **2007**, *20*, 35-54.

36. Osterloh, F. E. *Chem. Soc. Rev.*, **2013**, *42*, 2294-2320.

37. Vayssieres, L.; Beermann, N.; Lindquist, S.-E.; Hagfeldt, A. *Chem. Mater.*, **2000**, *13*, 233-235.

38. Kargar, A.; Kim, S. J.; Allameh P.; Choi, C.; Park, N.; Jeong, H.; Pak, Y.; Jung, G. Y.; Pan, X.; Wang, D.; Jin S. *Adv. Funct. Mater*., **2015**, *25*, 2609-2615.

39. McKone, J. R.; Warren, E. L.; Bierman, M. J.; Boettcher, S. W.; Brunschwig, B. S.; Lewis, N. S.; Gray, H. B. *Energy Environ. Sci.*, **2011**, *4*, 3573-3583.

40. Sun, K.; Madsen, K.; Andersen, P.; Bao, W.; Sun, Z.; Wang, D. *Nanotechnology*, **2012**, ***23***, 194013.

10. SOLUTION-PROCESSED COFE$_2$O$_4$ NANOPARTICLES ON 3D CARBON FIBER PAPERS FOR DURABLE OXYGEN EVOLUTION REACTION

10.1 Introduction

Water splitting for hydrogen fuel generation, either using electricity or sunlight as a driving force, is considered to be a viable pathway to fulfill the demanding energy requirements.[1-5] Catalysts play a significant role in the water splitting reactions, hydrogen or oxygen evolution reaction (HER or OER), to facilitate efficient gas evolution. Between the HER and OER, it is more difficult to achieve efficient and stable gas evolution in the OER, because the OER is kinetically slow and needs four electron transfer steps, compared to two electron transfer steps required for the HER. Therefore, the OER typically results in a considerable efficiency loss in the water splitting process.[6-9]

Among different OER catalysts, cobalt-based catalysts have attracted considerable attention due to their abundance, low cost, competitive OER activity to precious metal oxides, etc.[10-18] Cobalt phosphate (Co-Pi) has been demonstrated as a highly active OER catalyst working in neutral water by Nocera's group.[10, 11] Liang *et al.* have shown Co_3O_4/graphene hybrid as a very active OER catalyst which can also be used as an efficient oxygen reduction reaction (ORR) catalyst.[14] The cobalt-based catalysts can also be applied as OER catalyst/co-catalyst on the surface of semiconductor absorbers to simultaneously improve their OER performance and stabilize them.[19-21] McCrory *et al.* have reported $CoFeO_x$ as a promising OER electrocatalyst in 1 M NaOH solution with a low overpotential comparable to IrO_x but with much higher stability.[15] Particularly,

$CoFe_2O_4$ (cobalt ferrite) can be a promising electrocatalyst due to its unique properties.[22-25] On the other hand, size and morphology of catalyst are crucial to achieve efficient electrochemical or photoelectrochemical (PEC) water splitting and hydrogen production. For the electrochemical hydrogen generation, developing catalysts on high-surface-area substrates is very useful in order to achieve high-efficiency gas evolution, while for the PEC hydrogen production, developing small nanoparticles (NPs) to attach on the surface of semiconductor absorbers is necessary. Besides catalyst performance, catalyst electrode stability for long time is a key parameter to pave the way for practical hydrogen generation. Moreover, facile and scalable catalyst synthesis is also of significant importance in facilitating practical applications.

In this paper, we present $CoFe_2O_4$ NPs synthesized by a simple hydrothermal growth method and their attachment using spin coating on 3D carbon fiber papers (CFPs) for efficient and durable OER. The $CoFe_2O_4$ NPs-on-CFP electrode shows significantly enhanced OER performance compared to bare CFP due to high activity of the $CoFe_2O_4$ NPs. Noticeably, the $CoFe_2O_4$ NPs-on-CFP electrodes show long-term stability over continuous cycling (over 15 hrs) and operation with a high current density at a fixed potential (over 40 hrs) without any morphological and compositional changes. The $CoFe_2O_4$ NPs on CFP are characterized in detail before and after long-term stability tests. Furthermore, the $CoFe_2O_4$ NPs-on-CFP electrodes also show HER performance, which is substantially higher than that of bare CFP, acting as a bifunctional catalyst.

10.2 Experimental Section

Synthesis of $CoFe_2O_4$ NPs

Cobalt chloride ($CoCl_2{\cdot}6H_2O$) and iron chloride ($FeCl_2{\cdot}4H_2O$) were purchased from Alfa Aesar and utilized as precursors. 1 M of cobalt chloride aqueous solution and 1 M of iron chloride aqueous solution were mixed in a volume ratio of 1 to 2. The co-precipitation in hydroxide form of cobalt and iron was induced by adding 10 M NaOH aqueous solution gradually in the process of vigorous stirring until pH of the solution reached 11.5. The deionized (DI) water resistivity was 18.2 MΩ-cm for all the prepared solutions. The as-prepared solution with a high pH was transferred into a 45 mL sealed Teflon autoclave and subjected to hydrothermal growth for 20 hrs at a temperature of 150°C by putting the filled autoclave in a regular oven. The remaining precursor and reaction byproducts were removed with repeated washing in DI water followed by centrifuging, after which freeze-drying was employed for 24 hrs to dry the centrifuged particles.

Fabrication of $CoFe_2O_4$ NPs electrodes

The electrodes were prepared by spin coating of a $CoFe_2O_4$ solution onto the CFPs (FuelCellStore) or fluorine-doped tin oxide (FTO) substrates. The 0.66 wt% $CoFe_2O_4$ solution for spin coating was prepared in methanol followed by 30 mins sonication to have a uniform dispersion of NPs. The prepared solution was also underwent 15 mins sonication right before the spin coating process in order to have similar uniform concentration. The CFPs were subjected to 5 mins O_2 plasma before the spin coating. Note that the tested bare CFPs were also subjected to 5 mins of O_2 plasma for better comparison with the $CoFe_2O_4$-coated CFPs which were made using the plasma-treated CFPs. The O_2 plasma treatment before spin coating did not change the morphology of fibers. The FTO substrates were consecutively cleaned by sonication for 5 mins in acetone, isopropanol (IPA), and DI water, and finally rinsed with DI water and dried with N_2 gas. The CFP or FTO substrate was fixed on a clean glass slide as supporting substrate using a Kapton tape at one edge of substrate which also provided the contact area to attach a wire for measurement. To have a uniform distribution of $CoFe_2O_4$ NPs, three steps of spin coating were carried out with an optimized speed (rpm) and time for each step including (i) 500 rpm for 10 sec, (ii) 1500 rpm for 20 sec, and (iii) 4000 rpm for 60 sec. The three-steps spin coating was performed several times (16 times) to get as possible as uniform coating of the $CoFe_2O_4$ NPs on the CFP substrate, which will be shown in the following. The coating of NPs on the FTO substrate was also performed using the optimized three steps but with 6 times spin coating in which the NPs coating was not uniform due to aggregation of NPs. Coated Cu wire was then attached onto the CFP or FTO substrate using a conductive epoxy (CW2400) cured overnight at room temperature which provides an ohmic contact. The contact area was then sealed by the Hysol 1C epoxy, which was cured/dried over a long time, to prevent exposure to the electrolyte.

Characterization

The sample morphologies were examined on a Philips XL30 field-emission environmental scanning electron microscope (ESEM) at an accelerating voltage of 10.0 kV. Energy-dispersive X-ray spectroscopy (EDS) and elemental mapping analyses were used to examine the materials composition. Crystal structures of the $CoFe_2O_4$ NPs on

CFPs were characterized using X-ray diffraction (XRD) by a Bruker D2 Phaser X-ray diffractometer with Cu K_α (λ = 0.154 nm) as the radiation source.

Electrochemical measurements

Electrochemical measurements were performed in a ~80 mL aqueous solution of 1 M NaOH (Sigma-Aldrich) with a pH of 13.97 (DI water resistivity, 18.2 MΩ-cm) using a home-made setup with a teflon beaker and three electrodes configuration, including sample as working electrode (WE), Pt foil as counter electrode (CE), and Hg/HgO (1 M NaOH) as reference electrode (RE). The electrochemical measurements were collected using a potentiostat (Digi-Ivy, DY2300). A scan rate of 20 mV/s was employed for all the current density measurements. During the electrochemical measurements, a mild agitation was employed and the electrolyte was constantly purged with a small flow of N_2 gas. Also before the start of each electrochemical measurement, the electrolyte was purged with N_2 gas with higher flow than that used during the measurements. Note that for the evaluation of sample for both HER and OER performances (Figure 10.5), we did not use any gas purging during the test or before the test. The external biasing potentials here are versus Hg/HgO RE or reversible hydrogen electrode (RHE). The biasing potentials versus Hg/HgO RE ($E_{\mathrm{Hg/HgO}}$) were converted to the potentials versus RHE (E_{RHE}) using the Nernst equation as;

$$E_{\mathrm{RHE}} = E_{\mathrm{Hg/HgO}} + 0.059 \times \mathrm{pH} + E^{0}_{\mathrm{Hg/HgO}}\ (\mathrm{V}) \qquad (1)$$

where pH is the electrolyte pH and $E^0_{\mathrm{Hg/HgO}} = 0.098$ V versus normal hydrogen electrode (NHE) at 25°C for the Hg/HgO/1 M NaOH (CH Instruments, Inc.). The OER overpotential (η) was calculated using the below equation;

$$\eta = E_{\mathrm{Hg/HgO}} - E^0(\mathrm{O_2/H_2O})\ \ (\mathrm{V}) \qquad (2)$$

where $E^0(\mathrm{O_2/H_2O})$ is the thermodynamic potential for water oxidation (the OER) relative to Hg/HgO at pH = 13.97, which was calculated to be 0.307 V using;

$$E^0(\mathrm{O_2/H_2O}) = 1.23 - 0.059 \times \mathrm{pH} - E^0_{\mathrm{Hg/HgO}}\ \ (\mathrm{V}) \qquad (3)$$

The overpotential for the HER was also calculated using Equation 2 considering $E^0(\mathrm{H^+/H_2})$ instead of $E^0(\mathrm{O_2/H_2O})$. $E^0(\mathrm{H^+/H_2})$ is the thermodynamic potential for water reduction (the HER) relative to Hg/HgO at pH = 13.97, which was calculated to be -0.922 V using;

$$E^0(\mathrm{H^+/H_2}) = -0.059 \times \mathrm{pH} - E^0_{\mathrm{Hg/HgO}}\ \ (\mathrm{V}) \qquad (4)$$

All the potentials and plots reported here are without considering any *iR* correction. The current densities here are calculated using geometric surface areas.

10.3 Results and Discussion

Figure 10.1a-c show scanning electron microscopy (SEM) images of $CoFe_2O_4$ NPs spin-coated on the CFP. The coating of $CoFe_2O_4$ NPs on carbon fibers in the CFP is relatively uniform and dense, as shown in Figure 10.1b and c. SEM images of different parts of samples showed that most of the carbon fibers were uniformly coated with $CoFe_2O_4$ NPs. Note that there are some residues between some fibers which are due to

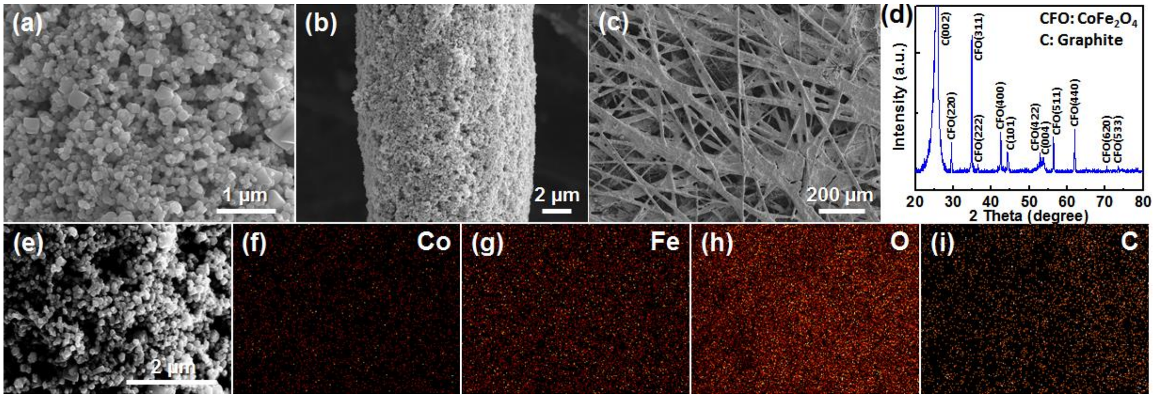

Figure 10.1. (a-c) SEM images (different magnification) and (d) XRD pattern of $CoFe_2O_4$ NPs on CFP. (e-i) Elemental mapping analysis of $CoFe_2O_4$ NPs on CFP; (e) SEM image of spot used for the elemental mapping, (f) Co map, (g) Fe map, (h) O map, and (i) C map. The scale bar for (f-i) is the same as that in (e).

the purchased CFP. The XRD pattern of $CoFe_2O_4$ NPs on CFP (Figure 10.1d) exhibits well-matched peaks with standard $CoFe_2O_4$ reference (JCPDS card no. 00-022-1086). The graphite peaks from the CFP can also be seen in the XRD pattern. The elemental mapping analysis shown in Figure 10.1e-i confirms the material composition of $CoFe_2O_4$ NPs on CFP.

The OER performance of $CoFe_2O_4$ NPs on CFP is shown in Figure 10.2a exhibiting a current density of 10 mA/cm^2 at an overpotential (η) of 378 mV. The achieved overpotential is consistent with that reported for the $CoFeO_x$ catalyst in 1 M NaOH.[15] The bare CFP shows a current density of 8 mA/cm^2 at η = 886 mV, demonstrating the remarkable catalytic effect of $CoFe_2O_4$ NPs. The $CoFe_2O_4$ NPs spin-coated on FTO substrate also show much higher OER performance than bare FTO substrate, confirming the high OER performance of $CoFe_2O_4$ NPs. The $CoFe_2O_4$ NPs on CFP do not show any hysteresis feature at high biasing potentials while there is a small

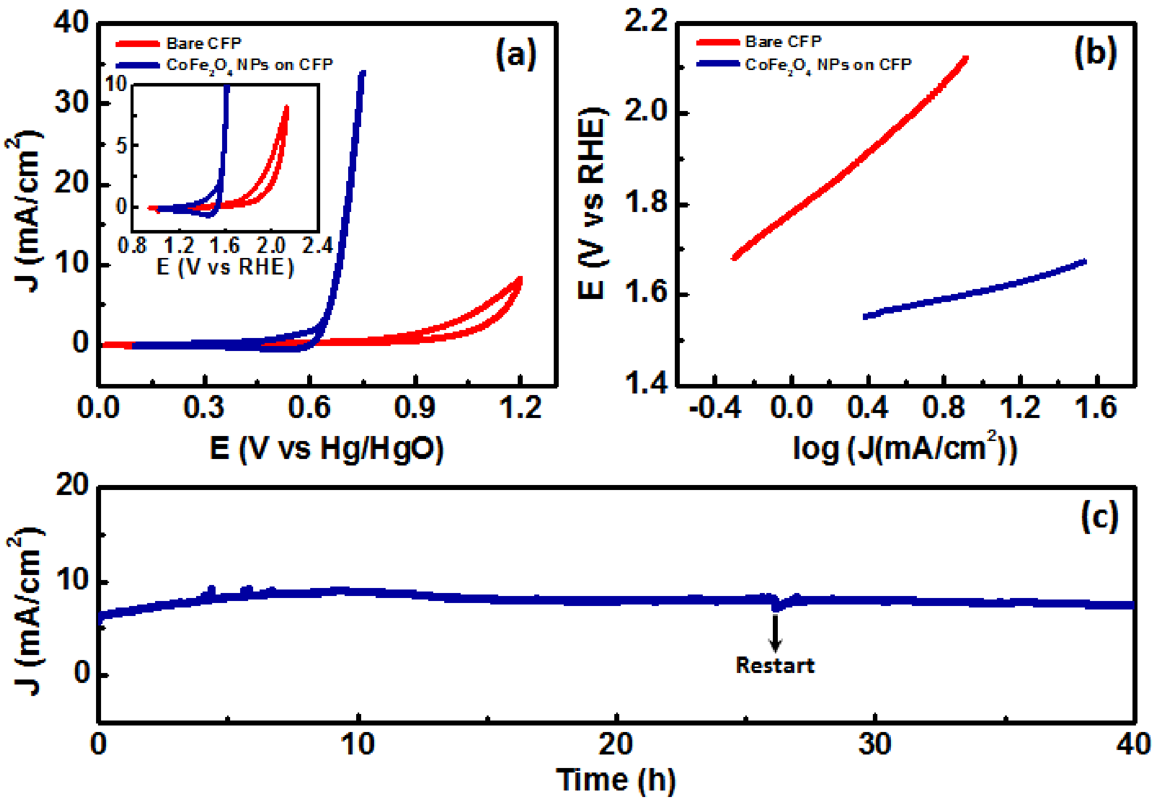

Figure 10.2. (a) Cyclic voltammetry (CV) measurement of $CoFe_2O_4$ NPs on CFP and bare CFP recorded at a scan rate of 20 mV/s in 1 M NaOH. Inset shows the zoomed-in current density versus RHE. (b) Tafel plot of corresponding samples in (a). (c) Current density versus time of $CoFe_2O_4$ NPs on CFP measured at a fixed potential of 0.675 V versus Hg/HgO RE in 1 M NaOH. The plots are without any *iR* correction.

hysteresis at low biasing potentials (see Figure 10.2a), which reaches a very small value over cycling (see Figure 10.3a and its inset). The $CoFe_2O_4$ NPs-on-CFP electrode shows a Tafel slope of ~73 mV/dec, much lower than that of bare CFP which is ~333 mV/dec (Figure 10.2b). The OER performance of the $CoFe_2O_4$ NPs may be further enhanced using electrochemical lithium tuning.[9] The developed catalyst structure can also easily be used for other metal oxide NPs catalysts to further reduce the overpotential and boost the performance. It is difficult to directly compare the achieved results with the reported $CoFe_2O_4$/biocarbon nanocomposite and $CoFe_2O_4$/graphene nanohybrid electrocatalysts as the test conditions and loading are different.[24, 25] The $CoFe_2O_4$ NPs-on-CFP electrode exhibits lower overpotential of 10 mA/cm^2 than the reported crystalline $CoFe_2O_4$ NPs on glassy carbon (η = 560 mV), though the catalyst loading may not be the same.[23] Importantly, the $CoFe_2O_4$ NPs-on-CFP electrode shows much longer investigated stability, which will be shown in the following, compared to the $CoFe_2O_4$ NPs-on-glassy-carbon,[23] $CoFe_2O_4$/biocarbon nanocomposite,[25] and $CoFe_2O_4$/graphene nanohybrid[24] catalysts.

The $CoFe_2O_4$ NPs-on-CFP sample exhibits a long stability of at least 40 hrs at a high current density without any morphological or materials changes (see Figure 10.2c). The electrode stability is also investigated by long cycling performance with detailed post characterization, which will be discussed in the following. As shown in Figure 10.2c, the current density first increases a little and then reaches a saturation state with minimal change over long time. No specific conditioning test before the long stability test was performed. After testing the sample for CV measurements and a short test of current density versus time, the sample was washed with DI water, the bubbles were removed from the electrolyte, and afterward the long stability test was run. To be certain about the performance and continuous operation, the measurement was stopped after 27.77 hrs and ran again (indicated in Figure 10.2c) without any change in the measurement setup and sample. As shown in Figure 10.2c, shortly after restarting, the current density reached saturation at the same current density as before stopping the measurement. To validate the morphology and materials preservation after such a long stability test, SEM imaging

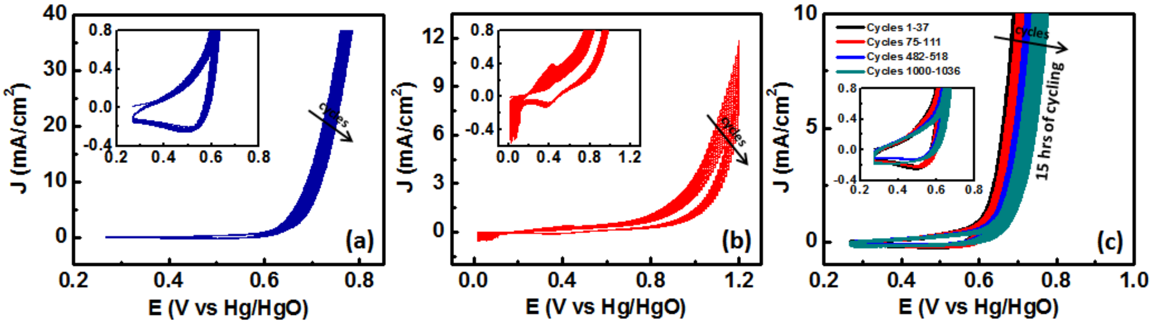

Figure 10.3. Consecutive cyclic voltammetry (CV) scans of (a) $CoFe_2O_4$ NPs on CFP (37 cycles) and (b) bare CFP (27 cycles) collected at a scan rate of 20 mV/s in 1 M NaOH. (c) Long cycling performance of over 1000 cycles, taking over 15 hrs, of $CoFe_2O_4$ NPs on CFP recorded at a scan rate of 20 mV/s in 1 M NaOH. Insets in (a-c) are the zoomed-in current density of the corresponding plots. Arrows in (a-c) show the direction of increase for the cycle number. The plots are without any *iR* correction.

was performed on the sample, showing that there is no noticeable morphological or material changes either in the $CoFe_2O_4$ NPs or in the carbon fibers. The achieved long-term stability of over 40 hrs is much longer than that investigated for the $CoFe_2O_4$/biocarbon nanocomposites (< 13 hrs),[25] $CoFe_2O_4$/graphene nanohybrids (< 13 hrs),[24] and $CoFe_2O_4$ NPs on glassy carbon (30 mins).[23] As the material itself is stable under such a high current density and alkaline electrolyte, we believe that much longer stability can be achieved.

The cycling performance of $CoFe_2O_4$ NPs-on-CFP electrode and bare CFP is shown in Figure 10.3a and b. Note that the data in Figure 10.3 was measured on another sample fabricated similarly to that shown in Figure 10.2. The overpotential of 10 mA/cm^2 for the $CoFe_2O_4$ NPs on CFP does not change over 37 consecutive CV cycles (see Figure 10.3a and its inset). Moreover, there is no hysteresis feature at high biasing potentials in all 37 CV scans (similar observation was seen for the $CoFe_2O_4$ NPs on the FTO substrate). At low biasing potentials, there is only a very small hysteresis for all CV scans

(Figure 10.3a inset). In contrast, the bare CFP shows hysteresis feature at both low and high biasing potentials with an increase in the overpotential over cycling (see Figure 10.3b and its inset). Also the high current densities at high biasing potentials do not change significantly for the $CoFe_2O_4$ NPs-on-CFP electrode while they decrease for the bare CFP over cycling. This may be an indication of the fact that the CFP and its surface may change in the NaOH solution and decoration of NPs helps the surface passivation.

The stability of $CoFe_2O_4$ NPs-on-CFP electrode was further investigated by a long cycling test of over 1000 cycles using a slow scan rate of 20 mV/sec and under continuous operation (measurement time was over 15 hrs) without any change in measurement setup and sample (Figure 10.3c). Up to over 100 cycles, there is no significant change in the overpotential at a current density of 10 mA/cm^2. Over larger number cycles, around 500 and 1000, there is only a very small change in the overpotential at a current density of 10 mA/cm^2 (overpotential difference between cycle 1 and cycle 1036 is about 100 mV (see Figure 10.3c and its inset)). Moreover, there is no hysteresis feature at high biasing potentials (Figure 10.3c) and at low biasing potentials, the hysteresis stays very small with negligible changes (Figure 10.3c inset). Over longer cycles of 500 and 1000, the current density at high biasing potentials starts to reduce which can be possibly due to the large amount of bubbles formed during the experiment. We performed 28 repeated tests of 37 consecutive cycles to get a total of 1036 cycles due to the limitation of our potentiostat. Thus, this can be another reason for the current density reduction at high biasing potentials. However, the current density at high biasing

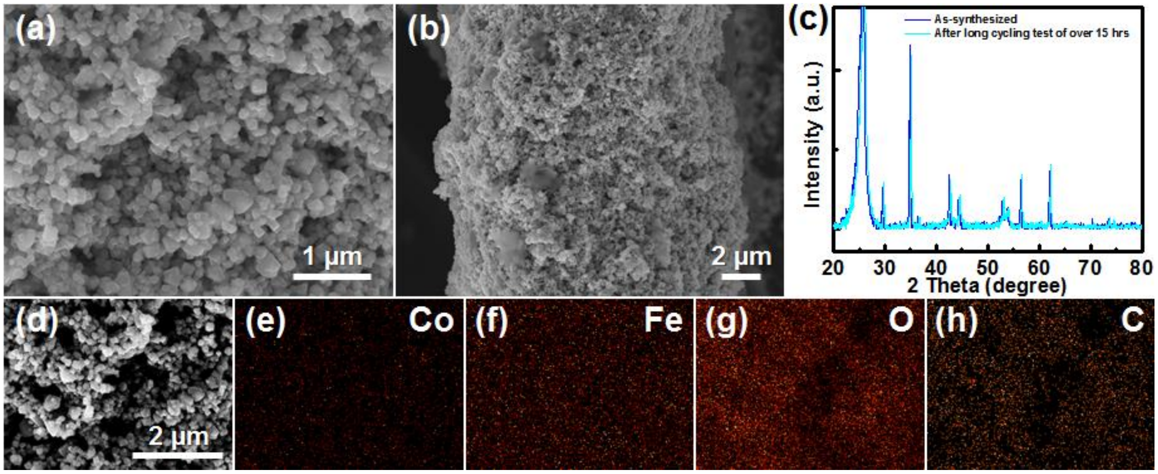

Figure 10.4. Characterization of $CoFe_2O_4$ NPs on CFP after long cycling test of over 15 hrs (shown in Figure 10.3c); (a,b) SEM images with different magnification, (c) XRD pattern along with the XRD of as-synthesized $CoFe_2O_4$ NPs on CFP for comparison, and (d-h) elemental mapping analysis of $CoFe_2O_4$ NPs on CFP; (d) SEM image of spot used for the elemental mapping, (e) Co map, (f) Fe map, (g) O map, and (h) C map. The scale bar for (e-h) is the same as that in (d).

potentials is not of particular interest for hydrogen production because the main purpose is to build full systems to run overall water splitting, which requires active electrodes with high current density at low biasing potentials.

It is useful to investigate the sample morphology and materials composition after long-time stability test to rule out any effect of side reaction affecting to achieve the long-term stability. The sample after the long cycling test of over 15 hrs was then investigated in detail using SEM imaging, XRD and elemental mapping analyses as shown in Figure 10.4. The morphology of $CoFe_2O_4$ NPs on CFP does not change significantly (Figure 10.4a and b) and all materials are preserved on the sample without any material transformation (Figure 10.4c-h). Note that the negligible shift (with the same degree) in all the diffraction peaks for the XRD pattern after the long cycling test (see Figure 10.4c)

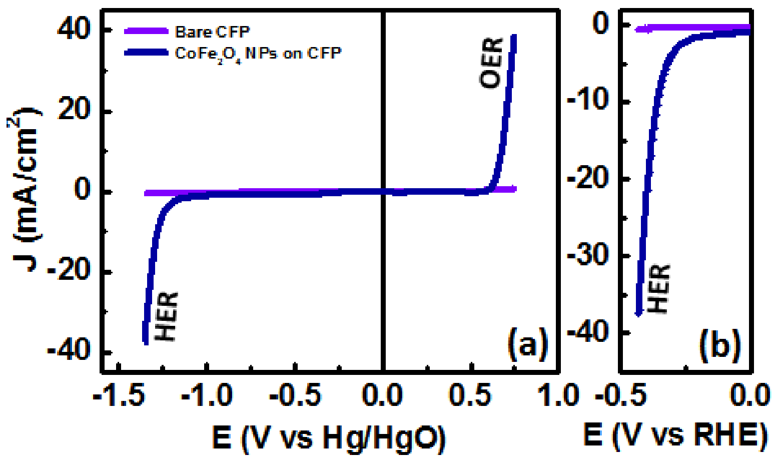

Figure 10.5. (a) Linear sweep voltammetry (LSV) measurement of $CoFe_2O_4$ NPs on CFP and bare CFP recorded at a scan rate of 20 mV/s in 1 M NaOH from positive to negative potentials. (b) Corresponding current density versus RHE for the HER performance. The plots are without any *iR* correction.

comes from the XRD machine. The achieved observation along with the long stability test of current density versus time clearly indicates that $CoFe_2O_4$ is a robust OER catalyst in alkaline electrolytes.

Another promising feature of the $CoFe_2O_4$ NPs on CFP is that they can also work as HER catalyst (Figure 10.5) making them a bifunctional electrocatalyst. As displayed in Figure 10.5a, the $CoFe_2O_4$ NPs-on-CFP electrode shows significantly enhanced OER and HER performances compared to bare CFP. The $CoFe_2O_4$ NPs-on-CFP electrode offers an HER current density of 10mA/cm^2 at 356 mV overpotential (see the zoomed-in current density versus RHE for the HER in Figure 10.5b). As mentioned in the experimental section, we did not use any gas purging for the measurement in Figure 10.5. This was because we want to evaluate the suitability of the bifunctional catalyst for a full PEC system, consisting of semiconductor photocathode and photoanode, to handle overall spontaneous solar water splitting in one specific electrolyte and cell. Although the

$CoFe_2O_4$ NPs-on-CFP electrode shows both HER and OER performances, it is more efficient for the OER due to low OER overpotential.

10.4 Conclusions

In summary, we showed $CoFe_2O_4$ NPs synthesized with a simple hydrothermal growth and their application on 3D CFPs for efficient and durable OER. The $CoFe_2O_4$ NPs on CFP exhibited orders of magnitude higher performance (current density, overpotential, and Tafel slope) than bare CFP, revealing the high activity of $CoFe_2O_4$ NPs for the OER. Significantly, the $CoFe_2O_4$ NPs-on-CFP sample showed long-term stability evaluated with 15 hrs of continuous cycling (>1000 cycles at a slow scan rate) and current density versus time for over 40 hrs without any morphological or compositional changes. Interestingly, the $CoFe_2O_4$ NPs-on-CFP electrodes also offered significantly enhanced HER performance compared to bare CFP, thus acting as a bifunctional catalyst. The obtained results reveal promising potential for efficient, cost-effective and durable hydrogen production at large scales using earth-abundant materials with low-cost fabrication processes.

Chapter 10 was published in *ACS Applied Materials & Interfaces* 2015, A. Kargar, S. Yavuz, T.K. Kim, C. H. Liu, C. Kuru, C. S. Rustomji, S. Jin and P. Bandaru, “Solution-processed $CoFe_2O_4$ nanoparticles on 3D carbon fiber papers for durable oxygen evolution reaction”. The dissertation author was the first author of this paper.

References

1. Walter, M. G.; Warren, E. L.; McKone, J. R.; Boettcher, S. W.; Mi, Q.; Santori, E. A.; Lewis, N. S. *Chem. Rev.* **2010**, *110*, 6446−6473.

2. Osterloh, F. E. *Chem. Soc. Rev.* **2013**, *42*, 2294−2320.

3. Kim, D.; Sakimoto, K. K.; Hong, D.; Yang, P. *Angew. Chem. Int. Ed.* **2015**, *54*, 3259−3266.

4. Gratzel, M. *Nature* **2001**, *414*, 338−344.

5. Wang, G.; Ling, Y.; Wang, H.; Xihong, L.; Li, Y. *J. Photochem. Photobiol. C Photochem. Rev.* **2014**, *19*, 35−51.

6. Chemelewski, W. D.; Lee, H.-C.; Lin, J.-F.; Bard, A. J.; Mullins, C. B. *J. Am. Chem. Soc.* **2014**, *136*, 2843−2850.

7. Trotochaud, L.; Ranney, J. K.; Williams, K. N.; Boettcher, S. W. *J. Am. Chem. Soc.* **2012**, *134*, 17253−17261.

8. Gong, M.; Li, Y.; Wang, H.; Liang, Y.; Wu, J. Z.; Zhou, J.; Wang, J.; Regier, T.; Wei, F.; Dai, H. *J. Am. Chem. Soc.* **2013**, *135*, 8452−8455.

9. Lu, Z.; Wang, H.; Kong, D.; Yan, K.; Hsu, P.-C.; Zheng, G.; Yao, H.; Liang, Z.; Sun, X.; Cui, Y. *Nat. Commun.* **2014**, *5*, 4345.

10. Esswein, A. J.; Surendranath, Y.; Reece, S. Y.; Nocera, D. G. *Energy Environ. Sci.* **2011**, *4*, 499−504.

11. Kanan, M. W.; Nocera, D. G. *Science* **2008**, *321*, 1072−1075.

12. Lutterman, D. A.; Surendranath, Y.; Nocera, D. G. *J. Am. Chem. Soc.* **2009**, *131*, 3838−3839.

13. Surendranath, Y.; Dincă, M.; Nocera, D. G. *J. Am. Chem. Soc.* **2009**, *131*, 2615−2620.

14. Liang, Y.; Li, Y.; Wang, H.; Zhou, J.; Wang, J.; Regier, T.; Dai, H. *Nat. Mater.* **2011**, *10*, 780−786.

15. McCrory, C. C. L.; Jung, S.; Peters, J. C.; Jaramillo, T. F. *J. Am. Chem. Soc.* **2013**, *135*, 16977−16987.

16. Yang, Y.; Fei, H.; Ruan, G.; Xiang, C.; Tour, J. M. *ACS Nano* **2014**, *8*, 9518−9523.

17. Deng, X.; Tüysüz, H. *ACS Catal.* **2014**, *4*, 3701−3714.

18. Suntivich, J.; May, K. J.; Gasteiger, H. A.; Goodenough, J. B.; Shao-Horn, Y. *Science* **2011**, *334*, 1383−1385.

19. Reece, S. Y.; Hamel, J. A.; Sung, K.; Jarvi, T. D.; Esswein, A. J.; Pijpers, J. J. H.; Nocera, D. G. *Science* **2011**, *334*, 645−648.

20. Yang, J.; Walczak, K.; Anzenberg, E.; Toma, F. M.; Yuan, G.; Beeman, J.; Schwartzberg, A.; Lin, Y.; Hettick, M.; Javey, A.; Ager, J. W.; Yano, J.; Frei, H.; Sharp, I. D. *J. Am. Chem. Soc.* **2014**, *136*, 6191−6194.

21. Liao, M.; Feng, J.; Luo, W.; Wang, Z.; Zhang, J.; Li, Z.; Yu, T.; Zou, Z. *Adv. Funct. Mater.* **2012**, *22*, 3066−3074.

22. Singh, R. N.; Singh, N. K.; Singh, J. P.; Balaji, G.; Gajbhiye, N. S. *Int. J. Hydrogen Energy* **2006**, *31*, 701−707.

23. Indra, A.; Menezes, P. W.; Sahraie, N. R.; Bergmann, A.; Das, C.; Tallarida, M.; Schmeißer, D.; Strasser, P.; Driess, M. *J. Am. Chem. Soc.* **2014**, *136*, 17530−17536.

24. Bian, W.; Yang, Z.; Strasser, P.; Yang, R. *J. Power Sources* **2014**, *250*, 196−203.

25. Liu, S.; Bian, W.; Yang, Z.; Tian, J.; Jin, C.; Shen, M.; Zhou, Z.; Yang, R. *J. Mater. Chem. A* **2014**, *2*, 18012−18017.